Probing living cells by terahertz Attenuated Total Reflection : permeabilization dynamics of the cell membrane

Xiujun Zheng

INSTITUT POLYTECHNIQUE DE PARIS

NNT : 2020IPPAX079

Thèse de doctorat

Probing living cells by terahertz Attenuated Total Reflection: permeabilization dynamics of the cell membrane

Thèse de doctorat de l'Institut Polytechnique de Paris
préparée à École Polytechnique

École doctorale n°626 l'Ecole Doctorale de l'Institut Polytechnique de Paris (ED IPP)
Spécialité de doctorat : Physique

XIUJUN ZHENG

Composition du Jury :

Juliette Mangeney Directeur de Recherche CNRS École normale supérieure, LPA	Présidente
Bruno Le Pioufle Professeur des Universités ENS Paris-Saclay, SATIE	Rapporteur
Mary Poupot Chargée de Recherche INSERM Centre de Recherche en cancérologie de Toulouse	Examinateur
Anne-Françoise Mingotaud Chargée de Recherche CNRS Université Paul Sabatier, IMRCP	Examinateur
Angelo Pierangelo Ingénieur de Recherche CNRS École Polytechnique, PICM	Examinateur
Guilhem Gallot Directeur de Recherche CNRS École Polytechnique, LOB	Directeur de thèse

Acknowledgments

The thesis for me was a period of joy to learn more about science though experiments than through meeting great people with whom I was able to talk. So, I want to express freely and sincerely my gratitude to people who helped me a lot.

First of all, I want to thank the members of my thesis jury, Juliette Mangeney, Bruno Le Piouffle, Mary Poupot, Anne-Françoise Mingotaud and Angelo Pierangelo, to be my thesis jury and to read carefully this manuscript then with helpful feedback on my work.

Foremost, I wish to express my gratitude to my supervisor, Guilhem Gallot who brought me into the Laboratoire d'Optique et Bioscience and guided my professional journey. I would like to say thank you for his outstanding and exceptional knowledge and patience during my thesis; for his helpful feedbacks on my publications, presentations and manuscripts. I am so glad to have had such a chance to work on an interesting and rewarding scientific project for three years.

I would like to thank all the members of the Laboratoire d'Optique et Biosciences, with whom I have shared three wonderful years. I wan to thank Francois Hache for his welcome in the laboratory as the head of laboratory, Jean-Marc, for the preparation of the many necessary elements to the realization of my experimental device, Rivo for his help on cell culture, as well as to Laure and Christelle for all administration work. Thank you Olga, Lipsa, Julia, Margeaux, Clothilde, Lien, Son, Thuy an Paul. Thank you also to Maxime, Rivo, Mayla for making our office so lively. I am so grateful for the many friends I have made here.

I would like to thank my parents for their unfailing support. It wouldn't have been possible to embark upon my scientific adventure without their support.

A thesis in physical science would be very hard to take on without funding, and I want to thank the Ecole Doctorale for the funding of my thesis work.

Thank you all!

Contents

List of acronyms

ATP : Adenosine TriPhosphate
ATR : Attenuated Total Reflectance
BCA : The BiCinchoninic Acid
Cell : HBSS solution without LED irradiation
DFG : Difference Frequency Generation
DMEM : Dulbecco's Modified Eagle Medium
FITC : Fluorescein Isothiocyanate
HBSS : Hanks' Balanced Salt Solution
HR-Si : High Resistivity Silicon
HRFZ-Si : High Resistivity Float Zone Silicon
L : HBSS solution with LED irradiation
LDH : Lactate DeHydrogenase
M : Empty PEO-PCL micelles solution without LED irradiation
MDCK : Madin-Darby Canine Kidney cell
ML : Empty PEO-PCL micelles solution with LED irradiation
MP : Pheo loaded in PEO-PCL micelles molecules
MPL : Pheo-PEO-PCL solution with irradiation
MTS : 3-(4.5-dimethylthiazol-2-yl)-5-(3-carboxymethoxyphenyl)-2-(4-sulfophenyl)-2H-tetrazolium
MTT : 3-(4.5-dimethylthiazol-2-yl)-2.5-diphenyltetrazolium
NEP : Noise Equivalent Power
P : Free Pheo solution without LED irradiation
PBS : Tampon Phosphate Salin
PCA : PhotoConductive Antennas
PDT : PhotoDynamic Theraphy
PEO-PCL : PolyEthylene Oxide-block-Poly(ϵ-caprolactone) micelles
PI : Propidium Iodide
PL : Free Pheo solution with LED irradiation
Pheo : Pheophorbide-a
Pheo-PEO-PCL : Pheo loaded in PEO-PCL micelles
QCL : Quantum Cascade Lasers
QCL-ATR : Attenuated Total Reflection based on Quantum Cascade Lasers
ROS : Reactive Oxygen Specifies

SECM : Scanning electrochemical microscopy
SNR : Signal-to-Noise Ratio
TEC : TermoElectric Coolers
THz-TDS : Terahertz Time-Domain Spectroscopy

Abstract in French

Le rayonnement térahertz se situe dans la gamme électromagnétique entre l'infrarouge lointain et les micro-ondes, correspondant à des fréquences comprises entre 0.1 et 10 THz. Cette zone spectrale est à l'heure actuelle très largement sous-exploitée, mais son application à l'étude d'objets biologiques a déjà montré un fort potentiel, dans la détection de cancers de la peau, le suivi de flux ioniques ou les biosenseurs. Dans le domaine de la biologie, qui nous intéresse particulièrement ici, la gamme des térahertz permet de quantifier et de discriminer des solutés d'intérêt biologique grâce à l'interaction avec les modes basse fréquence de l'eau liquide, et donc d'étudier les biomolécules, les microorganismes et les cellules dans leur environnement physiologique. La première partie de ce travail de thèse a consisté à étudier la dynamique de perméabilisation membranaire de cellules vivantes par réflexion totale atténuée (ATR) avec notre dispositif basé sur un laser femtoseconde et la génération d'impulsions térahertz ultracourtes. Des monocouches de cellules épithéliales MDCK ont été soumises à des concentrations variables de saponine, un détergent creusant des trous dans la membrane cellulaire. Les dynamiques obtenus ont ensuite été comparées à un modèle théorique décrivant le comportement physique de la couche cellulaire, et prenant en compte la diffusion des molécules de détergent ainsi que les caractéristiques physiques de la membrane. Le bon accord entre expérience et théorie nous indique que la perméabilisation membranaire est limitée principalement par la diffusion des molécules de détergent et leur fixation dur la membrane. Dans un second temps, nous avons développé un système totalement nouveau, basé sur une source QCL continue térahertz à 2,5 THz. Ce nouvel instrument est basé sur une conception très simplifiée, avec un seul prisme ATR et un seul détecteur, et sur une double modulation du faisceau térahertz à l'aide d'un hacheur mécanique. Ce hacheur synchronise la double modulation et définis les zones de mesure et de référence. La stabilité à long terme de cet appareil a été grandement améliorée grâce au contrôle précis de la température et de l'humidité à l'intérieur de l'appareil. Les performances sont excellentes tant à court terme qu'à long terme. Un rapport signal/bruit de 30 dB est obtenu sur 300 ms, 40 dB sur 30 s et il reste supérieur à 30 dB pendant plusieurs heures. En outre, une étude théorique et expérimentale a permis de calibrer l'instrument. Ainsi, les coefficients de réflexion ATR de plusieurs solutions d'intérêt biologique (ions, sucres et protéines) ont été obtenus sur une large gamme de concentrations. Une sensibilité au moins 20 fois supérieure à celle de la littérature existante a ainsi été obtenue. Grâce à ce nouveau système très performant, nous avons étudié la dynamique de la perméabilisation des membranes suite à l'action de la thérapie photodynamique

(PDT). Les premiers résultats ont montré que l'encapsulation des photosensibilisateurs par des vecteurs micellaires améliore significativement l'efficacité de la PDT.

Abstract in English

Terahertz radiation is located in the electromagnetic range between far infrared and microwaves, corresponding to frequencies between 0.1 and 10 THz. This spectral range is currently largely under-exploited, but its application to the study of biological objects has already shown a strong potential, in the detection of skin cancer, ion flow monitoring or biosensors. In the field of biology, which is of particular interest to us here, the terahertz range makes it possible to quantify and discriminate solutes of biological interest thanks to the interaction with low-frequency modes of liquid water, and thus to study biomolecules, microorganisms and cells in their physiological environment. The first part of this thesis work consisted in studying the dynamics of membrane permeabilization of living cells by attenuated total reflection (ATR) with our device based on a femtosecond laser and the generation of ultrashort terahertz pulses. Monolayers of MDCK epithelial cells were exposed to varying concentrations of saponin, a detergent that digs holes in the cell membrane. The dynamics obtained were then compared to a theoretical model describing the physical behavior of the cell layer, taking into account the diffusion of detergent molecules and the physical characteristics of the membrane. The good agreement between experiment and theory indicates that membrane permeabilization is limited mainly by the diffusion of detergent molecules and their binding to the membrane. In a second part, we developed a completely new system based on a continuous terahertz QCL source at 2.5 THz. This new instrument is based on a very simplified design, with a single ATR prism and a single detector, and on the dual modulation of the terahertz beam using a mechanical chopper. This chopper synchronizes the dual modulation and defines the measurement and reference zones. The long-term stability of this device has been greatly enhanced by the precise control of temperature and humidity inside the device. Performance is excellent in both the short and long term. A signal-to-noise ratio of 30 dB is achieved over 300 ms, 40 dB over 30 s and remains above 30 dB for several hours. In addition, a theoretical and experimental study has been carried out to calibrate the instrument. Thus, the ATR reflection coefficients of several solutions of biological interest (ions, sugars and proteins) were obtained over a wide range of concentrations. A sensitivity at least 20 times higher than that of the existing literature was thus obtained. Thanks to this new high-performance system, we studied the dynamics of membrane permeabilization following the action of photodynamic therapy (PDT). The first results showed that the encapsulation of photosensitizers by micellar vectors significantly improves the efficiency of PDT.

General introduction

My thesis took place at the Laboratory for Optics and Biosciences (LOB) of the Ecole Polytechnique in France. The general philosophy of the laboratory is to develop synergies between physics and biology in order to promote new concepts and tools, in particular for the understanding of the functioning of the biological systems, from tissues to the single molecule.

The study of substances via their interactions with light has long been a favored method for understanding their properties. This is particularly the case for the study of biological organisms using optical techniques. In particular, information obtained by biological or medical imaging is used to identify certain functional disorders and to study their interactions with various drugs, which can contribute to the development of new medical treatments. The electromagnetic domain of terahertz frequencies, located between the visible and infrared ranges, is a field in deep development, full of possibilities and new discoveries. The purpose of this thesis is to research and develop new tools for biology using this terahertz radiation.

In this paper, we will first discuss the main properties of terahertz waves, their advantages and possible applications. A fundamental characteristic of biological bodies is that they are mainly made of water. And it turns out that the interactions between water and biological solutes (ions, peptide, proteins, etc.) are very complex in the terahertz range. We will see that water is a new source of contrast for imaging despite its strong absorption in this spectral range.

This thesis is divided as follows:

In Chapter 1, we will begin by presenting the terahertz domain, located between the optical and radio-frequency wave domains. It thus shares certain aspects with these two frequency domains. We will then see how ultra-short terahertz pulses can be generated and how their electric field can be measured with a high temporal resolution. This will allow us to directly determine the amplitude and phase of these waves. We will analyze the characteristics and performances of terahertz spectroscopy systems in the time domain (THz-TDS) , before illustrating some practical applications. In the last section, we will present the previous work of our team to show how the interactions between the terahertz wave and substances in aqueous media can be understood. This section describes the origin of the experimental terahertz contrast signal as a function of the size of the solutes and their concentration. We propose to take advantage of terahertz radiation in biological samples and to use it as a tool for the study of biological samples, especially living cells.

In Chapter 2, we review the characteristics of mammalian cells and the structure and

functions of their cell plasma membrane. This review helps us to understand techniques to control and increase membrane permeability. The methods examined include direct membrane disruption (e.g. using detergents, an electrical pulse or an optical beam accompanied by photosensitizers) and carrier-mediated techniques. These techniques allow cargo to pass through the cell membrane and then arrive in the target area. In parallel with disruption techniques, methods to control the dynamics or the final state of membrane permeability are also discussed.

Based on the terahertz contrast measuring the intracellular protein concentration, we propose a tool for the analysis of protein exchanges between the inside and outside of living cells. In chapter 3, based on terahertz spectroscopy in the time domain (THz-TDS), we demonstrated that the attenuated total reflection geometry (ATR) is the ideal choice for probing cells in their physiological environment. Compared to other methods of probing cell membrane permeability, our tool is a non-invasive and non-labelled in vivo technique. We then applied this method to quantify membrane permeability in real time by chemical means. A physical model is proposed on the basis of experimental data to explain the dynamics of permeability perturbed by detergents.

In chapter 4, we describe the limitations of the THz-TDS ATR configuration, and propose a new, significantly more performing technique, based on a continuous quantum cascade laser, and on a double modulation of the beam. The calibration of the new device is presented, allowing the study of solutions of biological interest. This new tool is then used to study the effect of photodynamic therapy (PDT) on membrane permeability. Our collaboration with a group from IMRCP (Laboratoire des Interactions Moléculaires et Réactivité Chimique et Photochimique) at Toulouse allows us to obtain the first results of a real-time analysis of the dynamic information exchanges of the cell membrane during PDT.

Chapter 1

General concepts: Terahertz radiations and biology

Contents

The range of terahertz waves lies between microwaves and infrared, which gives terahertz radiation unique properties. In this chapter we will introduce the general properties of the terahertz domain as well as the main terahertz devices: sources, detectors. Then we will consider its interaction with matter. In particular, we will focus on time domain terahertz spectroscopy (THz-TDS) that we used during the first part of this thesis. We will explain the reasons for the recent interest in terahertz radiation, which distinguishes terahertz from other domains. The motivations and applications of terahertz radiation in biology and medicine will then be given, including the difficulties that may be encountered.

1.1 General properties of the terahertz radiations

Terahertz radiations are electromagnetic waves with an oscillation frequency between 0.1 and 10 THz (1 THz=10^{12} Hz)[1], between the microwave and infrared domains (see figure 1.1). This intermediate situation brings together the characteristics of these two domains, and many techniques are thus inherited from either the microwave or the infrared. Technological difficulties, both in generation and detection, have long slowed down the development of the terahertz domain. However, the "terahertz gap" has been gradually bridged over the last thirty years. Many techniques have been developed to take advantage of the unique properties of the terahertz radiations, particularly for spectroscopy and imaging. Nowadays, numerous applications are found in physics, chemistry and biology, as well as in industries.

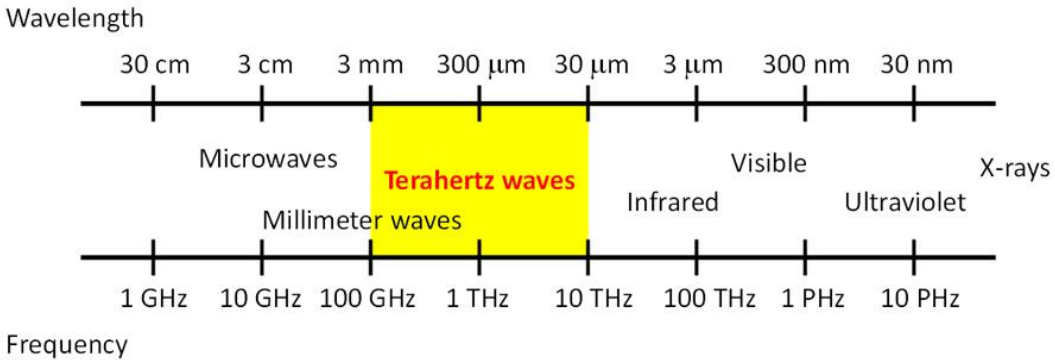

Figure 1.1: Position of the terahertz domain in the electromagnetic spectrum.

Two properties are fundamental for applications in biology. Firstly, terahertz radiation has a strong interaction with water molecules in the liquid state, which is essential for probing biological systems with terahertz waves. Its energy is comparable to that of hydrogen bonds, making it sensitive to various vital processes in living tissues and cells [1]. Its energy is also low enough to be harmless to tissues, unlike X-rays. But it also requires taking into account the strong absorption of water, which is very often problematic by restricting the penetration depth through the samples. Secondly, classical imaging techniques are constrained

[1] 1 THz $\equiv$ 300 µm $\equiv$ 33.3 cm^{-1} $\equiv$ 4.1meV.

by diffraction, whose limit is of the order of the wavelength (λ=300 µm at 1 THz). Near-field techniques must then be used to overcome this limit.

Over the full electromagnetic spectrum, the absorption coefficient and index of refraction of bulk water is showed in figure 1.2. In the terahertz range, the dielectric properties of bulk water have been studied by Møller et al [2]. The terahertz radiation corresponds to the dielectric response of the hydrogen bonding network, the low vibrational modes of water molecules [2]. We can observe that the terahertz domain (in gray) fulfill several important advantages. Absorption is lower than in the infrared. The dispersion of the index of the refraction remains strong, contrary to the visible range and preserve the sensitivity to liquids. And the wavelength is small enough to allow imaging, contrary to the microwaves.

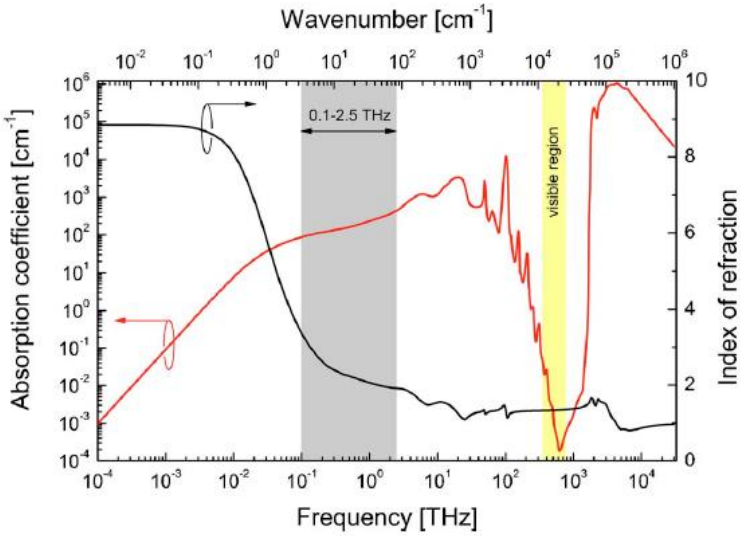

Figure 1.2: The broadband spectroscopy of bulk water including the absorption spectrum on a logarithmic scale (red curve) and the refractive index on a linear scale (black curve) in function of frequency (lower axis) or wavenumber (upper axis). The gray area includes the 0.1-2.5 THz region, and the yellow area indicates the visible part of the spectrum [2].

It should also be noted that even in the case of atmospheric water vapour, the attenuation of terahertz radiation remains strong. This is a crucial point for telecommunication applications, but it is also a concern in free space laboratory terahertz systems.

1.1.1 Terahertz sources and detectors

The terahertz range is difficult to reach using traditional techniques, both in terms of emission and detection. Many techniques have been developed to work in this frequency range. Each of them has its advantages and disadvantages. There is a review of the most important devices.

1.1.1.1 Sources

There are many sources of terahertz radiation and they can be separated into two categories: pulsed and continuous sources. Pulsed terahertz sources provide access to electric field measurements in the time domain and continuous terahertz sources generally have higher spectral resolution and higher power but phase information is usually lost.

Broadband ultrashort sources

Terahertz pulse generation methods are generally based on femtosecond (fs) lasers in the visible or infrared. The method using photoconductive antennas (PCA) was introduced by Auston in 1984 [3]. It is based on the creation of dipoles induced by accelerated transient charges in a static field [4]. The charges are photocarriers generated by a femtosecond laser illuminating a semiconductor substrate. The static field is imposed by a DC voltage applied to two metal lines embedded in the substrate. Thus, the charges accelerate and then emit a transient radiation: a terahertz pulse. The semiconductor substrate can be GaAs with femtosecond lasers in the near infrared ($\approx 800\,\text{nm}$) or InGaAs with a laser source at telecommunications wavelengths ($\approx 1550\,\text{nm}$). With a high femtosecond laser repetition rate, this technique generates relatively low-power terahertz pulses because the laser's incident power is limited so as not to destroy the antenna. Higher powers can be achieved with amplified femtosecond lasers. The frequency range generated is determined by the lifetime of the carriers in the semiconductor and the duration of the femtosecond pulses. Typical lifetimes are below 1 ps to achieve the generation of terahertz radiation. More details will be found in section in section 1.1.2.

The generation of terahertz pulses by optical rectification in non linear crystals is based on second order nonlinear optical phenomena that occur when a femtosecond laser interacts with certain types of crystals such as zinc telluride (ZnTe) or diethylaminosulfide trifluoride (DAST) [5]. The result of the femtosecond laser perturbation on the crystal transiently changes the polarization of the crystal. This change in polarization emits a pulsed electromagnetic field in the terahertz spectrum. With intense femtosecond lasers, it is possible to obtain an output power significantly higher than that generated by PCA. The spectral characteristics of the generated terahertz pulses can be adjusted by changing the temporal properties of the incident beams [6].

Mysyrowicz's team obtained a highly collimated terahertz beam from filamenting a femtosecond laser beam in the air [7]. The focusing of a short intense pulse ($\ll$100fs and $\gg$1mJ) in the air gives rise to a plasma. The competition between phase self-modulation (optical Kerr effect) and dispersion in the plasma leads to the creation of a filament in the non-linear interaction zone. The filament front moves at the speed of light and the space charges created behind the ionization front emit a radiation in the terahertz range in the form of a cone caused by the Cerenkov effect. This method generates intense terahertz radiation at the position determined by the focus of the incident laser.

Likewise, Zhang's group demonstrated the generation of terahertz waves by focusing two

optical pulses into the air to form a laser plasma filament [8,9]. The control of the polarization of the emitted THz radiation is allowed [8]. The creation of two filaments side by side allows to modulate the emitted intensity and to improve emission efficiency by adjusting the distance between the two filaments [10]. Besides, the plasma filament can serve as both a source and a detector [9].

Monochromatic continuous sources

The generation of continuous terahertz radiation has the advantage of good spectral fineness and high average powers. One of the generation methods, called "Quantum Cascade Lasers" (QCL) [11], uses periodic semiconductor devices with a finely adjustable bandgap in the terahertz range. The transition of electrons within the ultra-thin layers of the semiconductor structure results in the emission of photons at each period. Since the transition levels are determined by the band structures, it is possible to generate photons from the near infrared to the terahertz range. The emission of QCLs is coherent, powerful and continuous. A QCL source will be used in chapter 4 to develop our new terahertz cell sensor.

The difference frequency generation (DFG) of terahertz radiation is widely used. Two beams with similar wavelengths are focused on a non-linear crystal, resulting in an output beam whose frequency is the difference between the two input beam frequencies [12]. This output beam is a continuous terahertz radiation with a fine spectral waveform whose frequency can be adjusted by changing the input frequencies. The terahertz output gain depends on the non-linear second order properties of the crystal. Frequency mixing in a PCA is also widely used for high resolution spectroscopy [13].

Optically pumped molecular lasers can also generate terahertz radiation. The energy of the molecular rotations of gas molecules can correspond to terahertz energy levels [14]. By using a high power optical beam as a pump, a specific gas (such as CO_2) can generate stimulated amplification at frequencies corresponding to its discrete rotational transition levels. This technique provides good spectral accuracy at high power, but the frequency is fixed by the gas used.

The generation of a continuous source in the terahertz range can also be achieved with a back-wave oscillator (BWO) based on the Smith-Purcell effect, which is the interaction between an electron beam and a metal grating [15]. The modulation of the phase velocity of the beam creates terahertz radiations in the opposite direction. These devices generate intense terahertz radiation at low frequencies.

Free electron lasers and synchrotron radiation work on the same principle. The idea is to accelerate an electron beam and then deflect it using strong magnetic fields so that it emits synchrotron radiation in the terahertz range [12]. The terahertz radiation generated is very intense and generally incoherent. This technique requires a large space to install all the elements and is therefore not a conventional source in the terahertz range.

1.1.1.2 Detectors

For the detection of terahertz waves, two categories can be distinguished: coherent detection and incoherent detection. Coherent detection generally concerns pulsed waves, and the coupling of the emission and detection processes. The use of a femtosecond laser is standard. It allows electric field measurements in the time domain with excellent signal-to-noise ratio, but with the cost of acquisition speed. Conversely, incoherent detection uses intensity-sensitive detectors, which are not sensitive to the phase of the incident fields, but are simpler to use than coherent detection techniques.

Coherent detectors

Photoconductive antennas (PCA), already used as a source of terahertz radiation, are one of the techniques for coherent detection [12]. The principle of operation is reversed with respect to the emission process. The PCA consists of two metal lines on a semiconductor substrate. When a laser pulse illuminates the substrate, the photocarriers recombine in a very short time (τ<1 ps). If the laser pulse arrives at the same time as an incoming terahertz radiation, the latter will cause the motion of the photocarriers, creating a current between the metal lines. This current can be detected. By modifying the arrival time between the laser beams from the source and detector, it is possible to sample the terahertz field. This technique will be detailed in section 1.1.2.

Electro-optical effect detection is a coherent detection which consists in the temporal superposition of a terahertz beam and a femtosecond laser beam in a crystal having electro-optical properties (such as ZnTe). The terahertz radiation modifies the birefringence of the crystal, leading to a phase shift of the femtosecond laser pulse and resulting in a change in polarization [12]. By measuring the modified polarization state, it is possible to determine the amplitude of the terahertz field. By changing the delay between the two beams, the terahertz electric field can be temporally sampled. This technique is particularly useful for imaging because it is possible to spatially superimpose two beams in a large crystal. Thus, the use of a CCD camera makes it possible to obtain temporal and spatial information in a single measurement [16].

Air-biased-coherent-detection has similar working principles with the generation of terahertz radiation by filamentation in air assisted by short intense pulses. The focus of a terahertz pulse and an intense femtosecond laser beam between two polarized electrodes generates the second harmonic radiation. By detecting the intensity of the second harmonic as well as varying the time delay between the two beams, the amplitude of the terahertz pulses can be obtained over time [17]. It was showed that by using nitrogen fluorescence encoding, the plasma can serve for both emission and detection [9]. Therefore terahertz pulse detection is no longer restrained by electrodes or solid state materials.

Incoherent detectors

The second detection class is incoherent detection, which only detects the intensity in a

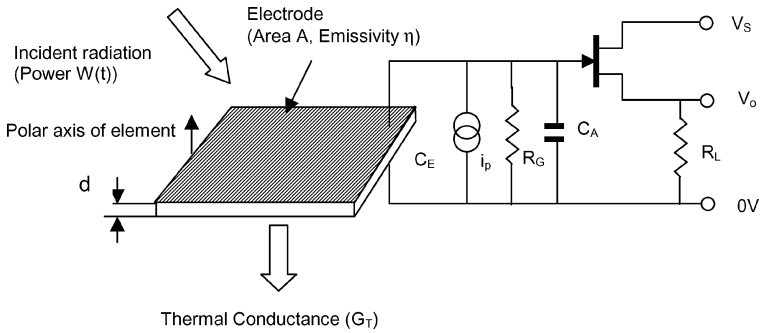

Figure 1.3: Schematic diagram of a pyroelectric detector element [21].

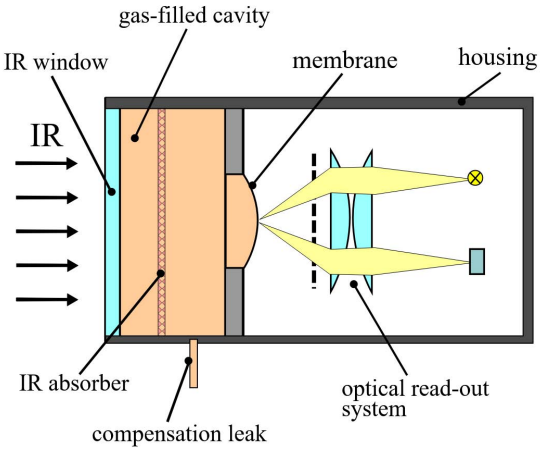

Figure 1.4: Principle of a gas-filled Golay sensor with optical read-out [22].

given frequency band, for example pyroelectric detectors [18], Golay cells [19], and bolometers or microbolometers [20].

A pyroelectric detector is a thermal sensor whose response range covers most of the electromagnetic spectrum, including the terahertz region. This detector is usually based on a thin, permanently polarized ferroelectric crystal that has a pyroelectric effect. This means that when the crystal is heated, its instantaneous electrical polarization is changed accordingly (see figure 1.3). With two electrodes on each side of the crystal, these temperature changes can be transformed into electrical charges and can be coupled out of the crystal and amplified. Finally, a calibration allows to determine the sensitivity of the detector (in A/W) [21]. The pyroelectric detector is only sensitive to radiation power.

A pneumatic Golay cell [23] contains an internal gas-filled enclosure, one side of which is made of a metallic infrared absorbing film, and the other side of a thin membrane (see figure 1.4). When infrared radiation is transmitted through the infrared window and then absorbed by the metal film, the gas in the enclosure is heated, causing it to expand, so that higher

Table 1.1: Comparison of terahertz detectors

Detector types	Golay cells	Pyroelectric detectors	Microbolometers
Detector size [mm]	6	1.5∼9 (could be lager)	to be designed as an array
NEP [W/Hz$^{1/2}$]	$10^{-9} \sim 10^{-10}$	$1\times10^{-9} \sim 3\times10^{-9}$	$1 \times 10^{-10} \sim 5\times10^{-11}$ [20,25,26]
Maximum power	∼10 µW	>50 mW/cm^2	∼150 µW
Operating temperature	5 to 40°C	-5 to 120°C	room temperature

pressure is applied to the thin membrane. The deformation of this membrane causes the deflection of a light sent to the reflecting membrane, which can be detected by a photodiode. The output signal of the photodiode is then proportional to the movement of the membrane, and the output can be calibrated to the input infrared radiation [22, 23]. A Golay cell can operate at room temperature.

A bolometer [24] is a device for measuring the strength of incident electromagnetic radiation by heating a material whose electrical resistance depends on temperature. A bolometer consists of an absorbent element, such as a thin layer of metal, connected to a thermal reservoir (a body at constant temperature) by a thermal connection. The result is that any radiation that strikes the absorber element raises its temperature above that of the reservoir - the greater the power input, the higher the temperature. The change in temperature can be measured directly with a resistive thermometer, or the resistance of the absorber element itself can be used as a thermometer.

The noise equivalent power (NEP) is one of the most important parameters to quantify the sensitivity of these detectors. It is related to the intrinsic thermal fluctuation of the detectors with the following formula [27]

$$NEP = (4k_B T G_{th})^{1/2} \tag{1.1}$$

where k_B is Boltzmann's constant, T is the temperature (K), and G_{th} is the thermal conductance (W/K) between the detector and the thermal reservoir. A low NEP value corresponds to a higher performance of the detector, resulting from a lower value of G_{th}. In the table 1.1, three types of terahertz detectors are compared. Golay cell detectors are very sensitive, even a power lower than nW can be detected in a wide spectral range. However, it has a slow response time (> ms) and a limited power threshold of about 10 µW due to the fragility of the thin membrane. Pyroelectric sensors are also sensitive to the nW power level, with a faster response time (microseconds to milliseconds). In addition, they can operate over a wider operating temperature range, and have a maximum detection power of more than 50 mW, which means that temperature fluctuations have less influence on pyroelectric sensors. As a

room temperature detector, microbometers can achieve the best noise performance, and can be used in sensor arrays to build terahertz cameras.

1.1.2 Terahertz time-domain spectroscopy

Terahertz time-domain spectroscopy (THz-TDS) is now a classic technique to measure the amplitude of a terahertz wave over a wide range of frequencies. In classic spectroscopy, the intensity of the wave is recorded in function of its frequency. In THz-TDS, the amplitude of the wave is recorded in function of time, and a Fourier transform provides the spectroscopic information. This technique was proposed in the 60s by Nicolson [28, 29] for the microwave domain. Common THz-TDS setups are based on titanium sapphire or fiber femtosecond lasers [30].

In what follows, we consider the scalar harmonic solutions of the Maxwell equations. In coordinates (x, y, z), the general waveform of a harmonic plane wave propagating in the z direction, which is the basis for the decomposition of scalar electromagnetic waves using Fourier transforms, is written as

$$E(\vec{r}, z, t) = \mathrm{Re}\left\{\vec{A}(\vec{r})e^{i(kz-\omega t)}\right\} \tag{1.2}$$

where $\vec{A}(\vec{r})$ is a slowly varying function of the transverse vector $\vec{r} = x\,\vec{e}_x + y\,\vec{e}_y$, ω is the wave pulsation and k is the wave vector. The amplitude $\vec{A}$ is complex and can be decomposed over the two polarization directions $\vec{e}_x$ and $\vec{e}_y$, as $\vec{A} = A_x\,\vec{e}_x + A_y\,\vec{e}_y$. Thus, $|A_x|$ and $|A_y|$ are the amplitudes of the two polarizations, while $\arg(A_x)$ and $\arg(A_y)$ are the phases of the waves. Linear polarization is the polarization state for which one of the field components is zero ($\mathrm{A}_x = 0$ or $\mathrm{A}_y = 0$) or the phase shift of two components is zero (φ_x-φ_y=0).

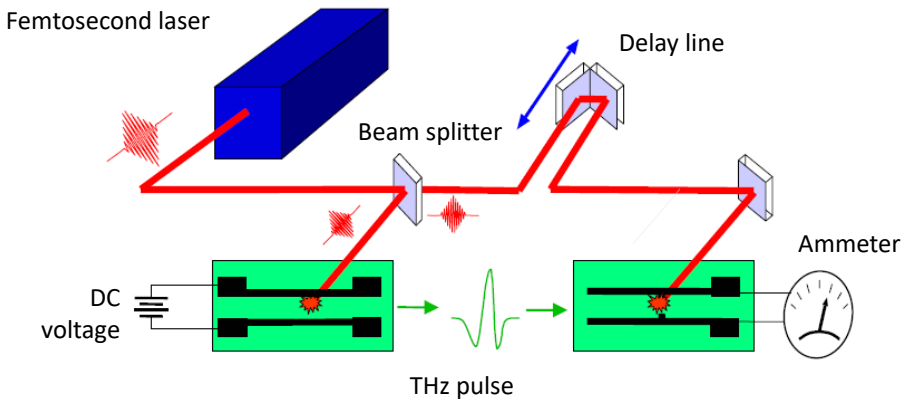

Figure 1.5: Schematic of the terahertz time-domain spectroscopy system (THz-TDS). The femtosecond laser beam is split in two parts with a beam splitter. One part is sent to the terahertz emitting antenna, while the other part arrives at the detecting antenna through a delay line [31].

Ultra-short pulses of terahertz waves can be generated using PCA or non-linear crystals (see section 1.1.1). Our first experimental setup used in the thesis is based on PCA. As previously presented, an impinging femtosecond near infrared pulse is focused on the biased source antenna (see figure 1.5). Carriers are generated in the semiconductor and accelerated by the static voltage, creating a time-varying current $i(t)$, which radiates an electromagnetic wave

$$E_{\mathrm{THz}}(t) \propto \frac{\partial i(t)}{\partial t} \tag{1.3}$$

which is proportional to the derivative of the current produced by the movement of the charges. Once generated, the terahertz wave can propagate in free space through optics and samples. Finally, the terahertz wave is detected by a second antenna triggered by a second synchronized impinging femtosecond pulse, delayed by a time Δt. This antenna generates a current proportional to the amplitude of the terahertz field, which is measured with a lock-in amplifier. The resulting signal is then given by

$$S_{\mathrm{THz}}(\Delta t) = \int_{-\infty}^{+\infty} E_{\mathrm{THz}}(t)\, R(\Delta t - t)\mathrm{d}t, \tag{1.4}$$

where $R(t)$ is the response from the detector, given by the convolution between the femtosecond pulse $P(t)$ and the PCA semiconductor response $D(t)$,

$$R(t) = P(t) * D(t). \tag{1.5}$$

The key point for THz-TDS is that the Fourier transform of Eq.1.4 is simply a product

$$\tilde{S}_{\mathrm{THz}}(\omega) = \tilde{E}_{\mathrm{THz}}(\omega) \times \tilde{R}_{\mathrm{THz}}(\omega). \tag{1.6}$$

Therefore, $\tilde{S}_{\mathrm{THz}}(\omega)$ is linear with respect to $\tilde{E}_{\mathrm{THz}}(\omega)$. A typical THz-TDS measurement then consists in two measures. The first without the sample is a reference

$$\tilde{S}_{\mathrm{ref}}(\omega) = \tilde{E}_0(\omega) \times \tilde{R}_{\mathrm{THz}}(\omega) \tag{1.7}$$

and the second with the sample of complex transmission $\tilde{T}(\omega)$,

$$\tilde{S}_{\mathrm{samp}}(\omega) = \tilde{T}(\omega) \times \tilde{E}_0(\omega) \times \tilde{R}_{\mathrm{THz}}(\omega). \tag{1.8}$$

Finally, the ratio of these two measures gives the complex transmission of the sample, in the terahertz domain

$$\frac{\tilde{S}_{\mathrm{samp}}(\omega)}{\tilde{S}_{\mathrm{ref}}(\omega)} = \tilde{T}(\omega). \tag{1.9}$$

The generation of terahertz pulses from commercial femtosecond mode-locked lasers and time-resolving techniques allows direct knowledge of the terahertz pulse spectrum by performing the Fourier transform of the measured signal. This system makes it very easy to determine the spectral properties of materials [1]. The emission and detection of THz-TDS is triggered

by the same femtosecond laser pulse, and the time delay is very precisely controlled. Since the detector only collects the signal when it is illuminated by the femtosecond laser pulse, the noise between two successive pulses is not collected, thus increasing the signal-to-noise ratio.

Equivalent principles apply to terahertz pulses generated and detected by other pulse techniques such as non-linear crystals or plasma. The equation 1.4 remains valid. When focusing an intense 10 fs pulse, frequencies up to 200 THz can be generated by a plasma [32]. Here, however, spectra above 10 THz are too noisy to characterize the spectoscopic information of the samples. The ultra wide band frequency range from 0.3 THz to over 30 THz was also obtained by [33, 34] for terahertz pulse generation and detection using plasma created by focusing a pulse of mJ energy into the air.

The spectroscopic information of a sample can be obtained from the complex transmission coefficient $\tilde{T}(\omega)$ in the equation 1.9. As a first approximation, the reduction in the amplitude of the terahertz pulse is due to absorption by the sample and reflection losses, while the phase shift is due to the refractive index of the sample. Specifically, it is necessary to analyze the propagation of the terahertz beam through the sample using Fresnel equations and taking dispersion into consideration.

The complex refractive index of a homogeneous sample is defined as $\hat{n}(\omega) = n(\omega) - i\kappa(\omega)$, where the real part is the index of refraction $n(\omega)$ and the imaginary part is the extinction coefficient $\kappa(\omega) = \dfrac{\alpha(\omega)c}{2\omega}$, where $\alpha(\omega)$ is the absorption coefficient and c is the speed of light in vacuum.

In the following, we consider a homogeneous sample with flat parallel faces. Equation 1.9 allows to obtain the complex refractive index, considering Fresnel equations at the interfaces and also Fabry-Perot effect [35, 36]. The total theoretical transmission of the sample writes

$$\tilde{T}_{\mathrm{th}}(\tilde{n},\omega) = \frac{4\tilde{n}\tilde{n}_0}{(\tilde{n}+\tilde{n}_0)^2} \frac{e^{-i(\tilde{n}-\tilde{n}_0)\,d\frac{\omega}{c}}}{1-\left(\dfrac{\tilde{n}-\tilde{n}_0}{\tilde{n}+\tilde{n}_0}\right)^2 e^{-2i\tilde{n}d\frac{\omega}{c}}} \tag{1.10}$$

where d is the thickness of the sample and $\tilde{n}_0(\omega)$ is the refractive index of the surrounding medium (usually air or vacuum where $\tilde{n}_0 = 1$). The complex values of $\tilde{n}(\omega)$ are obtained by solving the equation 1.10. However, the mathematical solution is not obvious due to the oscillatory behavior. The extraction of the complex reflective index is therefore done by iterative optimization methods with an error function proposed in [35] and defined as

$$\delta(\omega) = [\delta\rho(\omega)]^2 + [\delta\varphi(\omega)]^2 . \tag{1.11}$$

Here,

$$\begin{aligned} \delta\rho(\omega) &= \ln|\tilde{T}_{\mathrm{th}}(\omega)| - \ln|\tilde{T}_{\mathrm{meas}}(\omega)| \\ \delta\varphi(\omega) &= \arg(\tilde{T}_{\mathrm{th}}(\omega)) - \arg(\tilde{T}_{\mathrm{meas}}(\omega)) \end{aligned}$$

where $\tilde{T}_{\mathrm{meas}} = \tilde{S}_{\mathrm{sample}}/\tilde{S}_{\mathrm{ref}}$ is the experimental measured transmission. The solution of equation 1.10 is achieved when the error function approaches to zero. Other error functions and

zero-finding codes are also employed to extract the measured material parameter with higher accuracy [37–39].

In reflection configuration under normal incidence with a sample considered thick enough not to allow terahertz wave to propagate through the sample, the terahertz wave is reflected at the surface of the sample [36]. Thus, the complex reflection coefficient of amplitude extracted from reflection measurement is noted as [36]

$$\tilde{R}_{\text{meas}} = \frac{\tilde{S}_{\text{meas}}}{\tilde{S}_{\text{ref}}} = R_{\text{meas}} e^{i\,\varphi_R} = \frac{\tilde{n}_R - \tilde{n}_0}{\tilde{n}_R + \tilde{n}_0}, \tag{1.12}$$

where $\tilde{S}_{\text{ref}}$ is obtained using a quasi perfect reflector (such as a metal mirror) to replace the sample. $\tilde{R}_{\text{meas}}$ is the measured complex reflection coefficient, R_{meas} and φ_R are, respectively, the modulus and phase of $\tilde{R}_{\text{meas}}$. From the equation 1.12, we are able to directly calculate the real and imaginary parts of $\tilde{n}_R = n_R(\omega) - i\kappa_R(\omega)$ by [36, 40]

$$n_R(\omega) = \frac{\tilde{n}_0[1 - R^2_{meas}(\omega)]}{1 + R^2_{meas}(\omega) - 2R_{meas}(\omega)\cos\varphi_R} \tag{1.13}$$

$$\kappa_R(\omega) = \frac{\tilde{n}_0[2R_{meas}(\omega)\sin\varphi_R]}{1 + R^2_{meas}(\omega) - 2R_{meas}(\omega)\cos\varphi_R} \tag{1.14}$$

where $n_R(\omega)$ and $\kappa_R(\omega)$ are the values extracted from reflection measurement.

The THz-TDS reflection setup is generally more accurate than the transmission setup for a highly absorbent sample. This is because the measured signal is reflected from the sample surface, and is larger than in transmission, where it results from attenuated propagation through the sample. Furthermore, the knowledge of the thickness of the sample is not required in reflexion setup.

1.1.3 Interaction of terahertz radiation with matter

In the field of visible or infrared optics, a complete catalog of the properties of different materials is available. One of the major problems in the terahertz field is to find materials with the required properties. This relative lack of data is due to the fact that the terahertz field is rather recent, but also to the fact that materials often have quite similar properties, depending on the family to which they belong. And in general, transparent terahertz materials are rare. In order to give an overview of the main characteristics, we present in table 1.2 and 1.3, for several materials, the refractive index and the characteristic absorption length L_{abs}, which is proportional to the inverse of the intensity absorption coefficient.

$$L_{\text{abs}} = \frac{1}{\alpha} = \frac{c}{2\kappa\omega}. \tag{1.15}$$

Polar liquids with asymmetric bonds such as water and many solvents have a high absorption in the terahertz range [2]. On the contrary, hydrocarbon-based liquids or oils have much

Table 1.2: Dielectric properties of some liquids around 1 THz.

Substance at 1THz	n	L_{abs}[mm]	Reference
Distilled water	2.16	0.0422	[41, 42]
De-ionized water	2.04	0.0455	[43]
Glycerol	1.75	0.7	[44]
Sunflower seed oil	1.49	1.1	[45]
Gasoline (petroleum products)	1.41	3.3	[46]
Benzene (organic solvents)	1.51	4.1	[46, 47]
Acetone	1.52	0.0455	[48]
Methanol	1.61	0.0833	[48]
Ethanol	1.5	0.1	[49]

lower absorption. Many publications have studied the dielectric properties of these liquids (see table 1.2). Intrinsic semiconductors, such as gallium arsenide or silicon, are sufficiently transparent in the terahertz range but have a high refractive index (see table 1.3). When doped, the defects increase their conductivity so that they become much more absorbent.

Table 1.3: Dielectric properties of some semiconductors around 1 THz.

Substance at 1THz	n	L_{abs}[mm]	Reference
Silicon	3.41	20	[50]
High resistivity silicon	3.41	$\gg$30	[50]
Germanium	4	$\gg$10	[50]
Zinc telluride (ZnTe)	3.2	1.5	[50]

High resistivity silicon (HR-Si, R>10kΩ·cm) is a crystal having excellent properties in the terahertz domain [51] with very low dispersion, low absorption and high refractive index ($n \approx 3.41$). Unfortunately, silicon is opaque in the visible range.

Some plastics have fairly good properties for terahertz applications: they have a refractive index greater than 1.5 and have relatively low absorption coefficients (especially at low frequencies). Some plastics are also transparent in both the terahertz and visible ranges, making them compatible with imaging in the visible [52]. The most commonly used polymers are high-density polyethylene (HDPE) and teflon, which are employed to make lenses for terahertz beams. Similarly, expanded polystyrene, due to its low density, is transparent. Parafilm is a film based on polyolefins and waxes regularly used in biology and is also relatively transparent in the terahertz range.

1.1.4 Aplications in physics and chemistry

Terahertz waves are used in an increasing number of applications. We present here some applications in the academic and industrial fields, even if sometimes the technology is not yet

fully mature and still presents some challenges, especially in terms of transmitted power and measurement time.

In the terahertz range, many spectral lines allow the identification and analysis of materials. Many molecules show a good variety of rotational modes in the terahertz range [14, 53]. It is therefore possible to use THz-TDS to discriminate chemical compounds by their spectral fingerprints [53]. It is also possible to analyze chemical compounds present in the atmosphere (e.g. those that make up cigarette smoke [54]) or to recognize chemical elements (e.g. drugs, explosives, medicines) for safety [55] or pharmaceutical applications [56]. Figure 1.6 shows an example of measuring the thickness and uniformity of a drug layer. Characterization of the drug coating film is important for estimating drug quality.

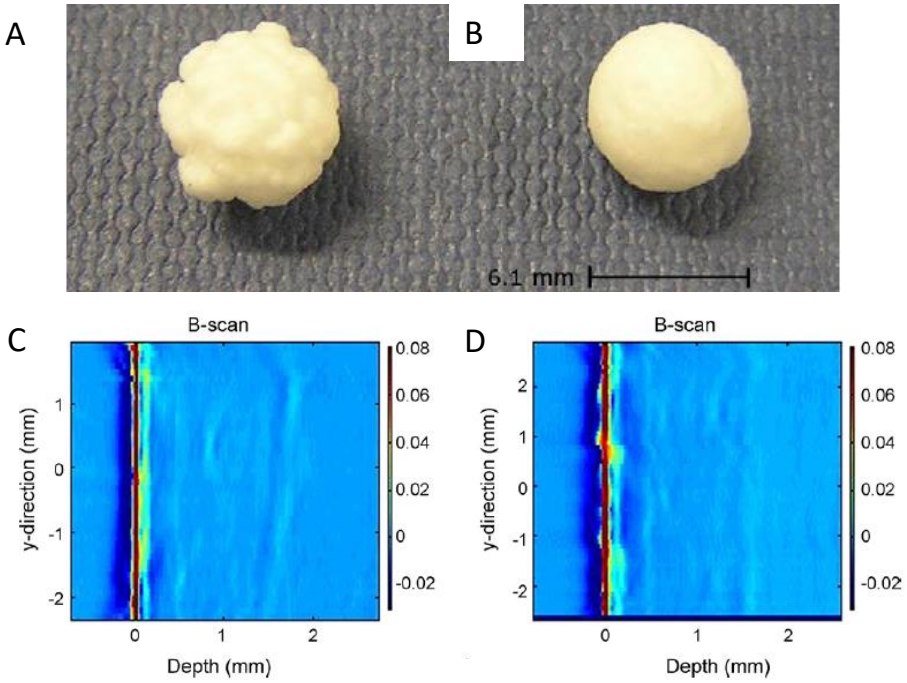

Figure 1.6: Photograph of a drug-filled tablet without additional spheronization of the drug layer (A) and a tablet with spheronization, showing a smoother surface morphology (B). Terahertz B-scan images of the A-pellet (C) and B-pellet (D). Images C and D are cross sections in the depth direction. The red band is the air/film interface, the lighter blue band is the film/drug layer interface, and the thicker light blue area at about 1.5 mm depth of penetration in terahertz is the drug layer/drug core interface [57].

In astronomy, terahertz spectroscopy is used to determine compounds present in space. The low temperatures of interstellar space (a few Kelvins) correspond to black body temperatures in the low terahertz frequency range: it is estimated that half of the luminosity and 98% of the photons emitted from the big-bang are in the range of 0.06-0.75 THz [58].

Terahertz radiation for security reasons are taken out of the laboratory mainly due to their non-ionizing properties (compared to X-rays). Terahertz full-body scanners are starting

to spread in airports (40 systems installed in 19 airports in 2010[1]). Terahertz is used to make clothing transparent and to check that passengers are not carrying dangerous objects (see figure 1.7). The Japanese post office has attempted to probe the contents of the envelopes for the possible presence of drugs using terahertz waves [59].

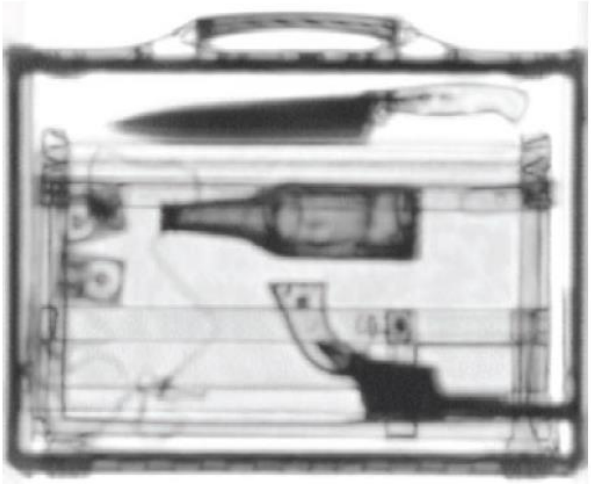

Figure 1.7: THz transmission image through a closed suitcase. A gun, a knife and a bottle are clearly identified [60].

1.2 Motivation and applications of terahertz in biology

1.2.1 Terahertz spectroscopy of biomolecules

For a long time, the role of water in biochemical reactions has been neglected, but water molecules are now recognized as major participants in biochemical processes [61]. The hydration layer consisting of water molecules surrounding any protein is necessary for structural flexibility related to conformational transitions [62]. In addition, the hydration layer has glassy dynamic properties, which protect the protein when the ambient temperature is close to the freezing point [63]. It has been shown that the water layer around ions is responsible for the selectivity of the ion channels in the cell membrane for ion transport [64]. Here, the water molecules in the hydration layer have different modes of vibration from that of the bulk solution. Some studies have shown the possibility of exploring the properties of this hydration layer, such as its thickness and the number of water molecules [65, 66].

Different methods to study the water-biomolecule interaction include neutron scattering [67], nuclear magnetic resonance [68], ultrafast optical spectroscopy [69] and numerical simulations of molecular dynamics [70]. But not all the details of the interaction are clearly

[1]data from STAC(02/2010)

identified. Therefore, terahertz spectroscopy presents a possible way to further study the dielectric response of liquid water based on the fact that the terahertz domain is very sensitive to intramolecular vibration modes [71, 72].

Terahertz spectroscopic research developed in the field of biomolecules and biological tissues in the early 2000s. A publication showed time-resolved terahertz absorption spectra of albumin and collagen, which indicated the collective vibratory modes of biomolecules [73–75]. Sugars and amino acids also have a characteristic absorption in terahertz [76]. In addition, spectroscopic information in the terahertz range can distinguish changes in protein conformation [77] due to hydration rate, temperature (see figure 1.8), change in oxidation state or binding [78]. Some studies have also shown that it is possible to analyze single base mutations in short DNA sequences without the need for a label [79].

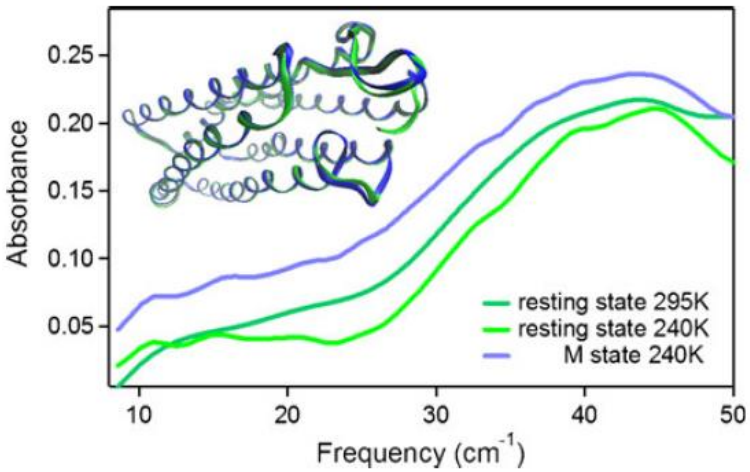

Figure 1.8: Illustration of the absorption measurements for a bacteriorhodopsin film between 0.1 and 1.5 THz. The inset shows the structural conformation change of the protein. It demonstrates a change in absorbance between the resting state at 240K (green, top line), the photoactivated M state at 240K (light green, bottom line) and the resting state at 295K (aquamarine, middle line) [75].

At the end of the 90s, several biological tissues were studied in the terahertz range, such as skin, muscle and fat, to measure their refractive index by spectroscopy [80]. A catalogue of the optical properties of human tissues has been listed in [43]. Human skin is one of the most studied tissues in vivo or in vitro in pulsed terahertz radiation, with applications in particular in the field of cancer [81].

1.2.2 Terahertz imaging in biomedical domain

Biomedical imaging is the first application of terahertz in biology. The most common operating principle is the intrinsic contrast of the terahertz signal between healthy and abnormal tissues. This contrast is mainly due to the distribution of water in different structures [82, 83]

or solutes [84]. But other details are still under investigation. For instance, neuron can be reconstructed with near-field ionic contrast (see figure 1.9) [84]. The working principle of the terahertz contrast of ions and proteins has been demonstrated in our team by previous students. The difference in the distribution of ions on the two sides of the membrane of an axon has thus made it possible to access the dimensional information of the axon during the perturbation of the ion equilibrium [84]. In the physiologically stable state, potassium ions are forty times more concentrated inside the axon than outside. On the contrary, sodium ions are mostly found in the surrounding environment. Since it was found that potassium solution absorbs more than sodium one in the terahertz domain, the axon exhibit stronger absorption.

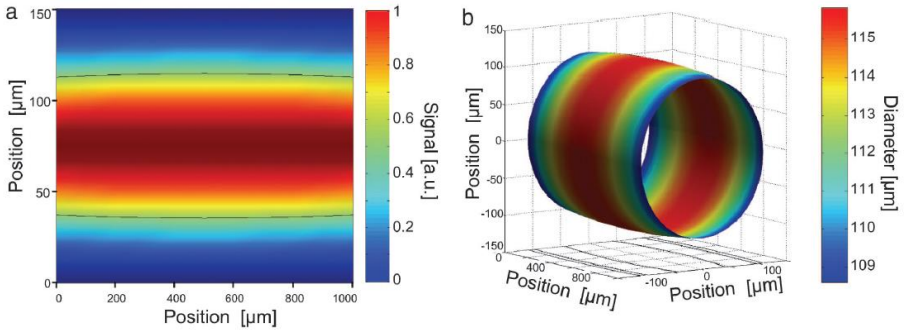

Figure 1.9: Reconstructed image of an axon (a) Two-dimensional image of an axon. The dotted line shows the half maximum profile. (b) Deconvoluted 3D image of the axon using finite element method (FEM) simulations [84].

Besides, terahertz imaging has the potential to distinguish tumor tissue, and offers a new approach to cancer diagnosis based on terahertz spectroscopy [76, 85]. The experiments are mainly carried out ex vivo, in comparison with histopathology techniques. In addition, the tissue tested is often prepared as frozen samples (porcine tissue [59]), embedded in paraffin slices [86] or formalin-fixed samples (human colon tissue, striated muscle and adipose tissue) [87] to prevent absorption by liquid water which hinders the measurement of thick samples. Experimental results have shown that terahertz can distinguish between the adipose zone, the healthy zone and the tumor zone with a lateral resolution of a few hundred micrometers. This resolution limits the depth of penetration into wet biomedical tissue, either ex vivo or in vivo. However, tissue freezing may increase this depth of penetration [1], but at the expense of the tissue structure.

The non-invasive investigation of skin tumours was studied using terahertz reflection mode pulse spectroscopy and imaging. The first tests were done in vivo on rat skin burns [88] and on human skin cancers [89, 90]. The increased reflectivity and widening of the terahertz pulses reflected by the malignant tissue allow the use of this non-invasive diagnostic technique. However, the limited depth of penetration of the terahertz wave (a few hundred micrometers) makes it possible to examine only the upper layers of skin tissue (the stratum corneum and epidermis). In addition, the stratum corneum is too thin to have a noticeable impact on the terahertz signal. Therefore, terahertz can only characterize the living epidermis of human

skin [91]. Nevertheless, different imaging results of healthy and malignant tissues have been demonstrated in vitro and in vivo for non-melanoma skin cancers [89, 92]. Figure 1.10 shows an example distinguishing nodular basal cell carcinoma (BCC) from normal skin. Thus, terahertz imaging could become an efficient tool for the early and non-invasive diagnosis of skin cancers.

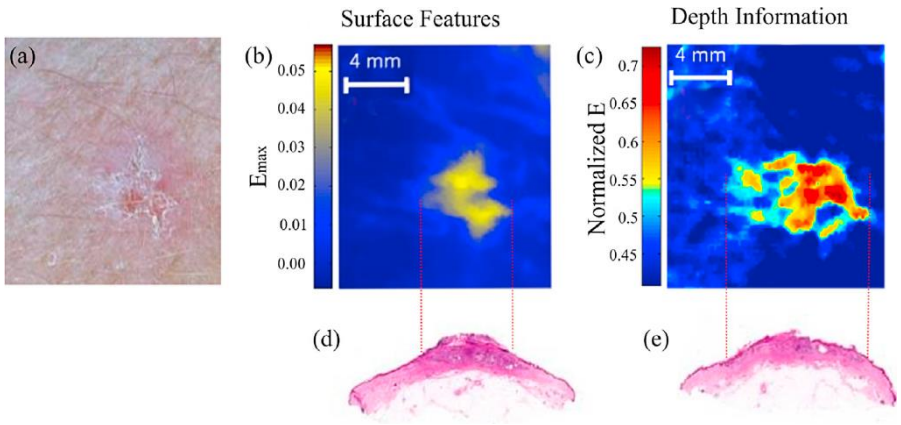

Figure 1.10: An example of THz pulse imaging of nodular basal cell carcinoma (BCC) in vivo: (a) a clinical picture of the lesion; (b) THz reflection imaging. Each pixel represents the amplitude of the THz pulse reflected from the sample; (c) THz reflection imaging with depth information indicating the extent of the tumour at depth ≈250µm; (d),(e) representative histological sections of the tissue [92].

Other applications on skin are also being explored, such as monitoring the diffusion and absorption of drugs after cutaneous application [93] or in vivo imaging of vessels. Other studies show the use of terahertz waves to detect cancer of oral mucosa [94], cancerous, dysplastic and healthy tissues of the colon [95], and normal and tumourous human gastric tissues [96]. Tomography of human bone [97] or ex vivo imaging of knee cartilage [98] and liver cirrhosis [82] were also performed.

Some techniques have been developed to reduce the acquisition time in pulsed terahertz experiments. One of them, [99, 100], consists in superimposing the image of the object on a ZnTe crystal with a femtosecond probe beam of a diameter greater than the terahertz image. The electro-optical effect modifies the probe, which is detected by a CCD camera. A 2D image is thus realized in only one measurement. Another interesting technique to reduce sampling time, proposed by Schirmer [101], is called real-time THz color scanner. It allows to obtain simultaneously two-dimensional information, spatial and temporal imaging, through the combination of a non-collinear electro-optical crystal (ZnTe crystal) and a CCD camera. The waveform of the pulsed electric field of terahertz corresponds to the horizontal dimension of the camera. The vertical dimension of the camera retains the transverse imaging of the sample. This technique has been successfully used to image a moving object at a speed of 10 mm/s on a translation stage.

1.2.3 Near-field terahertz microscopy

Traditional optical microscopy is limited, as the work of Abbe and Rayleigh [102, 103] has shown, by the diffraction of light which reduces the resolution of the obtained image. The best resolution Δx obtained from a lens of focal length f, focusing a beam of diameter D at the wavelength λ is given by [104]

$$\Delta x \approx 1.22\frac{\lambda f}{D} \tag{1.16}$$

It is well known that details smaller than the wavelength employed cannot be distinguished. But the Abbe limit only applies to devices using travelling waves propagating i the far field from the source to the detection system. There exist evanescent waves located near the surface that carry information about details of the structure smaller than the wavelength. One possible solution to observe these evanescent waves is to use scanning near-field optical microscopes. The principle was proposed by Synge in 1928: by scanning the surface of an object with an aperture of sub-wavelength dimension, one could obtain an image whose resolution depends only on the size of this aperture and its distance from the sample [105]. The first experiment was conducted in 1972 when Ash and Nicholls used microwaves to observe details at $\lambda/6$ [106]. With a terahertz single cycle pulsed source, the resolution reached $\lambda/600$ [107, 108]. Huber's group achieved a higher resolution of $\lambda/3000$ at 2.54 THz using a source with single frequency and a scattering tip in semiconductor nanodevices [109]. The acquisitions are realized via raster scanning therefore it is time-consuming. But with the development of video rate imaging, a sub-wavelength spatial resolution of $\lambda/4$ has been achieved at around 1 THz [110]. An example is given in figure 1.11. The resolution reached $\lambda/12$ (130 µm) at 0.36 THz for a parthenocissus leaf and a Laurus nobilis leaf [111]. Bitzer *et al.* obtained a 50 µm resolution for a frequency of 1.36 THz [112].

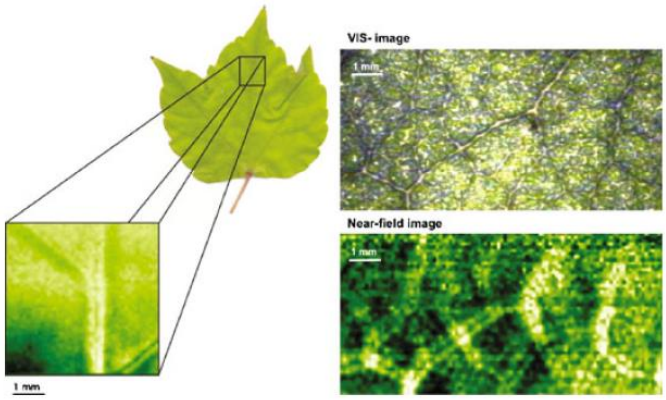

Figure 1.11: (left)Visible and near-field THz image of a section of a parthenocissus leaf. (Right) Visible and near-field THz image of a section of a Laurus nobilis leaf. Darker region in the THz image indicates less absorption [111, 113].

Generally, a near-field terahertz microscope is in reflection geometry. However, it is also possible to do so in a transmission configuration by exciting surface plasmons which will

contribute to the amplification of the transmitted signal [114].

An example of terahertz application is presented in [31] on drosophila melanogaster. Drosophila melanogaster is a model widely used in developmental biology because of its well-known genes. The difficulty of observing its development using conventional optical techniques has led to the development of alternative methods based on the use of fluorescent markers [115] or multiphoton microscopy [116]. It is possible to study the Drosophila embryo in terahertz because its size is close to the wavelength of terahertz (length of 400-500 µm and a diameter of 150-200 µm). The inhomogeneity of its structure provides a terahertz contrast (see figure 1.12). Terahertz imaging can provide additional information on the physico-chemical processes within the embryo, in particular the distribution of proteins and ions, which are difficultly accessible by other methods.

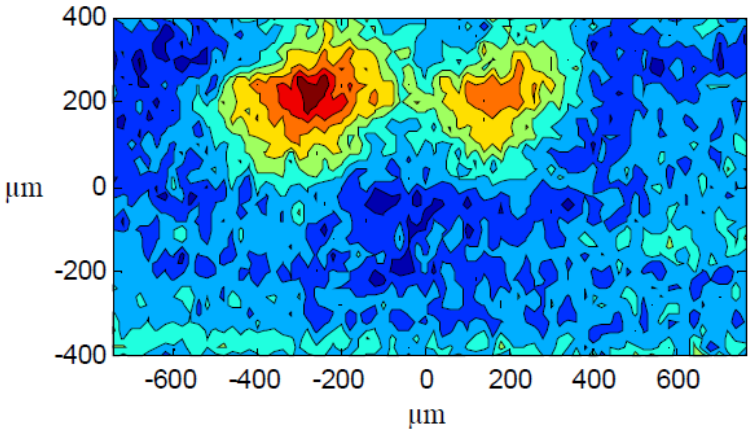

Figure 1.12: Terahertz image of a Drosophila embryo at a late stage of development [31].

Other publications [117] have demonstrated that it is possible to characterize small structural changes in the endothelial cells of bovine lung microvessels (BLMVEC) in their physiological environment, whereas, these changes were not observed with standard phase contrast light microscopy.

1.3 Origin and model of the terahertz contrast in biology

As presented in the sections 1.1.2 and 1.2.1, THz-TDS has been widely used to detect the molar absorption of soluble ions and proteins [66, 118–120]. The most important point is the delicate interaction between water molecules and solutes. The dielectric properties of any solution can be represented by the complex dielectric constant $\tilde{\epsilon}_s = (n_s - i\kappa_s)^2$, where n_s is again the index of refraction and κ_s is the extinction coefficient. In our experimental terahertz range of 0.2 to 1.6 THz (more details of the setup are presented in chapter 3), the spectrum of aqueous solutions was found to be homothetic to the spectrum of pure water [66,118,121,122]. Therefore, the variation of n and κ in the solutions can be considered as a linear relationship

with the bulk water values and given as

$$\begin{aligned} \Delta n &= n_{\mathrm{s}} - n_{\mathrm{w}} = \delta_n C\, n_{\mathrm{w}} \\ \Delta \kappa &= \kappa_{\mathrm{s}} - \kappa_{\mathrm{w}} = \delta_\kappa C\, \kappa_{\mathrm{w}} \end{aligned} \tag{1.17}$$

where n_{w} and κ_{w} are the refractive index and extinction coefficient of bulk water, respectively, and C is the solute concentration. The parameters δ_n and δ_κ are the mass relative refractive index and extinction coefficient. There, Δn and $\Delta \kappa$ are considered as the averaged variations of n and κ from the solution to bulk water in our experimental frequency range from 0.2 to 1.6 THz.

Our group has demonstrated that the refractive index and extinction coefficient of solutions of biomolecules of different molecular weights are measurable by THz-ATR [123]. A clear correlation between the terahertz dielectric properties and molecular weight is presented in [123]. In addition, a three-volume model is proposed to analyze the relative contributions of a solute to the total dielectric values.

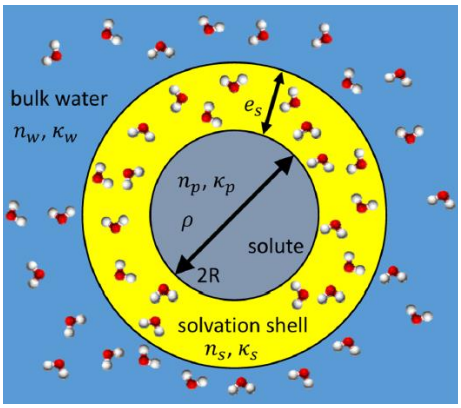

Figure 1.13: Three-volume model of a solute in water for the dielectric model of ion and protein solutions in the terahertz range. The spherical solute is surrounded by a solvation shell bathed in bulk water [123].

This model includes solute, a solvation shell around the solute, and bulk water, as shown in Figure 1.13. Assuming a total volume of solution V, the volume of solute V_p, the volume of the solute envelope V_s, and the volume of bulk water V_w, the effective dielectric value is taken as the sum of these three components and is given by

$$x_{\mathrm{eff}} = \frac{V_p}{V} x_p + \frac{V_s}{V} x_s + \frac{V_w}{V} x_w \tag{1.18}$$

where x can stand either for n or κ. The solute is considered to be a sphere of radius R, agreeing well with highly soluble molecules [124]. It is then necessary to calculate the different volume ratios in order to propose a model concerning the spectroscopic characteristics of the solutions. For N solute molecules having an individual mass m_p in the total solution, the solute volume V_p is given by

$$\frac{V_p}{V} = N \frac{m_p}{\rho V} = \frac{m}{\rho V} = \frac{C}{\rho} \tag{1.19}$$

where ρ is the density of the molecules, and C is the solute concentration. For the solvation shell, the solvation shell volume V_s is given by

$$\frac{V_s}{V} = \frac{V_{1s}N}{V} = V_{1s}\frac{\mathcal{N}_A}{M}C \tag{1.20}$$

where M is the molecular weight of the solute, $\mathcal{N}_A$ is Avogadro's number, and V_{1s} is the volume of one solvation shell given by

$$V_{1s} = 4\pi e_s \left[\left(\frac{3M}{4\pi\rho\mathcal{N}_A} \right)^{\frac{2}{3}} + \left(\frac{3M}{4\pi\rho\mathcal{N}_A} \right)^{\frac{1}{3}} e_s + \frac{e_s^2}{3} \right]. \tag{1.21}$$

Here e_s is the solvation shell thickness as noted in figure 1.13. This thickness e_s is considered to remain in a limited range, usually between 0.8 to 1.2 nm [125, 126]. As calculated in equation 1.21, the volume of the solvation shell of each solute V_{1s} only depends on the molecular weight of the solute M.

During the measurements, the relative variations Δn and $\Delta\kappa$ were obtained. From equation 1.18 to 1.21, these variations are found to be

$$\frac{1}{C}\frac{\Delta x}{x_w} = \frac{1}{C}\frac{x_{eff} - x_w}{x_w} = \frac{1}{\rho}\left(\frac{x_p}{x_w} - 1 \right) + V_{1s}\frac{N_A}{M}\left(\frac{x_s}{x_w} - 1 \right) \tag{1.22}$$

Table 1.4: Terahertz Dielectric Constants for Molecules and Solvation Shell [123].

	$(n - n_w)/n_w$	$(\kappa - \kappa_w)/\kappa_w$
Solute (p)	-0.14±0.02	-0.99±0.05
Solvation shell(s)	0.004±0.001	0.007±0.002

where x still represents n or κ. The right side of the equation 1.22 does not depend on C, which is expected, but is related to the thickness of the solvation shell and depends on a series of powers of M as well as on the dielectric constant of the solvation shell. Using this expression, one can obtain the dielectric constant of solutions of ions, peptides and proteins. In [123], Δn and $\Delta\kappa$ of biological substances in solution were measured for a wide range of molecular weights M. An overall decrease of δn and $\delta\kappa$ is observed with increasing M (see figure 1.14). The experimental values required for equation 1.22 can be found in table 1.4. In conclusion, this three-component dielectric model describes well the terahertz dielectric constant of biological solutions, and allows us to predict the behaviour of our biological samples.

The terahertz properties of the solution are found to be mainly controlled by the surrounded solvation shell for small molecules, such as peptides and amino acids. However, for larger biomolecules (for example the proteins above 2 kDa), the solute dielectric properties are responsible for the observed plateau saturation. What is more, the relative variations caused by the solute are much larger than the solvation shell.

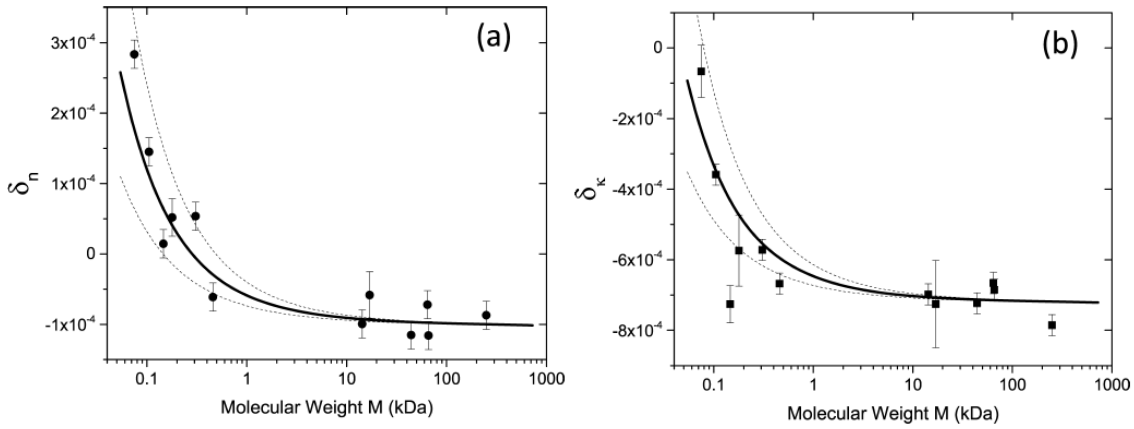

Figure 1.14: Variations in δn (a) and $\delta\kappa$ (b) vs molecular weight M. Dots are the experimental data. The solid lines are obtained from the three component model (see equation 1.22) with $e_s = 1\,\text{nm}$ and the dotted lines with $e_s = 0.8$ and $1.2\,\text{nm}$ for the same remaining parameters [123].

1.4 Conclusion

We have seen in this chapter that water is often considered a disturbing substance because of its high absorption. However, the terahertz range is very informative about the properties of water, whose dielectric constant is modified by physical or chemical conditions and especially by the presence of dissolved substances. For a biological sample in an aqueous medium, the terahertz domain is sensitive to the concentration of these substances: ions, peptides and proteins. Thus, possible differences in the distribution of these substances can be the source of contrast for a biological sensor in the terahertz range. These differences can also provide information on the exchange dynamics, for example, between the inside and outside of cells.

Spectroscopic investigations have been carried out to explore the sensitivity of terahertz waves to ions [127,128]. The demonstration of principle of studying live-cells in a physiological medium was made in [128]. The contrast between the inside of the cells and the outside allows to detect the dynamics of the information exchanges during the permeabilization of the membrane after the perturbation. The origin of the contrast is also demonstrated as presented in the section 1.3. A clear correlation between the terahertz dielectric properties and the size of the molecules was observed. A three-component dielectric model for biomolecules in solution was presented [123]. This model describes well the experimental terahertz dielectric parameters.

The ongoing work consists in quantifying the terahertz contrast during the perturbation of cell membranes. The long-term objective is to study cell dynamics during photodynamic therapy (PDT). The continuation of this thesis will first describe the biology of cell membranes and techniques for monitoring and measuring plasma membrane permeabilization (chapter 2), then present the measurements performed by chemical permeabilization (chapter 3). Finally, the last chapter will be devoted to the development of a new terahertz sensor with greatly

improved performance, and its use for the study of PDT.

Chapter 2

Cell membrane permeability

Contents

Just as the human skin is one of its vital organs, the cell membrane is an integral part of the cell and plays an essential role in many cellular processes and pathologies. In this chapter, we present the main properties of the plasma membrane of eukaryotic cells. The plasma membrane is a biological membrane that separates the cytoplasm from the extracellular medium. Consisting of a lipid bilayer, this membrane isolates the cell from its environment and controls the exchange of molecules between the inside and outside of the cell. With the help of membrane and peripheral proteins, the plasma membrane has passive or active selective permeability to ions and larger molecules, which regulates cell metabolism and communication. After a presentation of the structure and the different functions of the plasma membrane, we will review the main mechanisms that control membrane permeabilization and quantify transmembrane exchange. The membrane-disruption mechanisms cover mechanical, electrical, thermal, optical, and chemical strategies. Model cells for our studies in the terahertz domain, the MDCK cells, will also be presented in detail.

2.1 Characteristics of mammalian cells

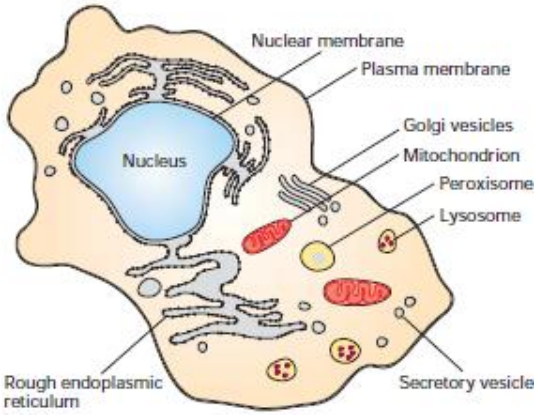

Figure 2.1: Schematic of the components of a mammalian cell [129].

There are more than 10 million different types of living organisms, all composed of cells [130]. Organisms are classified in 3 main domains: bacteria, archaea and eukarya (also called eukaryotes). The main difference concerns the nucleus. Bacteria and archaea are prokaryotes, which are micro-organisms without a defined nucleus, whereas eukaryotes include plants and animals with a defined nucleus. An eukaryotic cell is a basic living block consisting of a nucleus and cytoplasm enclosed by a plasma membrane (see figure 2.1). Inside the plasma membrane, the cytoplasm represents most of the cell volume comparing to the nucleus. The main components of the cell cytoplasm are: the cytosol which is a jellylike fluid ; the organelles with several physiological functions such as endoplasmic reticulum, mitochondrion and lysosome ; and various inclusions such as nutrients and secretory products. The

plasma membrane is made of lipids, which separate the cell from its environment and whose main feature is the delineation of the shape and size of the cell. Also, the plasma membrane regulates what enters and exits the cell, keeping inside the ions, proteins and others organic molecules required by the cell. The nucleus is a specialized organelle that serves as the information processing and administrative center of the cell. The nucleous stores the cell's DNA (deoxyribonucleic acid), and it coordinates the cell's activities, which include growth, intermediary metabolism, protein synthesis, and cell division. Among the organelles, the major parts are mitochondria, which convert energy; endoplasmic reticulum transports various molecules to their specific destinations; ribosomes transfer the cell's genetic material to produce proteins; cytoskeleton is a network of protein filaments close to the membrane, which gives cells their shape, cohesion, and ability to move.

If we consider the chemical components of a cell in the percentage of total cell weight, one cell consists of 70% of H_2O, 18% of various proteins, 5% of lipids (the major component of the cell membrane), 2% of polysaccharides and a very small amount of organelles [130] (see figure 2.2). Note that water and protein make up most of the mass of mammalian cells, nearly 90%. Particularly, proteins play a major role in cellular functions such as metabolic reactions, DNA replication, cell structure, transport of molecules, etc.

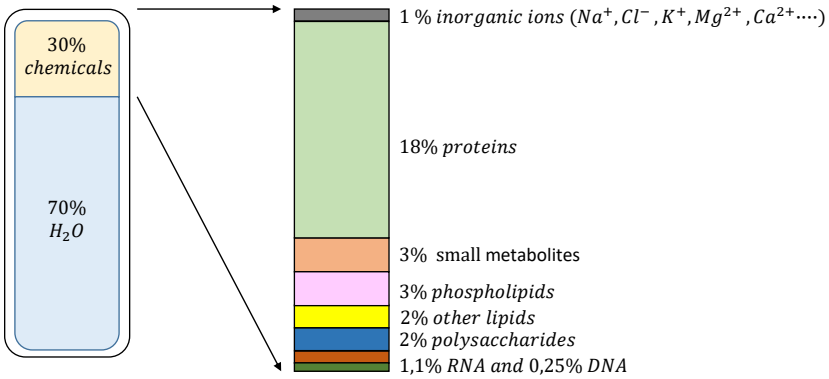

Figure 2.2: Components of a mammalian cell in percentage of cell total weight [130]

It is also well known that the percentage of each chemical component in a cell is dependent on the cell's function in the organism. For example, fibroblast cells contain a higher percent of millimeter or centimeter size proteins that make up muscles. The high percent of proteins in muscle cells contributes to contraction activity. It is important to keep in mind the great variety between the different cell types, especially the proportion of proteins in the cytosol.

Cells have many different shapes depending on their functions. The erythrocytes (red blood cells) help transfer oxygen into the bloodstream in a biconcave form without nucleus. Erythrocytes are several micrometers in size (see figure 2.3A). Other cells with specialized function are neurons, which have fewer proteins and multiple size and shapes. A typical shape is shown in figure 2.3B. Neurons are electrically excitable cells that trigger communications between cells via synapses. The epithelium is one of the four basic types of animal tissue, along

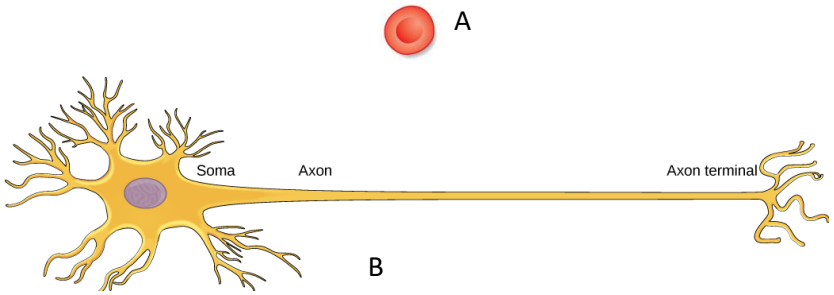

Figure 2.3: Schematic of the variety of mammalian cell types with different shapes. (A) An erythrocyte and (B) a neuron [129].

with connective tissue, muscle tissue and nerve tissue. Epithelial tissue lines the outer surfaces of organs and blood vessels throughout the body, as well as the inner surfaces of the cavities of many internal organs. In particular, epithelial cells can form a single-layer sticking to a substrate. In general, epithelium is classified into four major categories according to shape (see figure 2.4). The four classes are squamous, cuboidal, columnar and pseudostratified cells [131, 132].

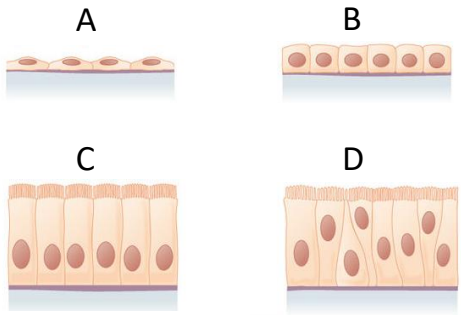

Figure 2.4: Schematic of different epithelium samples.(A) the squamous cell, (B) the cuboidal cell, (C) the columnar cell and (D) the pseudostratified cell [131].

2.2 Lipids and cell membrane function

One of the characteristics of all living organisms is that they contain different concentration of ions and other molecules than the environment. As we have previously seen, the barrier that separates the inside of the cell from the outside is the cell membrane (also called the plasma membrane or cytoplasmic membrane). Biological membranes perform several essential functions for cells based on their biochemical structure. One of these indispensable functions is the transport of specific molecules to or from the cytosol. These transport systems give membranes the essential property of selective permeability (permeabilization) [133].

The movement of molecules across the cell membrane can follow various processes. Here we introduce the most common ones. The types of cellular transport can be passive: osmosis and diffusion, which occur without cellular energy input, or active hydrolysis, which requires cellular energy (ATP: Adenosine triphosphate) to transport the molecules. Transport can also be achieved using transmembrane protein channels or protein transporters. Finally, endocytosis and exocytosis are also two important transport methods.

2.2.1 Mammalian plasma membrane structure

Gorter and Grendel proved in 1924 from red blood cells that the structure of the cell membrane is a lipid bilayer, by precisely measuring the surface of the lipid monolayer on water and then comparing it with the surface of the cells [134]. Then in 1935, Danielli and Davson proposed that the cell membrane should consist not only of lipids but also of proteins attached to both sides of the bilayer structure [135]. All proteins and lipids were considered to be homogeneously distributed in the cell membrane [136, 137]. These proposals were then updated by Singer and Nicolson with the fluid mosaic model in 1972 [138]. They suggested that proteins and lipids distribute freely in the cell membrane like in a sea. Then in 1988, Simons and Van Meer discovered that certain lipids (such as glycerolipids, phosphatidylcholine or sphingolipids) and certain proteins have a heterogeneous distribution between the apical and basolateral plasma membrane of epithelial cells. Other explanations for this lateral inhomogeneity in the cell membrane have been mentioned in the lipid raft model [139], which considers the existence of membrane microdomains, rich in cholesterol and sphingolipids, which contain specific lipids and proteins for specialized functions [140].

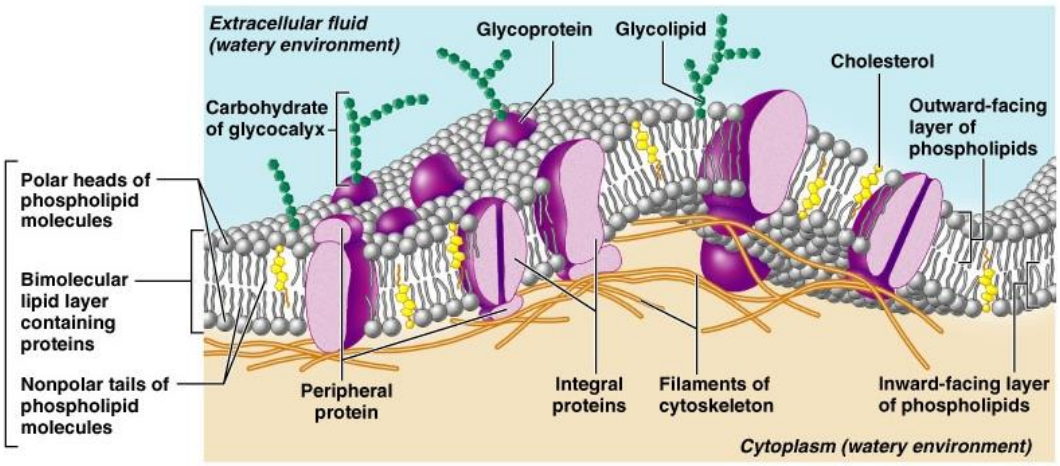

Figure 2.5: Plasma membrane structure of a mammalian cell [141].

Current knowledge is that a membrane is the assembly of phospholipids, glycolipids,

and cholesterol with various proteins inserted in the bilayer lipid structure (see figure 2.5). Membranes contain about 50% of lipid and 50% of proteins [142] to perform tasks such as signaling, tracking, ions pumping, adhesion and sensing. The viscosity of the membrane was recorded as 100 times higher than the viscosity of water. About 5% of the cells' genes are used to synthesize lipids, which indicates that lipid molecules are very important for cellular functions [143]. The plasma membrane is flexible, waterproof and only a few nanometers thick. Phospholipids (see figure 2.6) are the constituent molecules of the lipid bilayer and have a hydrophilic (polar) head group, which can form either favourable electrostatic interactions or hydrogen bonds with water molecules, and two hydrophobic (non-polar) tails which consist of two fatty acid chains linked together either by a glycerol molecule (the phosphoglycerides) or by a sphingosine (the sphingolipids) [144]. The polar head contains a phosphate group and the fatty acids are generally composed of 14 to 24 carbon atoms. The length of the carbon chain is also an important parameter for the fluidity of the membrane. Phospholipids spontaneously assemble into 3 to 5 nm-thick bilayer structures for most biomembranes due to hydrophilic and hydrophobic interactions [129]. The hydrophilic heads face water on both surfaces and the hydrophobic tails are protected from water on the inside. The entire lipid membrane is also supported by the underlying cytoskeleton composed of spectrin and actin.

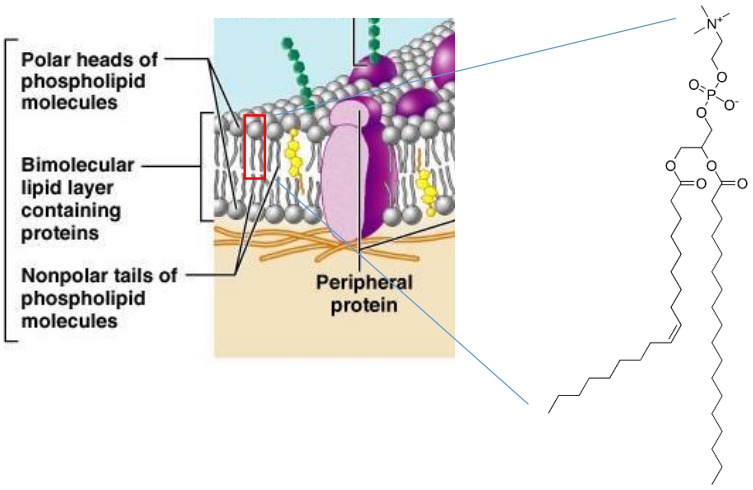

Figure 2.6: Phospholipid molecule [141].

Cholesterol is found exclusively in eukaryotic mammalian cells and is the second most abundant lipid component of the plasma membrane. Cholesterol has a steroid structure containing four rigid rings and a short branched chain of hydrocarbons that is inserted at the tails of the phospholipids bilayer (see figure 2.7). The hydrophilic properties of cholesterol are due to the presence of a single hydroxyl group, which is located in the polar head layer of the phospholipid. Its structure and properties help to reduce the movement of phospholipid chains where cholesterol is present, which results in a more solid structure of the membrane and possibly the creation of stiffer domains on the membrane. Depending on the type of cell, the percentage of cholesterol present in the membrane varies [145]. As an extreme case,

there is no cholesterol in prokaryotic cells [130]. Cholesterol molecules inserted in the cell membrane reduce the fluidity of the membrane, which keeps the membrane stronger at low temperature [141].

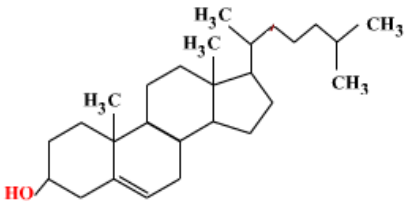

Figure 2.7: Cholesterol molecule.

Proteins constitute about 50% of the dry weight of plasma membranes. Proteins have a primary structure (the chain of amino acids), a secondary structure (the folding structures), a tertiary structure (the combination of different secondary structures of a polypeptide chain) and in some cases a quaternary structure (the three-dimensional structure consisting of different subunits of the same protein). Proteins can be involved in the membrane as integral proteins, which completely prenetrate the bilayer and are channels for the transport of certain molecules, or as peripheral proteins, which have a partial interaction with one of the membrane layers and are attached to a leaflet of lipid bilayer by a long hydrocarbon chain that is covalently bonded (see figure 2.8). Finally, peripheral proteins interact temporarily with the membrane, mostly through hydrophobic, electrostatic or specific non-covalent interactions with integral proteins or with the polar head groups of membrane phospholipids. Peripheral proteins do not penetrate the hydrophobic core of the membrane.

Membrane proteins play an essential role in the specific functions of the membrane. They can act as catalysts, signal receptors, switches, motors or tiny pumps, transport, catalyze membrane-associated reactions, and also detect and transduce chemical signals, etc [144]. For the membrane transport system, proteins serve as transporters to carry ions and chemicals across the cell membrane.

Cellular membranes are dynamic and fluid structures. Most plasma membrane molecules are capable of moving so that cell membranes have the capacity for rapid diffusion and reorganization of its components. In addition, membrane fluidity is related to many biological phenomena such as cell movement, growth and division, as well as to the endocytosis and exocytosis that will be introduced later. Thanks to the plasma membrane, cells are able to maintain their structure even when the external environment fluctuates strongly (e.g. ionic strength or pH value).

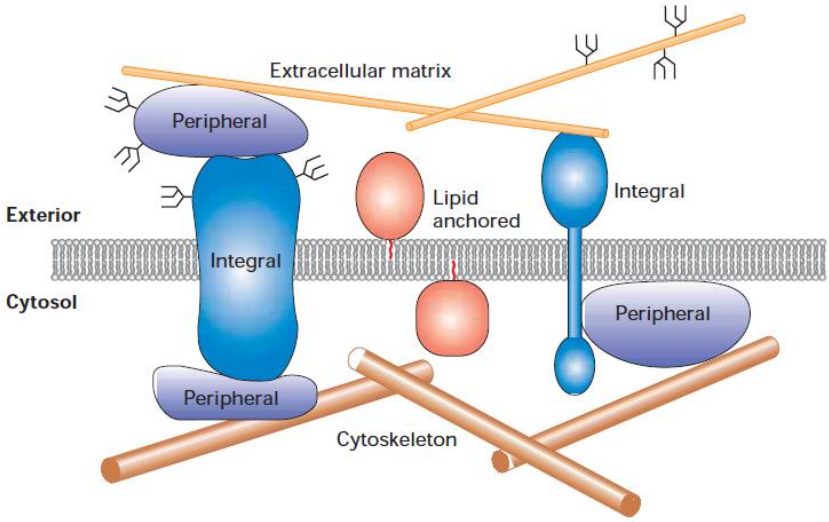

Figure 2.8: Scheme of the association of different classes of proteins with the lipid bilayer. Integral proteins cross the bilayer (blue). Lipid-anchored proteins are attached to a leaflet (orange). Peripheral proteins (Violet) associate with the membrane mainly through specific non-covalent interactions with integral proteins or membrane lipids [129].

2.2.2 Cellular membrane permeability

The permeability coefficient is defined as the amount of molecules diffusing across unit area of membrane in unit time [146]. Therefore, the permeability coefficient is usually in cm/s unit. The net flux j of molecules diffusing across the membrane is given by

$$j = -p\,(C_{in} - C_{out}) \tag{2.1}$$

where p is the permeability coefficient, C_{in} and C_{out} are respectively the concentrations inside and outside of the membrane.

As we mentioned before, the cell membrane is a selective barrier whose permeability is designed and controlled so that macromolecules greater than 20kDa are intrinsically blocked [147]. The size and chemical properties of the solutes in the cytosol are crucial parameters to explain their different transport properties and permeability coefficient (see figure 2.9). Here we will give more details on the intrinsic permeability of cell membranes.

Some substances diffuse passively across cell membranes by rapidly following the concentration gradient without the help of transport proteins, this is called passive diffusion. The input of metabolic energy is not necessary because the movement of the molecules follows the chemical pressure from a high to a low concentration. The passive transport reaction is spontaneous. In general, these substances are gases, small non-polar molecules such as oxygen, carbon dioxide and nitrogen. In addition, relatively hydrophobic but lipophilic small molecules such as fatty acids, urea and ethanol can also pass easily through the membrane by passive diffusion. The diffusion rate of these molecules is related to their concentration

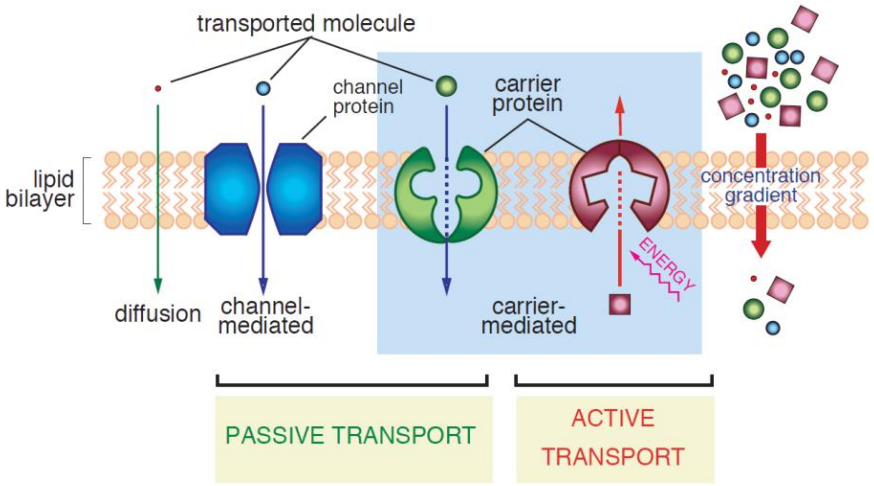

Figure 2.9: Membrane transport for different classes of molecules [144].

gradient between the two sides of the cell membrane, their hydrophobicity and their size. On the contrary, almost all polar and charged molecules such as sugars, amino acids and ions fail to pass through phospholipid membranes by passive diffusion (see figure 2.10).

We we observed that gazes have the highest permeability. Then cell membranes are more permeable to uncharged molecules and charged ions have the smallest permeability.

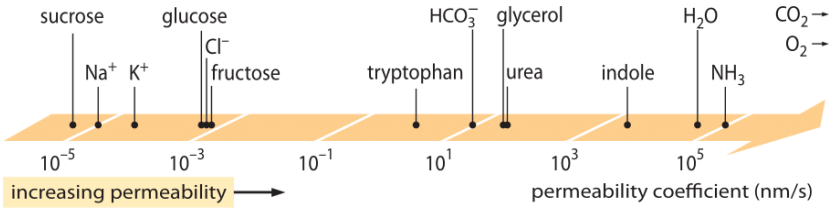

Figure 2.10: The wide range of membrane intrinsic permeabilities of different molecules in the cell [146].

Cell membranes are also selectively permeable to many polar and charged molecules, including water, peptides and hydrophilic ions, but with the help of proteins inserted in the cell's phospholipid membrane [148]. Different proteins located in the cell membrane help to effectively transport certain substances across the membrane, known as protein-mediated transfer. Even the transport of water and urea is regularly activated by specific channel proteins, because their delivery by passive diffusion is usually not fast enough to meet cellular needs. According to their function mechanisms, two major groups of transport proteins are defined: channel proteins and carrier proteins (see figure 2.9), which are transmembrane proteins. Channel proteins accelerate the delivery of water molecules and certain ions (like K^+, Na^+) by the formation of hydrophilic pores inserted in the membrane, through which several water molecules or ions can pass simultaneously. Carrier proteins can bind to specific

molecules and transfer them across the plasma membrane. Thus, proteins inserted in the membrane promote the transport of polar and charged molecules.

Facilitated diffusion is the transport of polar and charged molecules, respecting the concentration gradient, using channel proteins and certain carrier proteins . It does not require energy input. Furthermore, most ion channels open only with the presence of specific chemical or electrical signals, known as gated channels (see figure 2.11 B).

Active transport processes imply uphill movement of molecules by protein transporters (which may be channel proteins or carrier proteins) from a region of low concentration to a region of higher concentration, thus against the concentration gradient driving force see figure (2.9). Opposing the driving force of the chemical concentration gradient, this process is unfavorable and energy is required. In contrast, passive transport means a downhill movement of the molecules with the help of the carrier proteins, from a region of higher concentration to a region of lower concentration without energy input.

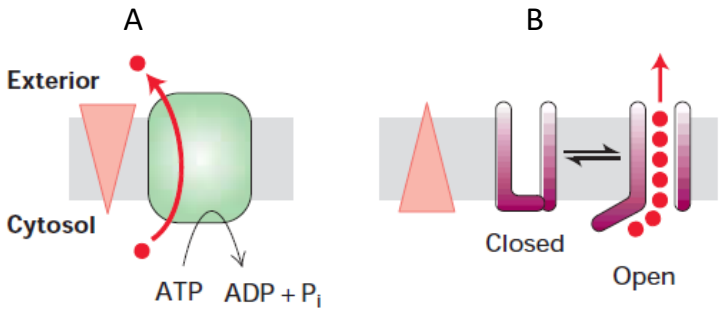

Figure 2.11: (A) Active transport which uses the energy of ATP hydrolysis to transport specific ions (red circles) against their electrochemical gradient and (B) Gated channel transport which transfers specific ions (or water) following the electrochemical gradient [144].

The main properties of the different diffusions are listed in the table 2.1. The limit between passive and active transport depends strictly on the molecules delivered and the specific needs of the targeted cells. For example, red blood cells use facilitated diffusion to transfer glucose across membranes, whereas intestinal epithelial cells rely on active transport to uptake glucose from the intestine. Facilitated diffusion is effective for red blood cells primarily because the concentration of glucose in the blood is stable and above the cellular level. In contrast, active transport is necessary for the intestine because diet causes large fluctuations in glucose levels.

For large molecules, such as proteins, polysaccharides and other soluble macromolecules, the cells internalize them from the extracellular medium by endocytosis (see figure 2.12). During this process, the targeted substances are enclosed in small vesicles that invaginate from a segment of the plasma membrane. The cytosolic side of the vesicles is always covered by a specific group of membrane proteins, including clathrin [129]. Clathrin plays a major role

Table 2.1: Comparison of the three main transport mechanisms [141].

Parameters	Passive diffusion	Facilitated diffusion	Active diffusion
Require specific protein	no	yes	yes
Concentration gradient	following	following	against
Require ATP hydrolysis	no	no	yes
Examples of transported molecules	CO_2,N_2,O_2, steroid hormones	Glucose, sucrose, amino acids, ions(K^+, Na^+), water (channel)	Ions, small hydrophilic molecules, lipids

in the formation of coated vesicles. After being internalized by endocytosis, some membrane proteins are transferred to the lysosomes, while others are returned to the surface of the plasma membrane.

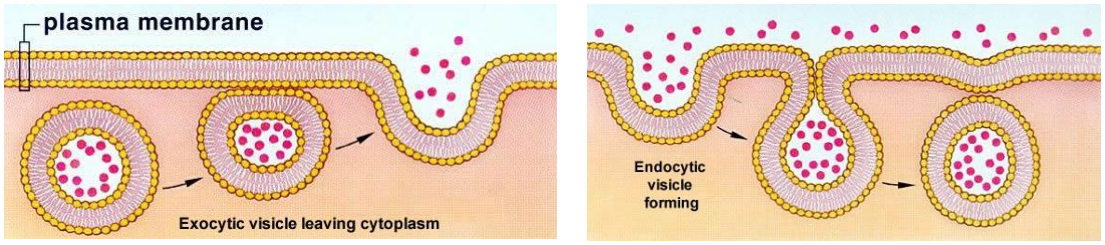

Figure 2.12: Exocytosis (left). Cells release substances to the outside when a vesicle's membrane fuses with the plasma membrane. Endocytosis (right). Parts of the plasma membrane pinches off as a vesicle containing liquid and substances from outside then move into the cytoplasm [149].

Two types of non-specific endocytosis are distinguished by the size of the endocytic vesicles formed. One is called phagocytosis ("cellular eating") when the vesicles are larger than about 250 nanometer in diameter, such as the ingestion of dead cells. The other type is called pinocytosis ("cellular drinking") when the diameter of vesicles is about 100 nanometer [144]. For pinocytosis and phagocytosis, small particles of the extracellular solution and solutes can be confined non-specifically. A specific endocytosis process, on the other hand, involves receptor mediation. When a specific receptor in the cell membrane recognizes and binds tightly to an extracellular macromolecular, the receptor-ligand binding region in the plasma membrane will swell inward and pinch to form a vesicle. In addition, receptor-mediated endocytosis is a mechanism that allows cells to absorb the nutrients in a complex macromolecular form. For example, vertebrate cells can use cholesterol in the form of lipoprotein particles by receptor-mediated endocytosis and then degrade them. Another example is that cells can absorb

the iron complexed with serum protein transferrin. The process opposite to endocytosis is called exocytosis. For example, cells produce and secrete proteoglycans [144] by exocytosis. The process of eliminating cellular waste is also based on exocytosis. Exocytosis is important for some signaling and regulatory functions of the cell (such as nervous and endocrine functions). Rat mast cells expel microgranules by exocytosis when they react to allergenic molecules [150]. In general, the production of macromolecules that will have a role outside the cell (such as membrane receptors, wall building material, extracellular matrix molecules, etc.) relies on exocytosis. Neurotransmitters are also emitted by exocytosis, a process in which synaptic vesicles filled with neurotransmitters fuse with the axonal plasma membrane, releasing neurotransmitters into the synaptic cleft in response to an increase of calcium [151].

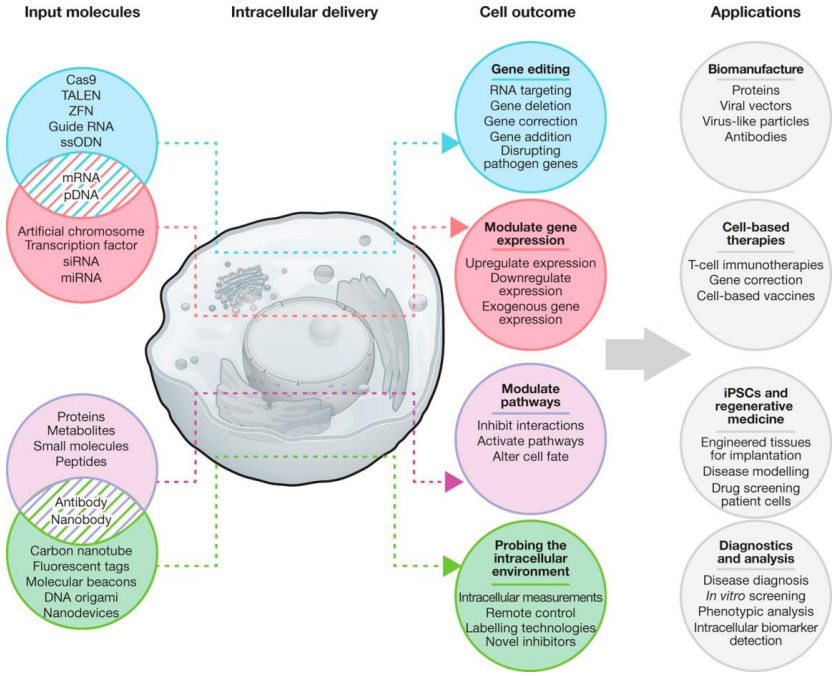

Figure 2.13: Examples of applications requiring intracellular delivery [152].

Based on the permeability properties of the cell membrane, the intracellular release of targeted biomolecules is possible by controlling the permeability of the membrane without disturbing the cell membrane for many biotechnological and medical applications [152–154]: cell gene therapy, biomanufacturing of proteins, vectors or antibodies, regenerative medicine of engineered tissues, disease modeling, cancer treatment, fundamental biology, drug screening, and diagnostics and analysis. Substances that may be delivered are gene editing molecules, DNA, RNA, proteins, metabolites, peptides, membrane-impermeable drugs, antibodies, engineered probes, etc. (see figure 2.13).

In the case of adherent cells, permeability is a process widely studied in the domain of markers in immunocytochemistry. However, not all studies involving adherent cells are

adaptable in vivo and some immunolabeling artifacts can be observed in fixed cells [155]. In the case of living cells, reversible permeability refers to the administration of contrast agents inside the cell for imaging purposes (fluorophores or quantum dots), to deliver medicines or DNA for gene therapy [156], while allowing the cells to recover after stopping the transient permeability.

2.3 Methods to increase cellular membrane permeability

A wide range of molecules have been introduced into cells using a variety of techniques. These techniques can be divided into two categories. One involves the direct disruption of the cell membrane to facilitate the uptake of the desired molecules, the other employs vectors that insert the targeted molecules into transporters such as in endocytosis (see figure 2.14).

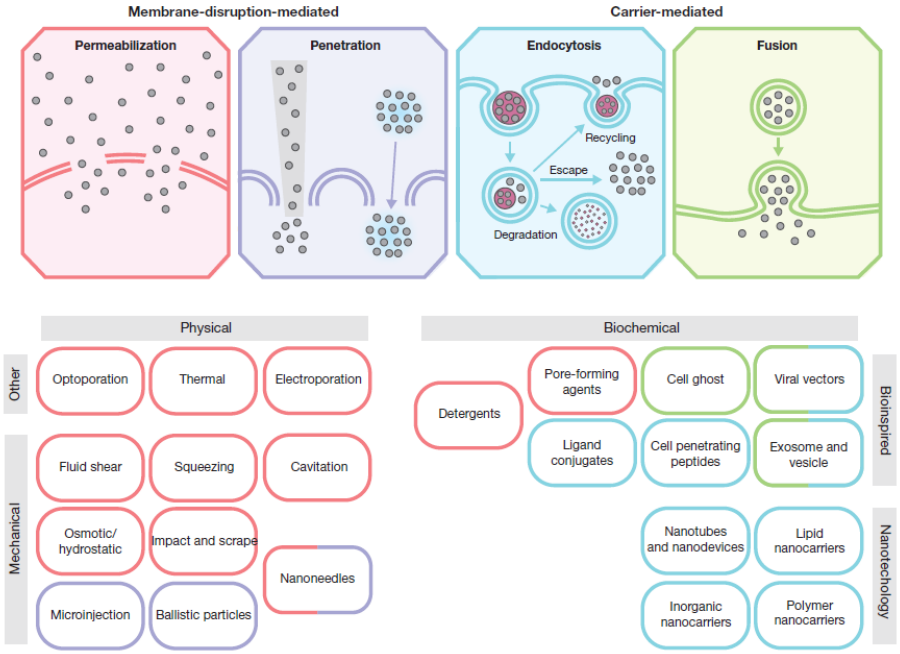

Figure 2.14: Classification of delivery methods and their associated mechanisms. Physical techniques disrupt the membrane by direct penetration, while most biochemical approaches use vectors such as viral vectors (from [152]).

Possible targets to be delivered are nucleic acids, peptides, molecular probes, nanoparticles, proteins, metabolites, membrane-impermeable drugs, etc. [152]. Cells only become permeable to a normally impermeable substance when the rupture of the membrane is large enough to allow the substance to pass through. Different methods are proposed according to the types of molecules targeted, depending on their chemical and physical properties. In living systems, efficient and safe performance is required. For instance, in the case of nucleic acid supply, viral vectors and plasmids are widely used to contain foreign DNA because they can express the DNA correctly while avoiding pathogenicity [157].

2.3.1 Membrane disruption techniques

Membrane rupture contributes to the formation of openings that increase the permeability of the plasma membrane to the targetted cargo. The most important property of the cargoes is their size. Holes in the membrane can be pores, defects, inhomogeneities, tears, lesions of all sizes and shapes. The objective is to increase the permeability of the membrane while avoiding unwanted associated cell death. In the following, we present several classic techniques.

2.3.1.1 Microinjection

Microinjection is a technique of direct penetration of a solution into living cells, fixed cells or cells in suspension, by a micrometer-sized glass capillary. It was the first technique of intracellular delivery, developed by Marshall Barber in 1911 [158]. This technique has long been used because of its ability to deliver virtually any material of any size (see figure 2.15) such as proteins [159] or complementary DNA [160]. The microinjection process is done cell by cell and is only suitable for a small number of cells (<100) [161].

Injected materials	Cell types	Reasons for using microinjection
Proteins, peptides, neutralizing antibodies	Cultured human primary neurons and astrocytes	Transduction-challenged cells
		Transduction-challenged materials
		Distinguish effects of injected materials in a mixed culture
cDNA expressing constructs	Cultured human primary neurons and astrocytes	Transduction-challenged cells
RNAs/interfering RNAs	Somatic cells, cultured cells, Xenopus laevis oocytes, zebrafish zygotes	Way to transduce antisense oligomers and interfering RNAs
Antisense and dominant negative mutants	Cultured human primary neurons and astrocytes	Transduction-challenged cells
sperms	Xenopus laevis, drosophila and mouse oocytes, human eggs	Create transgenic animals
		In vitro fertilization
nanoparticles	3T3 cells	Transduction-challenged materials

Figure 2.15: Examples of microinjection applications [162].

The cells targeted by the microinjection may be fixed or suspended cells. One needs to vary the injection angle slightly or to apply negative pressure with a holding needle (see figure 2.16). Theoretically, microinjection is almost 100% effective for a single cell. Another positive point is that the delivered dose can be precisely controlled. Compared to chemical transfection or viral infection, microinjection is safer and has less cytotoxicity, which is important for cell viability.

However, microinjection is limited to injecting cells one by one, which means low efficiency and long manipulation time. To identify the injected cells, an impermeable marker dye that can be observed under a fluorescence microscope is necessary, such as dextran Texas red

(DTR) [162] or Alexa fluor 488 hydrazine. Also, the expression of the injected DNA can be labeled by GFP (Green Fluorescent Protein). However, these dyes may be cytotoxic to cells.

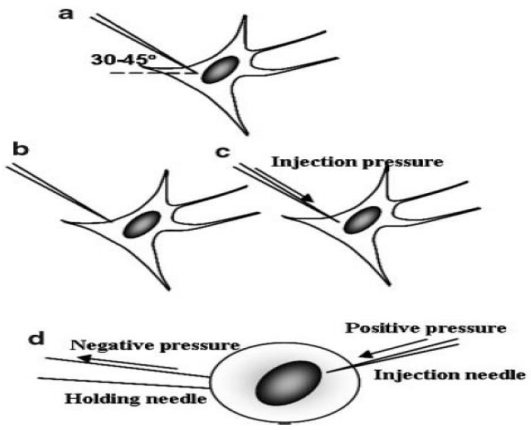

Figure 2.16: Shematic of microinjection for fixed (a b c) and suspended (d) cells [162].

2.3.1.2 Detergents

The technique using detergents to permeabilize the cell membrane is also widely used. Amphiphilic plant glycosides such as saponin [153, 163–165] and digitonin [153, 166, 167] are popular in biochemical research for reversibly permeating cell membranes. Saponin is a generic term for several sapogenin molecules. Sapogenins are complex sugars containing steroids or triterpenes. Digitonin is a specific molecule of sapogenin steroid. Triton X-100 is also widely used for its interaction with membrane cholesterol to dissolve phospholipids [168, 169]. The mechanism of action of Triton X-100 is slightly different from that of saponin and digitonin, but they have the same capacity to disrupt the membrane bilayer in detergent-lipid micelles [170]. For reversible permeabilization of the cell membrane, the detergent concentration must be limited to ensure cell viability. Although the exact mechanisms are still under investigation, it is known that the detergent molecules have a conical shape with a hydrophilic head group and a hydrophobic tail chain. The molecules can insert into the lipid bilayer and deform it. Due to their conical structure, the detergent molecules are believed to induce a convex curvature in the membrane, leading to the creation of a pore in the bilayer [161]. Alternatively, they may cause the excretion of micelles so that toroidal pores are formed [161] (see figure 2.17).

Saponins have a lipophilic sapogenin part, a steroid group (similar to cholesterol) and a hydrophilic glycoside group. They can create holes from a few nanometers to one micrometer when the concentration ranges from 10 to 1000 μg/mL, corresponding to 8 to 800 μM. The interaction of saponin molecules with cholesterol and its role in the disruption of the membrane bilayer is central. Frenkel et al [171] showed that digitonin molecules bind to cholesterol in the inner region of the membrane, extract them from the bilayer and form a new detergent-liked complexe on the membrane surface. This may disrupt the cell membrane structure because

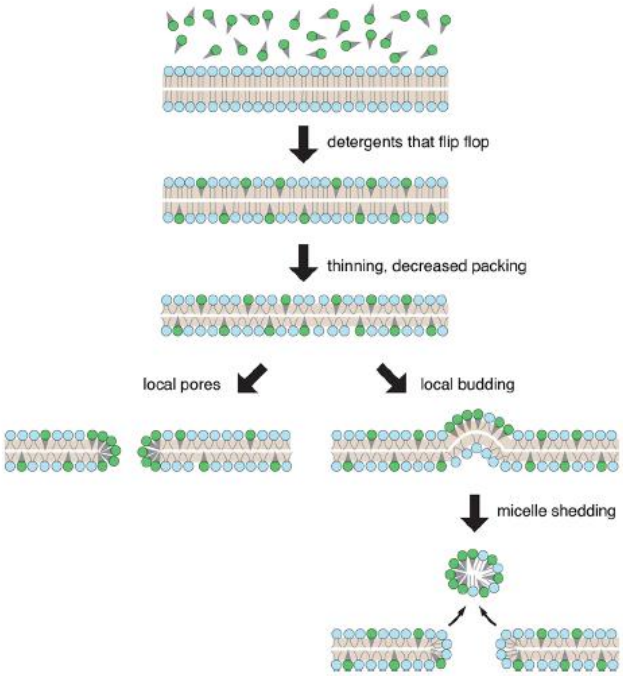

Figure 2.17: Proposed mechanisms of membrane permeabilization by detergents [161].

cholesterol is required to maintain the membranes over the physiological temperature range. Thus, the curvature of the cell membrane changes and disrupts the membrane, resulting in an alteration of the permeability of the cell membrane.

2.3.1.3 Pore forming toxins

In addition to chemical agents, pore-forming toxins, mainly in the form of amphiphilic peptides or proteins, can also cause a disruption of the plasma membrane. In general, the essential steps of the toxin action are divides into secretion, activation, coupling to the cell membrane, formation of a pre-pore, insertion of a β barrel and cell lysis [172]. All families of pore-forming toxins have homology and are all capable of forming small monomeric sub-units to perforate the plasma membrane (see figure 2.18). Streptolysin-O belongs to this family and can transiently and reversibly permeabilize cell membranes. Cells can repair Streptolysin-O lesions by adding a low concentration of Ca^{2+} ions. For example, it has been used to introduce antisense oligonucleotides in the membrane [173].

Toxin molecules can also bind to cholesterol in the cell membrane as monomers. Once coupled to the plasma membrane, the toxins can diffuse laterally to find other monomers. For the ϵ-toxin, it was observed that seven 29 kDa monomers can assemble into complexes of 155-210 kDa [174,175]. As they bind, they oligomerize into an arc- and ring-shaped structure (up to 35 nm), which is considered a large pore complex, allowing the flow of ions, micromolecules, and proteins [176,177].

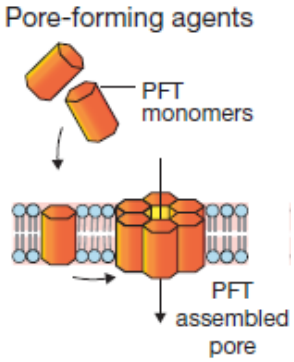

Figure 2.18: Pore forming agent mechanism [152]. Soluble pore-forming toxins as monomers are recruited on the host plasma membrane with specific interactions with lipids. Upon plasma membrane binding, the toxins concentrate and start to assemble into oligomers. As a result, they form as an assembled pore complex.

2.3.1.4 Electroporation

The electroporation technique consists of applying an electric field to disrupt the cell membrane and temporarily increase its permeability in order to boost the influx of certain molecules (see figure 2.19) [178,179]. Electroporation is applied to various groups of cells, from nucleated mammalian cells to plant cells. Although the mechanism of how the electric field influences the cell membrane is still debated [180], electroporation is widely used in clinical therapy for its ability to introduce a wide variety of molecules of different sizes and types, such as DNA or drugs [181], into millions of cells at the same time per run.

In electroporation, it is generally observed that the size of the pores created decrease exponentially on a time scale of a few minutes to tens of minutes after the end of the electrical pulses [182, 183].

When the potential difference applied to the cell reaches the transmembrane potential, the probability of generating a defect in the membrane is increased for a given electric field strength. Lipid membrane defects can be either hydrophobic or hydrophilic pores. The latter are usually larger, with a diameter greater than one nanometer. It is commonly believed that the size of the permeabilized region in the cell membrane is related to the strength of the impulses. In addition, the pore size in the plasma membrane is highly correlated with the duration and number of the electrical pulses (see figure 2.20) [181]. The response to electroporation is also dependent on the concentration of the cell population in the target area.

Depending on the type of cells, the response is sometimes heterogeneous. This means that differences in the size, surface area and physiological state of the cells, as well as variations in the composition of the plasma membrane, must be taken into account.

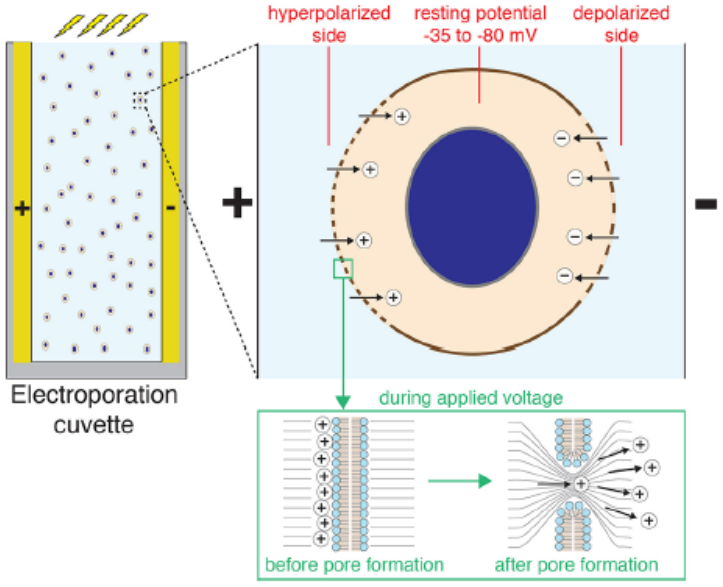

Figure 2.19: Typical configuration of a parallel cuvette for electroporation of suspended cells (left). Zoom in (right) shows the approximate pore distribution on the cell surface as a function of the orientation and polarization of the applied electric field [161].

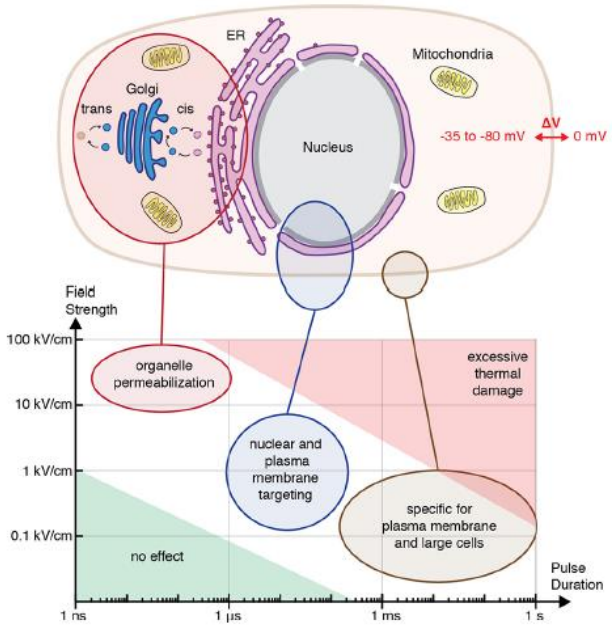

Figure 2.20: Relationship between the force-duration parameters of the pulse and subcellular targeting in electroporation [161].

2.3.1.5 Osmotic or hydrostatic methods

The application of osmotic shocks can also disrupt cell membranes. Indeed, there is a hydrostatic pressure across the cell membrane caused by the difference in osmotic potential between the inside and outside of the cell membrane (see figure 2.21). Most mammalian cells can normally survive in an aqueous condition of about 300 mOsm/L. When cells are placed into an aqueous environment with an osmotic condition below the standard value, called a hypo-osmotic or hypotonic solution, water molecules flow into cells and the cells swell. The flexible membrane can therfore expand and the volume of the cell increases.

As more water molecules rush into the cell, impermeant molecules can be carried through the aquaporins channels [161]. Scientists have successfully incorporated calcium-sensitive aequorin proteins (about 21kDa) into monkey kidney cells by hypo-osmotic treatment [184]. The procedure is inexpensive and relatively simple for the delivery of a large amount of molecules [161].

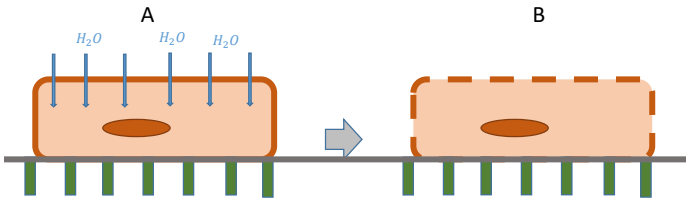

Figure 2.21: Adherent monolayer cells grown on a porous substrate which have been used to deliver a disruptive osmotic shock to the apical surface of the cells (A). Next, permeabilization occurs, localized in the apical surface of the cell (B).

2.3.1.6 Optoporation

Optoporation is a technique for permeabilizing the lipid membrane by direct interaction of a high-intensity laser with the plasma membrane (see figure 2.22). The objective of optoporation is to permeabilize the plasma lipid membrane only to targeted cargoes while other cell structures may remain intact, in order to maintain normal cell function as much as possible. The first demonstration was made by Tsukakoshi's group in 1984 [185]. They used optoporation to transfect DNA with a pulsed Nd:YAG UV laser at 355 nm with 1 mJ energy and a size of 0.5 µm, using adherent NRK cells. A single pulse of 5-10 ns was enough to open a hole several microns wide and allow the influx of DNA plasmids prior to wound repair. The repair time for a single large hole in the cell membrane was estimated to be 1-2 min [186]. However, transfection efficiency could only be achieved at 10% [187].

A second important advance in the field of optoporation was achieved in 2002 [188] through the application of femtosecond pulsed lasers. Tirlapur and König used a high-intensity (50-100 mW) femtosecond pulsed laser in the near infrared (λ=800 nm) to deliver DNA plasmid. High transfection efficiency and high viability (both close to 100%) were reported in

this publication. However, it was necessary to manually focus on each cell. So only a few cells per minute could be treated. Since then, in terms of cargoes, optoporation has been successful in delivering peptides [189, 190], proteins, dextrans, ions [191, 192], and sucrose [193].

The mechanisms of optoporation to disrupt the plasma membrane are multifactorial and complex. A focused laser can inflict a mixing of thermal and mechanical effects [161, 194]. The possible mechanisms involve thermoelastic mechanical stress [195], the growth of cavitation bubbles that produce shear stress [196], denaturation of membrane proteins [197], generation of reactive oxygen specifies (ROS) [198], extreme heat, and sonochemical phenomena [194, 199]. Dominant effect when combining these phenomena depends on parameters such as wavelength, continuous or pulsed laser source, laser energy, spot size, and absorbance properties of the samples.

The main problems with optoporation are the high cost of experimental optical systems and the low efficiency of treatments, including the time required and the success rate.

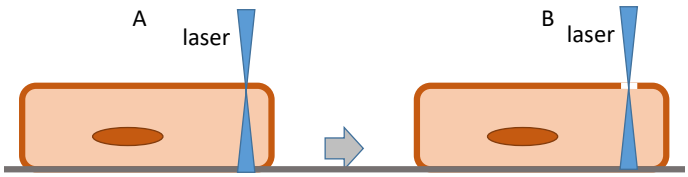

Figure 2.22: Adherent monolayer cells grown on a substrate. (A) A laser beam is focused on a small region of the plasma membrane. Then (B) permeabilization occurs in this small area.

2.3.2 Carrier mediated techniques

Most carrier-mediated delivery methods concern nucleic acid transfection. Scientists have developed a variety of carriers in this field, including lipids, liposomes, polymers, carbon nanotubes, protein-based nanoassemblies, and functional ligands. For example, lipid nanoparticles [200, 201] and cell-penetrating peptides (CPPs) [202] have been reported to deliver siRNAs and other nucleotide-based regulatory molecules. Most carriers enter the cell by endocytosis. Carriers should have several important properties. The first is the ability to encapsulate as many molecules as possible to prevent them from dissolving. The second is to be able to access the cytosol of the targeted cells. Finally, these carriers should release their content in an appropriate metabolic process.

2.3.2.1 Pinocytosis

Pinocytosis, discovered by Warren Lewis in 1929, is non specific to the substances it assimilates. It is a non-saturable form of membrane transport. In humans, pinocytosis takes place in cell wall to absorb mainly fat droplets [203]. It belongs to a type of fluid and spontaneous endocytosis: the plasma membrane invaginates towards the inside of the cell

encapsulating a small part of the extracellular medium and forming a vesicle inside the cytosol. The vesicles eventually fuse with the lysosomes. Then the content of the vesicle are digested. Pinocytosis requires a supply of cellular energy from ATP. This vesicle entry does not injure the cell while allowing the delivery of small amounts of targeted cargoes with a size below 100 nm [161]. Pinocytosis is achieved by clathrin-independent ways [204]. Clathrin-independent means that it does not need to internalize specific ligands in the cell membrane. For instance, synthesized $Y_{0.6}Eu_{0.4}VO_4$ nanoparticles have been successfully internalized by pinocytosis for imaging after nanoparticle photoreduction exposed to luminescence excitation [205].

2.3.2.2 Fusion of carriers

Exosome-inspired systems represent a new possibility for efficient and biocompatible intracellular delivery. Some carriers consisting of a phospholipid bilayer are capable of fusing with the plasma membrane to release their cargo directly into the cytosol. Initial observation has revealed that some viruses can deploy specialized peripheral proteins to trigger fusion with the targeted membranes [206, 207]. These surface proteins are called fusogenic proteins. Although the exact principles of the fusion are still under investigation, scientists have described that fusogenic carriers are able to bind with the phospholipid bilayer. The phospholipid bilayer is related to intrinsic fusion properties such as fusogenic liposomes (see figure 2.23) [208, 209]. In some cases, fusion can take place even without the fusogenic proteins [209, 210]. Another example using fusion activity is the injection of foreign substances into targeted cells with erythrocyte ghosts that have no cytoplasm or nucleus [206, 207], which are also called red cell ghosts [211, 212].

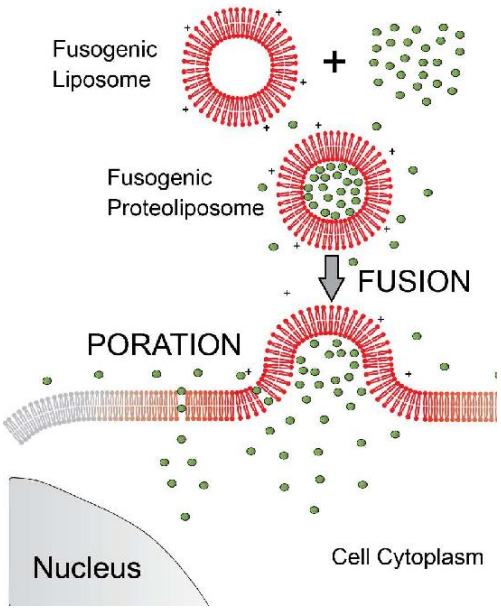

Figure 2.23: Fusion overlap on the plasma membrane to promote intracellular delivery [209].

2.3.2.3 Vector-mediated viral transduction

The main types of nucleic acid carriers are viral vectors. They are employed for precise gene correction using viral vectors that penetrate inside the cell without expressing the viral genes [157]. The main idea of producing a viral vector is to delete the coding regions of the chosen viral genome, then replace it with the targeted DNA. Finally, the viral vector with the targeted DNA can integrate into the host chromosomal DNA or can act as an episomal vector. However, the main challenges of viral-mediated transduction are safety issues and the risk of immune responses [157].

2.3.2.4 Conclusion

Appropriate intracellular methods are selected based on the intracellular delivery mode, the chemical and geometric properties of the target molecules, the required efficiency, the speed of delivery, etc. The common challenge for all these methods is to find the right balance between efficiency and viability of the cell.

2.4 Techniques to probe cellular permeability

When new methods are proposed to permeabilize cells, efficiency and toxicity should be systematically investigated. Therefore, once the molecules are introduced into the cell, the next step is to quantify the amount of cargo delivered and the viability of the cells. The methods used for DNA transfection are complex and specific, and will not be discussed here. For other targeted molecules, the best monitoring method is to systematically demonstrate the cell permeability that allows the molecules to enter and then simultaneously demonstrate cell viability after permeation. For specific permeability, ideal techniques would be able to directly quantify the targeted molecules already delivered inside the cells. However, most molecules are not quantifiable inside cells such as when the triggered cell permeability is non-specific. In the following, we introduce different techniques of quantification.

2.4.1 Exclusion test methods

The most common quantification methods are exclusion tests. Impermeable molecules can only enter the cell interior when the permeability of the cell membrane is altered, and then the quantification of these intracellular impermeant molecules is correlated with the permeability of the membrane. These impermeant molecules are also present in the extracellular medium, so that the extracellular medium should be rinsed totally before the quantification of the intracellular molecules. The most commonly used molecules are dyes such as trypan blue, fluorescent markers such as propidium iodide and fluorescein isothiocyanate (FITC). Here, we introduce two methods, one using trypan blue (0.87 kDa), a blue dye, and the other using propidium iodide, a marker of DNA and RNA.

2.4.1.1 Trypan blue

Trypan blue is an impermeant dye for the plasma membrane, and it has been used since the beginning of the 20th century. The principle can be explained as follows. When trypan blue dye is added to the extracellular medium, cells with altered plasma membranes are stained in blue while intact cells remain colorless [213]. During the experiments, the extracellular medium is replaced by a trypan blue dye solution and then an agent such as saponin is added to permeate the cells. For cells permeabilized by the agent molecules, the trypan blue molecules penetrate inside of the cell and then stain the inside in blue (see figure 2.24).

To quantify in real time with trypan blue, the idea is to grow the cells in 24-well cell culture plates. Next, trypan blue and agent molecules are added to permeabilize the cell membrane at time $t = 0$ in all wells, then after a given delay, the extracellular medium is removed in one well to observe the cells with a phase contrast optical microscope [128]. The permeabilization rate T is then equal to

$$T = \frac{\text{number of blue cells}}{\text{number of all cells}} \tag{2.2}$$

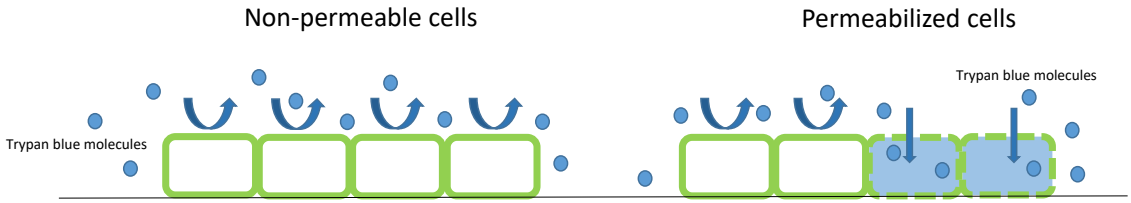

Figure 2.24: Principle of exclusion test using trypan blue.

Trypan blue molecules could also be similarly replaced by other dye molecules such as MTS[1] which stains the cells in yellow due to the presence of phenazine methosulfate [214] or tetrazolium dye MTT[2].

Trypan blue molecules, as well as other dye molecules, are toxic to cells in the long term, so all cells tested will die over time, and cannot be reused for future viability experiments.

2.4.1.2 Propidium iodide: a DNA/RNA stain

Another general type of quantification of permeability by an exclusion test is the use of fluorescent molecules, which can be read by flow cytometry or microplate photometers. One of the most common is propidium iodide (PI, 0.67 kDa), which is capable of combining irreversibly with the DNA in the nucleus, so that the fluorescent properties are strongly altered, especially the fluorescence yield [173, 178, 215]. But it should also be noted that propidium iodide can also bind to RNA in the cytosol with a lower fluorescence quantum

[1] 3-(4.5-dimethylthiazol-2-yl)-5-(3-carboxymethoxyphenyl)-2-(4-sulfophenyl)-2H-tetrazolium.
[2] 3-(4.5-dimethylthiazol-2-yl)-2.5-diphenyltetrazolium.

yield (about a factor 10). This makes quantitative measurements less accurate since the proportion of PI in the cytosol or nucleus is difficult to measure.

In the experiments, the extracellular medium is replaced by a solution of PI dye and then an agent such as saponin is added to permeate the cells. Once the cell membrane is damaged, PI molecules can penetrate into the cell and then bind to RNA or DNA directly into the nucleus since its membrane is permeable to PI (see figure 2.25). With a fluorescent microplate reader, the PI intercalation absorbs at 595 nm and then emits at 620 nm. The fluorescent intensity of the PI intercalation is 20-30 times stronger than the green fluorescence of calcein for DNA alone [215].

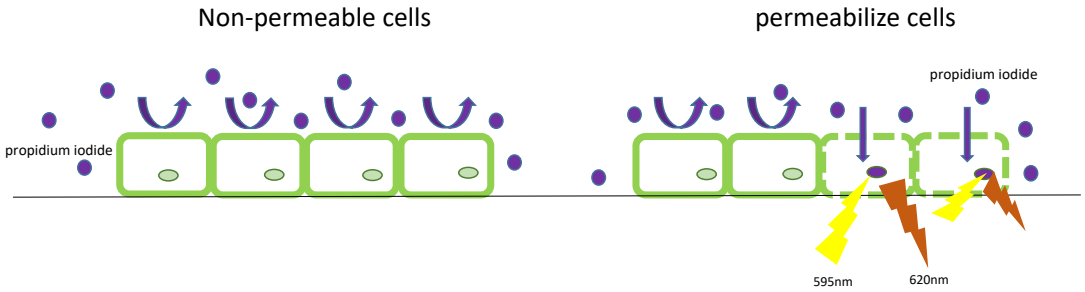

Figure 2.25: Principle of exclusion test using propidium iodide.

To calculate the rate of permeabilization, we note F_- the fluorescent signal of PI for non-permeable cells and F_+ the maximal fluorescent signal of PI for all permeated cells [128]. Thus, for a fluorescent signal F, the permeabilization rate T can be evaluated as

$$T = \frac{F - F_-}{F_+ - F_-}. \tag{2.3}$$

In experiments, to quantify in function of time after using PI, a subculture is performed on 24-well cell culture plates and then a solution containing agent molecules such as saponin and PI is added at $t = 0$. After a certain time, the permeabilization rate is calculated with equation 2.3 using a fluorescent microplate reader [128].

Like the use of trypan blue, the PI fluorescent dye is also an exclusion test, therefore an irreversible test even if it can partially quantify the permeability property for a large number of cells with good statistical precision.

2.4.2 Destructive quantification of molecules

The direct quantification of exiting intracellular molecules (proteins such as calmodulin [167]), ATP (Adenosine triphosphate), LDH (Lactate dehydrogenase) or noradrenaline, is also one of the methods used to study the permeability of the cell membranes [173, 178]. When the permeability is altered, cytosol molecules can cross the plasma membrane. The

collection and quantification of these molecules in a destructive way allows the permeability of the membrane to be quantified. Bicinchoninic acid (BCA) assay and mass spectrometry are able to quantify the amount of specific molecules. In addition, liquid chromatography is an analytical chemistry technique that can separate, identify and quantify every component of a solution, including organic molecules, biomolecules and ions.

2.4.2.1 BCA assay-for proteins

The bicinchoninic acid (BCA) assay is a method for determining the total dose of proteins or peptides in an extracellular sample [216]. It is a colorimetric test based on the analysis of the purple chelation of the cuprous ion and bicinchoninic acid molecules. The BCA protein assay involves two processes (see figure 2.26). The first is a combination of peptide bonds with cupric ions Cu^{2+} which results in the production of cuprous ions Cu^{+} in alkaline solution. The precise amount of reduced Cu^{2+} ions is proportional to the quantity of proteins in the sample solution. The second process is that two molecules of bicinchoninic acid chelate with each Cu^{+} ion, forming a purple 2BCA/Cu^{+} complex that strongly absorbs light at a wavelength of 562 nm. Then, colorimetric detection of the final solution at 562 nm is performed. Most importantly, the amplitude of absorbance increases linearly with the peptide bond concentration of the sample solution [216, 217].

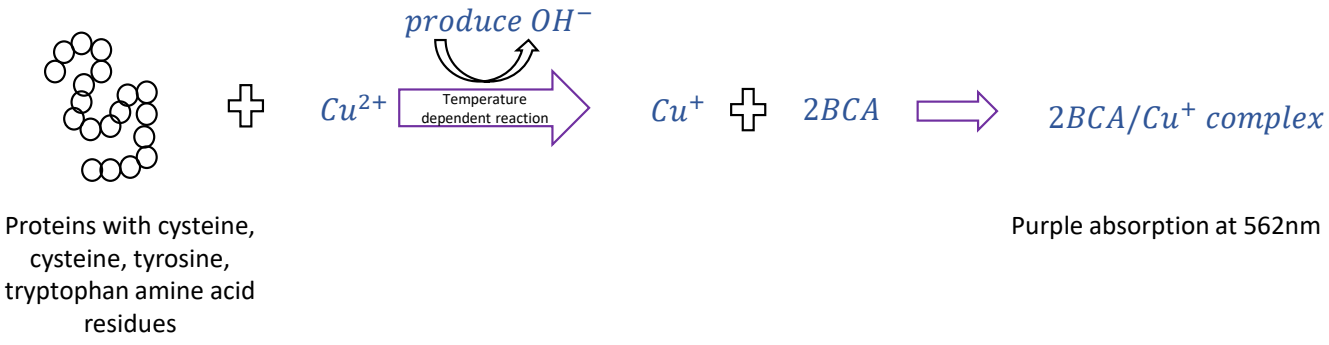

Figure 2.26: Principle of BCA assay. The first step is the reduction of copper by the protein bonds. The second step is the chelation of the cuprous ion generated in the first step with two molecules of acid, which finally produces a purple-colored 2BCA/Cu^{+}complex.

In the experiments [128], quantification in function of time of the membrane permeability is done using subculture cells in a 24-well cell culture plate prior to the experiment. The wells are then washed with PBS and then agent molecules such as saponin are added at $t = 0$ to all but one well as a control reference. After a certain time, all the extracellular medium is taken in one well to perform the BCA test, with an absorbance value A. To calculate the rate of permeabilization, A_{-} represents the absorbance value for non-permeable cells (control reference without saponin addition) and A_{+} represents the maximal absorbance value for

totally permeable cells [128]. Therefore, for any case between the minimum and maximum absorbance values, the permeabilization rate T can be calculated as

$$T = \frac{A - A_-}{A_+ - A_-}. \tag{2.4}$$

The value T indicates the percentage of maximum protein concentration. 0% means that no protein leaks out from the cell cytosol corresponding to non-permeable cells, 100% means that all proteins or peptides have left the cytosol corresponding to dead cells.

In conclusion, the BCA test is a classic technique for determining the protein dose. Bradford's protein assay is another optional essay to quantify proteins. As compared to Bradford assay, the BCA assay is less sensitive to detergent molecules or other components of the cell lysate, with the exception of proteins [216]. However, in order to quantitatively study permeability as a function of time, the BCA test requires a large number of samples due to the irreversible reaction between bicinchoninic acid and peptide bonds. This method is therefore destructive and cannot be used in real time.

2.4.2.2 Mass spectrometry

The detection of intracellular metabolites with a mass weight of less than 1000 Da are always a challenge as metabolites have a wide chemical diversity. However, mass spectroscopy is one of the choices for identifing the molecular composition and analyzing the structural profile of the metabolites [150,218,219]. Mass spectrometry is an analytical technique that can detect and identify unknown molecules in a mixture of many diverse molecules by measuring their mass-to-charge ratio and characterizing their chemical structure. Mass spectrometry data are often recorded in a mass spectrum plot. In this plot, the intensity is a function of the mass-to-charge ratio.

In particular, protein mass spectrometry is one of the important applications of mass spectrometry to determine the precise mass and structure of proteins. A typical mass spectrometer consists of three parts: an ionizer, a mass analyzer, and a detector. The ionizer converts samples into ions. The mass analyzer sorts the ion samples according to their mass-to-charge ratio. The detector records the number of ions at each mass-to-charge ratio value.

The workflow of a protein mass spectrometry is described as follows (see figure 2.27). Once the proteins in the cell cytosol are sucked through a thin glass capillary, they will be degraded into smaller peptides by enzymes such as trypsin or pepsin. After electrophoretic separation by liquid chromatography, the peptides are separated. The the peptide solution is ionized by electrospray ionization method and sent to the mass analyzer. Two methods are available to ionize all macromolecules without breaking their chemical bonds: electrospray ionization (ESI) and matrix-assisted laser desorption/ionization (MALDI). In the first mass analyzer, ionized peptides are accelerated in an electric and magnetic field. Small ionized pieces with the same mass-to-charge ratio are collected with the same deflection and detected. The result is a spectrum plot consisting of a series of peaks as a function of the mass-to-charge

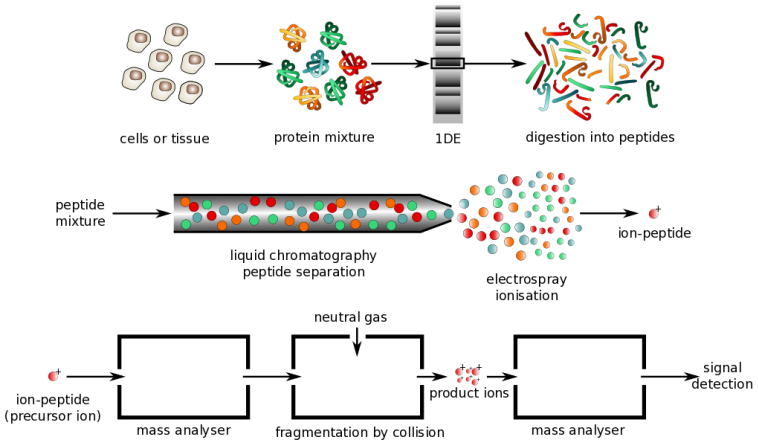

Figure 2.27: Mass spectrometry workflow. Proteins are extracted from cells or tissues and then a sub-proteome is selected for the next process. Proteins are digested into small pieces of peptide by trypsin or other enzymes, then separated by liquid chromatography (LC), ionized and finally sent to a mass analyzer to obtain a mass spectrum plot [219].

ratio values. The height of each peak indicates the relative abundance of the ions. In the case of peptides contamination, a second mass analyzer is added to allow identification of the amino acid sequence. Characterization of the peptide structure by peptide mass fingerprinting (PMF) is crucial for the identification of the protein.

Initially, mass spectrometry was limited to the detection of endogenous metabolites because of its insufficient sensitivity to small molecules present in the primary metabolism process. However, many studies have improved mass spectrometry. For example, nanostructure initiator mass spectrometry (NIMS) has been introduced in [220, 221], and has the ability to detect molecules with a mass to charge ration of less than 1000. However, this is an application for single cell mass spectra. In conclusion, mass spectrometry is a quantitative method for the analysis of the cytosol content, but as a BCA test, this method is also destructive for the molecules studied, especially proteins, due to the digestion process with trypsin or for the cells and enzymes.

2.4.3 In vivo quantification of molecules

Quantification of permeability in vivo is not common because it is difficult to measure intracellular content directly [167, 173]. The use of scanning electrochemical microscopy allows the specific quantification of redox ion leakage from within the cell for individual living cells [169]. Terahertz radiation measurements in our laboratory are also a real time in vivo quantification technique without isolating the intracellular liquid.

2.4.3.1 Scanning electrochemical microscopy (SECM) - for redox ion

Scanning electrochemical microscopy (SECM) is being applied to an increasing number of applications on living cells. For studies on the permeability of redox species in living cells, SECM is proving to be a valuable tool when redox molecules inside the cell exchange electrons with molecules outside the cell in the buffer solution.

The operating principles of SECM are presented in figure 2.28: cells are cultured in a buffer solution containing a highly hydrophilic redox mediator (ferrocyanide) which can be oxidized and then reversibly reduced [169]. The platinum probe of the SECM scans over a single isolated cell in a certain direction at a fixed height and at a fixed potential voltage. The cell blocks the diffusion of the ferrocyanide molecules towards the platinum probe and a current-distance profile is obtained. Once the cell membrane is partially permeabilized or completely detached from the substrate of the Petri dish, more ferrocyanide molecules can diffuse toward the platinum probe and then be oxidized, so that current-distance profile is different from that of the intact membrane.

Molecules such as ferrocene methanol and tetramethyl-p-phenylenediamine (TMPD) reduce SECM signal when they interact with cells (positive feedback behavior), while molecules like $(Co(bpy)_3)^{2+}$ and $(Co(phen)_3)^{2+}$ have opposite feedback behavior (negative feedback) in living HeLa cells [169]. SECM technique was also used to measure the permeability of MV^{2+} molecules through bovine articular cartilage by topographic information using the impermeant molecule $(Ru(CN)_6)^{4-}$ as a redox mediator.

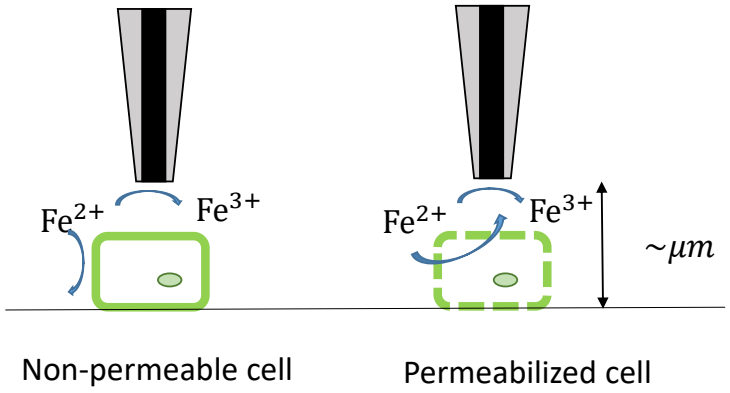

Figure 2.28: SECM technique. The distance between the probe and the dish is adjusted to several µm and scaned on a single cell: non-permeable cell (left) and permeabilized cell(right).

To probe the permeability of the cells as a function of time, the idea is to scan the current-distance profile as a function of time and then normalize the value of the current at a chosen fixed distance. The SECM technique allows a series of changes in cell membrane permeability to be studied in real time.

2.4.3.2 Attenuated total reflectance in terahertz domain

This technique was mostly developed in our laboratory at Ecole polytechnique, and is the main instrument used in this thesis. It will of course be described in much more details in the chapter 3. The property for terahertz waves to detect biomolecules in biological samples without makers is the core of this thesis, and are fully detailed in section 1.3. Here, we present a short summary of the basics of terahertz sensing [84, 222], in particular Attenuated Total Reflectance (ATR), as compared with other more classic techniques. Terahertz radiations strongly interact with liquid water. The presence of solutes in water modifies this interaction. The recording of the modification of transmission or reflection of the terahertz waves on a biological sample, such as cells, is directly correlated with the concentration of the solutes. Terahertz radiations can therefore detect the presence of ions, peptides or proteins in solution [123]. At LOB, we developed several probing techniques. ATR geometry showed very promising results [50, 128].

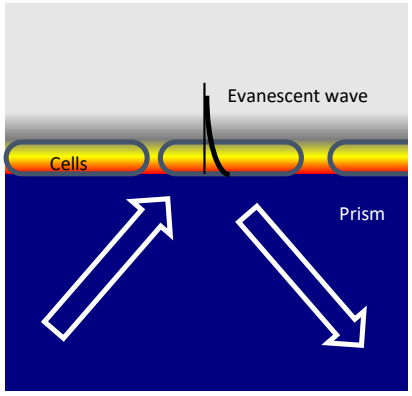

Figure 2.29: THz-TDS. The cell layer lyes in the evanescent field zone (in color gradient) on the top of the ATR prism.

The main idea is to prepare a cell monolayer (see figure 2.29) on top of a terahertz ATR prism. The cell cytosol gives a terahertz contrast with respect to the surrounding physiological medium. When cytosol molecules leak to the external medium, the terahertz contrast is modified. The probing is done by the evanescent field produced at the surface of the prism. This allows the direct quantification of molecules leakage through the cytosol in real time.

Here is a typical example recording from our THz-TDS setup (see figure 2.30) after addition of saponin (see section 2.3.1.2) [223]. Saponins trigger nonspecific permeability in the cell membrane, creating pores. Saponins at concentration 150 µm/mL have a quick interaction with the membrane without alteration of the cellular morphology [224]. A quick decrease of the terahertz contrast is due to the decrease of concentration in the cytosol due to the leakage to the extracellular medium. It has to be emphasized that these measurements are performed in vitro without staining nor labeling, and in real time.

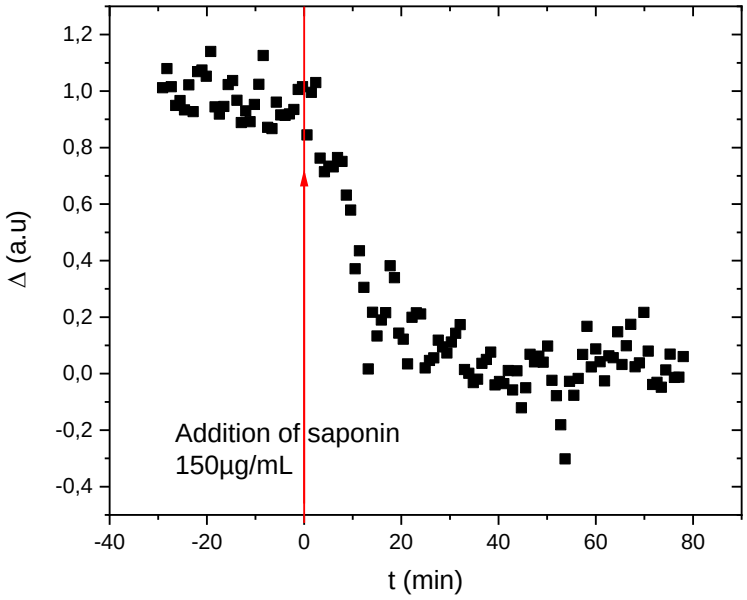

Figure 2.30: Variation of relative contrast Δ after cell membrane disruption by saponin detergent

2.4.4 Comparison of the listed techniques

In figure 2.31, we list the properties of the probing techniques previously presented, and used to detect and/or quantify the permeability of the plasma membrane. The recording of the leakage of proteins or peptides from the cell cytosol via the BCA assay technique is sensitive and semi quantitative, but it is intrusive and does not allow to investigate reversible permeability. BCA assay is more sensitive than the exclusive tests to quantifier proteins and peptides but more than one sample is required: one for each measurement, so real-time experiments are not possible.

The sensitivity of exclusion tests including trypan blue and propidium iodide dyes could be improved using Yo-Pro-1 ($C_{24}H_{29}I_2N_{30}$), which is one of the nucleic acid stains with green fluorescence for the identification of apoptotic cells. These tests are non quantitative, or at best semi-quantitative for Yo-Pro-1.

The terahertz ATR technique can probe the permeabilization of the plasma membrane in a noninvasive approach and in real-time using only one sample for the whole experiment. It probes the cytosol content, so the recorded signal is an average over the contribution of all the cytosol molecules. The SECM technique is sensitive to the redox ions and can only be used for a single cell, but the metal probe can influence the nearby cell.

From the comparison of these techniques, we conclude that our terahertz ATR setup shows several advantages to investigate cell plasma membrane permeability in physiological conditions.

Properties	Trypan blue	Propidium iodide	BCA assay	SECM	Mass Spectroscopy	Yo-Pro-1	THz
Non invasive	✗	✗	✗	✗	✗	✗	✓
Sensitive	✗	✗	✓	✓	✓	✓	✓
In real time	✗	✓	✗	✓	✗	✓	✓
One sample	✗	✗	✗	✓ Single cell	✓	✓	✓ Large number of cells
Quantitative	✗	✓/✗	✓	✓	✓	✓/✗	✓
Identification of molecules	Cell viability	DNA/RNA	Proteins	Redox ions	Metabolites	DNA/RNA	Cytosol content

Figure 2.31: Comparison of different probing techniques mentioned in this chapter.

2.5 MDCK (Madin-Darby Canine Kidney), an adherent cell line

We will see in the next chapter, in particular in section 3.4, that our terahertz biosensor needs a uniform layer of sample adhering closely to the surface of the ATR prism. As a result, epithelial cells are a good candidate. They are characterized by a strong adherence capability due to their membrane-bound proteins between their apical and basal surfaces. Also, an important point is that they can grow as a monolayer of cells.

MDCK cells (Madin-Darby Canine Kidney) are a cell line found and isolated in 1958 from the kidney tubule of an adult Cocker Spaniel dog by Madin and Darby [225]. A cell line means that the cells are able to reproduce themselves infinitely with exactly the same characteristics for all the generations. They are widely used as a model cell line for studies on epithelial polarization and transport, mechanisms of infection, regulation of tight junctions, etc [226]. MDCK cells have the ability to adhere to the basal support for all the generations of reproduction. Besides, MDCK cells have a biosafety level at 1, which does not complicate the cell culture conditions. MDCK cells form a homogeneous cuboidal epithelium adherent on the basal side. Several studies have detailed their morphological characteristics, which vary during the development of the monolayer in [227, 228]. MDCK cells are also widely used as a mammalian cell culture model for epithelial polarization in biomedical research [225, 229]. During experiments, MDCK cells were cultured on a silicon surface with complete growth medium (DMEM +10% FBS+1% penicillin-streptomycin, see Appendix A). They can grow quickly until the surface is occupied by a well-compact and adherent monolayer. Once a monolayer is formed, MDCK cells stay in a confluent state, where they reduce the speed of replication as well as their volume. This reduction of cell volume is possibly due to a decrease of the protein content in the cytosol [228].

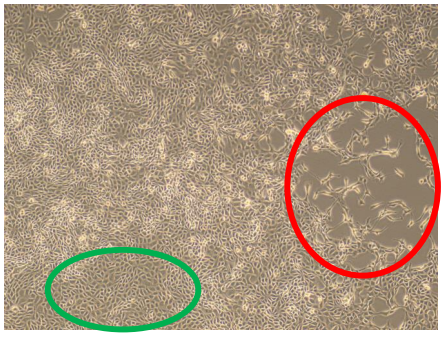

Figure 2.32: Photography of MDCK cells including a confluent zone (green circle) and a low density zone (red circle), taken with phase contrast microscope (20×).

In figure 2.32, we can observe a zone (in green circle) where MDCK cells grow well to form a monolayer confluent surface, to be compared to a zone (in red circle) where cells have a lower density. Inhomogeneity is an important factor in cell growth. When seeded at low density, MDCK cells form fibroblast-like shapes until they evolve into a confluent state in a well-polarized epithelium [230]. The low-density zone showed in figure 2.32 does not satisfy our experimental requirements since it would provide a weaker terahertz signal. It should also be noted that before confluence, the cell height is lower, less than ten micrometer [231]. When cells become denser, they start contacting each other with the decrease of the individual apical surface, as well as an increase of the cell height up to 10 micrometers. At the confluent state, cells form a mono stratified and quasi-homogeneous layer. This layer's height can vary from 8 to 12µm [232]. When cells continue to replicate after confluent state, they evolve to multilayer structures, which has to be avoid since it alters the geometry of the experimental sample, leading to an alteration of the experimental conditions.

For cellular culture, MDCK cells are seeded in a flask with complete growth medium, then placed in a cell incubator at 37°C and 5% CO_2 environment, according to the full protocol found in Appendix A. All biological manipulations are carried out under a biosafety cabinet (BSC) in a BSL-2 laboratory.

2.6 Conclusion

Biological membranes play a major role in cellular protection as well as in the transport and control of nutrients. The plasma membrane constitutes a fundamental barrier for the entry of hydrophilic molecules into the cell interior. The natural selective properties of the plasma membranes prevent the delivery of molecules that would be essential for biotechnological and medical applications. So the modification of the permeabilization of the plasma membrane in a controlled way is a key point for applications such as cell-based gene therapy, biomanufacture of proteins, vectors or antibodies, regenerative medicine of engineered tissues, disease modeling, treatment against cancer, drug screening as well as diagnostics and analysis.

The plasma membrane can be disrupted by physical means such as electroporation, mechanical force, optoporation or thermal effect, as well as by biochemical techniques, the most eminent of which being pore-forming toxins and detergents. Many active mechanisms exist for repairing the cell membrane after pore formation and they seem to depend relatively little on the origin of the damage whether the source is electrical, mechanical or chemical [233]. These mechanisms mostly depend on the pore size, temperature or cell medium. Studying the relevant parameters for pore formation and dynamics are therefore very important for developing pore models and for medical and industrial applications. This is the motivation for our next chapter to study more details about pore formation and dynamics of leakage from the formed pores.

To probe the membrane permeability properties, several methods were introduced in this chapter. Classic exclusive tests are invasive methods using the addition of external molecules, such as fluorescent molecules. Exclusive tests cannot track the dynamics of several molecules at the same time. As shown in section 2.4.3.2, the advantage of the terahertz ATR measurements is the intrinsic quantification in real time, with a time resolution much better than the minute, and without any use of fluorescent molecules. The terahertz domain can provide numerous information on the cell dynamics, and can profitably by used in parallel with more conventional techniques by correlating the information. Besides, our terahertz ATR setup shows several advantages to investigate cell plasma membrane permeability in a physiological condition. To demonstrate the advantages of terahertz ATR, the next two chapters provide applications of permeabilization measurement using chemical and optical perturbation.

Chapter 3

Investigating cell membrane dynamics with terahertz ATR sensing

Contents

3.1 Introduction

The localization of the terahertz radiations in the domain of the electromagnetic waves allows to take advantage of the two adjacent domains, the microwaves and the infrared. The terahertz sub-millimeter wavelengths enable to work on smaller samples than with microwaves. In addition, molecular vibration or rotation modes in the infrared region are still present and are the key for terahertz sensing. However, there are still few applications in the biological or medical fields. The unique optical properties of materials in the terahertz range, the good spatial resolution and the potential of near-field probes mean that many applications are possible. We will show here all the interest of the terahertz field for the biological samples, and that water, the main constituent of biological samples, is at the same time a challenge due to its high absorption, but also a unique source of contrast. We will present the attenuated total reflectance (ATR) technique in the terahertz domain, which overcomes the limitations imposed by the high absorption of polar liquids, by using evanescent waves as a local probe. We will also present the main advantages and limitations of this technique for biology.

Total reflection detection, briefly introduced in section 2.4.3 allows the study of samples composed largely of water when other imaging techniques are not suitable. It also makes it possible to take advantage, with sufficiently high sensitivity, of contrasts originating from the solutes (ions, peptides, proteins, etc.) present in the biological systems. This is the main motivation for using terahertz radiation, as conventional optical techniques have great difficulty in distinguishing the composition of solutions.

The principle of total internal reflectance and the performances of the setup existing at the beginning of this thesis work are presented in this chapter, as well as some improvements made. Next, we will explain why we chose the ATR configuration to investigate our biological samples, especially for the living cell mono-layers. After introducing the advantages of using the ATR setup in biological research in section 3.3.2, we will talk about our experimental setup in section 3.4 including the performances and the sampling procedure section 3.5.

Detergents operate by solubilizing cell membrane components. They penetrate the membrane lipid bilayer and induce stresses that deform the membrane, causing the bilayer to weaken and pores to form. Cytosol then begins to leak out of the cells. We used our TDS-ATR setup to investigate the permeabilization dynamics of the cell membrane, without any marking or staining of the sample, under the influence of saponin. In section 3.6, we will present our experimental results and then develop a physical model to analyze the data and obtain information on the diffusion of saponin molecules, cell geometry, diffusion of cytosol molecules and pore dynamics.

3.2 Transmission, reflection and ATR geometries

Transmission imaging is the simplest configuration to work with. It requires a focused terahertz beam transmitted through the object. But this geometry is limited by the thickness

of highly absorbent samples, and we know that liquid water absorbs a lot. This limits the thickness to a few hundred micrometers [234]. In addition, it requires very precise control of the thickness of the samples, which is not always possible with biological samples.

Another terahertz imaging method is to use a reflection geometry, which has a lower sensitivity to absorption and a higher sensitivity to the refractive index of the sample. As in transmission, the terahertz beam is focused on the target object and then the reflected beam is measured. Each interface of the target object causes reflection and partial absorption and the result depends on the structure and in dielectric constants. In the case of TDS measurements, the time shift between the incident and reflected beam is related, often in a complex way, to the depth of the object where the reflection occurs. In other words, the internal structure of the object can be studied in principle. Reflection geometry is a frequently used technique, especially when the target object is a biological sample, as it is compatible with a highly absorbent sample. This is why it is used to analyze skin samples, or even in-vivo. However, the depth of interaction with the sample is not well known because it depends mainly on its structure.

This configuration has allowed the study of certain tissue dehydration processes, or the identification of healthy tissue from cancerous tissue (see figure 3.1) [235].

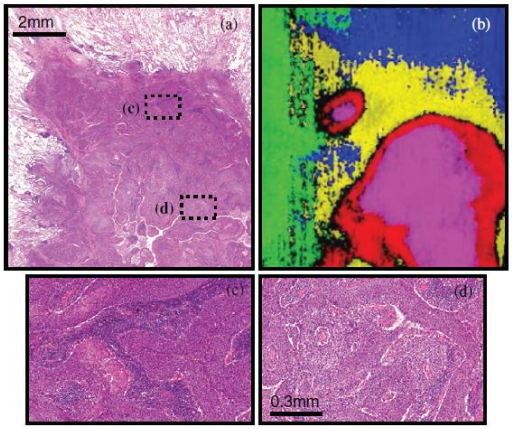

Figure 3.1: Histopathology of a tumor. (a) Microscope image of the hematoxylin-eosin-stained lung sample. (b) Corresponding segmented terahertz image by reflection on the sample. Supposed tumor cells are in red. (c) and (d) High magnification close-ups corresponding to the areas marked in (a) [235].

The two geometrical configurations described above offer interesting possibilities for the imaging of thin and/or weakly absorbent objects. However, they are not suitable for the study of cellular permeabilization, where it is necessary to discern cytosol modifications and their consequences in the terahertz domain. Indeed, in transmission geometry, the signal comes from the molecules, whether in the cytosol or in the extracellular medium. The measurement does not make it possible to locate them because they contribute in the same way to the signal. In reflection geometry, the problem arises from the fact that the reflected signal comes

from a rather poorly defined spatial area that depends very much on the structure of the cells. And the depth sensed in reflection is of the order of the wavelength, thus not well adapted to the 10 µm height of cells. Here again, this geometry is not the most suitable for our permeabilization studies [31].

On the contrary, we will see that the geometry of attenuated total reflectance (ATR) is well adapted to our objective, taking advantage of the existence of an evanescent field whose spatial extension is of the order of the height of the cells. In the following section, more details are presented.

3.3 Terahertz Attenuated Total Reflectance (ATR)

As we have seen in chapter 1, terahertz radiation is described by an electromagnetic wave. We represent the electric field (the magnetic field being directly linked to the electric field by Maxwell equations) by a vector $\vec{E}$ oscillating perpendicularly to the direction of propagation. If the medium of propagation is homogeneous and isotropic, the propagation is in a straight line. A wave is characterized by its frequency and polarization. For a non-polarized wave, $\vec{E}$ evolves in totally random directions transversely to the direction of propagation. A linear polarization corresponds to $\vec{E}$ always oscillating in the same plane which contains the axis of propagation. In this case, it can be described as the sum of plane polarized waves, each given by the following formula

$$E(\vec{r}, z, t) = \mathrm{Re}\left\{\vec{A}(\vec{r})e^{i(kz-\omega t)}\right\} \tag{3.1}$$

with $\vec{r} = (x, y)$ and $\vec{k}$ is the wave vector indicating the wave propagating direction along z, ω is the angular frequency, $\vec{A}$ represents the complex amplitude of the wave: $\vec{A} = |A_0|\, e^{i\phi}$ where ϕ is the phase of the wave.

In the case of wave interactions at the interface between two media, and in order to simplify the analysis, one divides the incident radiation into two components: the s-polarized (from the German word "senkrecht": perpendicular) and the p-polarized (parallel) components. These two components represent two perpendicular polarization directions (see figure 3.2). The s-polarized component is perpendicular to the plane of incidence while the p-polarized component is parallel. The total electric field is thus the sum of these two components. The advantage of two separate components is that a single pair of equations (one for s-polarization, the other for p-polarization) is sufficient to address all types of waves at an interface.

For an incident field $\vec{E}_i$ impinging with an incident angle α at the interface of two different media with complex refractive indices $\hat{n}_1$ and $\hat{n}_2$, the amplitude of the reflection coefficients $r_{s,p}^{n_1 \to n_2}$ are defined by the ratio of the amplitudes of the reflected electric field components to

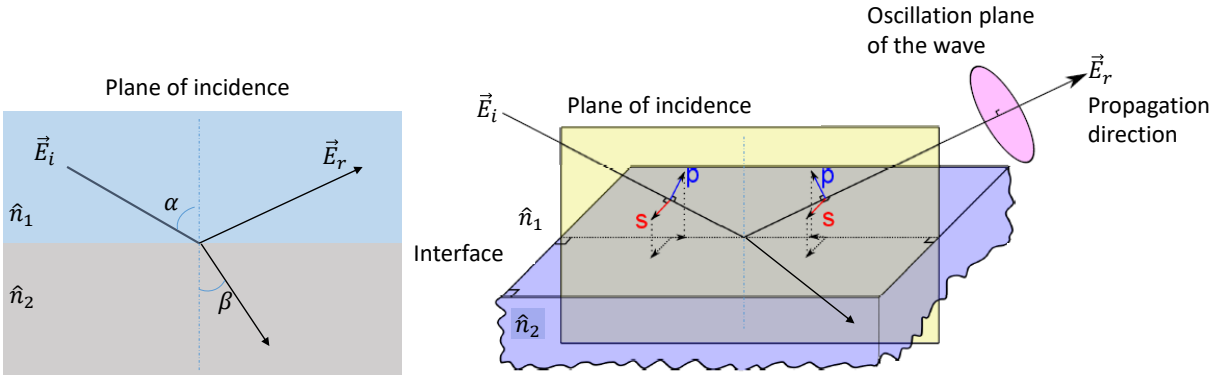

Figure 3.2: (Left) Schematic of Snell-Descarte's law with a incident angle α, a reflected angle equal to incident angle and a refractive angle β. (Right) Schematic of the s-polarized and p-polarized components of an electromagnetic wave at an interface between 2 media with complex refractive index $\hat{n}_1$ and $\hat{n}_2$.

the incident components. They are complex values given by Fresnel's equation [104]

$$\begin{aligned} r_p^{n_1 \to n_2} &= \frac{E_i^p}{E_r^p} = \frac{\hat{n}_2 \cos\alpha - \hat{n}_1 \cos\beta}{\hat{n}_2 \cos\alpha + \hat{n}_1 \cos\beta} \\ r_s^{n_1 \to n_2} &= \frac{E_i^s}{E_r^s} = \frac{\hat{n}_1 \cos\alpha - \hat{n}_2 \cos\beta}{\hat{n}_1 \cos\alpha + \hat{n}_2 \cos\beta} \end{aligned} \tag{3.2}$$

where β is the transmission refraction angle defined from Snell-Descarte's law of refraction (see figure 3.2) by

$$\hat{n}_1 \sin\alpha = \hat{n}_2 \sin\beta. \tag{3.3}$$

Also the Fresnel equations of the transmission coefficients $t_{s,p}^{n_1 \to n_2}$ are defined as

$$\begin{aligned} t_p^{n_1 \to n_2} &= (1 + r_p^{n_1 \to n_2}) \frac{\cos\alpha}{\cos\beta} &&= \frac{2\hat{n}_1 \cos\alpha}{\hat{n}_2 \cos\alpha + \hat{n}_1 \cos\beta} \\ t_s^{n_1 \to n_2} &= 1 + r_s^{n_1 \to n_2} &&= \frac{2\hat{n}_1 \cos\alpha}{\hat{n}_1 \cos\alpha + \hat{n}_2 \cos\beta} \end{aligned} \tag{3.4}$$

3.3.1 Principle of Attenuated Total Reflectance (ATR)

Using Eq.3.3 and considering here that $\hat{n}_1$ and $\hat{n}_2$ are real, one obtains

$$\beta = \arcsin\left(\frac{n_1}{n_2}\sin\alpha\right). \tag{3.5}$$

When $n_1 < n_2$, this relationship is always fulfilled and part of the incident wave is transmitted. However, when $n_1 > n_2$, β is defined only when α remains below a critical angle α_c

$$\frac{n_1}{n_2}\sin\alpha \in [0,1] \Longleftrightarrow \alpha \leq \alpha_c = \arcsin\left(\frac{n_2}{n_1}\right). \tag{3.6}$$

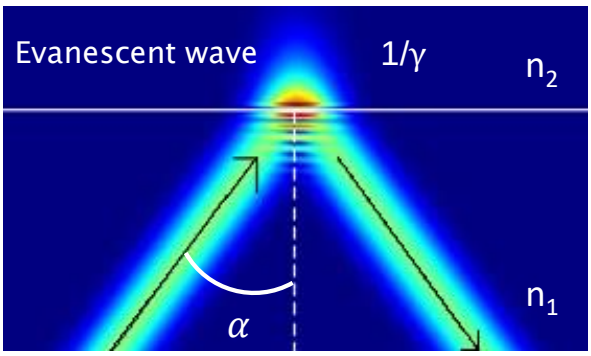

Figure 3.3: Schematic of total reflectance with an evanescent wave, obtained from FDTD simulations.

Total internal reflectance (TIR) occurs at the interface between two dielectric media when $n_1 > n_2$ and when $\alpha > \alpha_c$. When α approaches α_c, β approaches 90°, at which the refracted wave becomes parallel to the surface. It means that refraction no longer exists, and that total internal reflectance occurs. For total internal reflectance conditions $\alpha \geq \alpha_c$, one can replace β in equation 3.3 and 3.2 and obtain the reflection coefficient of s- and p-polarization,

$$\begin{aligned} r_p^{n_1 \to n_2}(\alpha) &= \frac{\hat{n}_2 \cos\alpha - \hat{n}_1 \sqrt{1 - \left(\frac{\hat{n}_1}{\hat{n}_2}\right)^2 \sin^2\alpha}}{\hat{n}_2 \cos\alpha + \hat{n}_1 \sqrt{1 - \left(\frac{\hat{n}_1}{\hat{n}_2}\right)^2 \sin^2\alpha}} \\ r_s^{n_1 \to n_2}(\alpha) &= \frac{\hat{n}_1 \cos\alpha - \hat{n}_2 \sqrt{1 - \left(\frac{\hat{n}_1}{\hat{n}_2}\right)^2 \sin^2\alpha}}{\hat{n}_1 \cos\alpha + \hat{n}_2 \sqrt{1 - \left(\frac{\hat{n}_1}{\hat{n}_2}\right)^2 \sin^2\alpha}}. \end{aligned} \tag{3.7}$$

It is important for the following analysis to note that the theory shows that in a condition of total internal reflectance, an evanescent wave, which cannot propagate, exists in the second medium (see figure 3.3). This evanescent wave decreases exponentially with the distance from the interface. The electric field therefore penetrates a short depth into the second material before being reflected and returning to the first material. This evanescent wave is notably at the origin of the Goos-Hänchen effect [236], a small lateral shift of the center of the incident wave after total reflection.

This evanescent wave localizes near the interface between the two media and exponentially decreases with the distance L from the interface according to equation

$$e^{-\gamma L} \tag{3.8}$$

where the evanescent coefficient γ is defined as

$$\gamma = Re\left[\frac{2\pi}{\lambda}\sqrt{\hat{n}_1^2 \sin^2\alpha - \hat{n}_2^2}\right]. \tag{3.9}$$

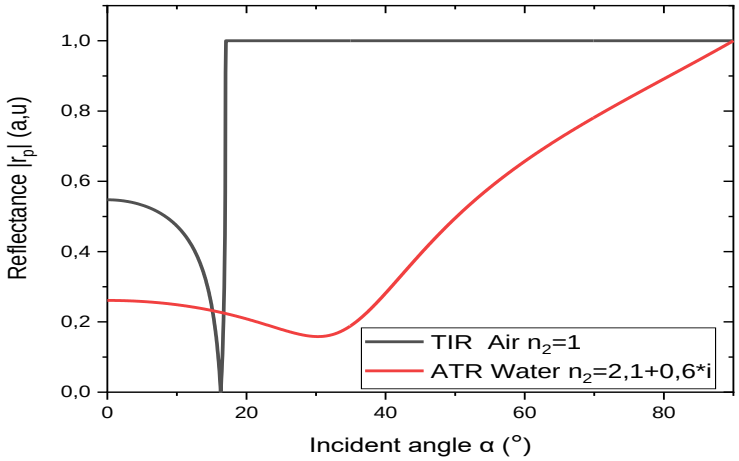

Figure 3.4: Reflectance of p-polarized wave in the case of TIR (black $\hat{n_2} = 1$) and ATR (red $\hat{n}_2$=2.1-0.6i) from the same incident medium, silicon (n_1=3.42).

One can define the penetration depth $\delta = \frac{1}{\gamma}$ corresponding to a decrease of the evanescent wave amplitude by $1/e$ (about 64%). The depth of the light penetration into the second medium, δ, is independent of polarization. Therefore, the choice of the wave polarization depends on the geometry of the setup, but not on the penetration depth.

When the second medium is absorbing (the refractive index is now complex), the reflection is no longer total and the critical angle does not have the same meaning; it only shows where the transition from low to high reflectance lies. In this case, the total reflection disappears, since the reflected beam is partially absorbed. This is referred to as attenuated total reflectance (ATR). In ATR, reflectivity at an angle of incidence larger than the critical angle is again greater than at a small angle of incidence, but the transition is smooth compared to the abrupt transition in total internal reflectance. In the following, we define the complex refractive index as

$$\hat{n}(\omega) = n(\omega) - i\kappa(\omega), \tag{3.10}$$

where $\kappa(\omega) = \frac{\alpha c}{2\omega}$. In this formula, α is the absorption coefficient in intensity ($\propto |E|^2$), n is real part of refractive index, c is the velocity of light and ω is the angular frequency. If we evaluate the penetration depth in the case of a total internal reflection at a silicon-air interface at an angle of 42° which corresponds to our experiemntal ATR prism, one finds $\delta \approx 23$ µm at 1 THz and $\delta \approx 10$ µm at 2.5 THz. These values are much lower than the characteristic absorption length of water $\frac{2}{\alpha_{water}} \approx 100$ µm; the absorption during the interaction with the evanescent wave will therefore remain reasonable.

The reflectance in function of the incident angle α for a non-absorbing medium (κ=0) and a strongly absorbing-medium ($\kappa \neq 0$) is showed in figure 3.4. The incident medium is high resistivity silicon (HR-Si) with index n_1=3.42. For TIR (black curve in figure 3.4), the reflectance can reach 1 when the incident angle α is greater then critical angle α_c. However, in the case of ATR (red curve in figure 3.4), the reflection is never total. Since ATR is

achieved with the reflexion from the denser medium, the use of a prism is required to couple the incoming beam to ATR geometry.

Since a biological sample is full of water and thus is an absorbing medium, ATR setup is particularly well adapted to the study of such samples.

3.3.2 Advantages and limitations of ATR geometry

ATR geometry has the advantage of being able to study biological samples of semi-infinite thickness due to the interaction between the evanescent wave of the terahertz radiation and the sample. The sensitivity as a function of depth is exponentially related, more precisely, the evanescent wave works as a local probe over a distance corresponding to the penetration depth δ [104]. Using the equation 3.9, the penetration depth can be calculated. For pure water at 1 THz, the penetration depth is about 20 µm for our setup, and this will be presented in more detail in the next section. This means that at a depth of 20 µm, about 60% of the incident wave intensity is coupled with water and solute molecules and then partially absorbed. Above 5δ, the interaction with the rest of the sample is negligible and therefore does not influence the measurement. Another advantage of ATR geometry is that the measurement is not dependent on the thickness of the sample as soon as the extracellular surrounding liquid extension is much longer than penetration depth δ, which is easily achieved.

However, the ATR geometry has also its limits. For example, the problem of the sample holder. The coupling of the evanescent wave and the sample medium requires that the sample is in a very close contact with the sample holder. In our case, this optical discontinuous contact causes problems during experiments, and will be presented in section 3.5.2.

3.4 Time-Domain Spectroscopy experimental setup

3.4.1 Description of the setup

We will present here the experimental setup used in the first part of the thesis' work. It is based on the TDS setup described in section 1.1.2 with the addition of an ATR prism, as seen in the previous section 3.3.

The setup is based on a femtosecond laser and the production of terahertz pulses of duration less than a picosecond. Emission and detection are performed with two photoconductive antennas (see figure 3.5). The principle of THz-ATR is presented in detail in section 1.1.2. Our experimental setup starts with a commercial femtosecond laser (Femtolaser M1), providing 12 fs pulses at 76 MHz (P≈500 mW). Only a fraction of the power is used in the ATR setup, about 60 mW. This beam is cut in two. One of the beams strikes the emitting antenna, a GaAs semiconductor substrate placed between two parallel metal lines. The femtosecond laser pulse provides enough energy to allow the passage of electrons from the valence band to the conduction band of the semiconductor. In addition, a static voltage of 50V is applied

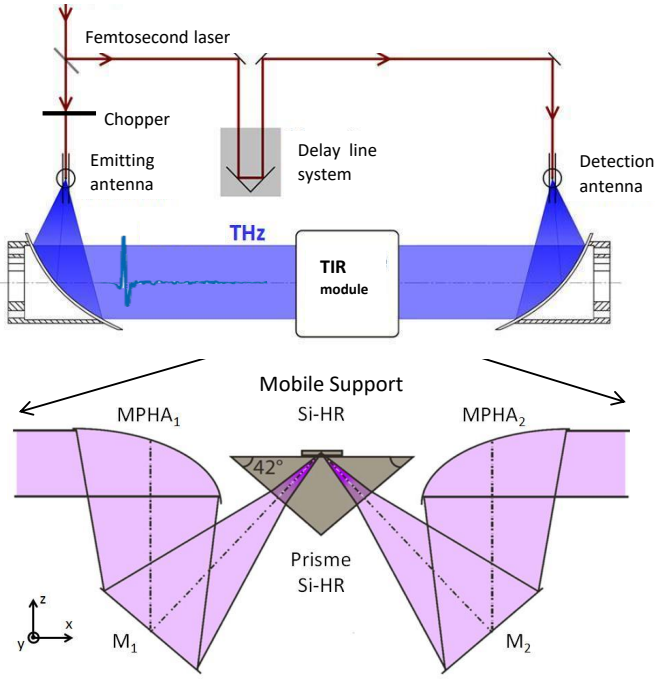

Figure 3.5: Schematic of the Time Domain Spectroscopy (TDS) setup (top) and of the ATR module with a HR-Si prism and a HR-Si mobile window (bottom).

between the two metal lines, so that the charge carriers undergo an accelerated movement, thus radiating a terahertz field E_{Thz},

$$E_{THz}(t) \propto \frac{\delta i(t)}{\delta t} \tag{3.11}$$

which is proportional to the derivative of the current produced by the time-varying movement of the charges. This generates a linearly polarized sub-picosecond pulse of electromagnetic radiation in the terahertz domain. The terahertz beam can then propagate in free space, guided by an off-axis parabolic mirror, and brought to the ATR module. In this module (Figure 3.5, bottom), the incoming terahertz beam undergoes attenuated total reflectance at the top of the prism, where the sample is positioned.

The beam then propagates to the receiving antennas, where a principle equivalent to the one of the emitting antenna applies. The second part of the initial femtosecond beam passes through a delay line and then is focused on a second GaAs detecting antenna, also creating charge carriers. These carriers can be accelerated by the superimposed terahertz field, producing a measurable current. Finally, this current is amplified and detected by a lock-in amplifier. Additionally, a mechanical chopper modulates the terahertz beam at a frequency of about 280 Hz, and drives the lock-in amplifier, which demodulates the input signal at the chopper frequency. Therefore, the lock-in output signal is proportional to the amplitude of the terahertz field, at the very moment of the arrival of the femtosecond beam. This delay can easily be adjusted by changing the position of the delay line and then the distance traveled

by the second beam. A measurement at a given delay requires about 300 ms, which makes it possible to record the full terahertz pulse in about one minute. A typical terahertz pulse is shown in figure 3.6.

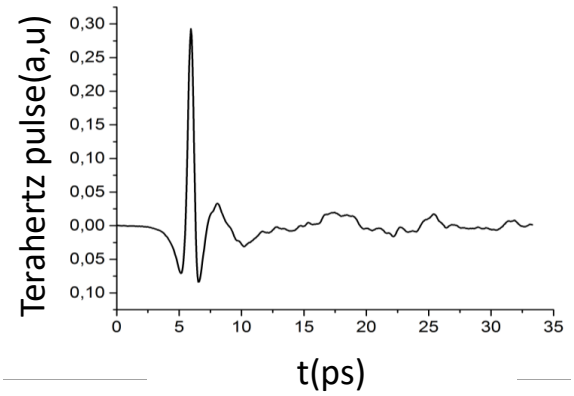

Figure 3.6: A typical terahertz pulse record by THz-ATR.

In the ATR module, the linearly polarized wave is directed onto a 42° angle prism as shown in figure 3.5 (bottom). This 50 by 50 mm square prism is made of high resistivity silicon, opaque in the visible range but very transparent in the terahertz range. Dielectric losses are very low, so we can assume that $\hat{n}_{\mathrm{HRSi}} = n_{\mathrm{HRSi}} = 3.41$. An evanescent wave is then produced at the top of the prism, with a depth of penetration $\delta \approx 23\,\mu\mathrm{m}$ at 1 THz. In addition, a second pair of parabolic mirrors concentrates the terahertz beam at the top of the prism, then recollimates it after reflection. The spot at the top of the prism has a transverse extension of about 1.5 mm, which corresponds to the spatial resolution of the system.

The ATR module allows to image an object. However, the movement of the prism or of the terahertz beam is not possible due to the impulsive nature of the terahertz wave. A displacement, even minimal, would deeply alter the signal. The solution is therefore to put the biological object on a parallel plate made of the same material as the prism, and to move this plate. The silicon plate is simply placed on the prism and allows the sample to be translated. If the optical contact between the prism and the slide is perfect, everything happens as if the two parts were one single piece. In reality, a small layer of air may be present at the interface, which modifies the reflected signal. We will study in the following the influence of this layer on our experiments.

Two translation stages allow to move the silicon plate in x and y directions over an area of 4 by 4 mm. A C# program automatically manages the x and y displacements, as well as the acquisition of terahertz signals. We were able to obtain, for each pixel of the image, the temporal signal reconstructed from the optical path delay.

3.4.2 Sampling

A CCD camera (1024×768 pixels) is installed on top of the ATR setup to monitor the surface of the cells. This camera allows us to easily track the position of the sample prior to measurement and the status of the cell layer.

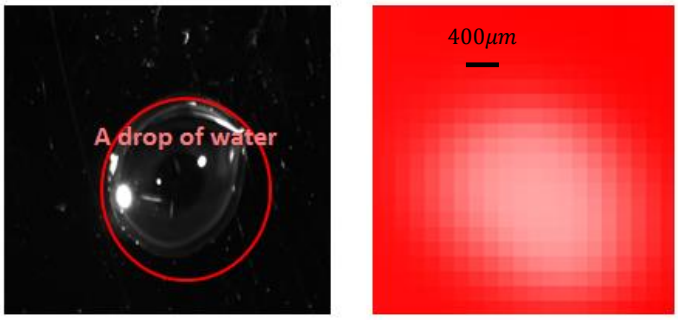

Figure 3.7: Photography of a water drop (left) and corresponding terahertz imaging (right). The TDS reflected signal decreased strongly due to water absorption, which allows the simultaneous observation of the water drop in the terahertz range and in the visible, and then the determination of the coordinates origin.

To superimpose the center of the camera and the center of the evanescent terahertz wave in order to determine the precise position of our cell sample, we use a small drop of water placed in the center of the silicon window. Once the terahertz image of this water drop is recorded (see figure 3.7 picture on the right), we can easily move the center of the camera to the one of the ATR field. Thus, we search for the boundary between the reference and the cell parts, as shown in figure 3.15. Once the moving silicon window is integrated on top of the ATR module, we move the window slightly on the surface to push out the air molecules between the prism and the silicon window. As described further in the subsection 3.5.2 on flatness problems, a micrometer level of air gap between the prism and the silicon window can significantly change the reflectivity of the incident terahertz wave, resulting in signal alteration. It is therefore important to expel as much air as possible. The respective position of the silicon window and the cell layer is shown in figure 3.8.

It was previously shown in [128,222] that the terahertz beam reflected from the cell layer and the reference zones (HBSS or PBS) show significant differences due to the variation in permittivity. This change can be identified from the peak amplitude of the terahertz pulse, as shown in figure 3.9. Thus, experimentally, we measure 10 time points around the position of the peak amplitude and then we fit them with a parabolic function to obtain the value of the peak amplitude with a better precision (figure 3.9). Fitting the curves helps us to reduce the sampling time.

Let PA_{ref} be the peak amplitude reflected by the reference zone and PA_{cell} the peak amplitude reflected by the cells zone. A single point is taking from 0.15 to 0.24 s, up to 1 s if the delay line movement time is considered. Several temporal points are needed in order

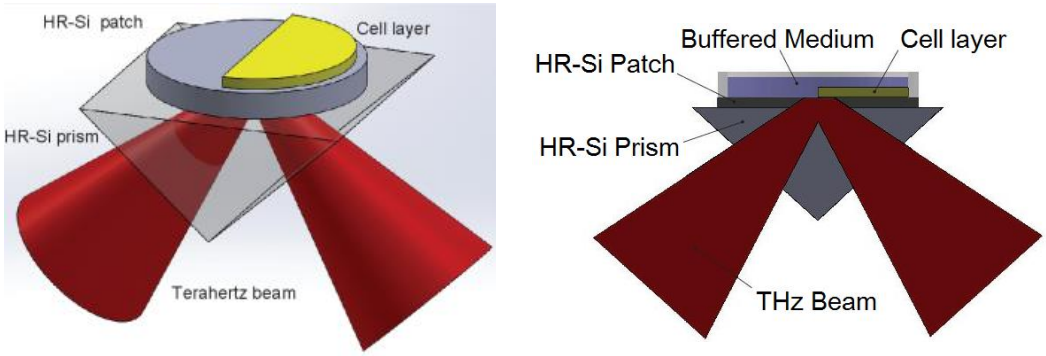

Figure 3.8: The cell layer in the ATR module with the silicon prism and the mobile window (left) and a transverse section of the setup (right).

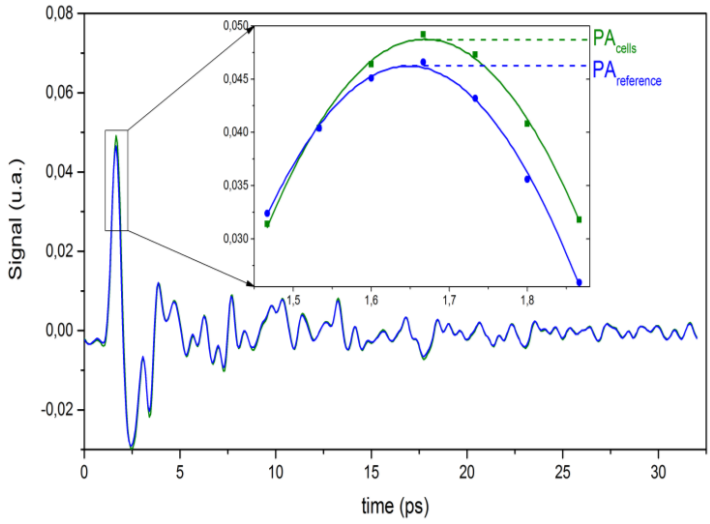

Figure 3.9: Terahertz signal from the cells (green) and the reference (blue) zones. In the inset, the experimental points provide the parabolic fit that improves the accuracy of the measurement [128].

to be sure to acquire the peak value during the whole acquisition. The movement of the XY translation stage takes a variable time, depending on the distance between 2 successive points chosen as cell zone and reference zone. A total acquisition time would be around 2 seconds per point on a 2 cm wide range. The relative contrast Δ_{rel} between the cell and reference zones (see figure 3.8) is then defined by

$$\Delta_{\text{rel}}(t) = \frac{\text{PA}_{\text{cell}}(t) - \text{PA}_{\text{ref}}(t)}{\text{PA}_{\text{ref}}(t)} \tag{3.12}$$

A positive Δ_{rel} means that the cell layer reflects more than the buffered medium area. A negative Δ_{rel} means the opposite. In our experiments, we found that the value of Δ_{rel} varies from 5 to 9% from experiment to experiment, due to the fact that the cell layer could not develop in the same confluent state.

In addition, each measurement consists in practice of two acquisitions by moving the sample plate: a sample data and a reference data when the sample is moved out of the terahertz beam on the prism. In total, a complete measurement therefore takes about 10 seconds.

3.5 Performance

3.5.1 Limits of the TDS-ATR setup.

The application of terahertz imaging in biology, particularly with the TDS-ATR configuration, presents two main challenges: resolution and sampling time.

Lateral resolution is a fundamental optical criterion for judging the performance of the installation. It is the minimum separation that a system can distinguish between two point-like objects. If we note f the focal length of a lens, D the beam size and n the refractive index of the medium, the numerical aperture of the system is $\text{NA} = \dfrac{n\,D}{f}$. The Rayleigh criterion R is then defined as follows

$$R = 1.22\frac{\lambda}{\text{NA}}. \tag{3.13}$$

The spatial resolution R calculated by the Rayleigh criterion allows to quantify the diffraction in a system and can be applied to our terahertz configuration. Since terahertz radiation has a wavelength of several hundred micrometers, the parameter R gives a much higher spatial resolution than in the visible range. The lateral resolution of our device is therefore of the order of 1.5 mm [31]. The longitudinal resolution is however much better because it is given by the penetration depth of the evanescent wave, which is about 20 µm, i.e. the order of magnitude of the height of a cell.

The sampling time is also an important parameter for the performance of our system. It takes about 300 ms to make a simple measurement at a specific delay t. To record a time signal of 10 ps over 200 points, then about 30 s are needed. If now we want to make these measurements on an image of 10 by 10 pixels, it takes more than an hour of measurement [50].

3.5.2 The problem of the flatness of the HR-Si elements

The penetration depth at the prism surface is much shorter than the wavelength. Therefore, a flatness defect of the silicon elements (prism or sample plate) can create a partial reflection at the interface and alter the signal. This phenomenon is called frustrated total internal reflection. In TDS experiments, this default can also create an echo in the time domain (see figure 3.10). Therefore, this air gap has to be as small as possible. In the visible range, or in medical ultrasound, index-matching liquids are often used to fill the gap at the interface in order to cancel unwanted reflections. However, our sample window has to move on top of the prism with as less friction as possible during measurement. We tried many liquids, from water to various oils or solvents, but unfortunately, we could not find an index-matching liquid working efficiently around 1 THz. The liquids were either inefficient to match the refractive index, or too sticky to allow the displacement of the plate.

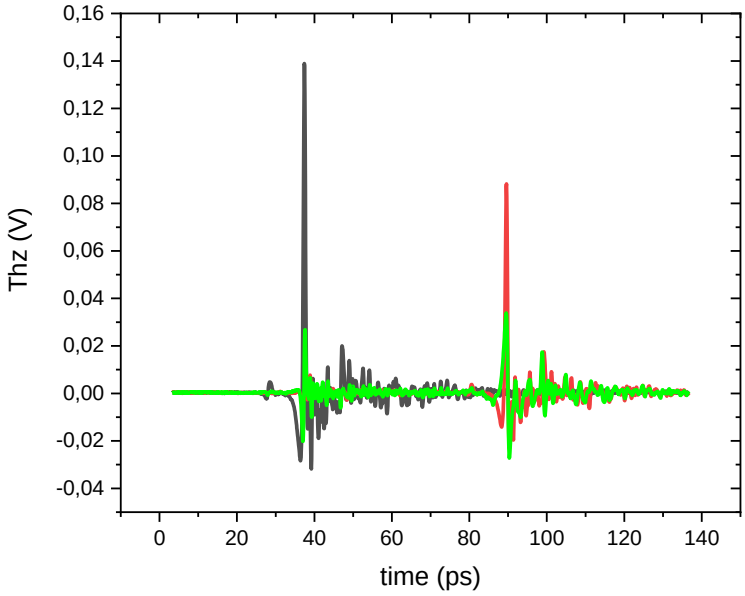

Figure 3.10: Terahertz pulses observed after total reflection on the prism (black curve) and on the prism/plate interface for an optimized silicon plate (red) and lower quality silicon plate (green).

In figure 3.10, we can observe the terahertz pulses recorded in the TDS setup for the prism only configuration (black curve) and for the prism/window couple (red and green). For the prism only configuration, we observe a neat pulse matching very well the reference pulse without the ATR additional setup. Adding a plate on top of the prism, we expect the same pulse shape, but delayed in time due to the additional path through the silicon plate. This is indeed observed when the plate matches perfectly the surface of the prism and there is no air gap in between (red curve). On the contrary, when the plate is not flat enough, an echo is clearly visible on the green curve. Two peaks are present, one corresponding to the prism/silicon plate interface, and one for the external plate surface. Since we have to

move the sample window to perform both cells and reference measurements, another problem resulting from a lack of flatness is that the beam will undergo an angular deflection with the displacement.

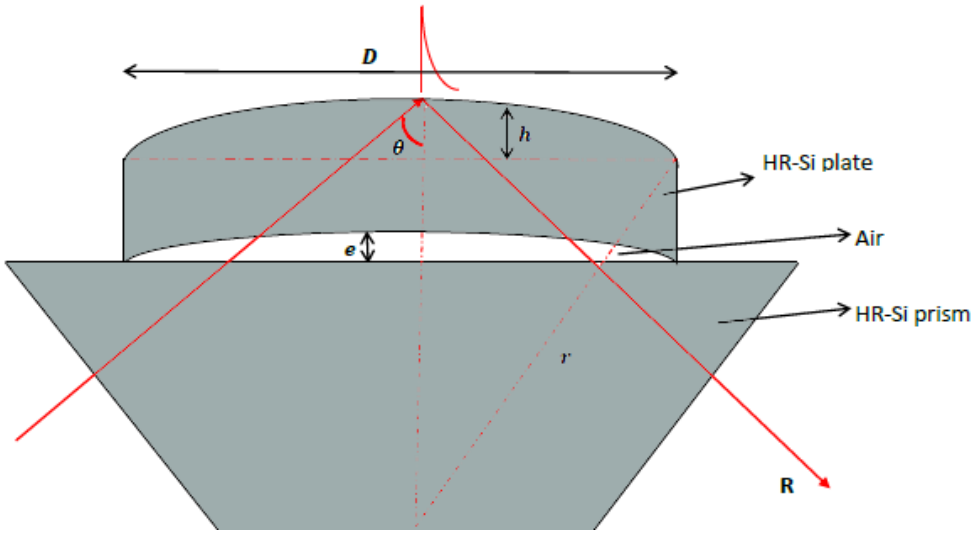

Figure 3.11: A schematic of non-flat Si-HR window with prism. e is the air gap between prism and Si-HR window, r is the curvature of the Si-HR plate surfaces, θ is the incident angle, D is the diameter of the Si-HR window, h is the protruding height of the Si-HR window, and R is the reflectivity

This question is then crucial, since we need to move the silicon plate between each measurement. Because the displacement is not perfectly reproducible, it would lead to problematic additional fluctuations. To investigate the influence of this air gap to the signal we detect, we present a simple model of the influence of the window flatness on signal modification due to both air gap and beam deflection.

We assume that the prism is flat, and that the HR-Si plate contains all the defects: an air gap $e(x, y)$ and a curvature r (see figure 3.11). Due to the displacement of the plate, the angle of reflection θ of the terahertz beam on the plate depends on its position. This leads to an unwanted variation of the detected signal.

First, we calculate the variation $\Delta\theta$ of the angle of incidence as

$$\sin(\Delta\theta) = \frac{D}{2r} \tag{3.14}$$

where D is the diameter of the silicon plate as showed is figure 3.11.

Using the trigonometric relationship between r, D and h, we can get the following relation:

$$r^2 = (\frac{D}{2})^2 + (r - h)^2 \tag{3.15}$$

where h is the height of protruding part of the unflat silicon window. We get at first order

$$r \approx \frac{D^2}{8h} \tag{3.16}$$

Finally, we get $\Delta\theta \approx \sin(\Delta\theta) \approx \frac{4h}{D}$. Then the reflected angle changes by $2\Delta\theta = \frac{8h}{D}$. For the numeric application, we have $D = 36\,\text{mm}$, a defect h given by the manufacturer[1] at $h_{max} = 2\lambda$, with $\lambda = 632\text{nm}$. Therefore, the modification of the reflected angle is $\Delta\theta \approx 0.13\,\text{mrad}$.

In order to estimate the effect of such an angular deviation on the TDS signal, we measured the influence of the rotation of the mirror M_1 in the ATR module (see figure 3.5). We recorded the variation of signal obtained in function of the angle of rotation of M_1 for both angular directions (figure 3.12).

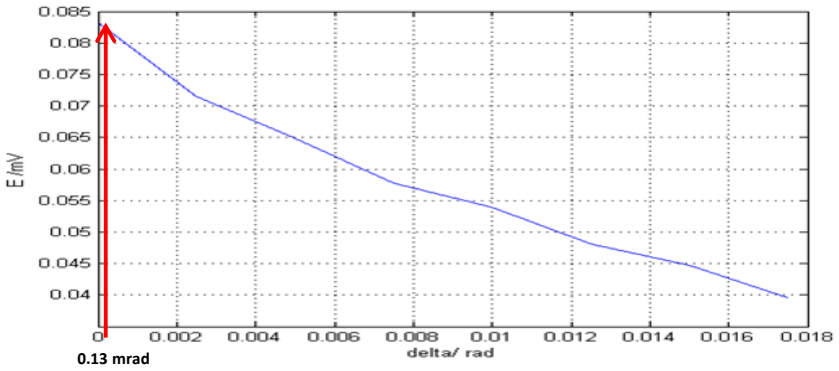

Figure 3.12: Relation between the change of the incident angle $\Delta\theta$ on the ATR and terahertz TDS signal, for one angular direction. The opposite direction shows equivalent behavior. The red arrow shows the deviation estimated for a 2λ-defect silicon window.

.

The conclusion is that the angular deviation of the beam due to the default of flatness of the silicon window has negligible effect on the TDS signal.

Second, we investigated the influence of the air gap between the silicon prism and the plate. Figure 3.13 describes the origin of the main TDS signal E_2 as well as the echo E_1, that are experimentally observed in Fig. 3.10. According to formulas 3.2, the complex reflection coefficient at the first Si-Air interface is r_{12}, and the coefficient at the second Air-Si interface is then $r_{21} = -r_{12}$, and for a p-polarized beam, which is the polarization of our setup,

$$r_{12}(\alpha) = \frac{\hat{n}_2 \cos\alpha - i\hat{n}_1\sqrt{\left(\frac{\hat{n}_1}{\hat{n}_2}\right)^2 \sin^2\alpha - 1}}{\hat{n}_2 \cos\alpha + i\hat{n}_1\sqrt{\left(\frac{\hat{n}_1}{\hat{n}_2}\right)^2 \sin^2\alpha - 1}}. \tag{3.17}$$

The transmission coefficients t_{12} and t_{21} in amplitude have the following expression [237]:

$$t_{12} \times t_{21} = 1 - r_{12}^2. \tag{3.18}$$

[1] www.tydex.com

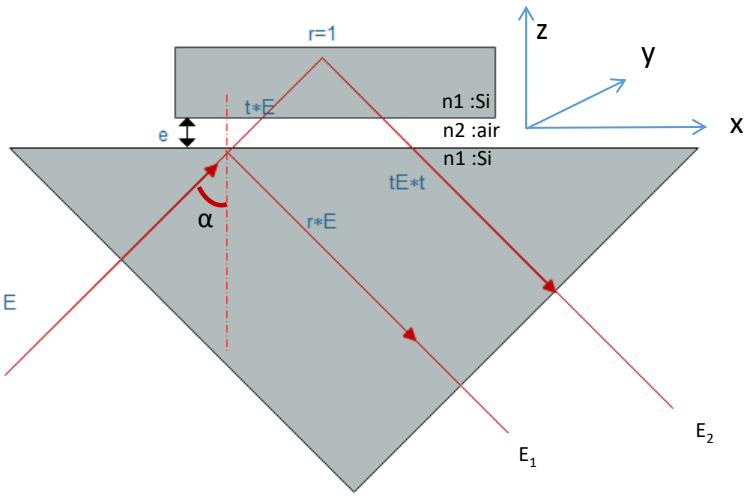

Figure 3.13: A schematic of a model about air gap between mobile support and prism

The total complex reflection and transmission coefficients at the Si-Air-Si interface, r and t respectively, can be obtained by summing all interfering propagating waves, namely the Fabry-Perot effect, as

$$\begin{aligned} r &= \frac{r_{12} + r_{21}\exp(2i\beta)}{1 + r_{12}r_{21}\exp(2i\beta)} \\ t &= \frac{t_{12}t_{21}\exp(i\beta)}{1 + r_{12}r_{21}\exp(2i\beta)} \end{aligned} \tag{3.19}$$

with

$$\beta = \frac{2\pi}{\lambda}\hat{n}_2\, e\cos\alpha. \tag{3.20}$$

What is more, the ratio between E_1 and E_2, which represents the fraction of echo we wish to minimize, can be simply obtained by

$$\frac{E_2}{E_1} = \frac{t^2}{r} \tag{3.21}$$

Since HR-Si is highly transparent in the terahertz domain, we assume that $\hat{n}_1$ is real and that $n_1 = 3.41$. The refractive index of air is $n_2 = 1$. We also assume that $\alpha \approx 45°$, and $\lambda = 300\,\mu\text{m}$. Therefore, we can calculate the ratio E_2/E_1 in function of the position of the plate.

According to the directions of the axes in figure 3.13, we measured the ratio E_2/E_1 as a function of the X axis, by scanning the plate along the X axis. From the value of this ratio, we can theoretically calculate the thickness of the air gap e as a function of X. In particular, we have characterized one of our best Si plates available. The ratio (figure 3.14, left) is converted to the thickness of the air gap (figure 3.14, right). We get a flatness defect of about 0.15 µm corresponding to $\lambda_{\text{visible}}/4$. Therefore, in order to avoid as much as possible the fluctuation of the terahertz signal due to the defects of the Si-HR windows, we have to use better quality

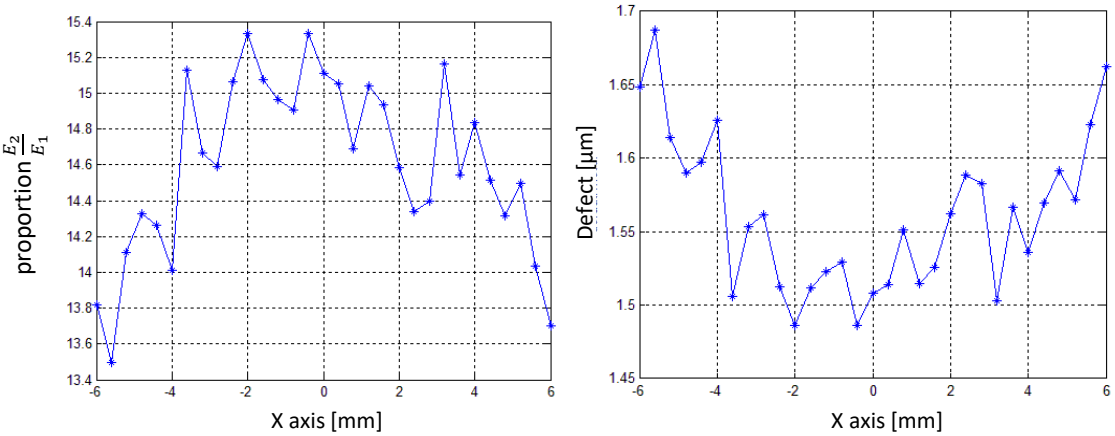

Figure 3.14: Experimental proportion E_2/E_1 in function of X axis (left) and estimated air gap thickness e versus X axis (left)

plates than those previously provided by the supplier. We have been able to obtain blades with slightly better specifications, but we have primarily tested all Si plates with a Fizeau interferometer. The Fizeau interferometer is an amplitude-division optical interferometer in which two partially reflecting surfaces are placed face to face and then illuminated by a coherent beam in the visible. The light reflected from the back side of the first surface is combined with the light reflected from the front side of the second surface. The two reflected waves interfere with each other to create interference bangs. The Fizeau interferometer allows to examine with great precision the palneity defects of the slides. During the experiments, we used the slides with the least defects.

3.5.3 Preparation of the MDCK cell line

For our experiments, MDCK cells (see section 2.5) are harvested by trypsin-EDTA after reaching a confluent state. The cells are counted and placed at a concentration of about 10^6 cells per milliliter of medium. Then, a drop of 1000 µL of quarter diluted solution is deposited and seeded on a 36 mm diameter HR-Si window with growth medium. After 2 days of incubation, the cells form a confluent monolayer. The use of a biological scalpel removes cells in half of the surface without removing the adherent MDCK cells. For more details, see Appendix B. Prior to each experiment, the HR-Si window is washed with HBSS and left at room temperature (21°C) in 3 mL PBS.

In the figure 3.15, we can observe that the distribution of cells is not perfectly homogeneous: grayer areas are observed at the top left of the image, interpreted as areas where the organization of cells is sparser, whereas in the center left of the image, the cells have replicated too much and form a multilayer. The height of the cells is then the mean of a height distribution.

When MDCK cells form a typical cuboidal single layer epithelium after grown to conflu-

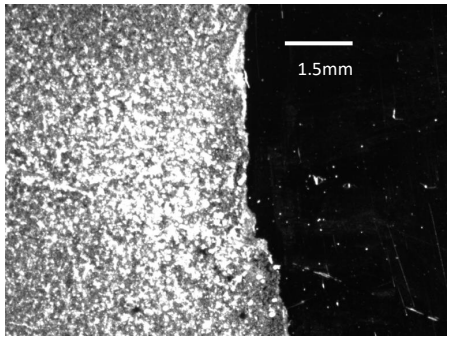

Figure 3.15: Photography of MDCK cells on the HR-Si support. The cell zone is visible on the left and the scrapped reference zone on the right.

ence, they display a height of 8 to 12 µm [227, 238–240]. During the experiments, the HR-Si window seeded with MDCK cells is inserted on the terahertz ATR setup with the addition of 3 mL of PBS. Under these conditions, the extracellular volume is approximately 1000 times larger than the total intracellular volume. Therefore, it can be assumed that the concentration of extracellular molecules remain constant during the leakage of intracellular fluid.

3.6 Dynamics of cell membrane permeabilization by saponins

Reversible permeabilization of live cells is a complex and increasingly addressed issue, whether it is for medical application [181, 241], or in lab research protocols where a constant effort is made to reach more realistic investigation conditions in biological systems [155, 242, 243]. As we introduced in chapter 2, it is characterized by increased molecule transfers through the cell membrane. Besides, comparing to other techniques (see section 2.4.4), the terahertz range is very intersting to follow the permeabilization dynamics of a live cells layer, without any marker nor sample preparation [222, 244]. The following resultats have been publied in [223].

Here, the non-specific permeability of cell membrane is achieved by saponins, one of the detergents presented in section 2.3.1.2. Saponins are glycosides mainly produced by plants that form soap-like foams in solution. Saponins consist of a sugar moeity linked to a hydrophobic aglycone [163]. Saponins at high concentration are more commonly used in immunocytochemistry to permeate the membranes of different types of fixed cells, but have also been reported to permeate the plasma membrane of live cells at low concentrations and in a reversible manner [165, 245]. Saponins are non-ionic detergents that create non-specific pores in the cell membrane, most likely by binding to cholesterol within the lipid components of the cell membrane [246]. More details of working principles about creating pores in the membrane are found in section 2.3.1.2. Cytotoxic tests on different mammalian cell types all show a survival rate greater than 50% with prolonged exposure to a saponin concentration of less than 0.002% (w/w). Saponins can trigger protein and ion transfers across the membrane.

Saponins used in our experiments (SigmaAldrich: 47036) is a mixture of sapogenin molecules at a mass fraction $f_r = 8$ to 25%, so the exact quantity of saponin is unknown. All the experiments were done with the same saponin sample in order to preserve the direct comparison between the experiments.

The saponin number concentration C_0 is related to the mass concentration γ_0 of the commercial saponin as

$$C_0 = \frac{f_r \mathcal{N}_A \gamma_0}{M} \tag{3.22}$$

where $\mathcal{N}_A$ is the Avogadro constant, and M is the molar mass.

3.6.1 Experiment

When an absorbing layer such as cells is put on top of the silicon plate, it couples with the evanescent field and modifies the amount of reflected signal (see figure 3.16). The measurement of the reflected beam is then directly correlated with the permittivity of the medium topping the silicon prism.

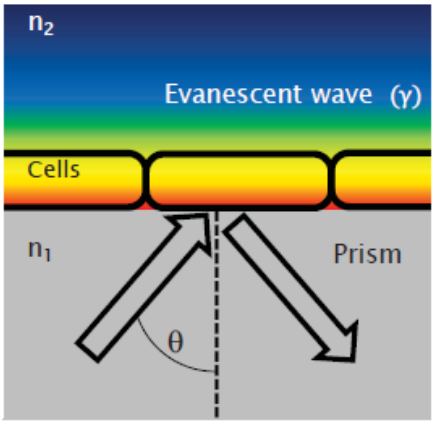

Figure 3.16: Schematic of the cells layer in the evanescent field zone (in color gradient).

Considering that the thickness of the cell layer matches the penetration depth of the evanescent wave (see Eq. 3.9), the reflected terahertz wave is modified by the terahertz dielectric properties of the cell layer on top of the silicon prism. The stronger coupling is obtained for a penetration depth of the same value as the cell layer thickness. The reflected terahertz signal is then correlated with the content of the cytosol. The extracellular PBS solution around the cell layer only weakly affects the terahertz signal since its volume is much larger than that of the intracellular solution. Therefore, leakage of cytosol from the cell to the surrounding solution can easily detect the modification of the cell content [123, 222].

We investigated the effect of the initial concentration of saponins on the dynamics of membrane permeability probed by TDS-ATR. Before each experiment, the silicon window is washed with PBS. For each measurement targeting a given concentration of saponins, a fresh 100-fold saponin solution is prepared. We place the silicon window on the TDS-ATR

silicon prism and allow it to reach room temperature for 15 min at 21°C in 3 ml PBS. As the diameter of the support is 36 mm, the cells are covered by a 3 mm high solution.

According to section 3.4.2, we use the relative contrast Δ_{rel} defined in equation 3.12 as the relevant experimental signal. The sample is placed on the prism, then test measurements are made to check the stability of the terahertz system for a duration of about 50 min. The dynamic biological process starts when we trigger the chemical permeation at time $t = 0$ with saponins. We then follow the dynamics during several tens of minutes.

To compare all experimental results, we normalize $\Delta_{\text{rel}}(t)$ by its value before we start the perturbation $\Delta_{\text{rel}}(t < 0)$ (see equation 3.23). All experiments are also monitored with a camera on top of the ATR module to make sure that cells layer is always attached to the silicon surface.

$$\Delta(t) = \frac{\Delta_{\text{rel}}(t)}{\Delta_{\text{rel}}(t < 0)}. \tag{3.23}$$

One example of dynamics is showed in figure 3.17. The saponin concentration is 150 µg/mL. This concentration is chosen to have a quick interaction with the membrane without alteration of cellular morphology [224].

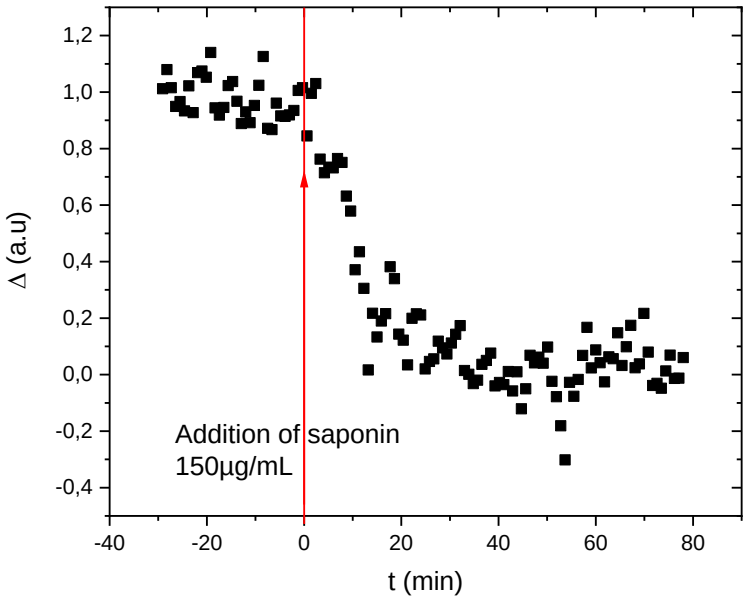

Figure 3.17: Variation of the THz-ATR contrast $\Delta(t)$ after the cell membrane permeation by saponin detergent ($\gamma_0 = 150$ µg/mL at time $t = 0$).

When saponin was added at $t = 0$, we observed a $\Delta(t)$ decrease as shown in figure 3.17. The rapid decrease in contrast is due to a drop in the concentration within the cell due to leakage of the cytosol to the extracellular medium. It is essential to remember that the origin of the contrast is an asymmetric distribution between the intracellular cytosol and the extracellular medium. It can also be envisaged that the contrast is due to the entry of the buffer medium into the extracellular medium inside the cells. However, this hypothesis is

less convincing because the buffered extracellular medium contains only ions. And Marianne Grognot demonstrated in her PhD thesis [128] that ions have a lower impact than peptides and proteins that are involved here. Thus, the decrease of $\Delta_{\text{rel}}(t)$ is mostly correlated with the decrease in the concentration of the intracellular medium via the pores created by the saponin molecules. It is important to note that this process is a non-specific permeability. At the end of experiments, camera images do not show any cell detachment, even under gentle medium movements.

We recorded a large number of dynamics similar to the one presented in figure 3.17 for many saponin concentrations. We then required to develop a model to explain and analyze these results. This model is presented in the following.

3.6.2 A physical model for cell permeabilization by saponin

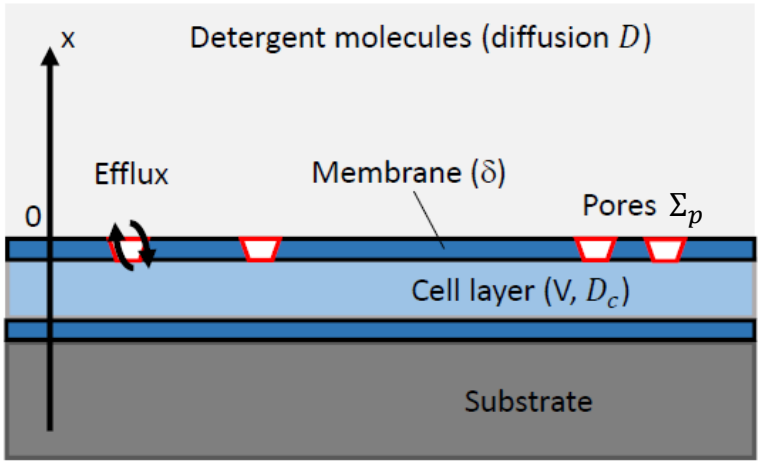

Figure 3.18: Model of the pore formation mechanism on the cell membrane. The cell layer is put on top of the silicon substrate. V is the volume of the cell cytosol, D_c is the diffusion coefficient of cytosol, δ is the cell membrane thickness, Σ_p is the surface of pores created in the membrane, and D is the diffusion coefficient for detergent molecules [223].

The system is considered to be a uniform cell layer (see figure 3.18) [223]. The basal plasma membrane is in contact with the silicon substrate while the apical membrane is in direct contact with saponin molecules in solution in PBS. The saponin molecules can move freely in the extracellular medium by diffusion or sedimentation. Once a saponin molecule encounters the apical membrane it creates a pore with a given probability, increasing the total number of pores with time. Then, effusion of molecules through the pores takes place and changes the concentration of molecules in the cytosol. The saponin concentration of the solution is not considered to be modified since the PBS/saponin solution volume is by far much larger than that of the cytosol. Pores are allowed to grow or shrink with a characteristic exponential time as it will be discussed later. The model is reduced by symmetry to a 1D-model along the x coordinate.

First, we consider the phenomenon of diffusion of saponin molecules. The Mason-Weaver equation [247] describes the diffusion and sedimentation effects under uniform gravity. In our case, sedimentation of saponin molecules is completely negligible compared to diffusion due to the small size of the saponin molecules. Therefore, the Mason-Weaver equation reduces to the classic diffusion equation. For a given saponin concentration $C(x,t)$ at position x and time t, we have

$$\frac{\partial C(x,t)}{\partial t} = D\frac{\partial^2 C(x,t)}{\partial x^2} \tag{3.24}$$

where D is the diffusion coefficient of saponins in PBS. For a semi-infinite volume above the uniform cell surface, and the apical membrane plane at $x = 0$, we have the boundary condition $C(x,t) = 0$, and the solution of equation 3.24 is then

$$C(x,t) = C_0 \text{ erf}\left(\frac{x}{2\sqrt{Dt}}\right) \tag{3.25}$$

where $\text{erf}(x)$ is the error function

$$\text{erf}(x) = \frac{2}{\sqrt{\pi}}\int_0^x e^{-t^2} dt. \tag{3.26}$$

The number of pores created in the membrane and then the total surface of pores are related to the number of saponin molecules that impinge the surface and fix onto the membrane. From Eq. 3.25, we can calculate the total number of saponin molecules $n_0(t)$ impinging the membrane for a cell surface A by

$$n_0(t) = A\int_0^\infty [C_0 - C(x,t)]\ \mathrm{d}x = \frac{2AC_0\sqrt{Dt}}{\sqrt{\pi}} = \alpha\sqrt{t}. \tag{3.27}$$

It corresponds to the number of molecules that fix onto the membrane, assuming no steric saturation effects. Therefore, $n_0(t)$ evolves as $\sqrt{t}$ and can potentially increase as large as possible by accumulation of molecules onto the membrane. Saturation effect will be discussed further.

After being created in the membrane, each pore is surrounded by a lipid border. The pore can find conditions of stability, or evolve dynamically towards growth or shrinkage. For instance, in [248], the pore growth dynamics was observed in polystyrene films and demonstrated a threshold above which pore size has an exponential growth. Other theoretical treatments and numerical simulations of pore dynamics are mentioned in [249, 250]. They describe the pore size evolution in 4 states in a few seconds (see figure 3.19): first an exponential growth driven by surface tension, then stop of the growth at a maximum radius, then a slow decay when the osmotic pressure is enough released, and finally a fast resealing driven by line tension. Based on these data, we suppose that each pore with initial surface S_{p0} can exponentially increase in size as

$$S_p(t) = S_{p0}\ e^{t/\tau} \tag{3.28}$$

or exponentially decay as

$$S_p(t) = S_{p0}\ e^{-t/\tau} \tag{3.29}$$

with τ the characteristic time.

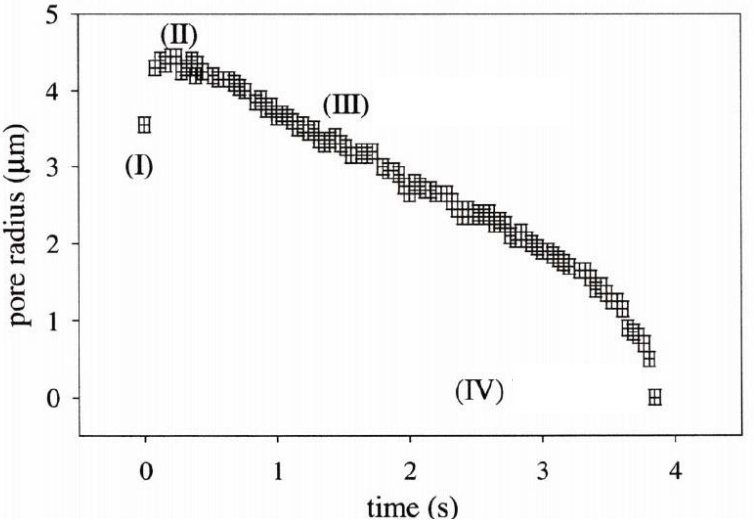

Figure 3.19: Measurement of pore radius versus time, showing four distinct stages in the pore dynamics. (I) grow exponentially, (II) stop growing at a maximum radius, (III) slow decrease, and (IV) fast reseal. [249].

3.6.2.1 Dynamics without pore overlapping

For the moment, we consider that there is no overlapping effect for the created pores. We define a pore creation efficiency η, which indicates the efficiency with which saponin molecules create pores in the membrane. So, the number of pores created in the membrane is given by $\eta \cdot n_0(t)$.

We introduce the rate of creation of pores

$$j(t) = \eta \frac{\mathrm{d}n_0(t)}{\mathrm{d}t}. \tag{3.30}$$

The total surface of pores $\Sigma_p(t)$ for $t > 0$ is given by the convolution between the rate of creation of pores $j(t)$ in equation 3.30 and the individual surface pore $S_p(t)$ as

$$\Sigma_p(t) = \int_0^t j(u) S_p(t-u) \mathrm{d}u. \tag{3.31}$$

The pores created in the membrane allow the effusion of cytosol molecules according to Fick's first law [251], which is a concept whereby a solute moves from a region of high concentration to a region of low concentration through a concentration gradient. The net flux J_c of molecules through the membrane from the cytosol (the variation of molecules per unit of time and per surface) is given by

$$J_c = \frac{1}{\Sigma_p} \frac{\mathrm{d}N_c}{\mathrm{d}t} = -D_c \frac{C_c - C_e}{\delta} = -D_c \frac{\Delta C}{\delta} \tag{3.32}$$

where N_c is the number of exiting molecules in cytosol, δ the cell membrane thickness, D_c the diffusion constant of molecules in the cytosol, C_c is the concentration of molecules in

the cytosol and C_e is the concentration of molecules in cell exterior. The concentrations C_c and C_e are defined with respect to the cell volume V_c and the volume of the cell exterior V_e, respectively, as

$$C_c = \frac{N_c}{V_c}\,;\, C_e = \frac{N_e}{V_e}$$

The diffusion coefficient in the cytosol is given by the Stokes-Einstein equation

$$D_c = \frac{k_B T}{6\pi\mu r_s} \tag{3.33}$$

where μ is the viscosity and r_s is the solute Stokes radius. For spherical molecules of molecular weight M and density ρ, we obtain r_s as

$$r_s = \left[\frac{3M}{4\pi\rho\mathcal{N}_A}\right]^{\frac{1}{3}}. \tag{3.34}$$

The total number of molecules being constant, the variation of N_c is given from equation 3.32 as

$$\frac{\mathrm{d}N_c}{dt} = \Sigma_p \cdot J_c = -\Sigma_p \frac{D_c}{\delta}\left(\frac{N_c}{V_c} - \frac{N_e}{V_e}\right). \tag{3.35}$$

Considering an infinite cell exterior medium ($V_e \to\infty$), we can simplify and obtain

$$\frac{\mathrm{d}N_c}{dt} = -\Sigma_p \frac{D_c}{\delta}\frac{N_c}{V_c}. \tag{3.36}$$

Considering the total surface of pores $\Sigma_p(t)$ in the plasma membrane, the evolution of the molecules efflux (the effusion rate) form exiting molecules N_c in cytosol is defined as

$$\frac{\mathrm{d}N_c(t)}{\mathrm{d}t} = -\gamma(t)N_c(t) \quad \text{with} \quad \gamma(t) = \frac{\Sigma_p(t)D_c}{V_c\,\delta}. \tag{3.37}$$

We define L as the cell thickness so that $V_c = A\,L$. After some calculations using equations 3.27, 3.31 and 3.37, we obtain an analytical solution for the evolution of the number of molecules in the cytosol with Mathematica[2], and [252] [253], in the case of pore growth

$$N_{\mathrm{inc}}(t) = N_{c0}\,\exp\left\{-\varphi\,\tau^{\frac{3}{2}}\left[\frac{\sqrt{\pi}}{2}\exp\left(\frac{t}{\tau}\right)\mathrm{erf}\left(\sqrt{\frac{t}{\tau}}\right) - \sqrt{\frac{t}{\tau}}\right]\right\} \tag{3.38}$$

or pore decay

$$N_{\mathrm{dec}}(t) = N_{c0}\,\exp\left\{-\varphi\,\tau^{\frac{3}{2}}\left[\frac{\sqrt{\pi}}{2}\exp\left(\frac{t}{\tau}\right)\mathrm{erfi}\left(\sqrt{\frac{t}{\tau}}\right) - \sqrt{\frac{t}{\tau}}\right]\right\} \tag{3.39}$$

where erfi is the imaginary error function defined as $\mathrm{erfi}(x) = -i\,\mathrm{erf}(ix) = \frac{2}{\sqrt{\pi}}\int_0^x e^{t^2}dt$, N_{c0} is the initial number of molecules in cytosol and φ is defined by

$$\varphi = \frac{2C_0 S_{p0}\,\eta D_c\sqrt{D}}{\sqrt{\pi}L\delta}. \tag{3.40}$$

[2]Wolfram Mathematica (usually termed Mathematica) is a modern technical computing system

Using Mathematica software, one obtains the limit

$$\lim_{\tau\to+\infty} N_{\text{inc}} = \lim_{\tau\to+\infty} N_{\text{dec}} = N_{10}\exp\left[-\frac{2}{3}\varphi\, t^{3/2}\right]. \tag{3.41}$$

Therefore, the population evolution of the lost cytosol molecules only depends on two parameters: the exponential pore size evolution time τ and a term φ which is related to the diffusion coefficients D_c and D, the initial saponin concentration C_0 , the cell geometry parameters including the thickness of the cell layer L and the thickness of the cell membrane δ, the surface of one pore in the membrane S_{p0} and the pore creation efficiency η.

3.6.2.2 Taking into account pore overlapping

We now consider the possible overlapping effect of the pores created in the membrane. Without overlapping, the total pore surface in the membrane would continuously increase toward infinity (see equation 3.27), which is not physically relevant because in reality, the total surface of the pores should be limited by the available cell membrane surface A. there, we will analytically consider the limit case of static pores when the characteristic time $\tau\to\infty$.

First, we consider a discrete model. Each pore has a surface S_p, and the total membrane surface is A. At the beginning, the pore surface is $\Sigma_0 = 0$. The first pore creates a hole of surface $\Sigma_1 = S_{p0}$. The following pore would add a surface S_{p0} without considering overlapping. The probability to overlap is the ratio between the total pore surface Σ_1 and the membrane surface A, so the total surface of the 2 pores, taking into account the probability of overlapping is

$$\Sigma_2 = \Sigma_1 + S_{p0}\left(1 - \frac{\Sigma_1}{A}\right). \tag{3.42}$$

Then, after N pores, one obtains

$$\Sigma_{N+1} = \Sigma_N + S_{p0}\left(1 - \frac{\Sigma_N}{A}\right) = S_{p0} + \Sigma_N\left(1 - \frac{S_{p0}}{A}\right). \tag{3.43}$$

At the limit, $\Sigma_\infty = \Sigma_\infty + S_{p0}\,(1 - \Sigma_\infty/A)$, so $\Sigma_\infty = A$ the total membrane surface, which is expected.

A continuous model is obtained noticing that $d\Sigma_p = \Sigma_{N+1} - \Sigma_N$ and that $\mathrm{d}t = T$ the interval between the creation of two pores. The pore creation flux is then $j = 1/T$.

Let us assume that a surface $\Sigma_p(t)$ of pores is created at the surface membrane. The increase of surface $\mathrm{d}\Sigma_p(t)$ is given by the surface ratio probability

$$\mathrm{d}\Sigma_p(t) = S_{p0}\left[1 - \frac{\Sigma_p(t)}{A}\right] \tag{3.44}$$

so we obtain the differential equation for the pore surface evolution considering pore overlapping

$$\frac{\mathrm{d}\Sigma_p(t)}{\mathrm{d}t} = j(t)S_{p0}\left[1 - \frac{\Sigma_p(t)}{A}\right]. \tag{3.45}$$

The flux depends on time (see Eq. 3.30), so

$$j(t) = \eta \frac{\mathrm{d}n_0}{\mathrm{d}t}(t) \qquad \text{with} \qquad n_0(t) = \alpha\sqrt{t} \quad \text{and} \quad \alpha = \frac{2A\, C_0\sqrt{D}}{\sqrt{\pi}}. \tag{3.46}$$

Therefore $j(t) = \eta \dfrac{\alpha}{2\sqrt{t}}$, and Eq. 3.45 becomes

$$\frac{\mathrm{d}\Sigma_p(t)}{\mathrm{d}t} = \eta \frac{\alpha}{2\sqrt{t}} \left[S_{p0} - f\, \Sigma_p(t)\right] \tag{3.47}$$

with $f = S_{p0}/A$.

Let $x = \sqrt{t}$, then $\mathrm{d}x = \frac{1}{2}\dfrac{\mathrm{d}t}{\sqrt{t}}$ and $\mathrm{d}t = 2x\mathrm{d}x$. The previous equation then becomes

$$\frac{\mathrm{d}\Sigma_p(t)}{\mathrm{d}x} = \eta\, \alpha \left[S_{p0} - f\, \Sigma_p(t)\right] \tag{3.48}$$

which is a first order linear differential equation with constant coefficients. Its solution for $t > 0$ is then

$$\Sigma_p(t) = \eta A \left[1 - \exp\left(-\frac{S_{p0}}{A}\alpha\sqrt{t}\right)\right]. \tag{3.49}$$

The limit for $t \to 0$ is

$$\lim_{t\to 0} \Sigma_p(t) = \eta S_{p0}\alpha\sqrt{t} = \eta S_{p0} \cdot n_0(t) \tag{3.50}$$

which is the product of the surface of one pore multiplied by the number of pore created without overlapping, taking into account the efficiency, as expected.

We can calculate the effect of pore overlapping in the limit case of static pores ($\tau \to \infty$). We use the solution of the time varying permeability in Eq. 3.37

$$N_c(t) = N_{c0} \exp\left[-\int_0^t \gamma(u)\, du\right] \tag{3.51}$$

where the permeability writes

$$\gamma(t) = \frac{\Sigma_p(t) D_c}{V_c\, \delta}. \tag{3.52}$$

Therefore,

$$N_c(t) = N_{c0} \exp\left[-\int_0^t \frac{\Sigma_p(u) D_c}{V_c\, \delta}\, \mathrm{d}u\right]. \tag{3.53}$$

Using Eq. 3.49, one obtains with $V_c = AL$

$$N_c(t) = N_{c0} \exp\left[-\int_0^t \frac{D_c\left[1 - \exp\left(-\frac{S_{p0}}{A}\alpha\sqrt{u}\right)\right]}{L\delta}\, \mathrm{d}u\right] = N_{c0} \exp\left[-I\right] \tag{3.54}$$

where

$$I = \frac{D_c}{L\delta} \int_0^t \left[1 - \exp\left(-\frac{S_{p0}}{A}\alpha\sqrt{u}\right)\right] \mathrm{d}u. \tag{3.55}$$

Using Mathematica software, one obtains

$$N_c(t) = N_{c0} \exp\left\{ -\frac{\varphi}{f\alpha} \left[t - \frac{1 - e^{-f\alpha\sqrt{t}} \left(1 + f\alpha\sqrt{t}\right)}{\frac{1}{2} f^2 \alpha^2} \right] \right\}. \tag{3.56}$$

The limit for very small holes (no overlapping) gives

$$\lim_{f \to 0} N_1(t) = \exp\left[-\frac{2}{3}\varphi\, t^{3/2} \left(1 - \frac{3}{8} f\alpha\sqrt{t} \right) \right] \approx \exp\left[-\frac{2}{3}\varphi\, t^{3/2} \right]. \tag{3.57}$$

At first order, the limit is the same as in the case of no overlapping and $T \to +\infty$ (Eq. 3.41).

3.6.2.3 Dimensionless number

Two mechanisms are opposing. The first one is the overlapping of the pores which results in a decrease of the total pore surface created by the detergent molecules as well as the saturation of the surface at long delays. Its characteristic time t_1 is given by Eq. 3.49 as

$$t_1 = \left[\frac{A}{S_{p0}\ \alpha} \right]^2. \tag{3.58}$$

The second mechanism is the molecules efflux from cytosol through the pores due to diffusion and pore size evolution. From the limit of $N_c(t)$ for $f \to 0$ found in Eq. 3.57, one obtain a second characteristic time

$$t_2 = \left(\frac{2\varphi}{3} \right)^{-\frac{2}{3}}. \tag{3.59}$$

We then define the dimensionless number G by

$$G = \left(\frac{t_2}{t_1} \right)^{\frac{3}{2}} = \frac{6\, S_{p0}^2\, C_0^2\, D\, \delta}{\pi D_c}. \tag{3.60}$$

This number G can be understood as follows. If $G \gg 1$ ($t_1 \ll t_2$), the limiting factor is the overlap of the pores, which takes place before the efflux of the molecules of the cytosol. The effusion rate is then approximately constant. On the contrary, if $G \ll 1$ ($t_1 \gg t_2$), the limiting factor is the diffusion of the cytosol molecules. Hence, the overlapping plays no role. We can notice that $\mathrm{G} \propto \dfrac{D}{D_c}$ which is expected since D_c is related to the diffusion of the effusing molecules, while D to the detergent molecules digging the pores.

For instance, if the diffusion of the cytosol molecules is much smaller than that of the detergent molecules, the leakage of the cytosol molecules would remain in the initial linear regime when the overlapping effects begin to be significant.

Finally, using the dimensionless number G of Eq. 3.60, Eq. 3.56 can be rewritten in a more compact form as

$$N(t) = N_{c0}\, e^{3/G} \exp\left[-\frac{D_c\, t}{L\delta} - \frac{3}{G} \left(1 + \sqrt{\frac{t}{\tau_G}} \right) e^{-\sqrt{\frac{t}{\tau_G}}} \right] \quad \text{with} \quad \tau_G = \frac{\pi}{4 S_{p0}^2 C_0^2 D}. \tag{3.61}$$

3.6.3 Results and discussion

Experiments refer to time T following a perturbation applied to the cells at $T = 0$. We record the THz-ATR signal Δ for 30 min to make sure the signal is stable. Then, at $T = 0$, we add 30 µL of 100X-concentrated solution of saponins in PBS with a micropipette so that final saponins concentration equals to γ_0. The liquid is pumped in and out several times to homogenize the saponin concentration. Then, the terahertz signal is further recorded during 120 to 150 min. A typical result is given in figure 3.20.

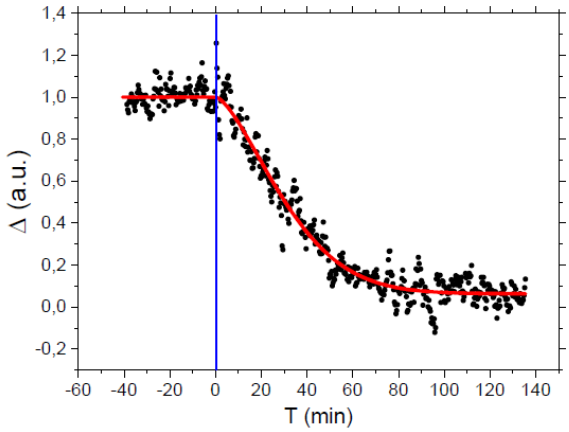

Figure 3.20: THz-ATR signal Δ(t) for MDCK cell layer after addition of saponins at T = 0 for experimental data (black dots) and best fit (red line). The blue vertical line shows addition of saponin ($\gamma_0 = 150$ µg/mL).

Using least-squares regression, we fit all experimental data with the equations 3.38 and 3.39, considering the cases of increasing or decreasing pore size. The best fitting result (see the red curve in figure 3.20) obtained by these two equations provides the parameters τ and φ. In the particular case of the τ parameter, we have conventionally assigned a positive sign if the best fit is obtained from the equation 3.38 (increase in pore size), or a negative sign if obtained from the equation 3.39 (decrease in pore size).

We recorded the THz-ATR dynamics of the permeabilization of MDCK cells after addition of saponins as a function of mass concentration γ_0. The results are presented in figure 3.21A for parameter φ and figure 3.21B for parameter $1/\tau$.

First, for the cell geometry and diffusion parameter φ, a linear dependency versus γ_0 is experimentally observed, as expected from equations 3.22 and 3.40. Precision at lower concentration ($\gamma_0 = 5$µg/mL) is relatively weaker since the amplitude of variation of the THz-ATR signal was lower. It was compensated for by more experiments at lower concentrations. The slope obtained from figure 3.21 A is related to equations 3.22 and 3.40 as

$$\frac{\varphi}{\gamma_0} = \frac{2N_A f\, D_c\sqrt{D}}{\sqrt{\pi} M L \delta}\eta S_{p0}. \tag{3.62}$$

We experimentally find that $\varphi/\gamma_0 \approx 7.1 \times 10^{-7}$ $m^3g^{-1}s^{-3/2}$. Using equation 3.62 and the values found in table 3.1, we obtain $\eta S_{P0} \approx 2.3 \times 10^{-5}$ nm^2 when supposing f=0.12. The last value is the average value given by the manufacturer of saponins.

In conjunction with an estimate of the size of the micelle-like pore structure formed by saponin in the bonding with cholesterol molecules [163], we can estimate the diameter of the pores to about 4 nm [254], thus the pore surface to about $S_{p0} = 12.5\,nm^2$. Assuming a transverse extension of saponin molecule of 0.6 nm [163], about 20 saponin molecules are found in average in the ring. Thus, pore creation efficiency $\eta \approx 1.8 \times 10^{-6}$ to form the 20-molecule ring. Assuming an individual probability p for a saponin molecule to bind to the cell membrane, one obtains p^{20}=1.8×10^{-6} and then $p \approx 52 \pm 2\%$ considering the uncertainty on the commercial concentration of saponin molecules. This simple calculation shows that the binding probability to cell membrane is very high for saponin molecules.

Second, we studied the evolution of the pore size evolution characteristic time (see figure 3.21B). This corresponds to $|1/\tau| < 0.005\,min^{-1}$ and then to $|\tau| > 200\,min$. This high τ value means that pores created by saponin exhibit a very slow dynamics during at least 200 min in any case. The experimental $1/\tau$ values are slightly negative for high saponin concentration which would evoke a large but not infinite decaying time for the pores. However, it is likely to be an artifact due to pore overlapping, as showed by the black line, which is the apparent $1/\tau$ evolution considering pore overlapping. This line is calculated fitting the evolution of cytosol molecules leakage with consideration of overlapping (see equation 3.61) and $1/\tau \to 0$ by the number of molecules without consideration of overlapping (3.39). The overall result is then fully compatible with the assumption of static pores created by saponin molecules. Due to partial overlapping, the total pore surface becomes slightly smaller than expected in our calculation, leading to an apparent misleading decay of the pore size. Using the data in table 3.1, we calculate $G = 1.9 \times 10^{-6} \ll 1$. This value confirms that the limiting factor in our experiments is not the membrane pore overlap but essentially the cytosol effusion process. The overall result is then fully compatible with the picture that pores remain static after they are created by saponin molecules, probably due to stable complexes or aggregates of saponin molecules with the membrane cholesterol. Taking into account pores overlapping effect, we find that two effects are opposing during permeabilization: the pore overlapping related to saponin molecules diffusion, and the efflux dynamics of cytosol molecules.

3.7 Conclusion

This chapter first focused on the characterization of different possible geometries to study biological samples: transmission, reflection, and ATR. The ATR regime proved to be a particularly suitable tool for probing the dynamics of cell layers. We then detailed our terahertz ATR configuration with a TDS source, and provided its sensitivity, which is sufficient to probe

[1]SigmaAldrich: 47036
[2]SigmaAldrich: 47036

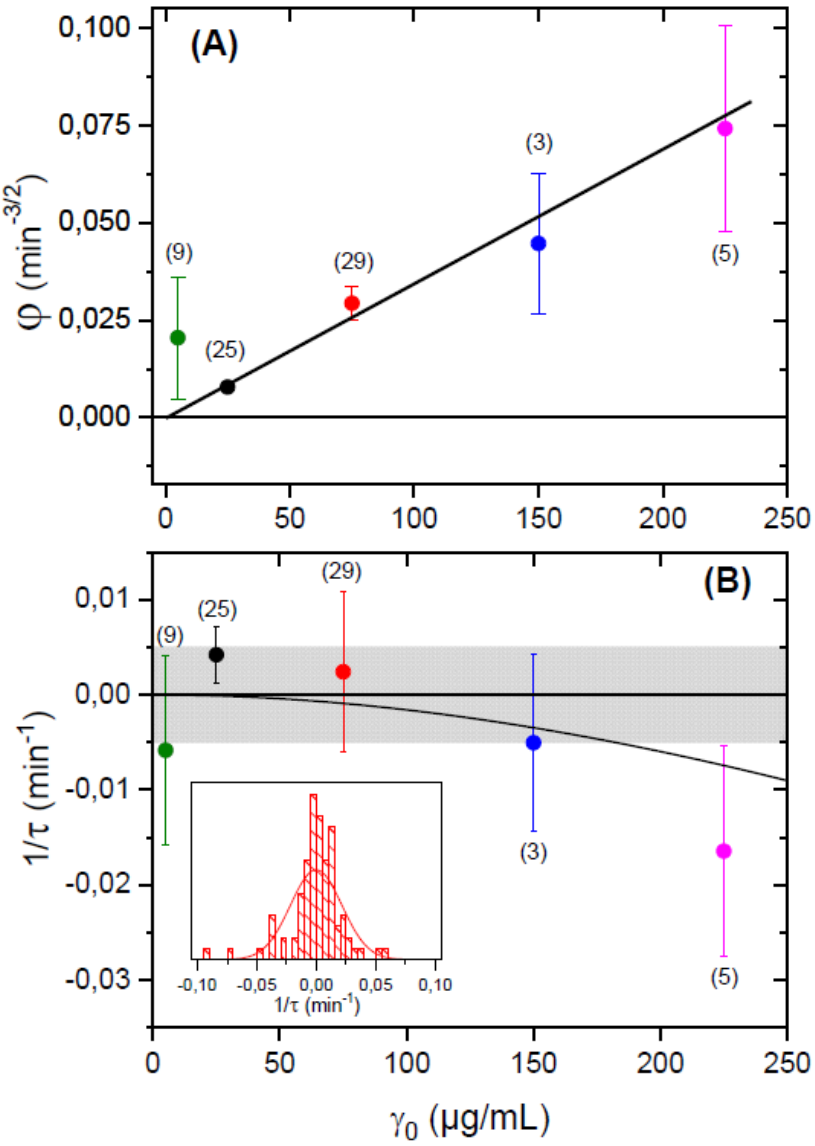

Figure 3.21: Model parameters φ (A) and $1/\tau$ (B) versus saponin mass concentration γ_0. (A) The line is the best fit proportional function. (B) The grey rectangle is a guide for the eye. The black line is the apparent $1/\tau$ evolution considering overlapping of the pores. Inset shows the distribution of $1/\tau$ for the whole concentrations and a Gaussian fit. For both, the number of experiments are shown in parenthesis.

Table 3.1: List of parameter values.

Parameters	Symbol	Value	Unit	reference
Cell Height	L	10	µm	
Membrane thickness	δ	4	nm	[255]
Cytosol diffusion	D_c	1	µm^2/s	[256]
Viscosity(H_2O,300K)	µ	10×10^{-3}	Pa·s	[257]
Protein density	ρ	1.37		[258]
Saponin molecule mass	M	120	g/mol	Sigma[1]
Saponin molecule fraction	f	8-25%		Sigma[2]

cells in contrast with their physiological environment.

We have demonstrated the possibility of observing a monolayer of MDCK epithelial cells. The most important point is that the cells remain under physiological conditions and the measurement is performed under non-invasive conditions without any prior treatment. Our results are in line with the previous work of the team, which characterized the origin of the cell contrast. Protein leakage dynamics is an essential piece of information to follow the permeabilization dynamics of living cells. Cytosol leakage also contains important information on the overall health of the cells, and provides an indication of the viability of the cells.

Using the TDS-ATR setup, we demonstrated non-invasive, non-staining real time measurements of cytoplasm leakage during permeabilization of live MDCK cells by saponin. Saponin was prepared 100-folds concentrated in solution and then diluted to the concentration we wanted. With added saponin solutions, a decrease of the contrast Δ is founded. This decrease corresponds to the leakage of cytoplasm. Understanding the controlled release of specific molecules across the cell membrane is essential for many applications, such as gene therapy, cancer treatment or biotechnology. The influence of the relevant parameters of pore formation during permeabilization is very difficult to understand.

We have developed an analytical model taking into account the diffusion of saponin molecules, cell geometry, diffusion of cytosol molecules and pore dynamics. In our physical model, several processes are involved: the arrival of permeabilizing molecules on the membrane, the efficiency of pore formation, and the efflux of cytosol molecules. The pores are found to be static within one hour after creation, suggesting that diffusion of saponin molecules to the membrane is the limiting factor in our experiments. Taking into account the pore overlap, we also found that two effects are opposing during permeabilization: pore overlap related to the diffusion of saponin molecules, and the efflux dynamics of cytosol molecules. The balance between these two mechanisms can be described by introducing a dimensionless number. We found a good correlation between the experimental data and the model. In particular, we found that the pores created by saponin molecules appear to be static within experimental uncertainty, and that the binding of a saponin molecule to the membrane is very efficient, with a probability greater than 50%.

Chapter 4

High precision QCL-based ATR setup: application to PDT measurements

Contents

4.1 Introduction

For many applications, it would be very advantageous to use a continuous, powerful, compact and coherent source, such as the laser diodes available in the visible or infrared range. In the terahertz domain, pulse sources based on femtosecond lasers have allowed a considerable development of terahertz applications, but these systems are expensive, bulky and difficult to align. Other technologies exist, but each has its own limitations. Some are limited in terms of output power, for example, for a Schottky diode multiplier, one can obtain 50 µW at 1.8 THz [259, 260]. Many are constrained by the signal-to-noise ratio and others are restricted by cost and size [261].

The semiconductor laser is a technology to which scientists pay a lot of attention, with a high output power, a frequency range covering the visible to infrared and potentially terahertz range, and the possibility of compact systems. Laser diodes can directly convert electrical energy into light. The doped p-n transition allows the recombination of an electron with a hole, emitting a photon by spontaneous emission. The stimulated emission can be produced as the process continues and generate more light with the same phase, coherence and wavelength. This is the general principle of a laser. The choice of semiconductor material determines the wavelength of the emitted beam, which in today's laser diodes ranges from UV to the infrared spectrum. Laser diodes are the most common type of laser, with a wide range of uses including fiber optic communications, bar code readers, laser pointers, CD/DVD/Blu-ray disc reading/recording, laser printing, etc.

Quantum cascade lasers (QCL) are semiconductor lasers that emit in the infrared range. They were developed in 1994 with an emission frequency of about 70 THz (4 µm) [11]. Afterwards, many improvements allowed an extension of the frequency range, not only in the mid-infrared (3-25 µm) but up to the terahertz range. The output power of QCLs can reach several hundred mW peak power in pulsed mode at 4.4 THz, and more than 100 mW in continuous mode [262].

Given the harmless nature of terahertz radiation, many publications have been devoted to the application of QCLs in defense, security, communication, environmental monitoring, medicine and biology. For example, thanks to the transparency of materials such as clothing and packaging in the terahertz range, non-invasive inspections in industry or security checks can be carried out. Most terahertz imaging applications with QCL operate in a single pixel configuration, which requires a mechanical scanning system [263, 264]. However, one of the important advantages of using a terahertz QCL source is the sufficient output power to illuminate matrix detectors such as micro-Golay cells or micro-bolometers.

In order to further study membrane permeabilization using our terahertz methods, a significant improvement in measurement accuracy is required, in particular a decrease in noise and increased long-term stability. In addition, a simplification of the experimental setup would also be particularly important. To this end, we have developed a new system based on a QCL source, much simpler than TDS setup, we presented in the previous chapter.

In this chapter, we will first describe the principle of the QCL sources and the realization

of our new experimental setup using a commercial QCL source. All the elements will be characterized, notably the performances in terms of signal-to-noise ratio and stability. Finally, we will present an experimental study of membrane permeabilization during photodynamic therapy (PDT).

4.2 Quantum Cascarde lasers (QCL)

4.2.1 The principle of QCL

Unlike the classic interband diode laser whose frequency is determined by the discrete difference between the conduction band and the valence band and in which a photon is emitted by the recombination of an electron and a hole (a bipolar anode), the quantum cascade laser relies only on one type of carrier, the electrons (a unipolar laser). The QCL is based on the use of electron or intersubband transitions in the conduction band of a semiconductor heterostructure [11]. Photons are emitted by a QCL due to quantum transitions of an electron between energy levels within a quantum well.

The structures are discrete electronic states parallel to the GaAs substrate with quantum confinement occurring perpendicular to the GaAs substrate layers, as shown in figure 4.1. These layers are several nanometers thick and consist of a semiconductor heterostructure, for example, GaAs layers separated by $Al_xGa_{1-x}As$ barriers [265]. The energy dispersion of these quantum well confinements is a quasi-planar wave dispersion (see figure 4.2) in the active region. When an electron undergoes a transition between sub-bands and sequentially emits a photon in one period of the confinements, it remains in the conduction band. Thus, the same electron can tunnel into the next adjacent active region of the structure to emit another lasing photon, and so on by applying an appropriate voltage between the substrate and the periodic layers to control the tunneling.

The periodic structure of the layers is designed to obtain this cascaded photon emission. Therefore, the more the number of cascades is important, the higher the number of photons emitted by an electron in a single pass. Here, the energy of the electrons confined in the quantum wells depends on the width and height of the quantum wells between neighboring wells. It does not depend on the material of the structure as is the case of traditional semiconductor lasers. Therefore, the wavelength of the quantum cascade laser can be adjusted up to 100 µm, depending on the size of the quantum wells. The layer design allows high levels of QCL output power (of the order of milliwatt). This technique also achieves a strong narrowing of the terahertz emission spectrum, e.g. 30 kHz in [266].

In summary, the multilayer heterostructure of QCLs consists of alternating active regions and injection regions (see figure 4.2) through which electrons travel to the next adjacent active region. Therefore, in order to increase the output power, it is necessary to increase the number of cascades [268]. One of the characteristics of QCLs that makes them exceptional is that the adjustment of the emission frequency is achievable over a wide range without modifying

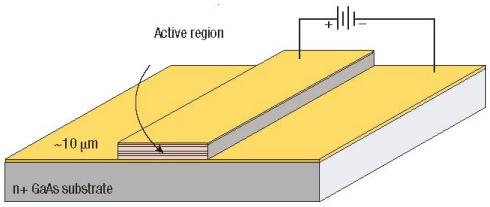

Figure 4.1: Terahertz QCL waveguide structure diagram. GaAs is the substrate material. In the active region, the layers are GaAs and $Al_xGa_{1-x}As$ [265, 267].

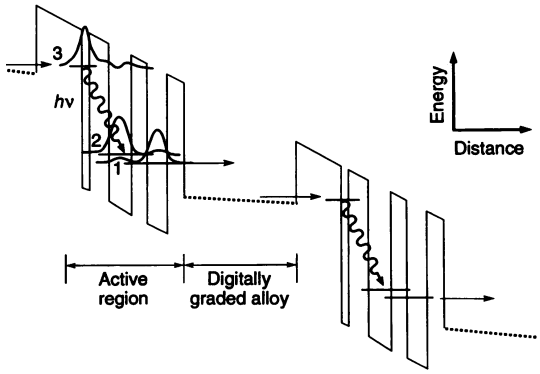

Figure 4.2: A diagram of the conduction band energy structure in two periods with active region and injector of the quantum cascade laser [11].

the semiconductor materials but only by changing the geometrical parameters (width and height) of the quantum wells, which leads to the modification of the energy separation of the electronic states.

4.2.2 Propagation of the terahertz beam

Theoretically, we will consider that the output of a QCL source is a quasi Gaussian beam that propagates along the positive z direction without any restricting aperture in the x or y direction[1]. The intensity profile is

$$I(r,z) = I_0 \left[\frac{w_0}{w(z)}\right]^2 e^{-\frac{2r^2}{w^2(z)}} \tag{4.1}$$

where I_0 is the peak intensity at the center of the Gaussian beam, r is the radial distance away from the center, $w(z)$ is the radius of the laser beam where the intensity is $1/e^2$ (13.5%) of I_0 [269]. At the maximum focalization position $z = 0$, the beam spot size is minimal and given by the waist radius $w_0 = w(0)$ (see figure 4.3). After a propagation over a distance

[1]In reality, interference and diffraction alter the regularity of the electric field distribution. The perfect Gaussian profile has to be understood as an average envelop of the propagating beam.

z, the Gaussian beam keeps its Gaussian shape and $w(z)$ changes according to the following expression

$$w^2(z) = w_0^2 \left[1 + \left(\frac{z}{z_R}\right)^2\right] \tag{4.2}$$

where z_R is the Rayleigh range given by

$$z_R = \frac{n\pi w_0^2}{\lambda} \tag{4.3}$$

where λ is the wavelength and n the refractive index of the medium of propagation. The Rayleigh range is the distance from the waist w_0 to where the radius has been multiplied by a factor $\sqrt{2}$. It covers a distance range where the beam can be assume to remain collimated.

At large distances ($z \gg z_R$), $w(z)$ increases quasi linearly with z. It means that far away from the waist ($z = 0$), the beam can be considered as spherical as in geometrical optics, with an angle of divergence θ given by

$$\theta = \frac{\lambda}{n\pi w_0} \tag{4.4}$$

which shows that the divergence is inversely proportional to w_0. Therefore, for a given wavelength, the more focused is the beam, the more divergence is found when the beam propagates far away from the focus. Conversely, the reduction of the divergence of the Gaussian beam in the far field is obtained for the largest w_0 possible.

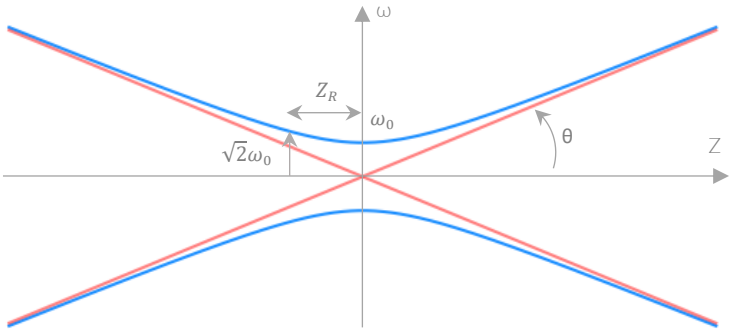

Figure 4.3: The intensity profile of a Gaussian beam defined by its beam waist radius (w_0), Rayleigh range (z_R), and divergence angle (θ).

Since the wavelength in the terahertz domain is much larger than in the visible, the diffraction plays a more important role. It is useful to introduce the Fresnel number F, a dimensionless number occuring in scalar diffraction theory. For an electromagnetic wave going through or hitting an object of characteristic size a, the Fresnel number [104] is

$$F = \frac{a^2}{L\lambda} \tag{4.5}$$

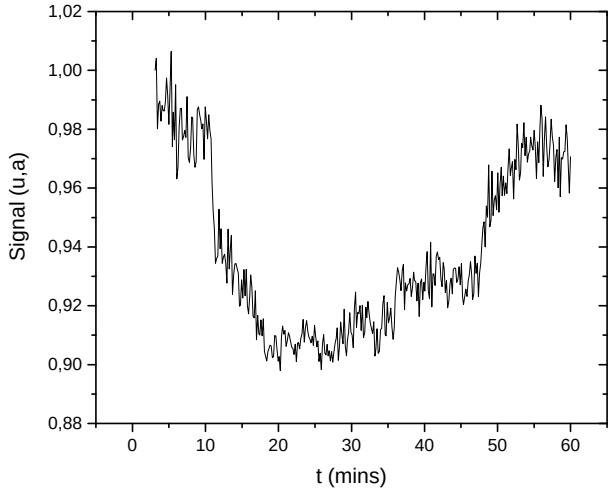

Figure 4.4: Typical stability of a TDS-ATR signal at a constant time delay, over more than one hour.

where L is the distance to the screen. The Fresnel number establishes a coarse criterion to define the near and far field approximations. Essentially, if F is small (less than 1) the beam is said to be in the far field. If Fresnel number is larger than 1, the beam is said to be in the near field and propagates according to Eq. 4.1, where diffraction plays a major role. As an example, using the frequency of 2.5 THz, the wavelength is $\lambda = 120\,\mu$m. If the beam travels through of a lens diameter $a = 10$ mm, Fresnel number at L=100 mm is $F \approx 8$. Therefore, the beam is in near field conditions. It means that the propagation of the terahertz beam is expected to differ from theoretical calculation provided by Gaussian calculation, and that "surprising" behavior may be observed.

The M^2 factor is given by the ratio between the experimental measured divergence angle θ_m and the theoretical divergent angle calculated from the measured waist size (see equation 4.6). The closer the value of M^2 is to 1, the better the quality of the Gaussian beam.

$$M^2 = \frac{\theta_m}{\frac{\lambda}{n\pi w_0}} \tag{4.6}$$

4.3 The terahertz QCL ATR system

In the previous TDS system (see section 3.4), the accuracy of the measurements is limited mainly by the stability of the entire system.This stability will be subsequently quantified by the following signal-to-noise ratio (SNR)

$$\mathrm{SNR}_{dB} = 10 \times \log_{10}\left(\frac{P_{\mathrm{signal}}}{P_{\mathrm{noise}}}\right) \tag{4.7}$$

where P_{signal} and P_{noise} are the power level of the average signal and of the noise, respectively.

A typical TDS signal at constant time delay is shown in figure 4.4. In the short term (1s), the SNR is about 16 dB, but in the long term, for 60 minutes, the ratio drops to only 10 dB. This low SNR thus severely limits our ATR measurement in the biological samples. A system with a higher SNR corresponding to a higher accuracy is necessary. We therefore developed a new sensor based on a QCL source.

4.3.1 The QCL source

The QCL source was purchased from Lytid[2], and has a QCL chip emitting at 2.5 THz with an average output power greater than 1 mW in quasi-continuous operation (QCW). The source operates with a cryogen-free cooling system, employing a Sterling engine to lower the diode temperature down to 40 K. The proper operation of the diode also requires a high frequency pulsed square-wave current modulation (about 10 KHz) with an adjustable duty cycle (see figure 4.5). An over-modulation, called gate frequency, can be added if necessary for use with a lockin amplifyer (5 to 1000 Hz). The drive voltage controls the output power, and can vary from 0 to 3400 mV.

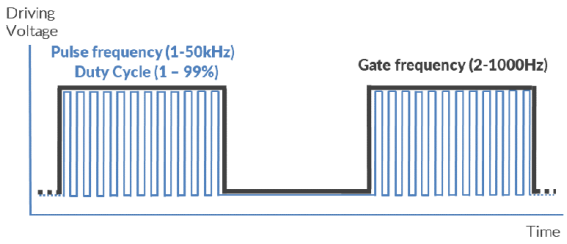

Figure 4.5: Driving signal of the QCL chip in QCW mode (from website of Lytid).

The detector used in our experiment is a pyroelectric detector (Terapyro, Lytid). It is a compact and highly sensitive sensor, based on a high-quality absorbing black coating, deposited on top of a 2 mm x 2 mm $LiTaO_3$ pyroelectric crystal. The principle of pyroelectric sensor is introduced in section 1.1.1.2. We chose a pyroelectric detector because of its very good sensitivity to small signal variations, even on a high signal, unlike Golay cells which saturate at high power. The detection frequency range of pyroelectric sensor is from 0.1 to 30 THz. The sensitivity could reach up to 2 kV/W. The sensor operates on a common +/-12 V DC power supply. This detector has 3 gain settings (low, medium, high).

The pyroelectric sensor, combined with a HRFZ-Si[3] collection lens placed directly at the output of the QCL source, were used to perform the first stability measurements on the QCL chip at 2.5 THz. The figure 4.6 shows the signal-to-noise ratio measurements for the 3 settings as a function of the modulation frequency. The ratio improves with higher gate modulation and is then limited very quickly by the bandwidth of the pyroelectric (not shown here). In

[2]TeraCascade 1000 series laser from Lytid Paris.
[3]HRFZ-Si: High Resistivity Float Zone Silicon

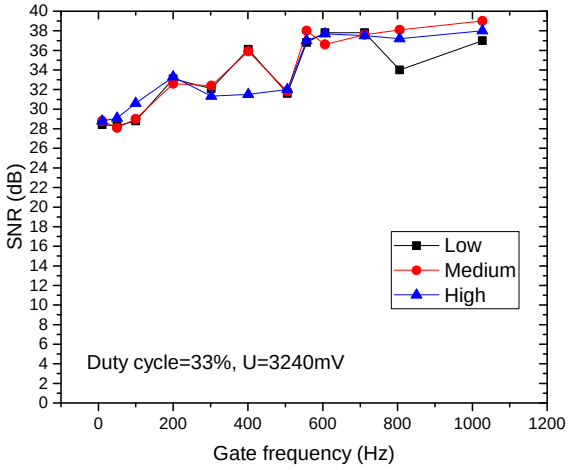

Figure 4.6: Quantum cascade laser SNR in function of the QCL gate frequency. Low mode, Medium mode and High mode correspond to the three modes of the pyroelectric sensor.

what follows, most of the measurements are performed using the average gain, which provided the best compromise between gain and rise time. Lock-in amplifiers are used to collect the signals.

4.3.2 Beam collimation in the QCL-ATR setup

One of the difficulties to construct the QCL-ATR system is the alignment of the lenses and mirrors due to the invisibility and the strong diffraction of terahertz radiation. With a ponctual detector such as the pyroelectric sensor we use, the proposed solution is to use a diaphragm. The idea is to obtain the beam size from the energy distribution. From equation 4.1, we obtain the intensity distribution at a given distance z

$$I(r) = I_0\, e^{-\dfrac{2r^2}{w^2(z)}}. \tag{4.8}$$

So the detected energy signal after a diaphragm of radius R is

$$S = \int_0^R \int_0^{2\pi} r\, I(r,\Phi) dr\, d\Phi = 2\pi \int_0^R I_0\, r\, e^{-\dfrac{2r^2}{w^2}}\, dr \tag{4.9}$$

$$S = 2\pi\, I_0 \left[-\frac{w^2}{4} e^{-\dfrac{2\,r^2}{w^2}} \right]_{r=0}^{r=R}. \tag{4.10}$$

Finally, we obtain

$$S = \frac{\pi\, w_0^2\, I_0}{2} \left(1 - e^{-\dfrac{2R^2}{w^2}} \right). \tag{4.11}$$

We define the total energy of the beam S_0 as

$$S_0 = \lim_{R \to +\infty} S = \frac{\pi\, w_0^2\, I_0}{2}. \tag{4.12}$$

So, for a given diaphragm radius R, the ratio between S and S_0 is

$$\frac{S}{S_0} = 1 - e^{\frac{-2R^2}{w^2}}. \tag{4.13}$$

Therefore, the beam size w is experimentally obtained by

$$w = \frac{\sqrt{2}R}{\sqrt{-\ln(1 - S/S_0)}}. \tag{4.14}$$

It is also useful to find $R = R_{1/2}$ so that $S = \frac{1}{2}S_0$. Then, the beam waist can be calculated as

$$w = \frac{\sqrt{2}R_{1/2}}{\sqrt{\ln 2}}. \tag{4.15}$$

We measured the total signal S_0 at each z position, then measured the energy S with a diaphragm of 2 mm in diameter. Thus, we were able to track the beam size during its propagation. A Gaussian beam is assumed parallel in the range $-z_R$ to $+z_R$. In order to obtain the most parallel beam when required, in particular in the ATR prisme zone, we aligned the lenses to maximize the beam waist w_0, by measuring the beam profile until a suitable position of the lenses is found, as showed in figure 4.7. Due to the very long wavelength of the terahertz beam, the collimation of the beam is limited at best to a distance of about 300 mm.

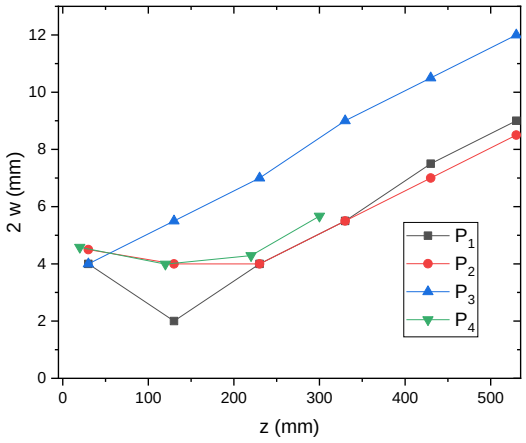

Figure 4.7: The waist size $2w$ versus the propagation distance z in 4 different positions of the collimating lens during alignment (P_1 to P_4). P_1 is a convergent beam and P_3 is divergent one. In position P_2 and P_4, the beam is considered to be collimated.

After a control visit to the manufacturer, we lost the correct alignment of the setup. But we could benefit from the loan of a 2D camera with micro-bolometers. from Lytid company.

The idea is to directly estimate the beam size from the 2D images, as shown in figure 4.8(left). Even if we have observed significant diffraction pattern on the images, we are able to estimate the size of the beam whose energy is reduced to half the energy of the center. We have given on the figure 4.8 (right) the beam size as a function of the propagation distance z for five positions of the lens at the direct output of the QCL. When the beam size remains stable for more than 200 mm, the beam is correctly collimated (like the P_5 position on the figure 4.8(right)). The interval between neighboring positions (such as P_1 and P_2 position) is about 0.5 mm, which indicates that the movement of the lens position must be particularly precise.

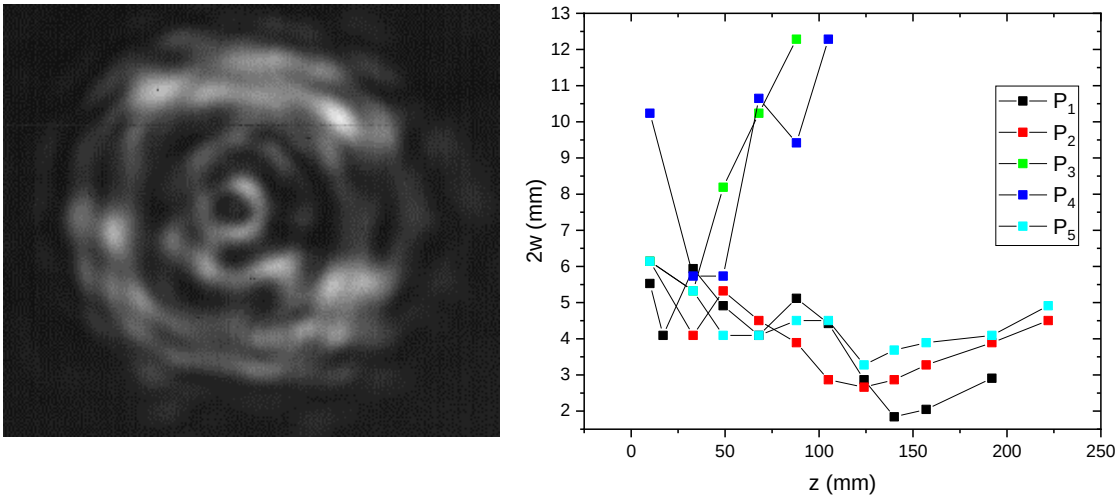

Figure 4.8: Left: An image taken by the 2D micro-bolometer camera. The structure is due to the strong diffraction of the terahertz wave. Right: The beam $2w$ as a function of the propagation distance z in five different positions of the lens during the alignment (P_1 to P_5). In positions P_3 and P_4, the beam is divergent. In position P_5, the beam is considered collimated within 200 mm.

4.3.3 The first QCL-ATR setup

Conventional spectrometers use a beamsplitter to separate the beam into two different optical paths that reach the reference and sample zones separately. And our precondition was to use only one prism since the biological sample could not be divided into two parts. Therefore, our first attempts to design the new QCL-ATR device used two pyroelectric sensors, one for the reference and one for the sample. After collimating the beam to be sent to the ATR prism, we divided the beam in two by a beam splitter (see figure 4.9). The purpose was to cancel the variation of the beam intensity by the ratio between the signals from the sample and the reference.

Figure 4.9 shows the experimental setup. The output of the QCL source at 2.5 Thz can be approximate as a divergent Gaussian beam with a 0.27 mm waist radius w_0 and the Rayleigh range is found to be $z_R = 1.9$ mm. The M^2 factor is then 1.17 for a divergence

$\theta = 166\,\text{mrad}$ (9.5°), which ensures a quasi-diffraction limited beam. The QCL is followed by a first lens (Lens 1, $D = 50\,\text{mm}$, $f = 50\,\text{mm}$) to collimate the output beam. An afocal system is then added to reduce the beam diameter. It consists of a parabolic mirror ($D = 50\,\text{mm}$, $f = 158\,\text{mm}$) and a second lens (Lens 2, $D = 25\,\text{mm}$, $f = 25\,\text{mm}$). The reduction ratio is therefore about 6. Then, a beam splitter cuts the beam into reference and sample beams. A mechanical chopper is required for detection of the two pyroelectric sensors by lockin amplifiers.

The operation of a lock-in amplifier is based on the orthogonality of sinusoidal functions. More clearly, A input signal modulated at frequency f_1 will be multiplied by another reference signal modulated at frequency f_2. When f_1 is not equal to f_2, then the integrated results over a time much longer than the period of the two signals is zero. Instead, when f_1 is equal to f_2 and also when the two signals are in phase, the average value is not equal to zero. Therefore, by adding a low-filter, the lockin amplifier can be served as a homodyne detector to extract a signal with a known reference frequency from an extremely noisy environment.

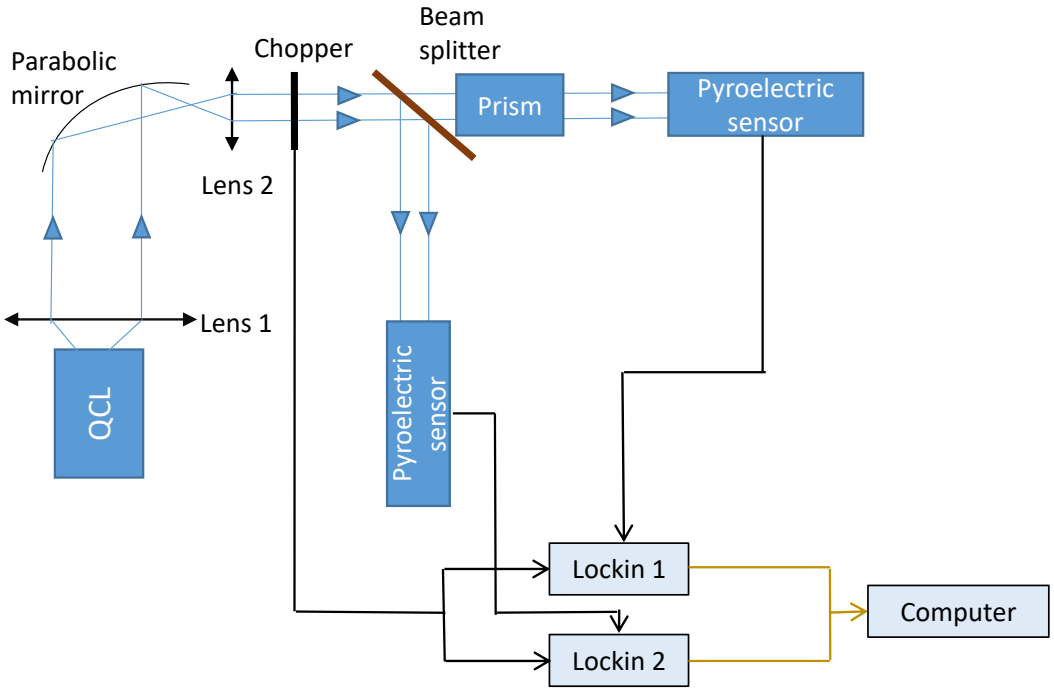

Figure 4.9: The first QCL-ATR setup.

Between the second lens and the sample's pyroelectric detector, a high resistivity silicon prism is placed. The beam is directed horizontally on the prism with an angle of incidence of 48° with respect to the entrance face. This prism is made of high resistivity silicon (HR-Si), opaque to the naked eye but transparent in the terahertz range. The dielectric losses are very low, so we can consider that $\hat{n}_{\text{Si}} = n_{\text{Si}} = 3.41$ [50]. The Gaussian beam propagates through the prism until it meets the Si-air interface. At this interface, the angle of incidence is 54°. This angle is calculated to satisfy the condition of total internal reflection. The penetration

depth is $\delta \approx 7\,\mu m$ for $f = 2.5\,THz$. As described previously in the TDS-ATR configuration, a HR-Si holder is used for the growth of the biological sample. This mobile holder, which must be in very good contact with the prism, should ultimately be considered as an outgrowth of the prism. However, we do not want to move the holder after positioning.

We first characterized the noise level of the QCL source, by directly measuring the signal at the output of the first lens. We used the direct internal modulation of the source to trigger the sensor. The signal-to-noise ratio (SNR) was measured over an integration time of 300 ms. The results (figure 4.10), show a variation of the SNR from 20 to 40dB as a function of the gate frequency. Overall, the higher the frequency, the higher the SNR value. However, the SNR drops rapidly after 1000 Hz due to the efficiency of the detector. We can notice locally lower SNR frequency zones around 500 and 900 Hz, which corresponds to mechanical resonances of the QCL setup. These zones will be further avoided. We have also studied the influence of adding rubber dampers under the QCL system supports. But no clear improvement was observed.

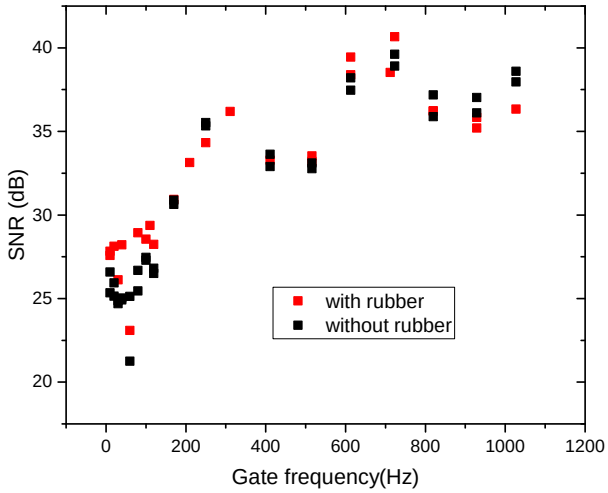

Figure 4.10: Signal to noise ratio in function of the QCL gate frequency.

We investigated the evolution of the signal on more than one hour on this setup. A high stability is indeed required to observe long dynamics in the biological systems. However, the signal showed in figure 4.11 gives a 12dB SNR during 60 minutes, which is clearly not enough.

4.3.4 Analyzing the problems

4.3.4.1 Symmetry of the device

The use of a beamsplitter in our device (see figure 4.9) can create problems in correcting the noise of the measurement signal by the reference signal. For instance, if Fabry-Perot effect is neglected, the transmitted and reflected beams on the beamsplitter are

$$\begin{aligned} S_{\text{trans}} &= t_{12}(\theta)\, t_{21}(\theta)\, S_0 \\ S_{\text{ref}} &= r_{12}(\theta)\, S_0 \end{aligned} \tag{4.16}$$

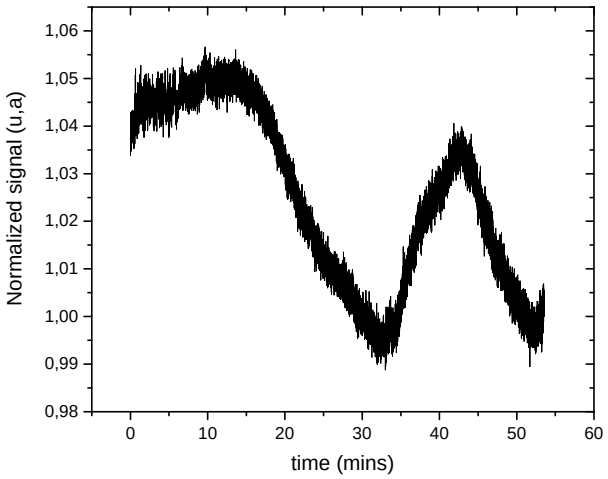

Figure 4.11: Fluctuation of QCL-ATR signal from the first QCL setup.

where the S_0 is the incident beam, S_{trans} and S_{ref} are the transmitted and reflected beams, θ is the incident angle, and $r_{12}(\theta)$ and $t_{12}(\theta)$ are the reflection and transmission Fresnel coefficients (see figure 4.12).

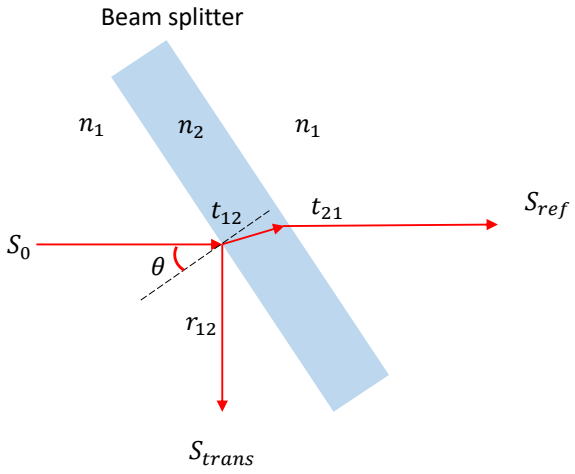

Figure 4.12: Schematic of transmitted and reflected beams by the beamsplitter.

According to Eq. 4.16, we see that the reflected and transmitted beams depend on the angle of incidence θ in different ways. This means that the variations of the transmitted and reflected beams are not symmetrical with respect to the variation of the angle of incidence. The correction of one of the beams by the other is therefore not possible.

4.3.4.2 Temperature influence

The oscillation observed in figure 4.11 may be caused by temperature variation. When the temperature changes, the thermal expansion of the instruments (e.g. aluminum support for parabolic lenses and silicon lenses) cannot be ignored. According to the formula of Wang

and Reeber, the coefficient of thermal expansion of aluminum is approximately equal to $23{\cdot}10^{-6}\,\mathrm{K}^{-1}$ to 20°C [270]. The parabolic mirror is particularly sensitive to angular variations. The optical breadboard can also be affected. A change in temperature will therefore lead to a tilt or shift of the terahertz beam and thus to an uncontrolled modification of the measured signal.

Another fluctuation caused by temperature is the change in refractive index. The perfect gas law gives the relationship between temperature and the amount of substance in the gas by the formula $PV = nRT$, where P is the pressure, V is the volume of gas, n is the amount of substance in the gas, R is the perfect gas constant and T is the absolute temperature. A variation in temperature thus leads to a variation in the quantity of matter on the optical path. However, the index of the dry atmosphere is very close to 1, so this effect seems negligible.

4.3.4.3 Water absorption

The humidity in the environment is not negligible as water molecules are very efficient absorbers of terahertz radiation, resulting in relatively short atmospheric propagation paths. In general, an increase in the water content of the atmosphere lead to a decrease in terahertz transmission. At around 2.5 THz (QCL), the water vapor absorption is stronger than at 1 Thz (TDS) (see figure 4.13). Besides, when the atmosphere temperature varied, the amount of water vapor molecules modified so that the absorption coefficient could be different in function of the humidity value. Therefore, the humidity fluctuation adds with temperature variation, resulting in a more important signal variation (as observed in figure 4.11).

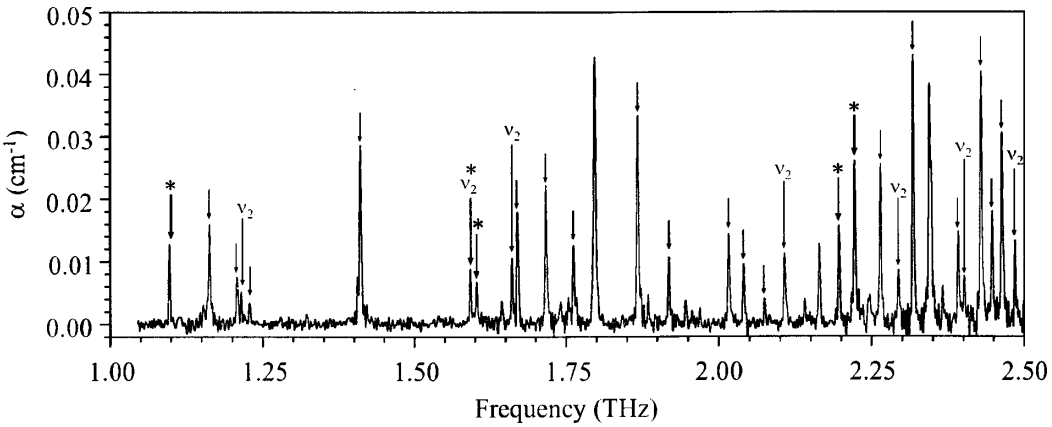

Figure 4.13: Absorption spectrum of atmospheric water vapor from 1 to 2.5 THz when the atmospheric pressure is equal to 620 torr. The relative humidity is 18.4±2% at average temperature 23.4°C. Water-vapor rotational transitions were measured in a near-stoichiometric propane–air flame at 1490 K with THz TDS [271].

4.3.5 the dual modulation QCL-ATR setup

4.3.5.1 A dual frequency setup

The main problem with the first configuration is that the two channels are not perfectly equal and symmetrical. For example, one beam is reflected by the beam splitter while the second is transmitted. When the beam changes direction, regardless of the origin, the reflected and transmitted coefficients evolve differently, and normalization is no more efficient. In addition, two different detectors were used, with potentially different response profiles. This is why we have designed a new setup, as symmetrical as possible, and using only one sensor (see figure 4.14 and figure 4.15 in 3D).

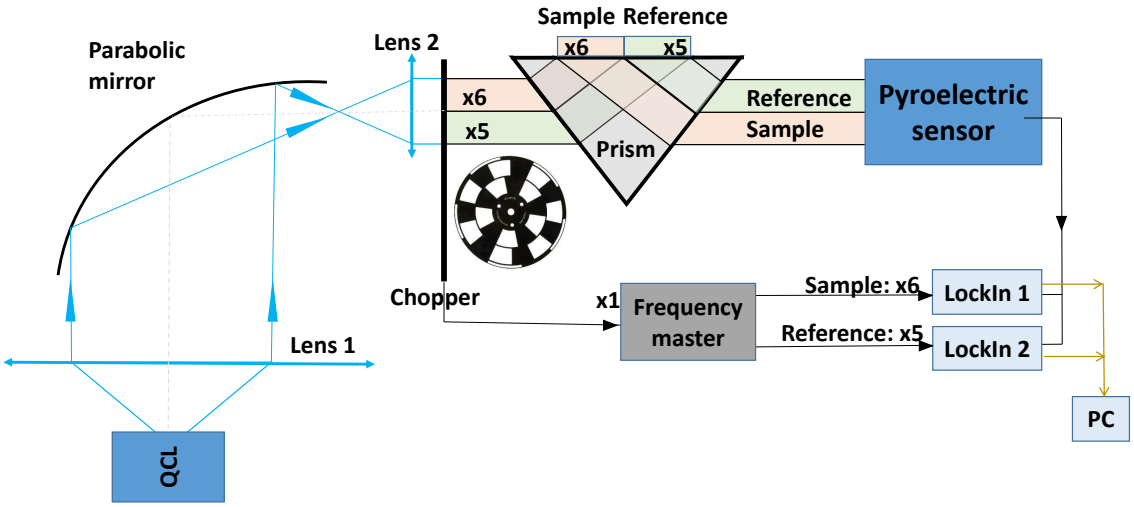

Figure 4.14: Dual modulation QCL-ATR setup. The output of the QCL is a terahertz divergent beam at 2.5 Thz. Lens 1 collimates the output beam. A parabolic mirror focuses the beam then Lens 2 collimates the beam into smaller size. A two-frequency chopper spatially separates the beam into two zones. One is the sample zone and the other is the reference zone. The beam is detected to the same pyroelectric sensor but sent on two different lockin amplifiers.

The key point is a mechanical chopper simultaneously modulating the terahertz beam at two different frequencies. The upper part of the beam is modulated at a frequency $\times 6$ and the lower part at a frequency $\times 5$, relative to a single master frequency. The chopper is positioned before the silicon prism so that the sample and reference zones are modulated at different frequencies. The entire beam is then focused on the pyroelectric sensor and its signal is sent to two locking amplifiers. The first lockin is driven by the $\times 6$ clock and provides the sample signal, while the second lockin is driven by the $\times 5$ clock and provides the reference signal. As a result, two different lockin can can separate signals at two frequencies form the mixed output signal detected by the same pyroelectric sensor.

In the most of our experiments, the motor clock is about 65 Hz, so the two frequencies

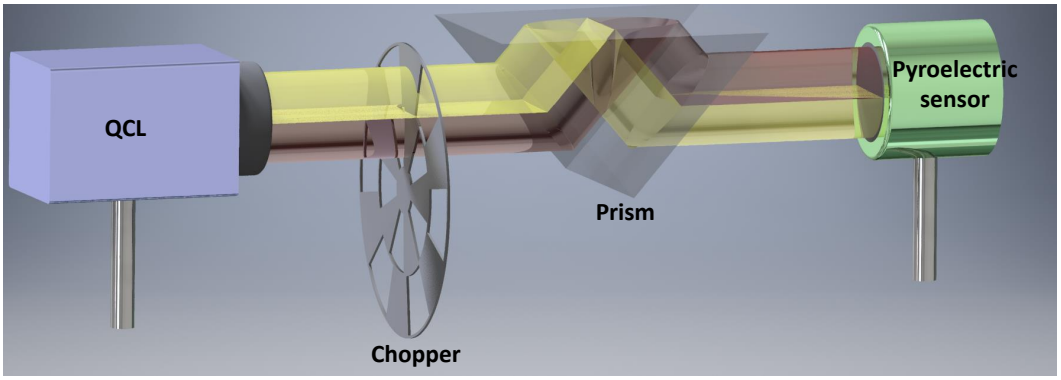

Figure 4.15: A 3D schematic of the dual modulation QCL-ATR setup with QCL, chopper, prism and pyroelectric sensor.

are 388 Hz and 324 Hz. In conclusion, by using a single sensor and a single prism, in a very symmetrical configuration, we can simultaneously measure the sample and the reference signals. With this system, we expect an improvement of the signal-to-noise ratio in the long term. As a preliminary result, a stability of 24 dB over 1 hour is observed (figure 4.16) compared to the 12 dB obtained previously (figure 4.11). This represents an improvement of more than an order of magnitude in long term stability.

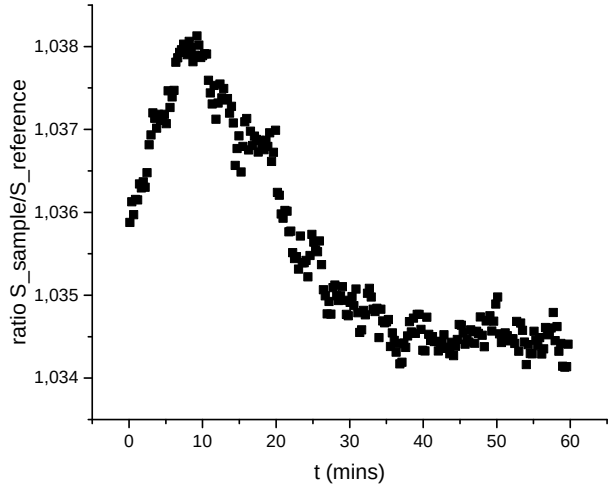

Figure 4.16: Fluctuation of the sample/reference signal using the dual modulation QCL-ATR setup. About 24dB SNR is found over 1 hour.

Before presenting the main features of this device, we also worked on the important issue of temperature fluctuation and humidity control.

4.3.5.2 Water cooled breadboard

Even though our laboratory is air-conditioned, temperature variation of typically $\pm 1°$ still remains. By tracking the relationship between the temperature and the ratio signal in

configuration of dual modulation, a correlation is clearly observed in figure 4.17. A hysteresis-like behavior is also observed. Partial cancellation of the temperature dependence of the signal was tested, but the correlation was not stable enough to be of real interest. Therefore, a water cooled breadboard was added under the whole setup to maintain the temperature fluctuation. This breadboard is filled with liquid water maintained at 21 ± 0.01°C by a Peltier-cooled water chiller.

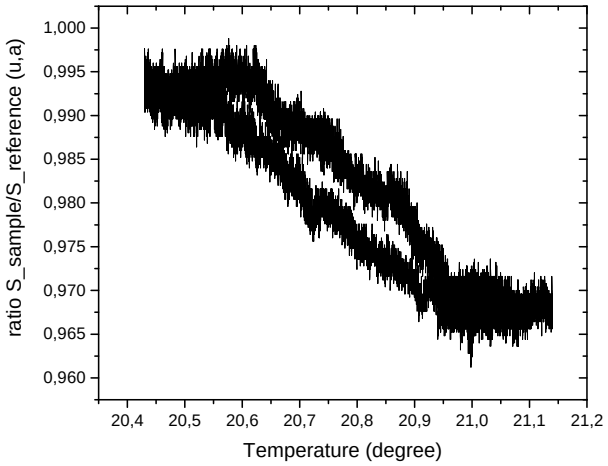

Figure 4.17: Correlation is found between the temperature and the ratio signal.

4.3.5.3 Setup box temperature and humidity control

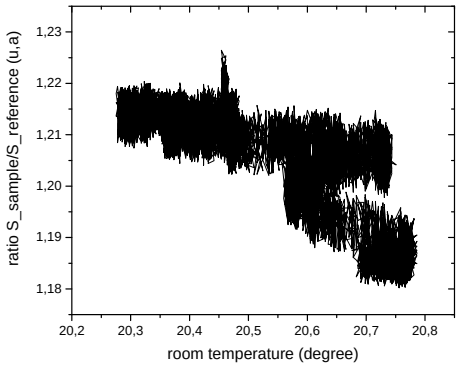

(a) Correlation between the temperature and the sample/reference ratio signal.

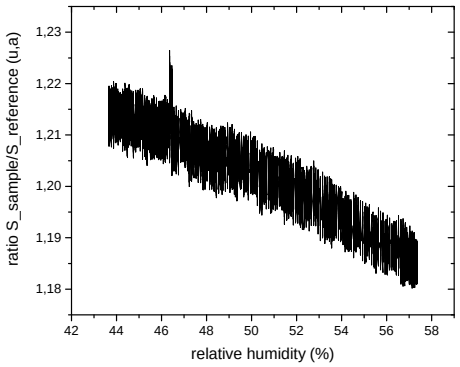

(b) Correlation between the relative humidity and the sample/reference ratio signal.

Figure 4.18: Correlations of the temperature (a) and relative humidity (b) with the normalized terahertz signal before controls.

In order to further control the temperature and humidity of the setup, we built an isolated box around the whole system. The ideal material of the enclosure to prevent heat

and air exchange is polypropylene, which is isolating, light and easy to cut. Figure 4.18a shows a remaining correlation between the sample/reference signal and the temperature of the laboratory, meaning that the thermal isolation of the box was not enough. The relative humidity (figure 4.18b) is also correlated with the signal. To further reduce the influence of temperature and relative humidity, dry air is injected in the box to maintain the relative humidity below 2%. This dry-air was also regultated in temperature using an air-water heat exchanger supplied by the 21°C water from the same chiller.

It also appeared that the fluctuation of the temperature of the absorbed air cooling the commercial QCL affects the stability of the QCL output. A thermally insulated enclosure with a heat exchanger was then added around the QCL setup. A heat exchanger block installed on top of the polypropylene enclosure is shown in the figure 4.19. When the ambient temperature varies by 1.5°C, the air under the block just passing through the heat exchanger varies by only 0.3°C, as does the temperature inside the QCL cover. This is a 5-fold reduction in the amplitude of temperature variation.

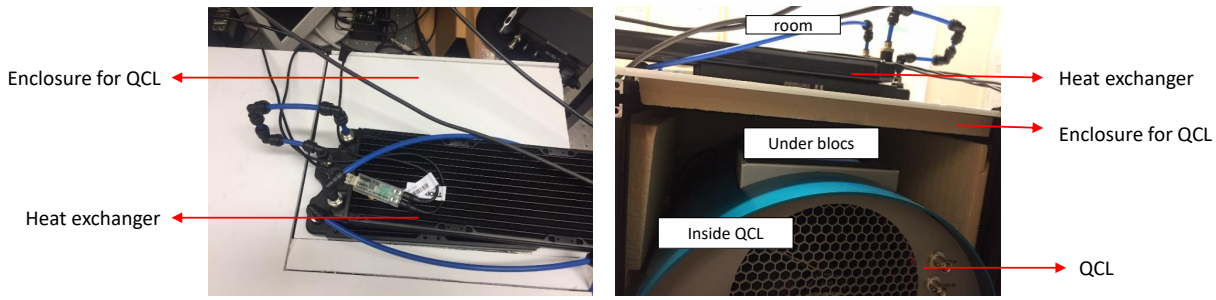

Figure 4.19: The heat exchanger with the QCL box (left) and the view of the commercial QCL setup (right).

4.3.5.4 Silicon prism temperature stabilization

Our lenses and prism are made of high-resistivity silicon (HR-Si). HR-Si is a material which, as we have seen previously, has excellent properties in the terahertz range including no measurable absorption coefficient [53], very high refractive index ($n_{si} = 3.41$) and negligible dispersion effect. The linear thermal expansion coefficient of silicon $\alpha_L = 2.6 \times 10^{-6} \times K^{-1}$ at 300 K [272, 273]. According to the linear expansion relation,

$$\frac{\Delta L}{L} = \alpha_L \Delta T \tag{4.17}$$

Where L is the initial length and ΔT is the temperature variation. We find that within a temperature interval of 2 K, for a 50 mm thick silicon plate (corresponding to the silicon thickness encountered by the beam), thermal expansion ΔL_{si} will be less than 260 nm which seems negligible.

The refractive index of silicon n_{si} is considered as frequency-independent in the far-infrared range (see the left curve in figure 4.20) but it is temperature-dependent at 1 THz

(see the right curve in figure 4.20) [274]. The thermo-optic coefficient of silicon is $\partial n_{\mathrm{si}}/\partial T = (1.886 \pm 0.03) \times 10^{-4}\,\mathrm{K}^{-1}$ at 1 THz [274] and $(1.86 \pm 0.08) \times 10^{-4}\,\mathrm{K}^{-1}$ at 200 THz [275]. Besides, $\partial \mathrm{n}_{si}/\partial \mathrm{T}$ value is estimated to be constant in the frequency range between 0.2 and 2.6 THz in the temperature interval of 295 to 335 K with a value $1.9{\times}10^{-4}$ K^{-1} [276].

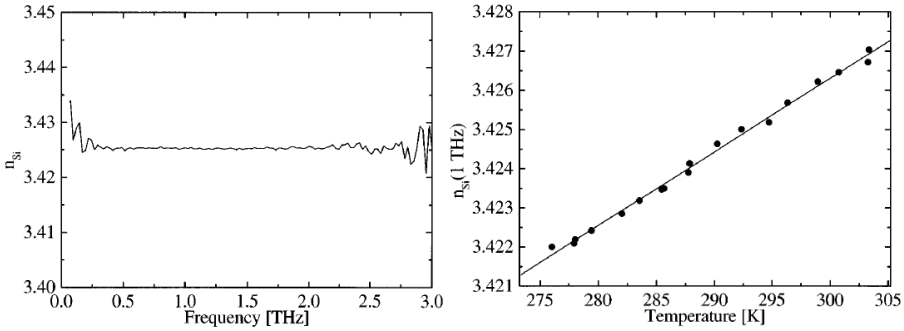

Figure 4.20: Left: the relation between the refractive index of silicon and the frequency in the far-infrared range at 295.5K. Right: The relation of the refractive index of silicon and the temperature at 1.0 THz [274].

Due to the temperature dependence of the refractive index of silicon, it is important to stabilize the temperature of the silicon prism as well as aqueous samples on the prism during experiments that can last for hours. It is also necessary to maintain the biological samples at their physiological temperature. We use two Peltier thermoelectric coolers (TEC) installed on two sides of the silicon prism perpendicular to the direction of the wave propagation (figure 4.21). A 12 W thermistor is in contact with the silicon prism. It sends the temperature of the prism to a laser diode temperature controller, which adjusts the temperature of the two TECs in a closed loop. This feedback allows us to control the temperature of the silicon prism with a relative precision of 0.01°C. The laser controller has the ability to vary the temperature from -45°C to +145°C with an accuracy better than 0.02°C. The wide range of temperature variation allows us to provide a cell-friendly environment (37°C).

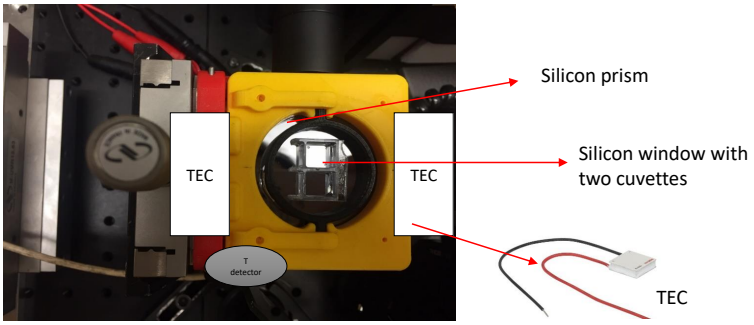

Figure 4.21: Peltier thermoelectric coolers in the two sides of the silicon prism.

This controlled temperature system also allows us to investigate the refractive index dependence of silicon on temperature. By varying the temperature of the silicon prism from

291 K to 298 K ($\Delta T = 7K$), we observe that the detected signal exhibit an interference-like pattern (see figure 4.22). A possible explication for this phase shift is the interference caused by the superposition of back and forth waves between the pyroelectric sensor and the chopper (see figure 4.14). Therefore the variation of the optical length per Kelvin, $\frac{\Delta\delta}{\Delta T}$, can be calculated as

$$\frac{\Delta\delta}{\Delta T} = \frac{\lambda/2}{\Delta T} = 8.5\,\mu\text{m} \cdot K^{-1} \tag{4.18}$$

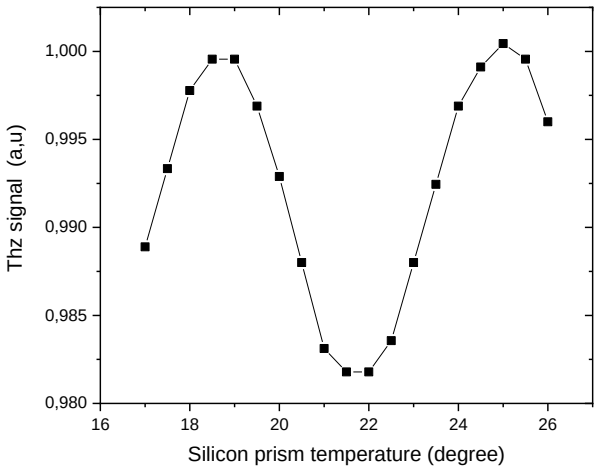

Figure 4.22: Measured Terahertz signal versus the temperature fo silicon prism. A periodic signal is found due to the interference between the back and forth wave between the pyroelectric sensor and the chopper (see figure 4.14).

Then, we can calculate the theoretical value of the variation of the optical length per Kelvin from the thermo-optic coefficient. In the case, the variation in optical path length $\Delta\delta$ occurs by the expansion and change in refractive index Δn. The relation is expressed by

$$\Delta\delta = (n + \Delta n) \cdot (L + \Delta L) - n \cdot L - \Delta L \approx L \cdot \Delta n + (n - 1) \cdot \Delta L. \tag{4.19}$$

The variation of the optical length is then expressed by

$$\frac{\Delta\delta}{\Delta T}(\text{Theo}) \approx L\frac{\Delta n}{\Delta T} + (n - 1)\frac{\Delta L}{\Delta T} \tag{4.20}$$

The silicon expansion length is $\Delta L = 9.156{\times}10^{-7}$ m according to equation 4.17 with ΔT = 7 K and L = 50 mm. With equation 4.20, we obtain $\frac{\Delta\delta}{\Delta T}(\text{Theo}) \approx 9.7\,\mu\text{m}{\cdot}K^{-1}$, which is in good agreement with the value mentioned above in equation 4.18, validating our hypothesis. Theo Theo

4.3.5.5 Index-matching liquid

As introduced in section 3.5.2, an air gap always exist between the prism and HR-Si sample plates. However, the evanescent wave decreases to 7 µm at 2.5 THz as compared to

20 µm at 1 THz. Therefore, the flatness problem is more acute at 2.5 THz, which results in the optical discontinuity between the prism and plates. The ideal case is to replace this air gap with a high refractive index but low absorption coefficient substance. A liquid is mandatory as only liquid can fill the defects of the plates. Finally, at the difference with the TDS-ATR setup, we can add a matching index liquid to insure the optical continuity so that we can observe in terahertz the signal from the silicon plates. Indeed, the Si plate is not moved during the experiments with our dual modulation QCL-ATR setup. During our experiments, we used α-pinene (P45702, Sigma-Aldrich) as the matching liquid. For α-pinene, the refractive index is n=1.66 and the absorption coefficient is $\alpha = 1.5\,\mathrm{cm}^{-1}$ [277]. It absorbs much less than water ($\alpha_{\mathrm{water}} = 230\,\mathrm{cm}^{-1}$) while more than HR-Si ($\alpha \ll 0.33\,\mathrm{cm}^{-1}$). Therefore, α-pinene is able to replace the air gap without stopping the propagation of terahertz wave by absorption.

4.3.5.6 Summary of the improvements

After all these improvements, a SNR of 40 dB was achieved in 300 ms acquition time, and a SNR of 30 dB is maintained for hours, approaching short-term stability in seconds (figure 4.23). This represents an improvement of nearly 2 orders of magnitude over the previous system. In conclusion, the QCL source delivers stable, continuous wave terahertz radiation with a mW level at 2.5 THz. When used with the latest generation lithium tantalite pyroelectric detector, we have designed an original dual-modulation ATR sensor with a signal-to-noise ratio improved by a factor of 100 over the best TDS results, also thanks to precise temperature and humidity control. Figure 4.24 summarizes the typical variations of the normalized terahertz signals obtained during each major improvement step.

Figure 4.25 shows a first long-term stability test. Two cell samples were prepared at the same seeding concentration. At $t = 0$, we added a saponin solution to obtain the final concentration $C_{\mathrm{sapo}} = 75\,\mu\mathrm{g/mL}$. Two measurements were performed in the QCL-ATR (Fig. 4.25, left) and TDS-ATR (Fig. 4.25, right) systems. We can clearly observe that the result obtained with the QCL-ATR system is much better.

4.4 Calibration of the terahertz QCL-ATR system

Before applying our QCL-ATR device to biological samples, we need to study its characteristics, in particular the beam profile at the silicon prism. Using this profile, the calibration of the device is discussed and used to demonstrate its ability to detect small concentrations of solutes.

4.4.1 Calibration and beam profile

We will study the relationship between the calibration of the QCL-ATR device and the beam profiles at the top of the ATR prism. We will first present the calibration calculation, then the profiles will be measured and the link with the calibration will be established.

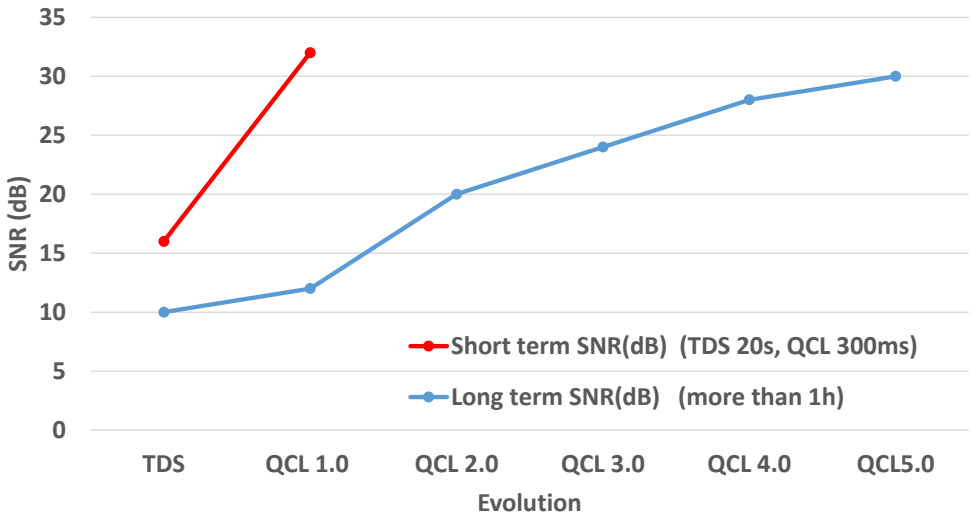

Figure 4.23: The improvement of SNR for short time stability during a few seconds (red line), and for long time stability, more than one hour (blue line). QCL1.0: The simplest configuration with one frequency. QCL2.0: Setup configuration with one detector and two-frequency-modulation ν_1 and ν_2. QCL3.0: Two-frequency-modulation + insulated box. QCL4.0: Two frequency-modulation + insulated box + input of dry air. QCL5.0: Two frequency-modulation + insulated box + input of dry air + QCL enclosure with heating exchange system.

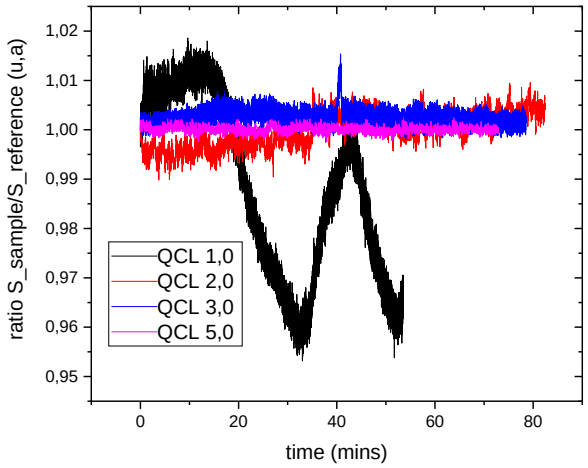

Figure 4.24: Typical variations of the normalized terahertz signals obtained during each major improvement step, over more than one hour.

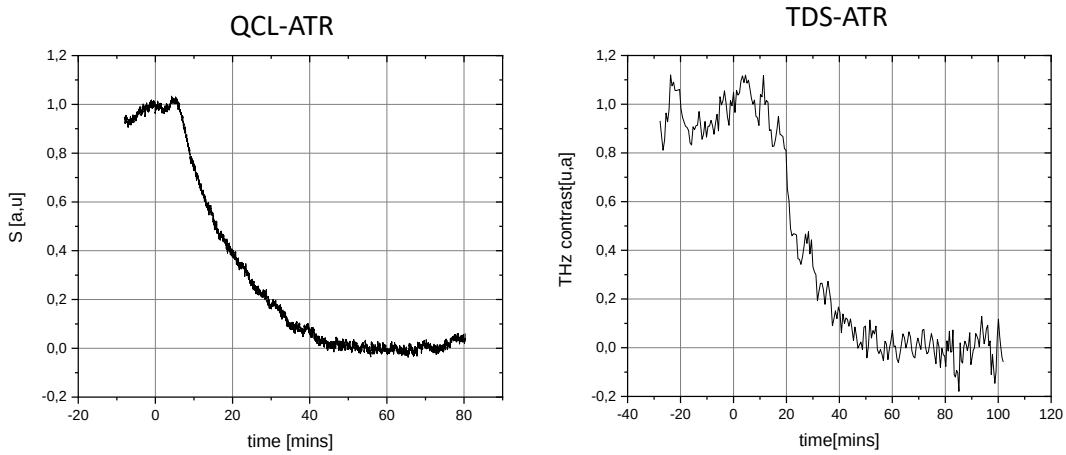

Figure 4.25: Chemical (saponin) permeability dynamics measured by QCL-ATR (left) and TDS-ATR (right) systems.

To calibrate the experimental measurements, we derived a model linking the contribution of the measured signals at both frequencies to the terahertz beam profile at the prism surface. For the experimental calibration, we used a double liquid reservoir (in black on the figure 4.26). Both reservoirs can be filled with liquid, or remain empty. We consider 4 areas on top of the ATR prism, A_z with $z = 1$ to 4. The samples areas A_1 (left gray square) and A_2 (right gray square), the cell wall area A_3 (black area) and the peripheral area A_4.Each zone has a different ATR reflection coefficient R_z. The recorded signals are S_ν with $\nu = 1$ and 2, for the 2 modulation frequencies ν_1 and ν_2.

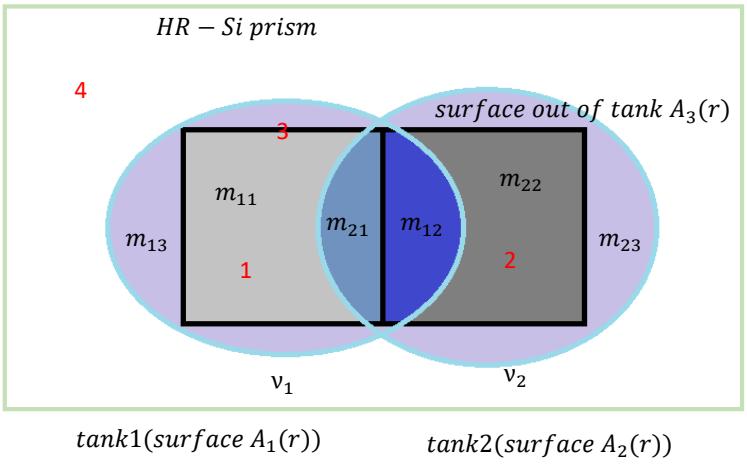

Figure 4.26: Schematic of the 2 square reservoirs. Ellipses represent the terahertz beam distributions at frequencies ν_1 and ν_2 on the ATR prism. Zones 1 and 2 are for the liquid samples, zone 3 is the wall of the reservoirs and zone 4 is the remaining external surface.

The intensity I_0 from the QCL is divided into two parts at 2 frequencies by the mechanical chopper and sent to the ATR prism. Therefore, the recorded signals are $S_\nu = R_T^{(\nu)} T_\nu I_0$, where

$R_T^{(\nu)}$ is the total refection coefficient, and the transmission coefficients T_ν gather all other propagation losses between the source and the detector, including the chopper and the lenses. The signals are then given by 4 contributions from their recovery integrals

$$\begin{aligned} S_1(\nu_1) &= R_T^{(\nu_1)} T_{\nu_1} I_0 \\ S_2(\nu_2) &= R_T^{(\nu_2)} T_{\nu_2} I_0 \end{aligned} \tag{4.21}$$

with

$$\begin{aligned} R_T^{(\nu)} &= \sum_{z=1}^{4} m_{\nu z} R_z \\ m_{\nu z} &= \int_{A_z} P_\nu(r) dr. \end{aligned} \tag{4.22}$$

$P_\nu(r)$ are the profiles of the terahertz beams, modulated at each frequency, at the surface of the prism, and $m_{\nu z}$ are the overlap integrals of these profiles over the 4 different zones. By definition, the sum of the integrals is equal to 1, thus $\sum_{z=1}^{4} m_{\nu z} = 1$.

We now consider several filling configurations. First, with empty reservoirs, $R_z = 1$, using Eqs. 4.21 and 4.22, the signals are

$$S_1^{EE} = (m_{11} + m_{12} + m_{13} + m_{14}) T_1 I_0 = T_1 I_0 \tag{4.23}$$
$$S_2^{EE} = (m_{21} + m_{22} + m_{23} + m_{24}) T_2 I_0 = T_2 I_0. \tag{4.24}$$

When we add pure water in reservoir 1 with the reflectivity R_W and nothing in reservoir 2, we get

$$S_1^{WE} = (m_{11} R_W + m_{12} + m_{13} + m_{14}) T_1 I_0 \tag{4.25}$$
$$S_2^{WE} = (m_{21} R_W + m_{22} + m_{23} + m_{24}) T_2 I_0. \tag{4.26}$$

When we add pure water in reservoir 2 and nothing in reservoir 1,

$$S_1^{EW} = (m_{11} + m_{12} R_W + m_{13} + m_{14}) T_1 I_0 \tag{4.27}$$
$$S_2^{EW} = (m_{21} + m_{22} R_W + m_{23} + m_{24}) T_2 I_0. \tag{4.28}$$

When we add pure water in both reservoirs,

$$S_1^{WW} = (m_{11} R_W + m_{12} R_W + m_{13} + m_{14}) T_1 I_0 \tag{4.29}$$
$$S_2^{WW} = (m_{21} R_W + m_{22} R_W + m_{23} + m_{24}) T_2 I_0. \tag{4.30}$$

Finally, when reservoir 1 contains the sample solution to be measured (for examples ions), with reflectivity R_I, and reservoir 2 contains pure water,

$$S_1^{IW} = (m_{11} R_I + m_{12} R_W + m_{13} + m_{14}) T_1 I_0 \tag{4.31}$$
$$S_2^{IW} = (m_{21} R_I + m_{22} R_W + m_{23} + m_{24}) T_2 I_0. \tag{4.32}$$

The ideal case is when the beam modulated at ν_1 is fully contained in reservoir 1, as well as the beam modulated at ν_2 in reservoir 2, so that there is no overlap between the 2 beams. In that case, $m_{11} = m_{22} = 1$ and the other coefficients are 0. Thus, equations 4.31 and 4.32 simplify as

$$S_1 = R_I T_1 I_0 \tag{4.33}$$
$$S_2 = R_W T_2 I_0. \tag{4.34}$$

the ratio $\frac{S_1}{S_2} = \frac{R_I}{R_W}\frac{T_1}{T_2}$ is independent on I_0 and can easily be calibrated, obtaining T_1/T_2 using pure water in both reservoirs.

Unfortunately, when the beams spread over other zones, such a simple calibration is not possible. In order to remove the variations of the QCL source I_0, the following normalized ratios could be experimentally obtained

$$\begin{aligned}
\rho_{\nu_1}^{WE} &= \frac{S_1^{WE} - S_1^{EE}}{S_1^{EE}} = \frac{m_{11}(R_W - 1)}{m_{11} + m_{12} + m_{13} + m_{14}} = m_{11}(R_W - 1) \\
\rho_{\nu_1}^{WW} &= \frac{S_1^{WW} - S_1^{EE}}{S_1^{EE}} = (m_{11} + m_{12})(R_W - 1) \\
\rho_{\nu_1}^{EW} &= \frac{S_1^{EW} - S_1^{EE}}{S_1^{EE}} = m_{12}(R_W - 1)
\end{aligned} \tag{4.35}$$

$$\begin{aligned}
\rho_{\nu_2}^{WE} &= \frac{S_2^{WE} - S_2^{EE}}{S_2^{EE}} = m_{21}(R_W - 1) \\
\rho_{\nu_2}^{WW} &= (m_{21} + m_{22})(R_W - 1) \\
\rho_{\nu_2}^{EW} &= m_{22}(R_W - 1).
\end{aligned} \tag{4.36}$$

The ratio

$$\frac{\rho_{\nu_1}^{WW}}{\rho_{\nu_2}^{WE}} = 1 + \frac{m_{12}}{m_{11}} \tag{4.37}$$

may experimentally provide the ratio of the integral overlaps over the 2 reservoirs. However these measurements would not be precise enough since I_0 fluctuates between the record of $\rho_{\nu_1}^{WW}$ and $\rho_{\nu_2}^{WE}$. Normalized measurements, using simultaneously S_1 and S_2, have to be taken into account to achieve the best precision.

Therefore, we consider now the simultaneously measure of both S_1 and S_2 and take their ration $r = S_1/S_2$ to remove the intensity fluctuation I_0. Finally, for both reservoirs with water (WW), ions/water (IW) and water/ions (WI), we have

$$\begin{aligned}
r_{WW} &= \frac{S_1^{WW}}{S_2^{WW}} = \frac{(m_{11}R_W + m_{12}R_W + m_{13} + m_{14})T_1}{(m_{21}R_W + m_{22}R_W + m_{23} + m_{24})T_2} \\
r_{IW} &= \frac{S_1^{IW}}{S_2^{IW}} = \frac{(m_{11}R_I + m_{12}R_W + m_{13} + m_{14})T_1}{(m_{21}R_I + m_{22}R_W + m_{23} + m_{24})T_2} \\
r_{WI} &= \frac{S_1^{WI}}{S_2^{WI}} = \frac{(m_{11}R_W + m_{12}R_I + m_{13} + m_{14})T_1}{(m_{21}R_W + m_{22}R_I + m_{23} + m_{24})T_2}.
\end{aligned} \tag{4.38}$$

We now assume that $R_I \simeq R_W = R$ and set $R_I = R(1+\epsilon)$ with $\epsilon \ll 1$, and $\Delta R = R_I - R_W = R\epsilon \ll R$. In other words,

$$\epsilon = \frac{R_I - R_W}{R_W} \tag{4.39}$$

is the relative reflection coefficient of the analyzed liquid compared to pure water. Practically, we want to determine ϵ in function of the solute and of its concentration.

The development at first order in ϵ of the ratio r_{IW}/r_{WW} gives

$$\frac{r_{IW}}{r_{WW}} \approx 1 + R\left(\frac{m_{11}}{(m_{11}+m_{12})R + m_{13} + m_{14}} - \frac{m_{21}}{(m_{21}+m_{22})R + m_{23} + m_24}\right)\epsilon \tag{4.40}$$

then we get

$$\frac{r_{IW}}{r_{WW}} \approx 1 + R\left[\frac{m_{11}}{1+(m_{11}+m_{12})(R-1)} - \frac{m_{21}}{1+(m_{21}+m_{22})(R-1)}\right]\epsilon = 1 + \beta_{IW}\epsilon \tag{4.41}$$

and symmetrically

$$\frac{r_{WI}}{r_{WW}} \approx 1 + R\left[\frac{m_{12}}{1+(m_{11}+m_{12})(R-1)} - \frac{m_{22}}{1+(m_{21}+m_{22})(R-1)}\right]\epsilon = 1 + \beta_{WI}\epsilon. \tag{4.42}$$

We note that if the profiles are symmetrical, $m_{11} = m_{22}$ and $m_{12} = m_{21}$, and then β_{IW}=-β_{WI}.

From the ratio r_{IW}/r_{WW}, the quantity $\beta_{IW}\epsilon$ is easily obtained. However, the knowledge of the coefficient β_{IW} is mandatory to retrieve ϵ. Therefore, β_{IW} is the calibration factor of our QCL-ATR setup. We notice that, using equations 4.35 and 4.36, one obtains

$$\beta_{IW} = \frac{R}{R-1}\left[\frac{\rho_{\nu_1}^{WE}}{1+\rho_{\nu_1}^{WW}} - \frac{\rho_{\nu_2}^{WE}}{1+\rho_{\nu_2}^{WW}}\right] \tag{4.43}$$

and

$$\beta_{WI} = \frac{R}{R-1}\left[\frac{\rho_{\nu_1}^{EW}}{1+\rho_{\nu_1}^{WW}} - \frac{\rho_{\nu_2}^{EW}}{1+\rho_{\nu_2}^{WW}}\right]. \tag{4.44}$$

The value of $R = R_W$ can easily be obtained from experimental data by the ratio between the terahertz signal collected with an empty prism and from the prism fully covered with pure water. We experimentally obtain $R = 0.54 \pm 0.06$.

We then measured the signals from several configurationd of the calibration reservoir: Empty/Empty, Water/Empty, Empty/Water and Water/Water. The normalized ratios ρ defined by Eqs. 4.35 and 4.36 we obtained are found in Table 4.1.

The values of the integrals $m_{\nu z}$ can now be obtained with Eqs. 4.35 and 4.36, and the calibration constants β_{IW} and β_{WI} from Eqs. 4.43 and 4.44, and found in Table 4.2.

According to the table 4.2, the total values $m_{11}+m_{12}$ and $m_{21}+m_{22}$ are about 80%. This means that most of the reflected terahertz signal comes from the surface of the dual reservoirs and not from zones 3 and 4 (figure 4.26). The dual reservoir is positioned almost symmetrically at the top of the ATR prism because $\beta_{IW} \approx -\beta_{WI}$. However, the uncertainties of β_{IW} and β_{WI} are quite large. The values obtained from r_{IW}/r_{WW} are therefore not extremely accurate

Table 4.1: Measured normalized signals for calibration.

Value	Mean	Std dev
$\rho_{\nu_1}^{WE}$	-0.324	8.7×10^{-4}
$\rho_{\nu_2}^{WE}$	0.017	4.8×10^{-5}
$\rho_{\nu_1}^{EW}$	-0.044	1.0×10^{-4}
$\rho_{\nu_2}^{EW}$	-0.404	1.6×10^{-3}
$\rho_{\nu_1}^{WW}$	-0.369	8.3×10^{-4}
$\rho_{\nu_2}^{WW}$	-0.390	1.1×10^{-3}

Table 4.2: Estimation of $m_{\nu z}$, β_{IW} and β_{WI} numerical values from calibration.

Value	Mean	Std
m_{11}	70%	6%
m_{12}	9.7%	0.8%
$m_{11} + m_{12}$	79%	7%
m_{21}	0%	0.3%
m_{22}	87%	7%
$m_{21} + m_{22}$	87%	7%
β_{IW}	0.62	0.15
β_{WI}	-0.68	0.16

in absolute value. This is due to the fact that the measurements made to estimate β are not normalized by I_0. Nevertheless, the relative values are much more precise since they benefit from the cancellation of the variations of I_0 and can therefore be used to detect very small quantities of solutes ($\epsilon \propto C_{ions}$). It should be noted that the data must be recorded during the same series of measurements without moving the position of the double reservoir for calibration.

To obtain the best contrast between the two modulation frequencies, it is essential that these frequencies ν_1 and ν_2 be separated as much as possible. However, the strong diffraction in the terahertz range causes the two beams to partially overlap. Our next step is to measure the profile of the terahertz beam on the silicon prism at both modulation frequencies. The objective of measuring the beam profile at the top of the silicon prism is also to confirm the calibration of the instrument obtained previously, by calculating the overlapping integrals.

Our first attempt to measure the profiles was to place a small piece of wet tissue on the prism and then move it using two translation stages. The liquid water locally modifies the signals of both modulations. A scan of the prism gave us a first idea of the profiles. However, the wet tissue left a badly controlled moisture residue on the prism, which altered the resolution.

The second measurement was to locally modify the dielectric constant of the silicon prism by illumination with an optical beam. The silicon gap is about 1.22 eV (corresponding to a

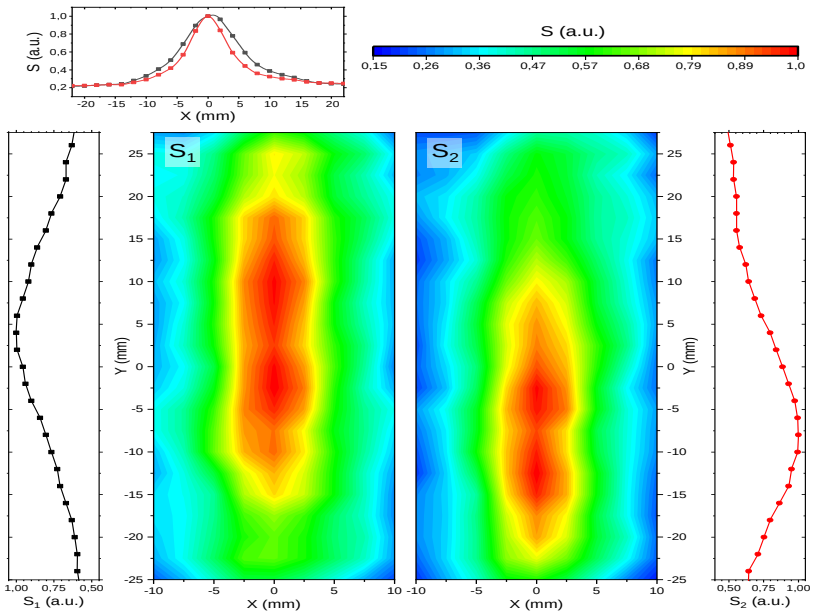

Figure 4.27: Beam profile using a focused visible beam to modulate the reflection of THz radiation via the creation of charge carriers in the semiconductor (HR silicon prism). S_1 and S_2 are the terahertz signals at ν_1 and ν_2 double frequency modulations. The red and black point lines are the section profiles at both frequencies.

wavelength of 1.1 µm). So if it is illuminated with photons of higher energy, for example visible light, these photons generate charge carriers that modify the reflection coefficient at the prism surface [278]. We have thus focused a white light source of about 5 mW on a spot of 2 mm diameter, and again recorded the modification of the S_1 and S_2 signals, in function of on the position of the light spot. The quantity of charges created being always constant, the variation of the signals is proportional to the intensity of the terahertz profile on the prism.

The profiles are presented in the figure 4.27. The results are very surprising, because the two frequencies strongly overlap in the y direction (in the expected direction of separation of the two modulations). Moreover, the numerical calculation of the integrals $m_{\nu z}$ gives that $m_{11} + m_{12} \approx 25\%$, which is in strong contradiction with previous measurements using the dual tank, where most of the signal comes from zones 1 and 2. Finally, the calculation of the calibration parameters β_{IW} and β_{WI} gives much smaller values, β are between 1/50 and 1/200. This high uncertainty comes from the minus sign in Eqs. 4.43 and 4.44 and the fact that both terms are here of the same magnitude due to the large overlap measured. These very low values (compared to 0.6 obtained in the table 4.2) are in total disagreement with the values previously found by direct calibration.

The problem may originate from the carrier diffusion in HR silicon when it is illuminated by the focused beam. The carrier diffusion length L is related to the carrier lifetime τ and

the diffusion constant D for the generated electrons and holes in the semiconductor by [279]

$$L = \sqrt{D\tau} \tag{4.45}$$

where D is related to the carrier mobility μ by

$$D = \frac{k_B T}{q}\mu \tag{4.46}$$

where k_B is the Boltzmann constant, T is the temperature and q is the charge value. The mobility and carrier lifetime are not precisely known for intrinsic high resistivity silicon, and can vary from the crystal growth process. From [279], the mobility of the electrons is μ_e=1450 cm^2/Vs and of the holes μ_h=500 cm^2/Vs for undoped silicon. The diffusion constants of electrons and holes are calculated, D_e=37 cm^2/s and D_h=13 cm^2/s. The carrier lifetime was estimated from 2 to 20 ms in [280–282]. With these values, for electrons and holes, we obtain

$$\begin{aligned} L_e &= 2.7 \text{ to } 8.6\,\text{mm} \\ L_h &= 1.6 \text{ to } 5.1\,\text{mm}. \end{aligned} \tag{4.47}$$

Consequently, the diffusion length of the carrier greatly reduces the spatial resolution in our previous profile measurement (Fig. 4.27). The resolution should be well above 2 mm. Moreover, the influence on the spatial resolution is not isotropic. Therefore, a more accurate method for estimating the beam profile is needed.

We tried a third method, by adding a 300 µm thick doped silicon wafer. The doped silicon wafer has a much shorter diffusion length, so we hoped to eliminate the resolution broadening. However, multiple reflection problems deeply alter the measured profile and do not allow to obtain the expected results.

We finally propose to use a small drop of water to scan the HR silicon prism because of the high water absorption. This allows a decrease of the reflected terahertz signal without worrying about electron diffusion. The idea is to use a 2 mm diameter water drop to scan the prism surface. A graduation mark is drawn on the prism surface and then 2µL of water is placed with a micropipette. We collect the reflected terahertz signal S_1 and S_2. For each position, we successively recorded 5 times the signal with and without the drop, to serve as a reference. The results are presented on figure 4.28. The difference with the figure 4.27 is quite spectacular. This time, we get much more concentrated profiles with very little overlap, as theoretically expected.

We can estimate the β_{IW} value from figure 4.28. We get $\beta_{WI} = 0.77 \pm 0.05$. It is very similar to the value $\beta_{WI} = 0.68 \pm 0.15$ in table 4.2, which is calculated from our calibration modeling. Therefore, the water drop method to estimate the beam profile is consistent with our modeling. The double reservoir used to contain the liquids consists of two 10 mm squares. The half-energy of the terahertz beam is concentrated in a 4 mm diameter circle inside these squares. This size thus corresponds well to the size of the double reservoir (see figure 4.29).

The calibrated β values can now be used for spectroscopic measures of biological solutions, such as ions and proteins solutions.

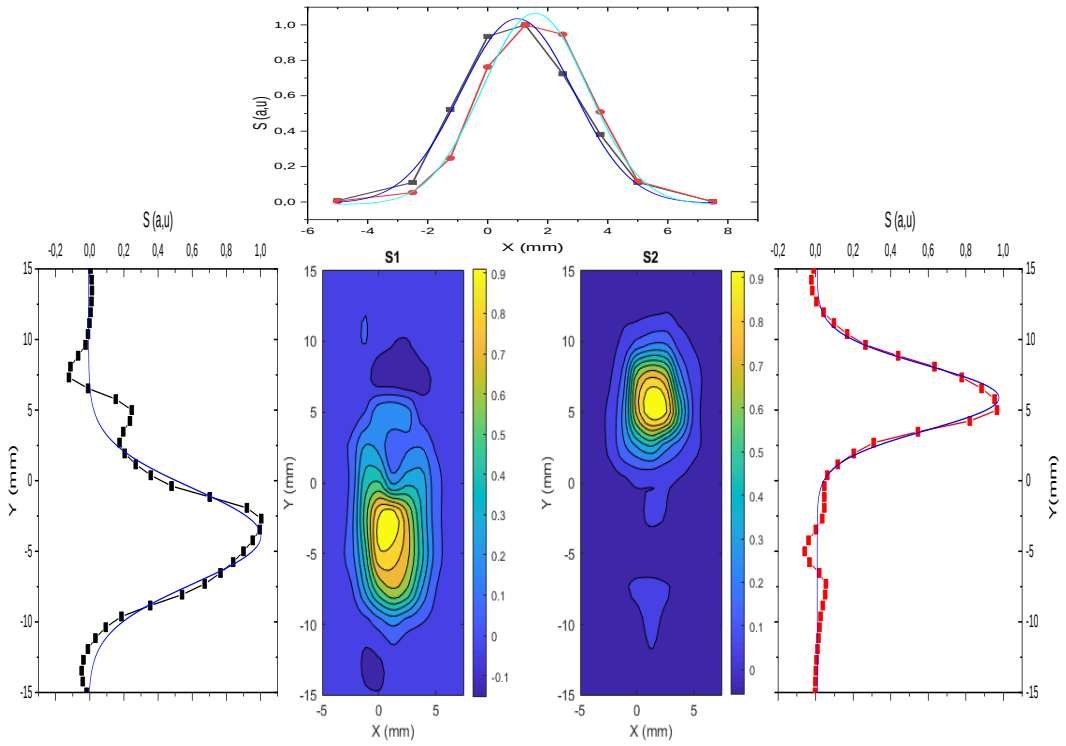

Figure 4.28: 2D beam profiles using a drop water to scan the HR silicon prism. S_1 and S_2 are the terahertz signals from ν_1 and ν_2 double frequency modulations. The section profiles are also presented on the sides. Dots are experimental data and solid lines are Gaussian fits.

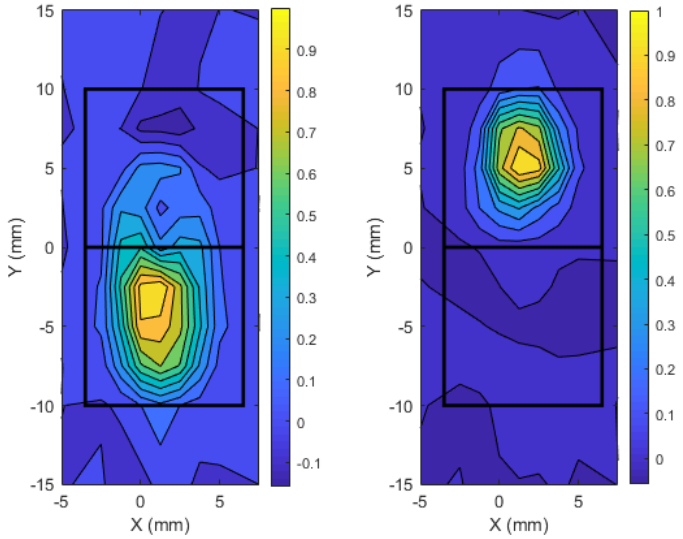

Figure 4.29: The two black squares represent the 10 by 10 mm double reservoir during experiments. The double reservoirs can be perfectly deposited in both centers of the beam profiles modulated at ν_1 and ν_2.

4.4.2 Terahertz spectroscopy of liquids

As we know, terahertz spectroscopy makes it possible to study the structural information of biomolecules (such as their conformation). Due to the high absorption of water molecules, terahertz spectroscopy has for a long time only been applied to lyophilized samples, crystalline samples, powder or thin film samples. However, the water molecule is crucial for the conformation, structure, stability, dynamics and functions of biological molecules [130, 283]. This is why water is considered as an integral and active component of biomolecules. Therefore, it is preferable to obtain more spectroscopic information of biomolecules when they are in their physiological state because their dissolution has a significant influence on their state and functions. During the last decade, many publications have attempted to measure the spectroscopic information of biomolecules in solution.

Some publications have shown that the absorption properties of a solution cannot be determined as the simple superposition of the spectroscopic properties of the solute particles and those of pure water molecules. The solute molecules studied are for example lactose [65], amino acids [284], and proteins [66, 118, 121]. It has been proposed that between the solute molecule and pure water a hydration layer is formed which contributes to the solvation properties. A 2006 publication showed that terahertz radiation can determine the size of the hydration layer of a lactose molecule, which is about 5.13 ± 0.24Å and corresponds to 123 water molecules in the hydration layer [65].

This hydration layer has been studied by different methods, including numerical simulation [285], nuclear magnetic resonance [286,287], 2D infrared spectroscopy [288] and terahertz spectroscopy [76]. The hydrated water layer has different physical properties from bulk water due to hydrophilic interactions with solute molecules [289]. In pure water, water molecules have permanent dipole moments. In solution, the dielectric loss is related to the amount of hydrated water in the terahertz frequency range. The hydrated water layer can therefore be characterized quantitatively by analyzing the decrease in dielectric loss and the change in the real part of the dielectric value. The dynamics of water molecules is discussed by analyzing the absorption of the solution corresponding to the imaginary part of the complex dielectric function.

Terahertz spectroscopy has the advantage of allowing a non-invasive study without sample preparation. TDS Terahertz is one of the most widely used techniques to obtain the dielectric properties of different solutions such as ions [84], sugar [290], peptides, and proteins [119,291]. The study of the hydration layer provides information on the vibrations of water molecules (picosecond dynamic movement) and on the thickness of this layer [65].

A terahertz absorption with a non-linear behavior as a function of the concentration of protein solutions was recorded (see figure 4.30) [125, 292]. This non-linearity could be interpreted as the overlapping effect of the hydration shells of each solute as the protein concentration increases.

A detailed model explaining the spectroscopic properties as a function of solute size has been proposed by [123], as presented in section 1.3. A clear correlation between the terahertz

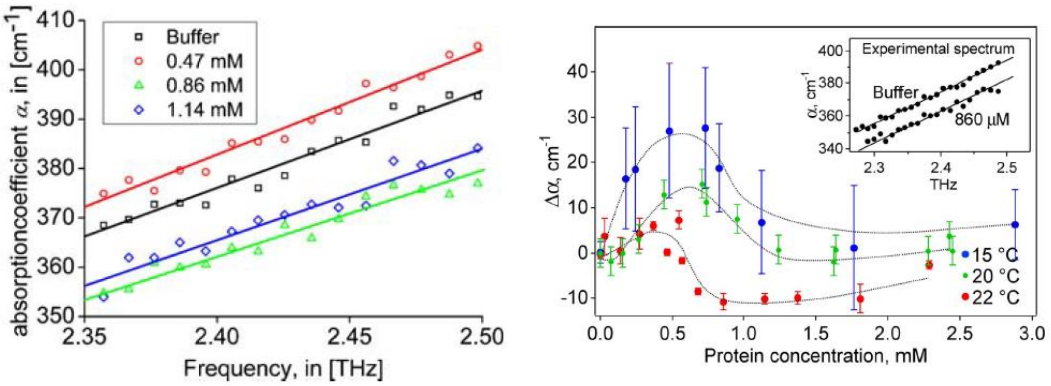

Figure 4.30: Left: Example of the absorption spectrum of lysozyme solution (14.3 kDa) from 2.35 to 2.5 THz at four concentrations. The absorption coefficient increases linearly with frequency; however, a non-linear relationship is observed with the change in concentration at each terahertz frequency [292]. Right: terahertz absorption coefficient of the 5-helix protein $\lambda^{\star}_{(6-85)}$ (14 kDa) at 2.25 THz as a function of concentration, up to 3 mM at 15°C, 20°C, and 22°C. The absorbance depends non-linearly on the concentration [125].

dielectric properties and the molar mass of the molecules is observed. However, the accuracy and resolution at low concentrations are limited. Using the QCL-ATR configuration, we should obtain a much higher accuracy.

To demonstrate the potential of our new device, we have chosen several representative solutions for QCL-ATR experiments, ranging from ions (potassium chloride, KCl), sugars (glucose, sucrose, dextran) to proteins (BSA[4]). Information on the selected molecules is presented in the table 4.3. Acquisitions are performed according to the same protocol. The ion/sugar/protein solutions were weighed on the same day and the concentration of each solution is directly calculated from the weight. Then the dilutions were made with distilled water, which is the reference of the measurements. In the case of BSA solution preparation, which is difficult to dissolve in water, especially at high concentrations, the solution is filtered to remove all suspended aggregated particles. The pore size of filters is of 0.45 µm then 0.22 µm[5]. Finally the concentration of BSA solution is analyzed by a spectrophotometer (NanoDrop^{TM} 2000c).

As presented in section 4.4.1 and by figure 4.21, a double 10 by 10 mm plastic reservoir is fixed on a plate of HR-Si. This double reservoir is placed in the region of the terahertz beam on top of the prism. Each reservoir can hold more than 500 µL of volume. The first one is placed at the center of the ν_1 modulation and the other one at ν_2. They contain respectively the studied solution and the reference (distilled water). As many measurements were carried out, the time needed to clean the reservoir and to refill it with the studied solution was not negligible. In order to reduce noise fluctuations in the long term as much as possible and to

[4]SigmaAldrich: A5253
[5]SigmaAldrich: Minisart filters 16534K

Table 4.3: List of molecules studied in order of increasing molecular size.

Molecule name	Chemical formula	Molar mass
Potassium chloride	KCl	74.5 g·mol^{-1}
Glucose	$C_6H_{12}O_6$	180.2g·mol^{-1}
Sucrose	$C_{12}H_{22}O_{11}$	342.3g·mol^{-1}
Dextran	$H(C_6H_{10}O_5)_xOH$	35kDa∼45kDa (Mass weight)
Bovin serum albumin	BSA	66.5kDa (Mass weight)

compensate for them, a reference measurement before and after each solution acquisition is necessary. Therefore, the normalized reflectivity variation ϵ (see equation 4.39) with respect to pure water and corrected by the calibration factor, is obtained from Eq. 4.41 as

$$\epsilon = \frac{1}{\beta_{IW}} \left(\frac{r_{IW}}{\bar{r}_{WW}} - 1 \right) \quad \text{with} \quad \bar{r}_{WW} = \frac{r_{WW}(\text{before}) + r_{WW}(\text{after})}{2}. \tag{4.48}$$

Then, with at least 4 measurements for each solution concentration, we obtained the mean value with the corresponding standard deviation. The lower concentrations required more measurements to improve the accuracy. Experimental results are presented on figure 4.31 for KCl ions and on figure 4.32 for sugars and albumin. For the KCl solution, a very clear linear relationship with a negative slope between the normalized reflectivity variation ϵ and the concentration of the solution can be observed from 0 to 1000mM/L with a sensitivity lower than 0.5mM/L. The slope of the linear fit is related to the dielectric constant of the KCl solution. But at very low concentrations below 4 mM/L, a non-linear relationship is observed that we are not sure to interpret (see inset graph in figure 4.31). It may come from the influence of the silicon plate on ions due to residual change in the semiconductor, or concentration uncertainties. It would need further investigation.

The results for sugar solutions are given by the figure 4.32. A globally linear behavior is observed for the three molecules with a positive slope. The detectable concentrations are less than 3 mM for glucose and sucrose and less than 2 g/L for dextran. However, they have different slope values, as suggested by the dependence of the terahertz dielectric properties with the molar mass in the three-volume model [128].

The results for the bovin serum albumin (BSA) solution are shown in figure 4.33. This time, the curve is still found as a linear relation between 0 and 2000 µM, agree with a publication that recorded a linear behavior for an albumin solution with a concentration up to 270 g/L (corresponds to 4.2 mM) [66]. However, with our experimental devices, 2 µM is detectable. A saturation behaviour is however logically expected when the protein concentration is such that the protein solvation layers overlap.

In conclusion, we had a improved sensitivity as well as higher accuracy for QCL-ATR system which means a smaller detectable concentration for all tested molecules solutions. For KCl ion solution, we can detect 0.5mM/L and for albumin protein, 2 µM is detectable. For glucose solution, the smallest concentration is 3 mM. Compared to the best results found in

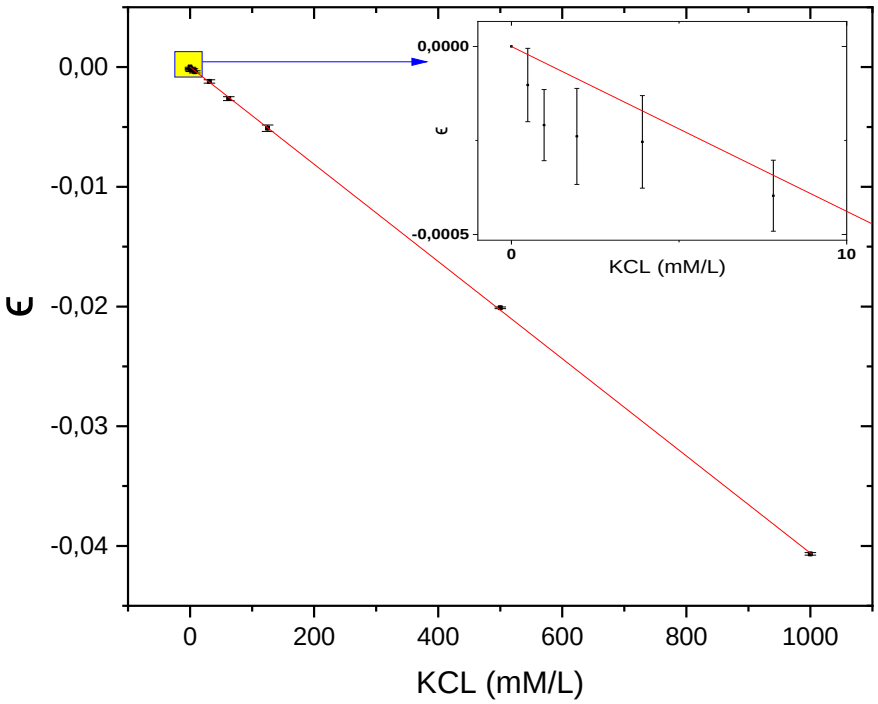

Figure 4.31: Reflectivity ϵ of the KCl solution at 2.5 THz in function of the concentration. An overall linear relationship is observed, but a non-linearity effect is observed at very low concentrations (see inset graph at concentrations below 10 mM/L).

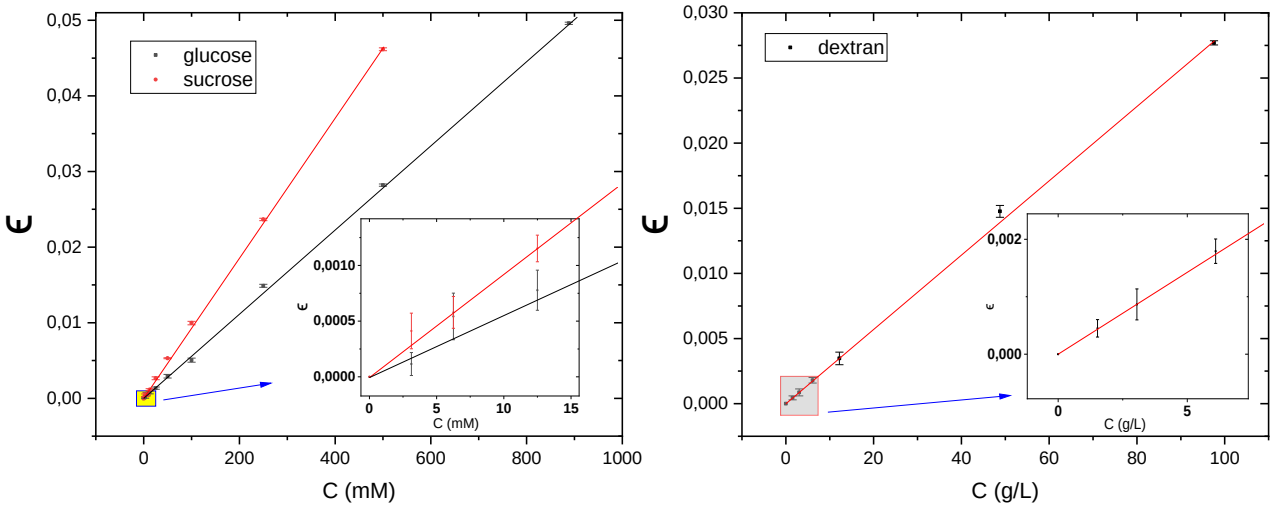

Figure 4.32: Reflectivity ϵ for the sugar family (glucose, sucrose, dextran) at 2.5THz as a function of concentration.

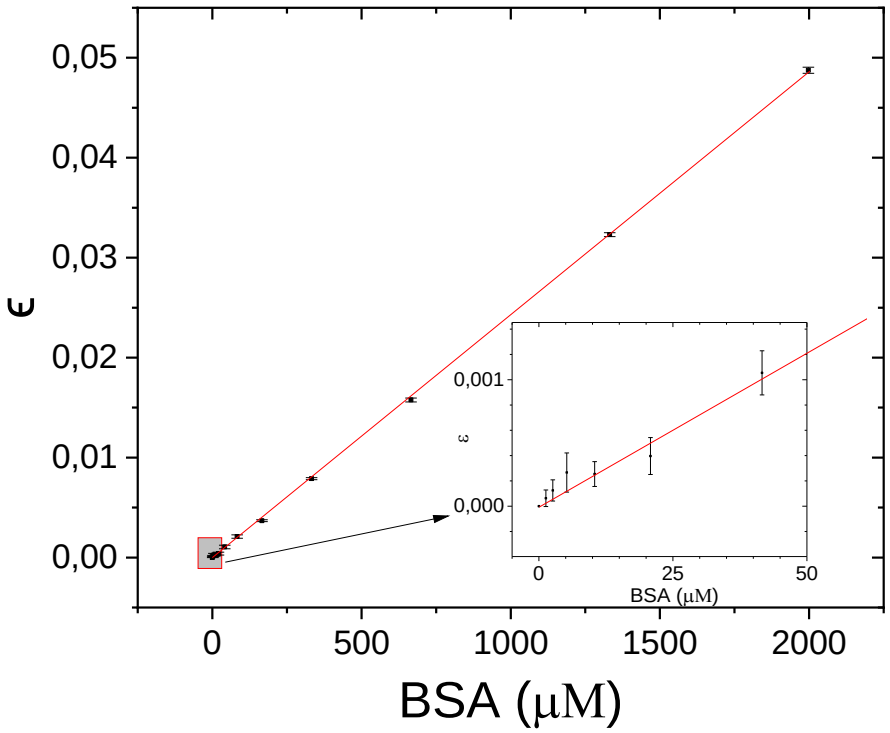

Figure 4.33: Reflectivity ϵ for BSA at 2.5 THz as a function of concentration in μM. The inset zoom graph shows the low concentrations below 50 μM.

the literature, we improved by a factor of approximate 20 in smallest detectable concentration for protein solution (≈160 μM in [66] and ≈100 μM in [125]) and by a factor of 15 for glucose solution (≈50 mM in [293]).

4.5 Investigation of chemical reversible permeabilization

As our device has demonstrated a much higher sensitivity and stability than the previous one, we now wish to verify whether it can demonstrate the reversibility of membrane permeabilization. To obtain a reversible permeabilization, the leakage of cysotol from the cells must be stopped (short-term reversibility). But the cells must also be capable of initiating repair mechanisms, and also of not dying (long-term reversibility). The first tests were carried out in [128]. However, the accuracy of the TDS-ATR setup was not sufficient to quantify short-term permeability in 20 minutes. The accuracy of the QCL-ATR device provides the ability to study membrane permeability in real time if the permeabilization is reversible in the short term (stopping the signal decrease) and in the long term (raising the terahertz signal to the initial level under appropriate living cell conditions, 37°C, 5% CO_2).

We performed experiments for short-term reversibility with the QCL-ATR system by comparing two measurements. Two samples were prepared at the same time and under the same conditions, and the acquisitions were performed sequentially over a 3-hour period after

48 hours of incubation. The first sample was exposed to a 25 µg/mL saponin solution starting at $t = 0$, and for 80 min. The second sample was also exposed to saponin solution at $t = 0$, but we removed the saponin molecules after 10 min, rinsing the liquid and replacing it with HBSS solution. These two measurements are realized at 37°C. The results are shown in figure 4.34.

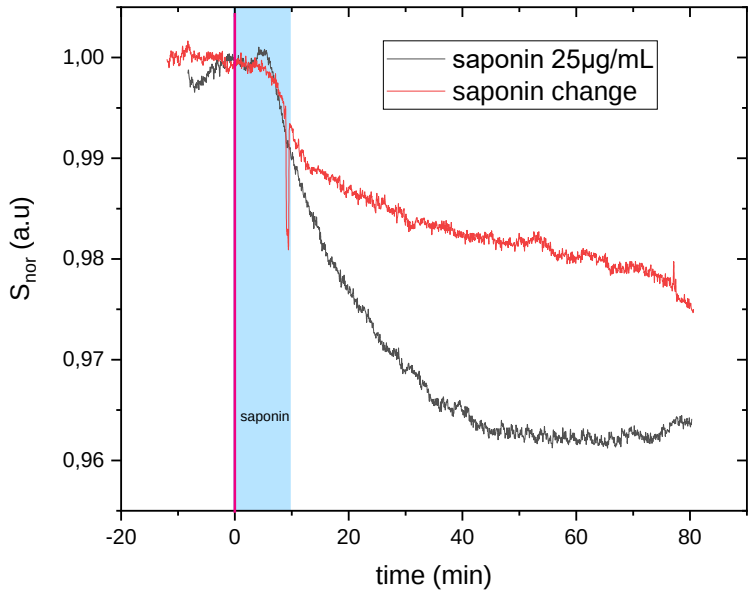

Figure 4.34: Dynamics of permeabilization of MDCK cells at 37 °C after addition of a 25 µg/mL saponin solution at $t = 0$, for a period of 80 min (black) and for 10 min then rinsed and replaced by HBSS (red). Cells are incubated for 48 hours.

We observe a clear difference between the two terahertz signals. The black curve in figure 4.34 represents the cells in the presence of saponin molecules at all times (25 µg/mL). The red curve represents cells exposed to saponin for only 10 min. Both curves are identical, within experimental errors, up to $t = 10$ min, then their behavior diverges. They show very fast dynamics, with a characteristic time of a few minutes. But after 10 min, the behaviors are very different. In the presence of saponin, the recorded dynamics continue on the same pace, whereas if the saponin is removed, the decay is strongly slowed down. This clearly indicates that by removing the saponin, the creation of defects in the cell membrane is suppressed or strongly reduced, and thus the leakage of the cytosol is slowed down. However, we do not observe any signal rise indicating a return to the physiological conditions of the cells.

To go further in this study, it is necessary to carry out the experiments in the physiological conditions of the cells for several hours, which was not the case here. Thermalization of the prism has been performed, but not yet the implantation of a real incubator. But, we can plan an experimental system with a small chamber where the cells remain at 37°C and 5 %CO_2.

4.6 Photodynamic Therapy (PDT) measurements

4.6.1 Principles of PDT

More than a hundred years ago in Munich, Oscar Raab noticed that infusoria (aquatic microorganisms) were killed by the presence of acridine orange dye combined with exposure to sunlight [294]. A few years later, von Tappeiner and Jesionek used this initial observation as the basis for the therapeutic treatment of basal cell carcinoma on a patient's skin using the combination of eosin dye and white light [295]. In addition, in Denmark, Niels Finsen discovered that exposure to red light can be used to treat smallpox pustules [296]. He also used ultraviolet light to treat cutaneous tuberculosis. This was the beginning of photodynamic therapy (PDT) in clinical treatment. In 1904, the important role of atmospheric oxygen in the phenomenon of cellular death was recognized and described as a photodynamic process [297]. Experiments to study the effect of combinations of reagents and light to find the optimal antimicrobial photosensitizers (chemicals) and wavelength range of light continued and led to standard photodynamic therapy. PDT is very prominent in medical and surgical aspects such as dermatology, gastroenterology, ophthalmology, neonatology as well as anti-viral therapy [298, 299].

PDT or photochemotherapy involve three non-toxic components (see figure 4.35). One of these components is the photosensitizer, which is a photosensitive molecule. It is delivered to the region of the target cells and/or tissues. Another component is the presence of light at a specific wavelength to activate the photosensitizers located around the target cells. The last component is oxygen that already exists in the target cells or tissues. After exposure to light under certain conditions (wavelength, exposure time, light density, etc.), the photosensitizers transfer the energy of the photons to the molecular energy of the oxygen. When photosensitizers are excited after absorbing light, they immediately interact with the molecular triplet oxygen to generate reactive oxygen species (ROS), such as singlet oxygen. These species attack all surrounding organic compounds and are therefore highly cytotoxic to cells. In addition, cell death induced by necrosis or apoptosis occurs only in the particular region that has been exposed to light. The key points of PDT are the ability to focus the light on the precise area, the ability to differentiate the concentration of potosensitizers between healthy and tumor tissues [300] and the type of photosensitizers.

Challenges for PDT development include details on the routes of photosensitizer delivery to infected tissue, photosensitizer selectivity and collateral damage to target tissue [301]. Many photosensitizers are amphiphilic or hydrophobic compounds, which have the ability to self-assemble in aqueous media. The transport system for water-insoluble photosensitizers is therefore important. One transport system is the use of liposomes consisting of several layers of low molecular weight surfactants. Liposomes release photosensitizers through the rapid exchange of lipids. However, in some cases the assembly of liposomes is too stable to release all photosensitizers [302]. Another medium for delivering photosensitizers is based on silica nanoparticles [303]. The photosensitizers can simply be trapped inside the nanoparticles

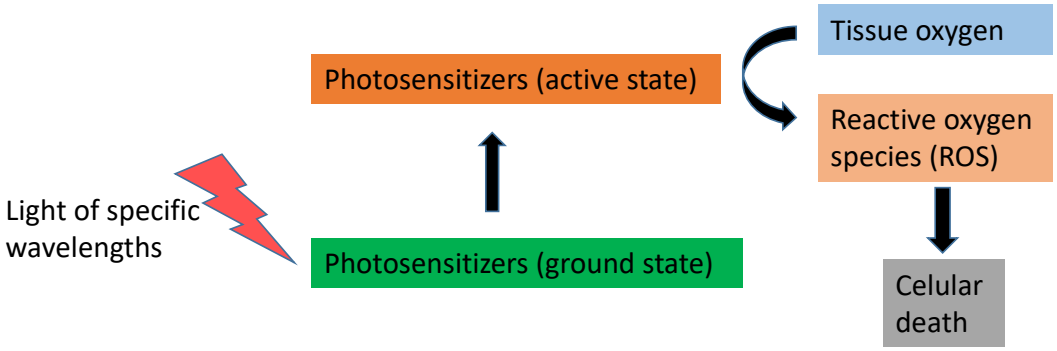

Figure 4.35: The PDT mechanism consists of three elements: light, photosensitizers and oxygen. When photosensitizers are exposed to light at specific wavelengths, they change from a ground state to an excited state. The active state of the photosensitizers transfers energy to oxygen and then induces the generation of ROS. These ROS molecules trigger cell death.

which have a porous structure. But one of the drawbacks of silica nanoparticles is the problem of their degradation in cells.

The last delivery system we will develop later is to use polymeric vectors to encapsulate the photosensitizers to effectively prevent them from interacting in a harmful way with the external environment. Studies on phthalocyanine ($C_{32}H_{18}N_8$) delivered by polyionic complex micelles have been published [304, 305]. In addition, delivery of porphyrin ($C_{20}H_{14}N_4$) also by polyionic complex micelles has been published [306, 307]. Polymeric micelles have reduced toxicity and side effects.

More than 400 types of photosensitizers are known to date, including dyes (such as acridine orange, proflavin, fluorescein, eosin), drugs, chemicals, etc [308]. Photosensitizers must have important success factors such as solubility, selectivity for the use of PDT [309–311]. The photosensitizer should also have low toxicity. The structure should be stable in an aqueous medium. In addition, the photosensitizer should be rapidly excreted from the body after treatment. To improve efficiency, the photosensitizer must have a high absorption coefficient at its specific wavelength. Chemically, photosensitizers are classified into five main groups: porphyrin derivatives, chlorins, pheophorbides, phthalocyanines and porphycenes [312,313]. Photofrin (porfimer sodium) is a derivative of hematoporphyrin, which is a mixture of monomeric, dimeric and oligomeric structures (see figure 4.36), which has the maximum absorption coefficient at wavelength 630 nm ($3000\,M^{-1}\,cm^{-1}$). Chlorins are generally not soluble in water and the basic structure is similar to that of photofrin but has differences in its two additional hydrogens of the pyrrole ring. Chlorins absorb light in the wavelength range of 640 to 700 nm [314]. Pheophorbides also have two additional hydrogens in a pyrrole unit, which is an effective photosensitizer due to its monomeric form [315]. A clinical trial has used pheophorbide to treat prostate cancer [316]. The structure of phthalocyanines involves the formation of metal complexes with high absorption in the far red range.

The encapsulation of photosensitizers within polymeric nanovectors (carriers) should

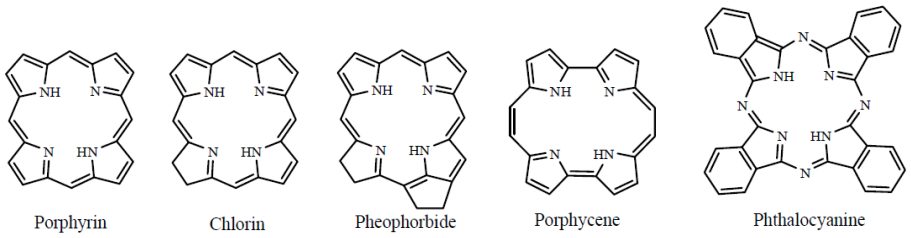

Figure 4.36: Structures of five main photosensitizers: porphyrin, chlorins, pheophorbides, porphycenes and phtalocyanines.

overcome undesirable pharmacokinetic properties, such as improved aqueous solubility. Two methods are mainly envisaged for selective drug delivery. One is the use of targeting components in transporters [317–319]. Another is based on the discovery of enhanced vascular permeability and retention (EPR) [319–321]. The EPR effect indicates that large molecules with a molecular weight greater than 40 kDa accumulate more in tumor tissue than in normal tissue. This is due to the fact that disjunctions, which are found between the endothelial cells of the blood vessels close to the tumor areas and the severely limited lymphatic system of the tumors, prevent the rapid elimination of carriers. For this reason, carriers with photosensitizers are able to spontaneously accumulate in tumor areas.

During our experiments, in collaboration with Anne-Françoise Mingotaud's group at the IMRCP laboratory (Laboratoire des Interactions Moléculaires et Réactivité Chimique et Photochimique - équipe IdeAS) in Toulouse, the photosensitizer chosen was pheophorbide-a[6] (Pheo, $C_{35}H_{36}N_4O_5$), which is a chlorophyll degradation product of green plant cells (a Chinese medicinal herb Scutellaria Barbata) with an antitumor effect. Pheo has been shown to act as a photosensitizer to induce inhibitory effects on Hep3B cells of human hepatocellular carcinoma, with in vitro efficacy [322]. Therefore, we used this approved photosensitizer, loaded in poly (ethylene oxide)-block-poly(ϵ-caprolactone) (PEO-PCL) polymeric micelles in our study on MDCK cells.

The copolymer micelles, used in our laboratory and sent by our collaborators in Toulouse, were formed by PEO-PCL micelles. The size of PEO-PCL molecules is about 30 nm. The loading of the copolymer micelles with pheophorbid was performed by adding Pheo in acetone solution, dropwise in a PBS solution. The molar ratio of Pheo to copolymer is 1/30 in order to solubilize as much as possible Pheo in the hydrophobic center of the copolymer micelles [323, 324].

The principle for confirming that Pheo is well loaded in the PEO-PCL micelle vectors is to check the intensity of the fluorescence. When Pheo is dissolved in an acetone solution in a monomeric form, the fluorescence is weak [315]. Then, as the number of copolymer micelle molecules increases, the intensity of fluorescence will increase because the Pheo molecules enter the hydrophobic center of the micelles. Therefore, the absorbance spectrum of the Pheo

[6](3S,4S)-9-Ethenyl-14-ethyl-21-(methoxycarbonyl)-4,8,13,18-tetramethyl-20-oxo-3-phorbinepropanoic acid.

loaded in PEO-PCL (Pheo-PEO-PCL) is similar to that of the organic solution [325].

Although the processes of transfer of Pheo from the micelle to the cell membrane and the cellular processes of internalization of photosensitizers are not yet fully known, the ability of the photosensitizer to cross the cell membrane would depend on the difference in affinity between the copolymer and the plasma membrane. The presence of copolymer micelles does not a priori affect the thermodynamics of Pheo transfer to artificial lipid membranes. Different hypotheses are proposed: mass transfer pathway between vector micelles and cells [325] ; endocytosis mechanisms helping to transfer pheophorbide-a [326]; direct transfer of pheophorbide from micelle vectors to the cell membrane [326, 327].

In addition, ROS after light irradiation is considered to have the potential to diffuse to nearby target cells and then oxidize them because ROS has a sufficient lifetime (6.4 to 16 µs) [328]. In practice, the complete mechanism is likely to be a mixture of these different mechanisms.

4.6.2 Experimental conditions

To check the efficacy of PDT, a viability test is required. The viability process is as follows. MDCK cells are seeded in a 96-well plate and incubated for 48 hours. On the day of the experiment, the cells are in contact with different solutions including PEO-PCL micelles alone, loaded PEO-PCL micelles, free Pheo molecules and PBS for control, and then the cells are incubated again for 30 minutes at 37°C. After incubation, the 96-well plate is exposed to a LED lampe with a broad white spectrum with an energy of 20 W. The duration of light irradiation of the cells is 4 min in total (2 min light on, 2 min light off and 2 min light on). At the end of the LED exposure, the 96-well plate is put back into incubation and continues to have 24 h incubation at 37°C. At the end of the incubation, PrestoBlue reagent solution (Invitrogen, Carlsbad, CA, USA) is used to determine the viability of the cells and read on a plate reader.

However, the PrestoBlue viability measurements do not provide any information on the leakage dynamics during the 24 hours after the LEDs are illuminated. We now present the experimental results obtained with our new QCL-ATR device.

To realize the lighting of PDT experiments with our QCL-ATR experiment, a LED lamp (20 W) is installed 40 mm above the prism. The MDCK cells are seeded on a 3-mm-thick HR silicon window and are incubated for 48 hours according to the protocol in appendix B. We put the window in close contact with the prism using 5 µL of α-pinene (P45702, Sigma-Aldrich, see section 4.3.5.5) to ensure optical continuity, then we start the measurements. For an experiment, one of the following solutions is added: empty PEO-PCL micelles, Pheo-PEO-PCL micelles, free Pheo molecules or PBS for control. We respect the protocol established by the Toulouse team. 30 min are necessary to ensure the diffusion of the added molecules. After these 30 min, the cells are exposed to the same lamp as the Toulouse group (LED lamp with an energy of 20 W) with the same lighting time (2 min on, 2 min off then 2 min on). During the experiment, the prism and the liquid solution with the cells remain at 37°C.

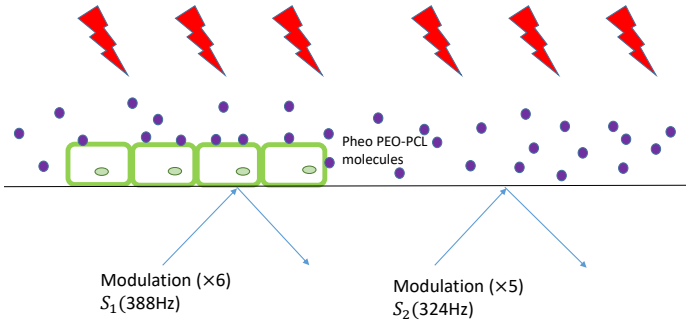

Figure 4.37: Scheme of the ATR prism with monolayer cells and pheophorbide-loaded micelles under light irradiation.

The experimental scheme with a monolayer of cells on the silicon plate is presented in figure 4.37. The extracellular medium is hanks' balanced salt solution (HBSS) with a volume of 2.2 mL corresponding to a height of 3 mm, which is the same condition as in Toulouse to ensure the same diffusion times of different molecules. The R signal is always calculated by the ratio of the two modulation zones, the zone with cells and the reference zone without cells. One notes $t = 0$ the moment when the irradiation is stopped. Thus, the normalized signal S_{nor} is noted as

$$S_{\text{nor}} = \frac{R(t)}{R(t=0)}. \tag{4.49}$$

Measurements last 60 to 80 minutes after the LED lighting is turned off. At the end of the experiment, the cell layer is scraped to check the state of the cell layer and determine the absolute signal level.

4.6.3 Preliminary experimental results on PDT with QCL-ATR

A first result of the leakage dynamics using Pheo-PEO-PCL solution with LED irradiation (MPL) and without LED irradiation (MP) is presented in the figure 4.38. Two cell layer samples were seeded under the same conditions and the experimental acquisitions were made one after the other with only 3h delay. We can therefore consider that the cell layer remains in the same condition. Normalization to a value of 1 is done at $t = 0$. We observe first of all that the two dynamics are the same before irradiation. At $t = -2160$ s, we added Pheo-PEO-PCL at a concentration of 3.3 µM. There is a slight decrease in the terahertz signal (see the pink area in figure 4.38), probably due to the change in the dielectric constant when mixing HBSS with the Pheo-PEO-PCL solution. A thermal effect is also possible because these first results were realized before we stabilized the temperature of the prism as introduced in 4.3.5.4. After 30 min of stabilization, we illuminate one sample and keep the second sample in the dark. For the sample under light irradiation, we observe a discontinuity artifact due to a well known photoelectric effect in silicon, the same as used in our attempts to measure the beam profile (see section 4.4.1). The time $t = 0$ has been defined as the moment of the irradiation stop.

Then, after the LED illumination, we observe a very clear decrease of the signal over 40-50 min, compared to the sample without LED illumination, which does not show any significant variation. At the end, the cell layer is scraped to verify that the cells were still in contact with the prism during the experiments. This also allows the terahertz measurement to be quantified in absolute value. We can notice that the signal level after scraping in the same for both experiments, which shows that both samples were equivalent.

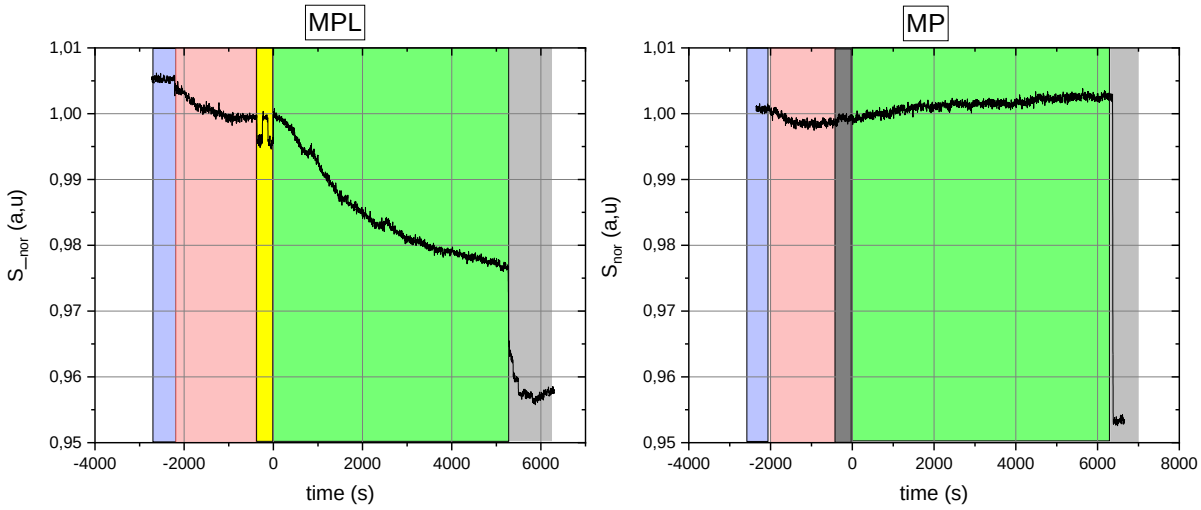

Figure 4.38: Dynamics of membrane permeability after the addition of Pheo-PEC-PCL (C=3.3 µM) with LED irradiation (left) and without LED irradiation (right). $t < -2160$ s: cell surrounded by HBSS (light blue zone); $t = -2160$ s: addition of Pheo-PEC-PCL solution then wait 30 min to stabilize the molecules diffusion (pink zone); $t = -180$ s, start 20 W LED irradiation: 2 min irradiation + 2 min dark + 2 min irradiation (yellow zone in left) or 6 min in dark (gray zone in right); $t > 0$: PDT dynamics inverstigation during more than one hour (green zone); scraping of the cell layer (light gray zone).

This observed decrease in signal after illumination with Pheo-PEC-PCL at a concentration of 3.3 µM is fundamentally related to membrane permeability. Once the Pheo is activated, the ROS (see section 4.6.1) start to diffuse at the cell level. Thus, the decrease of the signal in the cell area provides information on cytosol leakage. The seemingly exponential decrease may be due to an output of molecules in constant number or to an output of proteins of increasing mass if the pore size increases over time. This decrease can also be understood by the progressive exit of larger and larger proteins, despite a general slowdown in the number of molecules passing through the membrane. These encouraging results will allow us to study the dynamics of the membrane permeability by PDT with QCL-ATR.

During the first trial measurements, we realized that it is important to carry out these experiments under conditions that are as identical as possible, especially with regard to sample preparation. As we cannot run the experiments simultaneously, the series of measurements must be performed on the same cell subculture. In particular, we observed the effect of the

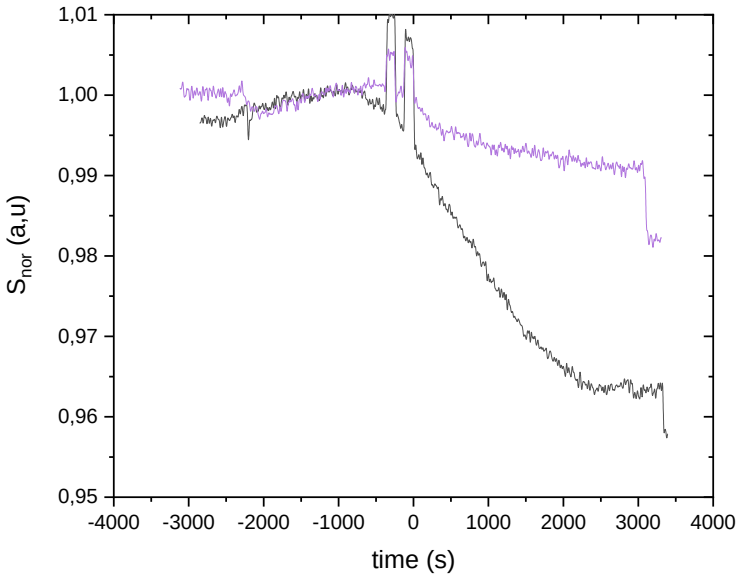

Figure 4.39: Dynamics of membrane permeability at MPL condition on the same seeding series but with different incubation times: 45.5 h (purple), 65.5 h (black).

confluence state of the cells. The incubation time of the cells leads to a difference in the characteristics of the cell layer. An example is given for two different confluence states (figure 4.39). The two samples come from the same seeding series while the incubation times are different. Acquisitions are performed in a delay of 20 hours, with the same concentration of Pheo-PEC-PCL solution at 3.3 µM. Even if this result is one of the most extreme obtained during our measurements, it shows a strong impact of the confluence, both on the dynamics and on the amplitude of the terahertz signal. This difference may be due to the thickness of the cell layer. After 65.5 h of incubation, the cell layer was probably significantly denser than at 45.5 h. For example, the cell layer shows an intrinsic contrast modified from 1.5 to 4% compared to the medium alone when the cell layer was simply removed and the medium was renewed, corresponding to a thicker layer at 65.5 hours.

As previously mentioned, this PDT study is a project in close collaboration with the IMRCP group in Toulouse. Therefore, we have chosen the same cell seeding concentration at 31250 cells/cm^2 and the same Pheo-PEC-PCL and free Pheo concentration at 1.65 µM. These concentrations were decided from a primary assay (see figure 4.40), where the action of Pheo-PEC-PCL and free Pheo have the greatest difference for MDCK1[7] cells. As mentioned in section 4.6.2, cell viability is an important parameter which quantify the number of live cells (usually expressed as a percentage of control) to analyze the efficiency of Pheo-PEO-PCL and free Pheo molecules. In figure 4.40, we observed clearly that the cell viability decreases with the increase of Pheo concentration in Pheo-PEO-PCL as well as free Pheo. However, more MDCK1 cells remain alive with free Pheo than with Pheo-PEO-PCL when the Pheo

[7]MDCK1 cells are derived from a line obtained from a different supplier than MDCK cells, but have the same characteristics. Here, MDCK1 cells are subcultured from the IMRCP group cells.

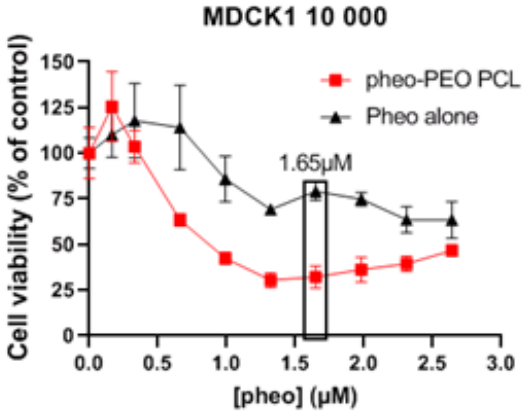

Figure 4.40: The viability of MDCK1 cells versus the doses of free Pheo (black) and Pheo loaded in PEO-PCL micelles (red) with LED irradiation. The viability was measured after 24-hour addition of free Pheo or Pheo-PEO-PCL solution.

concentration is higher than 0.5 µM after 24 hours incubation. A concentration of 1.65 µM was chosen to maximize the effect of encapsulation.

4.6.4 Main PDT results and discussion

4.6.4.1 Comparison of photosensitizers' dynamics

We now present a series of experiments with the same seeding concentration (31250 cells/cm^2) and almost the same incubation time (48h±5h) but with different solutions and different irradiation conditions including the addition of empty PEO-PCL micelles solution without LED irradiation (M) and with LED irradiation (ML), the addition of Pheo-PEO-PCL solution without LED irradiation (MP) and with LED irradiation (MPL), the addition of free Pheo solution without LED irradiation (P) and with LED irradiation (PL), the addition of HBSS solution without LED irradiation (Cell) and with LED irradaition (L). All measurements were performed at 37°C. The results are presented in figure 4.41. The value $R_{\text{nor}}(t)$ is given by

$$R_{\text{nor}}(t) = \frac{R(t) - R(t=\infty)}{1 - R(t=\infty)}. \tag{4.50}$$

In all curves, we observe the same flat signal before illumination, indicating no membrane permeation activity. A discontinuity always appears at the moment of light irradiation between $t = -360\,\text{s}$ and $0\,\text{s}$. This measurement artifact can vary greatly from one measurement to another, and can be greater or less than 1 depending on the exact position of the sample on the ATR prime, with respect to the two modulation areas ν_1 and ν_2. The discontinuity comes from the photoelectric effect in silicon, and more precisely from the difference of two large signals coming from the two zones. As these two contributions more or less compensate each other, the final value can be higher or lower than the reference signal. At $t > 0$, the R_{nor}

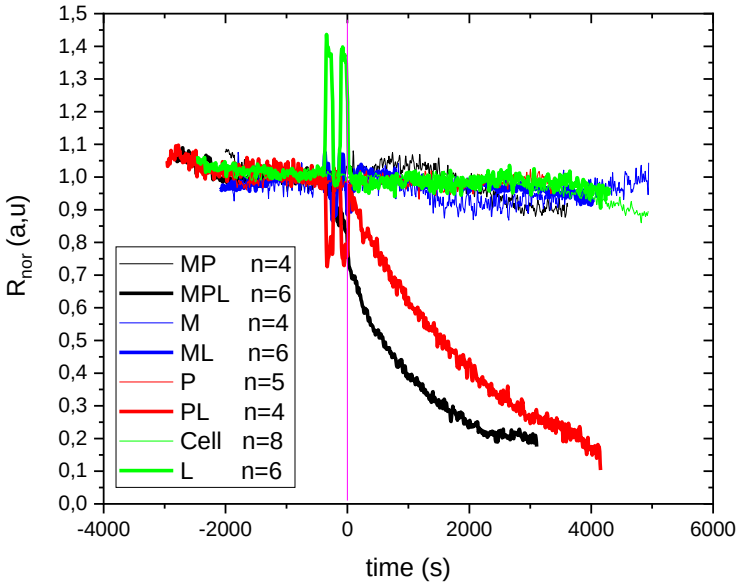

Figure 4.41: QCL-ATR experiments of PDT with different treatment conditions. The solutions are composed of the following molecules: micelles (M) and/or pheophorbide-a (P). If existing, the illumination (L) is done by LED. "Cell" are measurements with only HBSS and no light. All concentrations are 1.65 µM. The end of illumination corresponds to t=0 (vertical pink line). The average value is taken from n equivalent experiments.

values remain unchanged in most configurations except after the addition of Pheo-PEO-PCL or free Pheo, and always with irradiation.

A similar decrease of R_{nor} can be found with MPL and PL, but the latter has a clearly slower dynamics, and with a delay of a few minutes. This difference is probably due to the efficiency of Pheo. Furthermore, the signal decay slope is significantly greater at $t > 0$ for MPL compared to PL. This slope indicates the leakage rate of the cytosol and of the extracellular solution. Afterwards, both curves show a plateau, after 2000 s for MPL, and after more than 4000 s for PL.

These results confirm those obtained in cell viability (figure 4.40). The permeabilizing action of Pheo-PEO-PCL is clearly more effective than free Pheo. The results therefore suggest that PEO-PCL micelles can lead to a greater efficiency of photosensitizer activity. But unlike viability measurements, QCL-ATR measurements provide a real-time measurement of cellular permeabilization.

4.6.4.2 Variation of photosensitizers concentration

To quantify the influence of the concentration of active molecules, we measured the dynamics with different concentrations of Pheo-PEO-PCL and free Pheo, at 0.33 µM, 0.99 µM and 1.65 µM with irradiation. For PL (figure 4.42 right), the dynamics of R_{nor} are very different when going from a concentration of 0.33 µM to concentrations of 0.99 µM or 1.65 µM.

A higher concentration gives a faster activity. However, the same dynamics is observed at 0.99µM and 1.65 µM, which may be due to a saturation effect of Pheo at the cell level. This point needs to be studied in more detail.

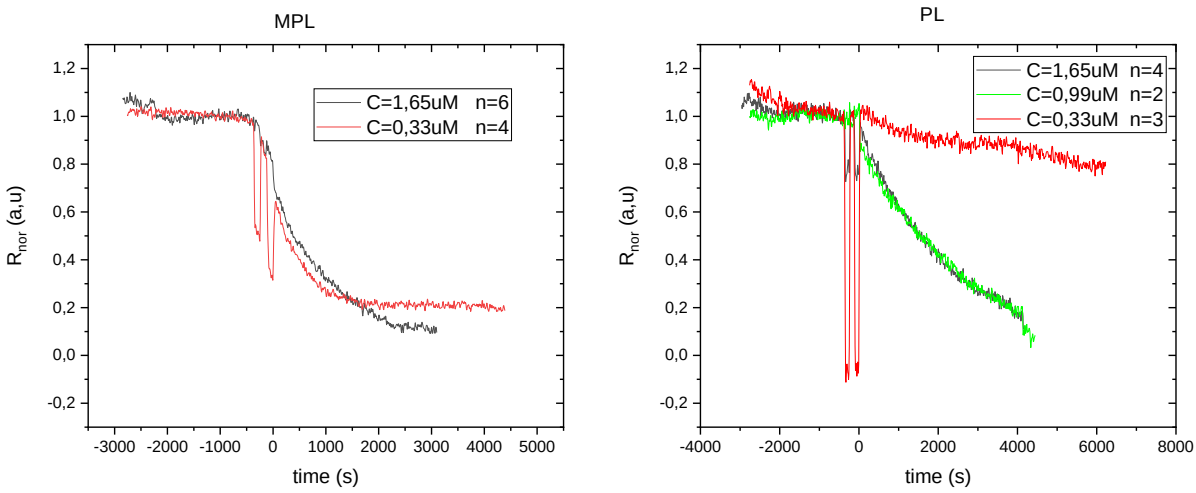

Figure 4.42: Comparison of different concentrations of Pheo-PEO-PCL and free Pheo with irradiation. Left: MPL (1.65 µM (black), 0.33 µM (red)); Right PL (1.65 µM (black), 0.99 µM (green), 0.33 µM (red)).

At MPL condition, the dynamics of R_{nor} are relatively identical when we compare the curves at 0.33 µM and 1.65 µM (figure 4.42 left). Membrane activities are therefore at first sight seemingly apparent this time, unlike PL. It thus seems that the improvement of efficiency by micelles, already observed in figure 4.40, occurs for lower concentrations than PL. Lower concentrations must therefore be tested to confirm the existence of a threshold of cell membrane permeability.

To quantify more precisely the action of the free Pheo and Pheo-PEO-PCL solutions, we calculated the time constant t_1 by fitting the curves with an experiential decay function as follows

$$R_{\text{nor}}(t) = R_0 + A_1 e^{-t/t_1}. \tag{4.51}$$

The time constant t_1 is a time parameter indicating when R_{nor} reduces to R_{nor}/e. It also represents the efficiency rate of short-term membrane activation. The smaller the value of t_1, the faster the activation of the membrane, so the more efficient the photosensitizers are at disrupting the membrane. The result of the fits is given in figure 4.43. For the same concentration (4.43 left), we observe that MPL has always values t_1 smaller than with PL. This indicates that the disturbance by MPL is faster than by PL for the same concentration whether at 0.33 or 1.65 µM. A first hypothesis is that MPL molecules have a higher probability of binding to the membrane. Another hypothesis is that PML creates larger pores in the membrane so that molecules come out faster and for larger sizes.

In addition, we observe that t_1 decreases with increasing PL concentrations (figure 4.43 right), most likely by the increase in the number and size of the pores generated. The existence of a plateau for the PL experiments is the hint of an optimal concentration, which makes it possible to maximize the effect while limiting the number of molecules. Since the plateau is already obtained in the two MPL experiments, no clear conclusion can be deduced for MPL.

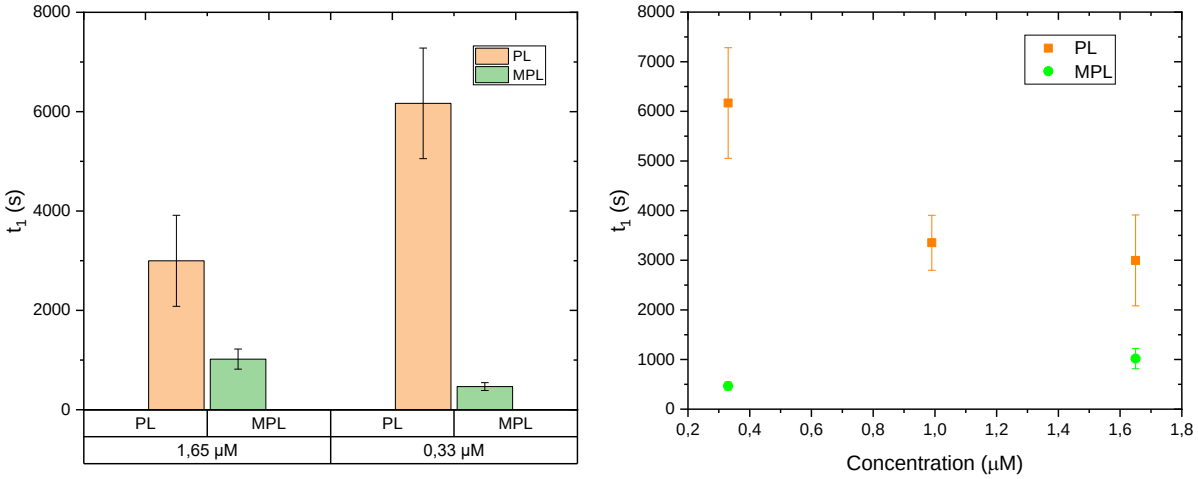

Figure 4.43: Left: Bar graph of fitting parameter t_1 for two concentrations (0.33 µM and 1.65 µM for Pheo-PEO-PCL (green) and free Pheo (orange) with irradiation. Right: t_1 parameter in function of the concentration of PL (orange) and PML (green).

We observed that the 24-hour viability test to estimate membrane permeability does not differentiate at 0.33 µM between MPL and PL (see figure 4.40). On the other hand, our method can detect a significant difference between these two solutions, in terms of membrane permeability in the short term (a few minutes after the addition of the solution).

Thus, our QCL-ATR system offers very interesting possibilities for PDT studies. We show greater sensitivity at lower concentrations than by 24-hour viability. In addition, our method provides results from the first minutes of measurement, and can follow the behavior of cells in real time over several hours.

4.7 Conclusion

In this chapter, we present a new terahertz ATR system based on a quantum cascade laser (QCL). The most important principle is the use of a dual modulation of the terahertz beam, in a geometry simplified to the maximum using only one ATR prism and one detector. The dual modulation is performed with a mechanical modulator that chops half of the beam at frequency ×6, and the other half at frequency ×5, with the same master frequency. It makes it possible to modulate two separate areas at the same time on the ATR prism. The TDS-ATR system required the movement of the sample holder to allow the evanescent wave

to reach the reference area and the cell area, which added significant mechanical noise. In contrast, the QCL-ATR dual modulation system eliminates this displacement, which speeds up the measurement. Finally, we obtained very good performances: SNR > 30dB (300 ms), and 30dB more than one hour.

Next, we calibrated the QCL-ATR system by measuring the profile of the beam in contact with the samples on the ATR prism. We found that the measurement of the profile with a light spot was not possible because it was too inaccurate due to the diffusion in the HR silicon prism, leading to a strong degradation of the spatial resolution. The measurement was made possible using small drops of water successively deposited on the prism surface. A simple model of the method of measurement allowed the calibration of the device, which was necessary because of the spread of the two modulations and their partial superposition. Calibration is then possible either by reflection measurements of liquid water in a double tank, or directly from the measured profiles. Both methods provide us with the same correction coefficient, taking into account the uncertainties. We thus obtain an instrument of high sensitivity and stability, allowing quantitative measurements after calibration [329].

This sensitivity has been demonstrated on solutions of solutes of biological interest (KCl, sugars and proteins). We searched for the evolution of the ATR signal as a function of the concentration, as well as the smallest detectable concentration. Our results represent an improvement by one to two orders of magnitude compared to the best measurements in the literature. We thus obtain lower detectable concentrations with better precision for all the solutions tested.

We have used the accuracy of this new instrument to study the effect of PDT on membrane permeabilization, in collaboration with the IMRCP laboratory in Toulouse. Very promising results have already been obtained during this thesis work [330]. We have shown that the variation of the terahertz contrast signal R_{nor} allows to study very precisely the variation of the membrane permeabilization. With different membrane permeabilization agents (photosensitizers, vectors, photosensitizers loaded in vectors), we have been able to quantify the efficiency of these molecules on the membrane activity. We found that encapsulation of photosensitizing molecules in vectors (micelles) significantly increases the efficiency of permeabilization. We obtain results in overall agreement with the viability measurements performed in Toulouse, but with a much better sensitivity. For example, we measure a clear improvement in efficiency due to encapsulation for a concentration of 0.33 µM, whereas no difference is visible by viability at 24 hours. Moreover, our measurements already show effects at short times (a few minutes) whereas one has to wait one day for viability measurements. These measurements are therefore very promising and should be continued further to quantify the effects of concentrations and illumination times for example.

General conclusion

In the first chapter, after having given an overview of the characteristics and possibilities of the electromagnetic field in the terahertz domain, we focused particularly on terahertz spectroscopy in the time domain. Using femtosecond pulsed lasers, it offers a particularly interesting approach for the study of the interactions between terahertz radiation and matter. We described the principle of operation of these spectroscopy systems in the time domain, and presented typical applications in the terahertz domain ranging from physics to biology. In the field of biology, which is of particular interest to us here, the terahertz range makes it possible to quantify and discriminate solutes of biological interest thanks to the interaction with the low frequency modes of liquid water, and thus to study biomolecules, microorganisms and cells in their physiological environment. This is the main motivation of our team to use terahertz radiation as a tool for investigating living cells. We have also described a model of interaction between terahertz radiation and biological liquids that allows us to better understand the measurements performed.

In chapter 2, we reviewed the structure of mammalian cell membrane, as well as the main mechanical and biochemical mechanisms of membrane disruption. Particular emphasis was placed on the use of a detergent, saponin, to modify the permeability of the cell membrane in a controlled manner. We also presented different methods for probing cell permeability. Exclusive methods using dyes are harmful to living cells and do not allow quantification. Destructive quantitative methods such as BCA tests are also harmful to living cells. We then demonstrated that the terahertz ATR technique offers particularly interesting possibilities to quantify in real time the dynamics of cell permeability without disturbing the functioning of the cellular mechanism.

In Chapter 3, we described our own experimental system of terahertz spectroscopy in the time domain, based on an attenuated total reflectance prism. An analysis of the performance of the system was then given. The key point is the coupling of a layer of living cells with the longitudinal extension of the evanescent field produced at the top of the prism. We first studied the influence of the flatness of the silicon elements (prism and support) and showed the need for a very strict control of the surface state. By choosing the best supports, this allowed us a better reproducibility of the experiments. Taking advantage of these improvements, we undertook a large study of the effect of saponin on the membrane permeabilization of MDCK cells. The dynamics of the terahertz ATR signal after permeabilization was recorded over a wide range of saponin concentrations and shows a strong concentration dependence. To

analyze these results, we developed an analytical model taking into account the diffusion of saponin molecules, as well as the physical parameters of the cell membrane and cytosol. The competition between overlapping of the pores and molecular diffusion was also investigated. The results showed surprisingly that the chemical permeability is controlled mainly by the diffusion of the detergent molecules and that the size of the generated pores remains constant during the 2 hours following the addition of saponin.

In the last chapter, we developed a totally new device, based on a continuous terahertz QCL source at 2.5 THz. This new instrument is based on a very simplified design, with a single ATR prism and a single detector, and on a double modulation of the terahertz beam using a mechanical chopper. This chopper synchronizes by construction the double modulation defining the measurement and reference zones. The long-term stability of this device has been greatly improved also by the precise control of temperature and humidity inside the device. The performance is excellent both in the short term and long term. A signal-to-noise ratio of 30 dB is achieved over 300 ms, 40 dB over 30 s and it remains above 30 dB for several hours. In addition, a theoretical and experimental study has allowed the calibration of the instrument. Thus, the ATR reflection coefficients of several solutions of biological interest (ions, sugars and proteins) were obtained over a wide range of concentrations. In particular, a sensitivity at least 20 times higher than that of existing literature was obtained. For the albumin solution, 5 µM are thus easily detectable. Thanks to this new high-performance system, we studied the dynamics of membrane permeabilization following the action of photodynamic therapy (PDT). The first results showed that the encapsulation of photosensitizers by micellar vectors significantly improves the efficiency of PDT. These results are very encouraging and should be continued.

Publications and conferences

Papers

- Zheng Xiujun, and Guilhem Gallot. "Dynamics of Cell Membrane Permeabilization by Saponins Using Terahertz Attenuated Total Reflection." Biophysical Journal 119.4 (2020): 749-755.

- Zheng Xiujun, and Guilhem Gallot. "High precision, high stability, dual modulation terahertz ATR sensor" In preparation.

- Zheng Xiujun, and Guilhem Gallot, et al. "PDT investigating on living cells using terahertz ATR sensing." In preparation.

Proceeding

- Gallot Guilhem, Zheng Xiujun, et al. "Probing living cells by terahertz attenuated total reflection. Application to permeabilization dynamics." SPIE Proceedings (Optical Society of America, 2019), paper 11075_13.

Conferences

- VPH (Virtual Physiological Human) 2020 online, August, 2020.

- IRMMW-THz, 44th International Conference on Infrared, Millimeter, and Terahertz Waves Paris, France, September 2019.

- Lasers and Electro-Optics Europe and European Quantum Electronics Conference, Munich, Germany, June 2019.

- European Conference on Biomedical Optics, Munich, Germany, June 2019.

- German Terahertz THz conference, Kaiserslautern, Germany, April, 2019.

- OptDiag 2018, Paris, France, May 2018.

Appendix A

Protocol of MDCK cells sub-culture

Material

- 10 mL minimum of complete medium: DMEM (Dulbecco's Modified Eagle Medium, ThermoFisher: 61965026) +10% FBS (fetal bovin serum, ThermoFisher: 10500064) +1% penicillin-streptomycin (ThermoFisher: 15140122)
- 4 mL penicillin-streptomycin (ThermoFisher: 15140122)
- 1 mL trypsin-EDTA (ThermoFisher: R001100)
- 6 mL PBS (Phosphate Buffer Saline, ThermoFisher: 20012019)
- 1 T-25 flask
- 1 Falcon tube(15 or 50 mL)

Operating procedure

- Empty the used medium of the T-25 flask containing the confluent cells.
- Rinse the cell surface by aspirations/returns of 6 mL PBS.
- Empty PBS into the trash.
- Add 1mL trypsin-EDTA into the T-25 containing the cells, swing slightly to make sure all the cell surface contacts with trypsin-EDTA.
- Empty trypsin-EDTA, then close the T-25, and put in the incubator for 7 ($\pm$1) min.
- Check the cell layer state using microscopy (cells should be round), and hit the box against a hard surface to help detach the cells.
- Add 3mL of complete medium to gently re-suspend the cells. The cell concentration (with a Malassez counting chamber) after this step is approximate 1$\sim$5$\times 10^6$ cells/mL.
- Take the required volume (see Table A.1) and add to a new T-25 flask.

- Add 7 mL of complete medium then close the flask. Note the name of the cells, date of sub culture, volume, and number of sub culture.
- Put the new T-25 in the incubator and change the medium every 48 hours.

Remarks

The concentration of cells in 3 mL of medium varies from one time to another. Cells having a concentration higher than 8×10^6 cells/mL should not be used. As well, MDCK cells with a number of sub culture higher than 15 should not be used anymore.

Table A.1: The needed volume from 3mL medium with suspending cells and the confluent days

Volume from 3mL medium with suspending cells	Confluent days
6 μL	1 week
300 μL	3 days
1 mL	1 day

Appendix B

Protocol of seeding MDCK cells on the silicon window

Material

- 10 mL minimum of complete medium: DMEM (Dulbecco's Modified Eagle Medium, ThermoFisher: 61965026) +10% FBS (fetal bovin serum,ThermoFisher: 10500064) +1% penicillin-streptomycin (ThermoFisher: 15140122)
- 4 mL penicillin-streptomycin (ThermoFisher: 15140122)
- 1 mL trypsin-EDTA (ThermoFisher: R001100)
- 6 mL PBS (Phosphate Buffer Saline, ThermoFisher: 20012019)
- Ethanol 70% and ethanol 90%
- Silicon windows
- Cell culture dishes with a diameter of 24 cm.

Operating procedure

- Clean silicon window firstly with ethanol 70% then ethanol 90% inside the hood then put in a cell culture dish.
- Empty the used medium of the T-25 flask containing the confluent cells.
- Rinse the cell surface by aspirations/returns of 6 ml PBS.
- Empty PBS into the trash.
- Add 1mL trypsin-EDTA into the T-25 containing the cells, swing slightly to make sure all the cell surface contacts with trypsin-EDTA.
- Empty trypsin-EDTA, then close the T-25, and put it in the incubator 7 ($\pm$) min.
- Check the cell layer state with microscopy (cells should be round), and hit the box against a hard surface to help detach the cells.

- Add 3mL of complete medium to gently re-suspend the cells. The cell concentration (with a Malassez counting chamber) after this step is approximate $1\sim5\times10^6$ cells/mL.
- Dilute the cells to $\frac{1}{5}$ of the initial concentration.
- Add 1mL of the diluted medium with the suspending cells on every silicon window. Close the cell culture dish.
- Note the name of the cells, date of sub culture, volume and number of sub culture.
- Put all dishes in the incubator and change the medium every 24 hours.
- Scrape half of the cells with a biological scraper before change the complete medium.
- Take for experiment after 72 hours.

Remarks

The confluent state of the cells may differ from one preparation to another. So the experimental date is approximately within 1 day.

Bibliography

[1] O.A. Smolyanskaya, N.V. Chernomyrdin, A.A. Konovko, K.I. Zaytsev, I.A. Ozheredov, O.P. Cherkasova, M.M. Nazarov, J.-P. Guillet, S.A. Kozlov, Yu. V. Kistenev, J.-L. Coutaz, P. Mounaix, V.L. Vaks, J.-H. Son, H. Cheon, V.P. Wallace, Yu. Feldman, I. Popov, A.N. Yaroslavsky, A.P. Shkurinov, and V.V. Tuchin. Terahertz biophotonics as a tool for studies of dielectric and spectral properties of biological tissues and liquids. *Progress in Quantum Electronics*, 62:1–77, November 2018.

[2] U. Møller, D. G. Cooke, K. Tanaka, and P. U. Jepsen. Terahertz reflection spectroscopy of Debye relaxation in polar liquids [Invited]. *JOSA B*, 26(9):A113–A125, 2009.

[3] D. H. Auston, K. P. Cheung, and P. R. Smith. Picosecond photoconducting Hertzian dipoles. *Applied Physics Letters*, 45(3):284, 1984.

[4] Jean-Louis Coutaz. *Optoélectronique terahertz*. EDP Sciences, December 2012. Google-Books-ID: ZvAaiQOUi5gC.

[5] A. Bonvalet, M. Joffre, J. L. Martin, and A. Migus. Generation of ultrabroadband femtosecond pulses in the mid-infrared by optical rectification of 15 fs light pulses at 100 MHz repetition rate. *Applied Physics Letters*, 67(20):2907–2909, November 1995.

[6] Sébastien Vidal. *Étude théorique et expérimentale de la génération et de la mise en forme d'impulsions térahertz*. thesis, Bordeaux 1, December 2009. Publication Title: http://www.theses.fr.

[7] C. D'Amico, A. Houard, M. Franco, B. Prade, A. Mysyrowicz, A. Couairon, and V. T. Tikhonchuk. Conical Forward THz Emission from Femtosecond-Laser-Beam Filamentation in Air. *Physical Review Letters*, 98(23):235002, June 2007.

[8] Jianming Dai and X.-C. Zhang. Terahertz wave generation from gas plasma using a phase compensator with attosecond phase-control accuracy. *Applied Physics Letters*, 94(2):021117, January 2009. Publisher: American Institute of Physics.

[9] Benjamin Clough, Jingle Liu, and X.-C. Zhang. "All air–plasma" terahertz spectroscopy. *Optics Letters*, 36(13):2399, July 2011.

[10] M. Durand, Y. Liu, A. Houard, and A. Mysyrowicz. Fine control of terahertz radiation from filamentation by molecular lensing in air. *Optics Letters*, 35(10):1710–1712, May 2010. Publisher: Optical Society of America.

[11] Jerome Faist, Federico Capasso, Deborah L. Sivco, Carlo Sirtori, Albert L. Hutchinson, and Alfred Y. Cho. Quantum Cascade Laser. *Science*, 264(5158):553–556, April 1994.

[12] Jean-Louis Coutaz, Frederic Garet, and Vincent P. Wallace. *Principles of Terahertz Time-Domain Spectroscopy: An Introductory Textbook*. CRC Press, December 2018. Google-Books-ID: zah8DwAAQBAJ.

[13] J. F. Lampin, G. Mouret, S. Dhillon, and J. Mangeney. THz spectroscopy for fundamental science and applications. *Photoniques*, (101):33–38, March 2020. Number: 101 Publisher: EDP Sciences.

[14] A. I. McIntosh, B. Yang, S. M. Goldup, M. Watkinson, and R. S. Donnan. Terahertz spectroscopy: a powerful new tool for the chemical sciences? *Chemicals Society Reviews*, 41(6):2072–2082, 2012.

[15] S. J. Smith and E. M. Purcell. Visible Light from Localized Surface Charges Moving across a Grating. *Physical Review*, 92(4):1069–1069, November 1953. Publisher: American Physical Society.

[16] Zhiping Jiang and Xi-Cheng Zhang. Terahertz imaging via electrooptic effect. *IEEE Transactions on Microwave Theory and Techniques*, 47(12):2644–2650, December 1999. Conference Name: IEEE Transactions on Microwave Theory and Techniques.

[17] I-Chen Ho, Xiaoyu Guo, and X.-C. Zhang. Design and performance of reflective terahertz air-biased-coherent-detection for time-domain spectroscopy. *Optics Express*, 18(3):2872, February 2010.

[18] Adrian Dobroiu, Masatsugu Yamashita, Yuichi N. Ohshima, Yasuyuki Morita, Chiko Otani, and Kodo Kawase. Terahertz imaging system based on a backward-wave oscillator. *Applied Optics*, 43(30):5637–5646, October 2004.

[19] S. Hargreaves and R. A. Lewis. Terahertz imaging: materials and methods. *Journal of Materials Science: Materials in Electronics*, 18(1):299, March 2007.

[20] Alan W. M. Lee, Benjamin S. Williams, Sushil Kumar, Qing Hu, and John L. Reno. Real-time imaging using a 4.3-THz quantum cascade laser and a 320 x 240 microbolometer focal-plane array. *IEEE PHOTONICS TECHNOLOGY LETTERS*, 18(13-16):1415–1417, August 2006.

[21] Roger W. Whatmore. Pyroelectric Arrays: Ceramics and Thin Films. *Journal of Electroceramics*, 13(1):139–147, July 2004.

[22] David Klocke, Anke Schmitz, Helmut Soltner, Herbert Bousack, and Helmut Schmitz. Infrared receptors in pyrophilous ("fire loving") insects as model for new un-cooled infrared sensors. *Beilstein Journal of Nanotechnology*, 2:186–197, March 2011.

[23] Marcel J. E. Golay. Theoretical Consideration in Heat and Infra-Red Detection, with Particular Reference to the Pneumatic Detector. *Review of Scientific Instruments*, 18(5):347–356, May 1947.

[24] P. L. Richards. Bolometers for infrared and millimeter waves. *Journal of Applied Physics*, 76(1):1–24, July 1994.

[25] Tien-Lai Hwang, S. E. Schwarz, and D. B. Rutledge. Microbolometers for infrared detection. *Applied Physics Letters*, 34(11):773–776, June 1979.

[26] Erich N. Grossman and Aaron J. Miller. Active millimeter-wave imaging for concealed weapons detection. page 62, Orlando, FL, August 2003.

[27] F. Sizov and A. Rogalski. THz detectors. *Progress in Quantum Electronics*, 34(5):278–347, September 2010.

[28] A. M. Nicolson. Broad-Band Microwave Transmission Characteristics from a Single Measurement of the Transient Response. *IEEE Transactions on Instrumentation and Measurement*, 17(4):395–402, December 1968. Conference Name: IEEE Transactions on Instrumentation and Measurement.

[29] A. M. Nicolson and G. F. Ross. Measurement of the Intrinsic Properties of Materials by Time-Domain Techniques. *IEEE Transactions on Instrumentation and Measurement*, 19(4):377–382, November 1970. Conference Name: IEEE Transactions on Instrumentation and Measurement.

[30] C. Fattinger and D. Grischkowsky. Terahertz beams. *Applied Physics Letters*, 54(6):490, 1989.

[31] A. Podzorov. *Spectroscopie et imagerie térahertz des systèmes d'intérêt biologique.* PhD thesis, Ecole Polytechnique, 2009.

[32] Eiichi Matsubara, Masaya Nagai, and Masaaki Ashida. Ultrabroadband coherent electric field from far infrared to 200 THz using air plasma induced by 10 fs pulses. *Applied Physics Letters*, 101(1):011105, July 2012.

[33] Tianwu Wang, Pernille Klarskov, and Peter Uhd Jepsen. Ultrabroadband THz Time-Domain Spectroscopy of a Free-Flowing Water Film. *IEEE Transactions on Terahertz Science and Technology*, 4(4):425–431, July 2014. Conference Name: IEEE Transactions on Terahertz Science and Technology.

[34] Korbinian J. Kaltenecker, Binbin Zhou, Nicolas Stenger, Sebastian Engelbrecht, Bernd Fischer, and Peter U. Jepsen. Bridging the gap between the THz and IR frequency regime. In *2017 42nd International Conference on Infrared, Millimeter, and Terahertz Waves (IRMMW-THz)*, pages 1–2, August 2017. ISSN: 2162-2035.

[35] L. Duvillaret, F. Garet, and J.-L. Coutaz. A reliable method for extraction of material parameters in terahertz time-domain spectroscopy. *Selected Topics in Quantum Electronics, IEEE Journal of*, 2(3):739–746, 1996.

[36] Maxime Bernier, Frederic Garet, and Jean-Louis Coutaz. Precise Determination of the Refractive Index of Samples Showing Low Transmission Bands by THz Time-Domain Spectroscopy. *IEEE Transactions on Terahertz Science and Technology*, 3(3):295–301, May 2013.

[37] Timothy D. Dorney, Richard G. Baraniuk, and Daniel M. Mittleman. Material parameter estimation with terahertz time-domain spectroscopy. *Journal of the Optical Society of America A*, 18(7):1562, July 2001.

[38] Ioachim Pupeza, Rafal Wilk, and Martin Koch. Highly accurate optical material parameter determination with THz time-domain spectroscopy. *Optics Express*, 15(7):4335, 2007.

[39] Maik Scheller. Data Extraction from Terahertz Time Domain Spectroscopy Measurements. *Journal of Infrared, Millimeter, and Terahertz Waves*, 35(8):638–648, August 2014.

[40] Cecilie Rønne. Intermolecular Liquid Dynamics Studied by THz-Spectroscopy. page 140.

[41] K. Jeong, Y.-M. Huh, S.-H. Kim, Y. Park, J.-H. Son, S. J. Oh, and J.-S. Suh. Characterization of blood using terahertz waves. *Journal of biomedical optics*, 18(10):107008, 2013.

[42] K. Shiraga, Y. Ogawa, T. Suzuki, N. Kondo, A. Irisawa, and M. Imamura. Characterization of Dielectric Responses of Human Cancer Cells in the Terahertz Region. *Journal of Infrared, Millimeter, and Terahertz Waves*, 35(5):493–502, 2014.

[43] A. J. Fitzgerald, E. Berry, N. N. Zinov'ev, S. Homer-Vanniasinkam, R. E. Miles, J. M. Chamberlain, and M. A. Smith. Catalogue of human tissue optical properties at terahertz frequencies. *Journal of Biological Physics*, 29(2-3):123–128, 2003.

[44] O. A. Smolyanskaya, I. J. Schelkanova, M. S. Kulya, E. L. Odlyanitskiy, I. S. Goryachev, A. N. Tcypkin, Ya V. Grachev, Ya G. Toropova, and V. V. Tuchin. Glycerol dehydration of native and diabetic animal tissues studied by THz-TDS and NMR methods. *Biomedical Optics Express*, 9(3):1198–1215, March 2018.

[45] Li Jiusheng. Optical Parameters of Vegetable Oil Studied by Terahertz Time-Domain Spectroscopy. *Applied Spectroscopy*, 64(2):231–234, February 2010. Publisher: Society for Applied Spectroscopy.

[46] Geun-Ju Kim, Seok-Gy Jeon, Jung-Il Kim, and Yun-Sik Jin. Terahertz time domain spectroscopy of petroleum products and organic solvents. In *2008 33rd International Conference on Infrared, Millimeter and Terahertz Waves*, pages 1–2, September 2008. ISSN: 2162-2035.

[47] Takeshi Ikeda, Akira Matsushita, Michiaki Tatsuno, Yukio Minami, Mariko Yamaguchi, Kohji Yamamoto, Masahiko Tani, and Masanori Hangyo. Investigation of inflammable liquids by terahertz spectroscopy. *Applied Physics Letters*, 87(3):034105, July 2005. Publisher: American Institute of Physics.

[48] H. Hirori, T. Arikawa, M. Nagai, H. Ohtake, M. Yoshida, and K. Tanaka. Accurate determination of complex dielectric constants by terahertz time domain attenuated total reflection spectroscopy. In *Infrared and Millimeter Waves, Conference Digest of the 2004 Joint 29th International Conference on 2004 and 12th International Conference on Terahertz Electronics, 2004.*, pages 251–252, September 2004.

[49] Peter Uhd Jepsen, Uffe Møller, and Hannes Merbold. Investigation of aqueous alcohol and sugar solutions with reflection terahertz time-domain spectroscopy. *Optics Express*, 15(22):14717, 2007.

[50] A. Wojdyla. *Polarisation des impulsions térahertz et développement de l'imagerie par réflexion interne totale pour l'étude d'objets d'intérêt biologique.* Thèse, Ecole Polytechnique, 2011.

[51] Jianming Dai, Jiangquan Zhang, Weili Zhang, and D. Grischkowsky. Terahertz time-domain spectroscopy characterization of the far-infrared absorption and index of refraction of high-resistivity, float-zone silicon. *Journal of the Optical Society of America B*, 21(7):1379, July 2004.

[52] A. Podzorov and G. Gallot. Low-loss polymers for terahertz applications. *Applied optics*, 47(18):3254–3257, 2008.

[53] D. Grischkowsky, S. Keiding, M. van Exter, and C. Fattinger. Far-infrared time-domain spectroscopy with terahertz beams of dielectrics and semiconductors. *Journal of the Optical Society of America B*, 1990.

[54] Damien Bigourd, Arnaud Cuisset, Francis Hindle, Sophie Matton, Eric Fertein, Robin Bocquet, and Gaël Mouret. Detection and quantification of multiple molecular species in mainstream cigarette smoke by continuous-wave terahertz spectroscopy. *Optics Letters*, 31(15):2356–2358, August 2006. Publisher: Optical Society of America.

[55] A. G. Davies, A. D. Burnett, W. Fan, E. H. Linfield, and J. E. Cunningham. Terahertz spectroscopy of explosives and drugs. *Materials today*, 11(3):18–26, 2008.

[56] Y.-C. Shen. Terahertz pulsed spectroscopy and imaging for pharmaceutical applications: A review. *International Journal of Pharmaceutics*, 417(1-2):48–60, 2011.

[57] L. Ho, Y. Cuppok, S. Muschert, K. C. Gordon, M. Pepper, Y. Shen, F. Siepmann, J. Siepmann, P. F. Taday, and T. Rades. Effects of film coating thickness and drug layer uniformity on in vitro drug release from sustained-release coated pellets: A case study using terahertz pulsed imaging. *International Journal of Pharmaceutics*, 382(1-2):151–159, 2009.

[58] David T. Leisawitz, William C. Danchi, Michael J. DiPirro, Lee D. Feinberg, Daniel Y. Gezari, Mike Hagopian, William D. Langer, John C. Mather, Samuel Harvey Moseley Jr, Michael Shao, Robert F. Silverberg, Johannes G. Staguhn, Mark R. Swain, Harold W. Yorke, and Xiaolei Zhang. Scientific motivation and technology requirements for the SPIRIT and SPECS far-infrared/submillimeter space interferometers. In *UV, Optical, and IR Space Telescopes and Instruments*, volume 4013, pages 36–46. International Society for Optics and Photonics, July 2000.

[59] H. Hoshina, A. Hayashi, N. Miyoshi, F. Miyamaru, and C. Otani. Terahertz pulsed imaging of frozen biological tissues. *Applied Physics Letters*, 94(12):123901, 2009.

[60] P.U. Jepsen, D.G. Cooke, and M. Koch. Terahertz spectroscopy and imaging - Modern techniques and applications. *Laser & Photonics Reviews*, 5(1):124–166, 2011.

[61] Martin Chaplin. Do we underestimate the importance of water in cell biology? *Nature Reviews Molecular Cell Biology*, 7(11):861–866, November 2006.

[62] Philip Ball. Water as an Active Constituent in Cell Biology. *Chemical Reviews*, 108(1):74–108, January 2008.

[63] Anna Rita Bizzarri and Salvatore Cannistraro. Molecular Dynamics of Water at the Protein-Solvent Interface. *The Journal of Physical Chemistry B*, 106(26):6617–6633, July 2002.

[64] Sergei Yu. Noskov and Benoît Roux. Importance of Hydration and Dynamics on the Selectivity of the KcsA and NaK Channels. *Journal of General Physiology*, 129(2):135–143, February 2007.

[65] U. Heugen, G. Schwaab, E. Bründermann, M. Heyden, X. Yu, D. M. Leitner, and M. Havenith. Solute-induced retardation of water dynamics probed directly by terahertz spectroscopy. *Proceedings of the National Academy of Sciences*, 103(33):12301–12306, 2006.

[66] J. Xu, K. W. Plaxco, and S. J. Allen. Probing the collective vibrational dynamics of a protein in liquid water by terahertz absorption spectroscopy. *Protein Science*, 15(5):1175–1181, 2006.

[67] Daniela Russo, Greg Hura, and Teresa Head-Gordon. Hydration Dynamics Near a Model Protein Surface. *Biophysical Journal*, 86(3):1852–1862, March 2004.

[68] Bertil Halle. Protein hydration dynamics in solution: a critical survey. *Philosophical Transactions of the Royal Society of London. Series B: Biological Sciences*, 359(1448):1207–1224, August 2004.

[69] L. Zhang, L. Wang, Y.-T. Kao, W. Qiu, Y. Yang, O. Okobiah, and D. Zhong. Mapping hydration dynamics around a protein surface. *Proceedings of the National Academy of Sciences*, 104(47):18461–18466, November 2007.

[70] F. Pizzitutti, M. Marchi, F. Sterpone, and P. J. Rossky. How Protein Surfaces Induce Anomalous Dynamics of Hydration Water. *J. Phys. Chem. B*, 111:7584–7590, 2007.

[71] P. Petrone and V. S. Pande. Can Conformational Change Be Described by Only a Few Normal Modes? *Biophysical Journal*, 90(5):1583–1593, 2006.

[72] F. Tama and Y.-H. Sanejouand. Conformational change of proteins arising from normal mode calculations. *Protein Engineering*, 14(1):1–6, 2001.

[73] A. G. Markelz, A. Roitberg, and E. J. Heilweil. Pulsed terahertz spectroscopy of DNA, bovine serum albumin and collagen between 0.1 and 2.0 THz. *Chemical Physics Letters*, 320(1-2):42–48, 2000.

[74] A. G. Markelz. Terahertz Dielectric Sensitivity to Biomolecular Structure and Function. *IEEE Journal of Selected Topics in Quantum Electronics*, 14(1):180–190, 2008.

[75] R. J. Falconer and A. G. Markelz. Terahertz Spectroscopic Analysis of Peptides and Proteins. *Journal of Infrared, Millimeter, and Terahertz Waves*, 33(10):973–988, 2012.

[76] X. Yang, X. Zhao, K. Yang, Y. Liu, Y. Liu, W. Fu, and Y. Luo. Biomedical Applications of Terahertz Spectroscopy and Imaging. *Trends in Biotechnology*, 2016.

[77] R. Balu, H. Zhang, E. Zukowski, J.-Y. Chen, A.G. Markelz, and S.K. Gregurick. Terahertz Spectroscopy of Bacteriorhodopsin and Rhodopsin: Similarities and Differences. *Biophysical Journal*, 94(8):3217–3226, 2008.

[78] A. Markelz, S. Whitmire, J. Hillebrecht, and R. Birge. THz time domain spectroscopy of biomolecular conformational modes. *Physics in medicine and biology*, 47(21):3797, 2002.

[79] M. Tang, Q. Huang, D. Wei, G. Zhao, T. Chang, K. Kou, M. Wang, C. Du, W.-L. Fu, and H.-L. Cui. Terahertz spectroscopy of oligonucleotides in aqueous solutions. *Journal of Biomedical Optics*, 20(9):095009, 2015.

[80] D.M. Mittleman, M. Gupta, R. Neelamani, R.G. Baraniuk, J.V. Rudd, and M. Koch. Recent advances in terahertz imaging. *Applied Physics B*, 68(6):1085–1094, 1999.

[81] E. Pickwell, B. E. Cole, A. J. Fitzgerald, M. Pepper, and V. P. Wallace. In vivo study of human skin using pulsed terahertz radiation. *Physics in Medicine and Biology*, 49(9):1595, 2004.

[82] S. Sy, S. Huang, Y.-X. J. Wang, J. Yu, A. T. Ahuja, Y.-T. Zhang, and E. Pickwell-MacPherson. Terahertz spectroscopy of liver cirrhosis: investigating the origin of contrast. *Physics in Medicine and Biology*, 55(24):7587–7596, 2010.

[83] T. Löffler, T. Bauer, K. J. Siebert, H. G. Roskos, A. Fitzgerald, and S. Czasch. Terahertz dark-field imaging of biomedical tissue. *Optics Express*, 9(12):616, December 2001.

[84] J.-B. Masson, M.-P. Sauviat, J.-L. Martin, and G. Gallot. Ionic contrast terahertz near-field imaging of axonal water fluxes. *Proceedings of the National Academy of Sciences of the United States of America*, 103(13):4808–4812, 2006.

[85] C. Yu, S. Fan, Y. Sun, and E. Pickwell-MacPherson. The potential of terahertz imaging for cancer diagnosis: A review of investigations to date. *Quantitative imaging in medicine and surgery*, 2(1):33, 2012.

[86] T. C. Bowman, M. El-Shenawee, and L. K. Campbell. Terahertz Imaging of Excised Breast Tumor Tissue on Paraffin Sections. *IEEE Transactions on Antennas and Propagation*, 63(5):2088–2097, 2015.

[87] F. Wahaia, G. Valusis, L. M. Bernardo, A. Almeida, J. A. Moreira, P. C. Lopes, J. Macutkevic, I. Kasalynas, D. Seliuta, R. Adomavicius, R. Henrique, and M. Lopes. Detection of colon cancer by terahertz techniques. *Journal of Molecular Structure*, 1006(1-3):77–82, 2011.

[88] P. Tewari, C. P. Kealey, D. B. Bennett, N. Bajwa, K. S. Barnett, R. S. Singh, M. O. Culjat, A. Stojadinovic, W. S. Grundfest, and Z. D. Taylor. In vivo terahertz imaging of rat skin burns. *Journal of biomedical optics*, 17(4):0405031–0405033, 2012.

[89] R. M. Woodward, V. P. Wallace, D. D. Arnone, E. H. Linfield, and M. Pepper. Terahertz pulsed imaging of skin cancer in the time and frequency domain. *Journal of Biological Physics*, 29(2-3):257–259, 2003.

[90] J. Y. Suen, P. Tewari, Z. D. Taylor, W. S. Grundfest, H. Lee, E. R. Brown, M. O. Culjat, and R. S. Singh. Towards medical terahertz sensing of skin hydration. *Stud. Health Technol. Inform*, 142:364–368, 2009.

[91] Kirill I. Zaytsev, Arseniy A. Gavdush, Nikita V. Chernomyrdin, and Stanislav O. Yurchenko. Highly Accurate in Vivo Terahertz Spectroscopy of Healthy Skin: Variation of Refractive Index and Absorption Coefficient Along the Human Body. *IEEE Transactions on Terahertz Science and Technology*, 5(5):817–827, September 2015. Conference Name: IEEE Transactions on Terahertz Science and Technology.

[92] V. P. Wallace, A. J. Fitzgerald, S. Shankar, N. Flanagan, R. Pye, J. Cluff, and D. D. Arnone. Terahertz pulsed imaging of basal cell carcinoma ex vivo and in vivo. *British Journal of Dermatology*, 151(2):424–432, 2004. _eprint: https://onlinelibrary.wiley.com/doi/pdf/10.1111/j.1365-2133.2004.06129.x.

[93] K. W. Kim, K.-S. Kim, H. Kim, S. H. Lee, J.-H. Park, J.-H. Han, S.-H. Seok, J. Park, Y. S. Choi, Y. I. Kim, and others. Terahertz dynamic imaging of skin drug absorption. *Optics express*, 20(9):9476–9484, 2012.

[94] Yookyeong Carolyn Sim, Jae Yeon Park, Kang-Min Ahn, Chansik Park, and Joo-Hiuk Son. Terahertz imaging of excised oral cancer at frozen temperature. *Biomedical Optics Express*, 4(8):1413, August 2013.

[95] Caroline B Reid, Anthony Fitzgerald, George Reese, Robert Goldin, Paris Tekkis, P S O'Kelly, Emma Pickwell-MacPherson, Adam P Gibson, and Vincent P Wallace. Terahertz pulsed imaging of freshly excised human colonic tissues. *Physics in Medicine and Biology*, 56(14):4333–4353, July 2011.

[96] Dibo Hou, Xian Li, Jinhui Cai, Yehao Ma, Xusheng Kang, Pingjie Huang, and Guangxin Zhang. Terahertz spectroscopic investigation of human gastric normal and tumor tissues. *Physics in Medicine and Biology*, 59(18):5423–5440, September 2014.

[97] M. Bessou, B. Chassagne, J.-P. Caumes, C. Pradère, P. Maire, M. Tondusson, and E. Abraham. Three-dimensional terahertz computed tomography of human bones. *Applied optics*, 51(28):6738–6744, 2012.

[98] W.-C. Kan, W.-S. Lee, W.-H. Cheung, V. P. Wallace, and E. Pickwell-MacPherson. Terahertz pulsed imaging of knee cartilage. *Biomedical optics express*, 1(3):967–974, 2010.

[99] Zhiping Jiang and Xi-Cheng Zhang. Terahertz imaging via electrooptic effect. *IEEE Transactions on Microwave Theory and Techniques*, 47(12):2644–2650, December 1999. Conference Name: IEEE Transactions on Microwave Theory and Techniques.

[100] Xinke Wang, Ye Cui, Dan Hu, Wenfeng Sun, JiaSheng Ye, and Yan Zhang. Terahertz quasi-near-field real-time imaging. *Optics Communications*, 282(24):4683–4687, December 2009.

[101] Markus Schirmer, Makoto Fujio, Masaaki Minami, Jiro Miura, Tsutomu Araki, and Takeshi Yasui. Biomedical applications of a real-time terahertz color scanner. *Biomedical Optics Express*, 1(2):354, September 2010.

[102] Lord Rayleigh. On the Theory of Optical Images, with special reference to the Microscope. *Journal of the Royal Microscopical Society*, 23(4):474–482, 1903. _eprint: https://onlinelibrary.wiley.com/doi/pdf/10.1111/j.1365-2818.1903.tb04831.x.

[103] E. Abbe. Beiträge zur Theorie des Mikroskops und der mikroskopischen Wahrnehmung. *Archiv für Mikroskopische Anatomie*, 9(1):413–468, December 1873.

[104] M. Born and E. Wolf. *Principles of Optics, 7th (expanded) ed.* Cambridge U. Press, 1999.

[105] E. H. Synge. A suggested method for extending microscopic resolution into the ultramicroscopic region. *The London, Edinburgh, and Dublin Philosophical Magazine and Journal of Science*, 6(35):356–362, August 1928. Publisher: Taylor & Francis _eprint: https://doi.org/10.1080/14786440808564615.

[106] E. A. Ash and G. Nicholls. Super-resolution Aperture Scanning Microscope. *Nature*, 237(5357):510–512, June 1972. Number: 5357 Publisher: Nature Publishing Group.

[107] A. J. L. Adam, J. M. Brok, M. A. Seo, K. J. Ahn, D. S. Kim, J. H. Kang, Q. H. Park, M. Nagel, and P. C. M. Planken. Advanced terahertz electric near-field measurements at sub-wavelength diameter metallic apertures. *Optics Express*, 16(10):7407–7417, May 2008. Publisher: Optical Society of America.

[108] Markus Wächter, Michael Nagel, and Heinrich Kurz. Tapered photoconductive terahertz field probe tip with subwavelength spatial resolution. *Applied Physics Letters*, 95(4):041112, July 2009. Publisher: American Institute of Physics.

[109] A. J. Huber, F. Keilmann, J. Wittborn, J. Aizpurua, and R. Hillenbrand. Terahertz Near-Field Nanoscopy of Mobile Carriers in Single Semiconductor Nanodevices. *Nano Letters*, 8(11):3766–3770, November 2008. Publisher: American Chemical Society.

[110] A. Doi, F. Blanchard, H. Hirori, and K. Tanaka. Near-field THz imaging of free induction decay from a tyrosine crystal. *Optics Express*, 18(17):18419, August 2010.

[111] U. Schade, K. Holldack, P. Kuske, G. Wüstefeld, and H.-W. Hübers. THz near-field imaging employing synchrotron radiation. *Applied Physics Letters*, 84(8):1422–1424, February 2004.

[112] Andreas Bitzer, Alex Ortner, and Markus Walther. Terahertz near-field microscopy with subwavelength spatial resolution based on photoconductive antennas. *Applied Optics*, 49(19):E1, July 2010.

[113] A. Adam. Review of Near-Field Terahertz Measurement Methods and Their Applications: How to Achieve Sub-Wavelength Resolution at THz Frequencies. *Journal of Infrared, Millimeter, and Terahertz Waves*, 32(8-9):976–1019, 2011.

[114] Stefan A. Maier, Steve R. Andrews, L. Martín-Moreno, and F. J. García-Vidal. Terahertz Surface Plasmon-Polariton Propagation and Focusing on Periodically Corrugated Metal Wires. *Physical Review Letters*, 97(17):176805, October 2006.

[115] E Yeh, K Gustafson, and G L Boulianne. Green fluorescent protein as a vital marker and reporter of gene expression in Drosophila. *Proceedings of the National Academy of Sciences of the United States of America*, 92(15):7036–7040, July 1995.

[116] Delphine Débarre. Microscopie par génération de troisième harmonique appliquée à la biologie. page 245.

[117] H.-B. Liu, G. Plopper, S. Earley, Y. Chen, B. Ferguson, and X.-C. Zhang. Sensing minute changes in biological cell monolayers with THz differential time-domain spectroscopy. *Biosensors and Bioelectronics*, 22(6):1075–1080, 2007.

[118] C. Zhang and S. M. Durbin. Hydration-induced far-infrared absorption increase in myoglobin. *The Journal of Physical Chemistry B*, 110(46):23607–23613, 2006.

[119] J.-Y. Chen, J. R. Knab, S. Ye, Y. He, and A. G. Markelz. Terahertz dielectric assay of solution phase protein binding. *Applied Physics Letters*, 90(24):243901, 2007.

[120] H. Yoneyama, M. Yamashita, K. Kawase, R. Ueno, H. Ito, and T. Ouchi. Terahertz spectroscopy of native-conformation and thermally denaturated bovine serum albumin (BSA). *Phys. Med. Biol.*, 53:3543–3549, 2008.

[121] J. Xu, K. W. Plaxco, and S. J. Allen. Collective Dynamics of Lysozyme in Water: Terahertz Absorption Spectroscopy and Comparison with Theory. *The Journal of Physical Chemistry B*, 110(47):24255–24259, 2006.

[122] B. Born, H. Weingärtner, E. Bründermann, and M. Havenith. Solvation Dynamics of Model Peptides Probed by Terahertz Spectroscopy. Observation of the Onset of Collective Network Motions. *Journal of the American Chemical Society*, 131(10):3752–3755, 2009.

[123] Marianne Grognot and Guilhem Gallot. Relative Contributions of Core Protein and Solvation Shell in the Terahertz Dielectric Properties of Protein Solutions. *The Journal of Physical Chemistry B*, 121(41):9508–9512, October 2017.

[124] A. C. Fogarty and D. Laage. Water Dynamics in Protein Hydration Shells: The Molecular Origins of the Dynamical Perturbation. *Journal of Physical Chemistry B*, 118(28):7715–7729, 2014.

[125] S. Ebbinghaus, S. J. Kim, M. Heyden, X. Yu, U. Heugen, M. Gruebele, D. M. Leitner, and M. Havenith. An extended dynamical hydration shell around proteins. *Proceedings of the National Academy of Sciences*, 104(52):20749–20752, 2007.

[126] O. Sushko, R. Dubrovka, and R. S. Donnan. Terahertz spectral domain computational analysis of hydration shell of proteins with increasingly complex tertiary structure. *J Phys Chem B*, 117(51):16486–92, 2013.

[127] Antoine Wojdyla. Polarisation des impulsions térahertz et développement de l'imagerie par réflexion interne totale pour l'étude d'objets d'intérêt biologique. page 177.

[128] Marianne Grognot. *Imagerie térahertz par réflexion interne totale pour la biologie. : Application à l'étude de la perméabilisation cellulaire.* thesis, Paris Saclay, October 2016.

[129] Harvey Lodish, Arnold Berk, S. Lawrence Zipursky, Paul Matsudaira, David Baltimore, and James Darnell. *Molecular Cell Biology.* W. H. Freeman, 4th edition, 2000.

[130] B. Alberts, A. Johnson, J. Lewis, M. Raff, K. Roberts, and P. Walter. *Molecular biology of the cell.* Garland Science, New York, 2002.

[131] Elaine Nicpon Marieb. *Human anatomy and physiology.* Redwood City, Calif. : Benjamin/Cummings, 1995.

[132] J. G. Betts, P. DeSaix, E. Johnson, and J. E. Johnson. *Anatomy and Physiology.* OpenStax College, 2013.

[133] Jeremy M. Berg, John L. Tymoczko, Lubert Stryer, Jeremy M. Berg, John L. Tymoczko, and Lubert Stryer. *Biochemistry.* W H Freeman, 5th edition, 2002.

[134] E. Gorter and F. Grendel. ON BIMOLECULAR LAYERS OF LIPOIDS ON THE CHROMOCYTES OF THE BLOOD. *The Journal of Experimental Medicine*, 41(4):439–443, April 1925.

[135] James Frederic Danielli and Hugh Davson. A contribution to the theory of permeability of thin films. *Journal of Cellular and Comparative Physiology*, 5(4):495–508, 1935. _eprint: https://onlinelibrary.wiley.com/doi/pdf/10.1002/jcp.1030050409.

[136] Michael Edidin. Lipids on the frontier: a century of cell-membrane bilayers. *Nature Reviews Molecular Cell Biology*, 4(5):414–418, May 2003. Number: 5 Publisher: Nature Publishing Group.

[137] Richard A. Cone. Rotational Diffusion of Rhodopsin in the Visual Receptor Membrane. *Nature New Biology*, 236(63):39–43, March 1972. Number: 63 Publisher: Nature Publishing Group.

[138] S. J. Singer and Garth L. Nicolson. The Fluid Mosaic Model of the Structure of Cell Membranes. *Science*, 175(4023):720–731, February 1972.

[139] Kai Simons and Elina Ikonen. Functional rafts in cell membranes. *Nature*, 387(6633):569–572, June 1997. Number: 6633 Publisher: Nature Publishing Group.

[140] K G Rothberg, Y S Ying, B A Kamen, and R G Anderson. Cholesterol controls the clustering of the glycophospholipid-anchored membrane receptor for 5-methyltetrahydrofolate. *The Journal of Cell Biology*, 111(6):2931–2938, December 1990.

[141] N. A. Campbell and J. B. Reece. *Biologie*. De Boeck Université, 2004.

[142] Geoffrey M. Cooper and Robert E. Hausman. *The cell a molecular approach*. Washington, D.C ASM Press, 4th ed edition, 2007.

[143] Gerrit van Meer, Dennis R. Voelker, and Gerald W. Feigenson. Membrane lipids: where they are and how they behave. *Nature Reviews Molecular Cell Biology*, 9(2):112–124, February 2008.

[144] A. Uzman. *Molecular biology of the cell (4th ed.): Alberts, B., Johnson, A., Lewis, J., Raff, M., Roberts, K., and Walter, P.*, volume 31. 2003.

[145] K. Boesze-Battaglia and R. Schimmel. Cell membrane lipid composition and distribution: implications for cell function and lessons learned from photoreceptors and platelets. *Journal of Experimental Biology*, 200(23):2927–2936, December 1997.

[146] R. N. Robertson and Rutherford Robertson. *Lively Membranes*. CUP Archive, July 1983. Google-Books-ID: ZYI6AAAAIAAJ.

[147] Paul Matsudaira Chris-A Kaiser Collectif Harvey Lodish, Arnold Berk. *Molecular Cell Biology. 5th Edition - Harvey Lodish,Arnold Berk,Paul Matsudaira,Chris-A Kaiser, Collectif*.

[148] R Fettiplace and D A Haydon. Water permeability of lipid membranes. *Physiological Reviews*, 60(2):510–550, April 1980.

[149] Cecie Starr and Beverly McMillan. *Human Biology*. Cengage Learning, 2000. Google-Books-ID: EQMGAAAAQBAJ.

[150] Tsutomu Masujima. Live Single-cell Mass Spectrometry. *Analytical Sciences*, 25(8):953–960, 2009.

[151] Richard C. Lin and Richard H. Scheller. Mechanisms of Synaptic Vesicle Exocytosis. *Annual Review of Cell and Developmental Biology*, 16(1):19–49, 2000. _eprint: https://doi.org/10.1146/annurev.cellbio.16.1.19.

[152] Martin P. Stewart, Armon Sharei, Xiaoyun Ding, Gaurav Sahay, Robert Langer, and Klavs F. Jensen. *In vitro* and *ex vivo* strategies for intracellular delivery. *Nature*, 538(7624):183–192, October 2016.

[153] I. Hapala. Breaking the Barrier: Methods for Reversible Permeabilization of Cellular Membranes. *Critical Reviews in Biotechnology*, 17(2):105–122, 1997.

[154] Marc Eeman and Magali Deleu. From biological membranes to biomimetic model membranes. *BASE*, January 2010.

[155] U. Schnell, F. Dijk, K. A. Sjollema, and B. N. G. Giepmans. Immunolabeling artifacts and the need for live-cell imaging. *Nat Meth*, 9(2):152–158, 2012.

[156] S. Keeney and S. Linn. A critical review of permeabilized cell systems for studying mammalian DNA repair. *Mutation Research/DNA Repair*, 236(2-3):239–252, 1990.

[157] C. E. Thomas, A. Ehrhardt, and M. A. Kay. Progress and problems with the use of viral vectors for gene therapy. *Nature Reviews Genetics*, 4(5):346–358, 2003.

[158] M. A. Barber. A Technic for the Inoculation of Bacteria and Other Substances into Living Cells. *The Journal of Infectious Diseases*, 8(3):348–360, 1911.

[159] Carl M. Feldherr. THE INTRACELLULAR DISTRIBUTION OF FERRITIN FOLLOWING MICROINJECTION. *The Journal of Cell Biology*, 12(1):159–167, January 1962.

[160] Yan Zhang, Yanguo Hong, Younes Bounhar, Megan Blacker, Xavier Roucou, Omar Tounekti, Emily Vereker, William J. Bowers, Howard J. Federoff, Cynthia G. Goodyer, and Andrea LeBlanc. p75 neurotrophin receptor protects primary cultures of human neurons against extracellular amyloid beta peptide cytotoxicity. *The Journal of Neuroscience: The Official Journal of the Society for Neuroscience*, 23(19):7385–7394, August 2003.

[161] Martin P. Stewart, Robert Langer, and Klavs F. Jensen. Intracellular Delivery by Membrane Disruption: Mechanisms, Strategies, and Concepts. *Chemical Reviews*, 118(16):7409–7531, August 2018.

[162] Yan Zhang and Long-Chuan Yu. Single-cell microinjection technology in cell biology. *BioEssays*, 30(6):606–610, 2008.

[163] G. Francis, Z. Kerem, H. P. S. Makkar, and K. Becker. The biological action of saponins in animal systems: a review. *British Journal of Nutrition*, 88(06):587, 2002.

[164] J. C. Brooks and S. W. Carmichael. Ultrastructural demonstration of exocytosis in intact and saponin-permeabilized cultured bovine chromaffin cells. *American journal of anatomy*, 178(1):85–89, 1987.

[165] M. Wassler, I. Jonasson, R. Persson, and E. Fries. Differential permeabilization of membranes by saponin treatment of isolated rat hepatocytes. Release of secretory proteins. *Biochem. J*, 247:407–415, 1987.

[166] M. J. H. Geelen. The use of digitonin-permeabilized mammalian cells for measuring enzyme activities in the course of studies on lipid metabolism. *Analytical Biochemistry*, 347(1):1–9, 2005.

[167] T. Sarafian, D. Aunis, and M.-F. Bader. Loss of proteins from digitonin-permeabilized adrenal chromaffin cells essential for exocytosis. *Journal of Biological Chemistry*, 262(34):16671–16676, 1987.

[168] A. L. van de Ven, K. Adler-Storthz, and R. Richards-Kortum. Delivery of optical contrast agents using Triton-X100, part 1: reversible permeabilization of live cells for intracellular labeling. *Journal of Biomedical Optics*, 14(2):021012, 2009.

[169] Dipankar Koley and Allen J. Bard. Triton X-100 concentration effects on membrane permeability of a single HeLa cell by scanning electrochemical microscopy (SECM). *Proceedings of the National Academy of Sciences*, 107(39):16783–16787, 2010.

[170] Heiko Heerklotz. Interactions of surfactants with lipid membranes. *Quarterly Reviews of Biophysics*, 41(3-4):205–264, November 2008.

[171] Nataliya Frenkel, Ali Makky, Ikhwan Resmala Sudji, Michael Wink, and Motomu Tanaka. Mechanistic Investigation of Interactions between Steroidal Saponin Digitonin and Cell Membrane Models. *The Journal of Physical Chemistry B*, 118(50):14632–14639, December 2014.

[172] Sarah J Tilley and Helen R Saibil. The mechanism of pore formation by bacterial toxins. *Current Opinion in Structural Biology*, 16(2):230–236, April 2006.

[173] I. Walev, S. C. Bhakdi, F. Hofmann, N. Djonder, A. Valeva, K. Aktories, and S. Bhakdi. Delivery of proteins into living cells by reversible membrane permeabilization with streptolysin-O. *Proceedings of the National Academy of Sciences*, 98(6):3185–3190, 2001.

[174] L. Petit, M. Gibert, D. Gillet, C. Laurent-Winter, P. Boquet, and M. R. Popoff. Clostridium perfringens ε-toxin acts on MDCK cells by forming a large membrane complex. *Journal of Bacteriology*, 179(20):6480–6487, October 1997. Publisher: American Society for Microbiology Journals.

[175] Shigeru Miyata, Junzaburo Minami, Eiji Tamai, Osamu Matsushita, Seiko Shimamoto, and Akinobu Okabe. *Clostridium perfringens* ε-Toxin Forms a Heptameric Pore within the Detergent-insoluble Microdomains of Madin-Darby Canine Kidney Cells and Rat Synaptosomes. *Journal of Biological Chemistry*, 277(42):39463–39468, October 2002.

[176] Mirko Bischofberger, Ioan Iacovache, and F. Gisou van der Goot. Pathogenic Pore-Forming Proteins: Function and Host Response. *Cell Host & Microbe*, 12(3):266–275, September 2012.

[177] Matteo Dal Peraro and F. Gisou van der Goot. Pore-forming toxins: ancient, but never really out of fashion. *Nature Reviews Microbiology*, 14(2):77–92, February 2016.

[178] M.-P. Rols and J. Teissié. Electropermeabilization of mammalian cells to macromolecules: control by pulse duration. *Biophysical journal*, 75(3):1415–1423, 1998.

[179] T. Kotnik, G. Pucihar, M. Reberšek, D. Miklavcic, and L. M. Mir. Role of pulse shape in cell membrane electropermeabilization. *Biochimica et Biophysica Acta (BBA) - Biomembranes*, 1614(2):193–200, 2003.

[180] C. Chen, S.W. Smye, M.P. Robinson, and J.A. Evans. Membrane electroporation theories: a review. *Medical & Biological Engineering & Computing*, 44(1-2):5–14, 2006.

[181] J. Gehl. Electroporation: theory and methods, perspectives for drug delivery, gene therapy and research. *Acta Physiologica Scandinavica*, 177(4):437–447, 2003.

[182] J. Teissie, M. Golzio, and M. P. Rols. Mechanisms of cell membrane electropermeabilization: A minireview of our present (lack of ?) knowledge. *Biochimica et Biophysica Acta (BBA) - General Subjects*, 1724(3):270–280, August 2005.

[183] Marie Breton and Lluis M. Mir. Investigation of the chemical mechanisms involved in the electropulsation of membranes at the molecular level. *Bioelectrochemistry*, 119:76–83, February 2018.

[184] A. B. Borle and K. W. Snowdowne. Measurement of intracellular free calcium in monkey kidney cells with aequorin. *Science (New York, N.Y.)*, 217(4556):252–254, July 1982.

[185] M. Tsukakoshi, S. Kurata, Y. Nomiya, Y. Ikawa, and T. Kasuya. A novel method of DNA transfection by laser microbeam cell surgery. *Applied Physics B*, 35(3):135–140, November 1984.

[186] Giuseppe Palumbo, Matilde Caruso, Elvira Crescenzi, Mario F. Tecce, Giuseppe Roberti, and Alberto Colasanti. Targeted gene transfer in eucaryotic cells by dye-assisted laser optoporation. *Journal of Photochemistry and Photobiology B: Biology*, 36(1):41–46, October 1996.

[187] Shun-Ichi Kurata, Motowo Tsukakoshi, Takahiro Kasuya, and Yoji Ikawa. The laser method for efficient introduction of foreign DNA into cultured cells. *Experimental Cell Research*, 162(2):372–378, February 1986.

[188] Uday K. Tirlapur and Karsten König. Targeted transfection by femtosecond laser. *Nature*, 418(6895):290–291, July 2002. Number: 6895 Publisher: Nature Publishing Group.

[189] Andrei G. Pakhomov, Shu Xiao, Olga N. Pakhomova, Iurii Semenov, Marjorie A. Kuipers, and Bennett L. Ibey. Disassembly of actin structures by nanosecond pulsed electric field is a downstream effect of cell swelling. *Bioelectrochemistry*, 100:88–95, December 2014.

[190] Kamal Dhakal, Bryan Black, and Samarendra Mohanty. Introduction of impermeable actin-staining molecules to mammalian cells by optoporation. *Scientific Reports*, 4(1):6553, May 2015.

[191] Kate Rhodes, Imran Clark, Michelle Zatcoff, Trisha Eustaquio, Kwame L. Hoyte, and Manfred R. Koller. Cellular Laserfection. In *Methods in Cell Biology*, volume 82 of *Laser Manipulation of Cells and Tissues*, pages 309–333. Academic Press, January 2007.

[192] Imram Clark, Elie G. Hanania, Janine Stevens, Marijo Gallina, Annabeth Fieck, Rolf Brandes, Bernhard O. Palsson, and Manfred R. Koller. Optoinjection for efficient targeted delivery of a broad range of compounds and macromolecules into diverse cell types. *Journal of Biomedical Optics*, 11(1):014034, January 2006. Publisher: International Society for Optics and Photonics.

[193] Olena M. Nesin, Olga N. Pakhomova, Shu Xiao, and Andrei G. Pakhomov. Manipulation of cell volume and membrane pore comparison following single cell permeabilization with 60- and 600-ns electric pulses. *Biochimica et Biophysica Acta (BBA) - Biomembranes*, 1808(3):792–801, March 2011.

[194] A. Vogel, J. Noack, G. Hüttman, and G. Paltauf. Mechanisms of femtosecond laser nanosurgery of cells and tissues. *Applied Physics B*, 81(8):1015–1047, December 2005.

[195] Cui-Ping Yao, Zhen-Xi Zhang, Ramtin Rahmanzadeh, and Gereon Huettmann. Laser-Based Gene Transfection and Gene Therapy. *IEEE Transactions on NanoBioscience*, 7(2):111–119, June 2008.

[196] Thomas J. Flotte, Joan K. Frisoli, Margaret Goetschkes, and Apostolos G. Doukas. Laser-induced shock wave effects on red blood cells. In *Proceedings of SPIE - The International Society for Optical Engineering*, pages 36–44. Publ by Int Soc for Optical Engineering, 1991.

[197] S. Lee, D. J. McAuliffe, H. Zhang, Z. Xu, J. Taitelbaum, T. J. Flotte, and A. G. Doukas. Stress-wave-induced membrane permeation of red blood cells is facilitated by aquaporins. *Ultrasound in Medicine & Biology*, 23(7):1089–1094, January 1997.

[198] David J. Stevenson, Frank J. Gunn-Moore, Paul Campbell, and Kishan Dholakia. Single cell optical transfection. *Journal of The Royal Society Interface*, 7(47):863–871, June 2010.

[199] Alfred Vogel, Norbert Linz, Sebastian Freidank, and Günther Paltauf. Femtosecond-Laser-Induced Nanocavitation in Water: Implications for Optical Breakdown Threshold and Cell Surgery. *Physical Review Letters*, 100(3):038102, January 2008.

[200] Philip L. Felgner. Particulate systems and polymers for in vitro and in vivo delivery of polynucleotides. *Advanced Drug Delivery Reviews*, 5(3):163–187, September 1990.

[201] Jerome Gilleron, William Querbes, Anja Zeigerer, Anna Borodovsky, Giovanni Marsico, Undine Schubert, Kevin Manygoats, Sarah Seifert, Cordula Andree, Martin Stöter, Hila Epstein-Barash, Ligang Zhang, Victor Koteliansky, Kevin Fitzgerald, Eugenio Fava, Marc Bickle, Yannis Kalaidzidis, Akin Akinc, Martin Maier, and Marino Zerial. Image-based analysis of lipid nanoparticle–mediated siRNA delivery, intracellular trafficking and endosomal escape. *Nature Biotechnology*, 31(7):638–646, July 2013.

[202] Peter Lönn and Steven F Dowdy. Cationic PTD/CPP-mediated macromolecular delivery: charging into the cell. *Expert Opinion on Drug Delivery*, 12(10):1627–1636, October 2015.

[203] William Stillwell. Chapter 19 - Membrane Transport. In William Stillwell, editor, *An Introduction to Biological Membranes (Second Edition)*, pages 423–451. Elsevier, January 2016.

[204] Gaurav Sahay, Daria Y. Alakhova, and Alexander V. Kabanov. Endocytosis of nanomedicines. *Journal of Controlled Release*, 145(3):182–195, August 2010.

[205] C. I. Bouzigues, T.-L. Nguyên, R. Ramodiharilafy, A. Claeson, P.-L. Tharaux, and A. Alexandrou. Regulation of the ROS response dynamics and organization to PDGF motile stimuli revealed by single nanoparticle imaging. *Chemistry & biology*, 21(5):647–656, 2014.

[206] Mitsuru Furusawa, Toshikazu Nishimura, Masaru Yamaizumi, and Yoshio Okada. Injection of foreign substances into single cells by cell fusion. *Nature*, 249(5456):449–450, May 1974.

[207] Ari Helenius, Stephen Doxsey, and Ira Mellman. Viruses as Tools in Drug Delivery. *Annals of the New York Academy of Sciences*, 507(1):1–6, 1987.

[208] Nils Hersch, Benjamin Wolters, Zoltan Ungvari, Tripti Gautam, Dhruva Deshpande, Rudolf Merkel, Anna Csiszar, Bernd Hoffmann, and Agnes Csiszár. Biotin-conjugated fusogenic liposomes for high-quality cell purification. *Journal of Biomaterials Applications*, 30(6):846–856, January 2016.

[209] Sarah Kube, Nils Hersch, Elena Naumovska, Thomas Gensch, Johnny Hendriks, Arne Franzen, Lisa Landvogt, Jan-Peter Siebrasse, Ulrich Kubitscheck, Bernd Hoffmann, Rudolf Merkel, and Agnes Csiszár. Fusogenic Liposomes as Nanocarriers for the Delivery of Intracellular Proteins. *Langmuir : the ACS journal of surfaces and colloids*, 33(4):1051–1059, 2017.

[210] Rejhana Kolašinac, Christian Kleusch, Tobias Braun, Rudolf Merkel, and Agnes Csiszár. Deciphering the Functional Composition of Fusogenic Liposomes. *International Journal of Molecular Sciences*, 19(2), January 2018.

[211] Robert A. Schlegel and Martin C. Rechsteiner. Microinjection of thymidine kinase and bovine serum albumin into mammalian cells by fusion with red blood cells. *Cell*, 5(4):371–379, August 1975.

[212] A Loyter, N Zakai, and R G Kulka. "Ultramicroinjection" of macromolecules or small particles into animal cells. A new technique based on virus-induced cell fusion. *The Journal of Cell Biology*, 66(2):292–304, August 1975.

[213] Kristine S. Louis and Andre C. Siegel. Cell Viability Analysis Using Trypan Blue: Manual and Automated Methods. In J. Martin Stoddart, editor, *Mammalian Cell Viability: Methods and Protocols*, pages 7–12. Humana Press, Totowa, NJ, 2011.

[214] Gregor Malich, Boban Markovic, and Chris Winder. The sensitivity and specificity of the MTS tetrazolium assay for detecting the in vitro cytotoxicity of 20 chemicals using human cell lines. *Toxicology*, 124(3):179–192, 1997.

[215] M. Cemazar, C. S. Parkins, A. L. Holder, D. J. Chaplin, G. M. Tozer, and G. Sersa. Electroporation of human microvascular endothelial cells: evidence for an anti-vascular mechanism of electrochemotherapy. *British journal of cancer*, 84(4):565, 2001.

[216] J. M. Walker. The Bicinchoninic Acid (BCA) Assay for Protein Quantitation. In *The Protein Protocols Handbook*, Springer Protocols Handbooks, pages 11–15. Humana Press, 2009.

[217] Lei Chen, Zhi Yu, Youngju Lee, Xu Wang, Bing Zhao, and Young Mee Jung. Quantitative evaluation of proteins with bicinchoninic acid (BCA): resonance Raman and surface-enhanced resonance Raman scattering-based methods. *The Analyst*, 137(24):5834, 2012.

[218] Koichi Tanaka, Hiroaki Waki, Yutaka Ido, Satoshi Akita, Yoshikazu Yoshida, Tamio Yoshida, and T. Matsuo. Protein and polymer analyses up to m/z 100 000 by laser ionization time-of-flight mass spectrometry. *Rapid Communications in Mass Spectrometry*, 2(8):151–153, 1988. _eprint: https://onlinelibrary.wiley.com/doi/pdf/10.1002/rcm.1290020802.

[219] Emmanuel Barillot, Laurence Calzone, Philippe Hupe, Jean-Philippe Vert, and Andrei Zinovyev. *Computational Systems Biology of Cancer*. CRC Press, 0 edition, August 2012.

[220] Andrea Amantonico, Joo Yeon Oh, Jens Sobek, Matthias Heinemann, and Renato Zenobi. Mass Spectrometric Method for Analyzing Metabolites in Yeast with Single Cell Sensitivity. *Angewandte Chemie International Edition*, 47(29):5382–5385, 2008. _eprint: https://onlinelibrary.wiley.com/doi/pdf/10.1002/anie.200705923.

[221] Trent R. Northen, Oscar Yanes, Michael T. Northen, Dena Marrinucci, Winnie Uritboonthai, Junefredo Apon, Stephen L. Golledge, Anders Nordström, and Gary Siuzdak. Clathrate nanostructures for mass spectrometry. *Nature*, 449(7165):1033–1036, October 2007.

[222] M. Grognot and G. Gallot. Quantitative measurement of permeabilization of living cells by terahertz attenuated total reflection. *Applied Physics Letters*, 107(10):103702, 2015.

[223] Xiujun Zheng and Guilhem Gallot. Dynamics of Cell Membrane Permeabilization by Saponins Using Terahertz Attenuated Total Reflection. *Biophysical Journal*, 119(4):749–755, August 2020.

[224] M. Yamawaki, A. Zurbriggen, A. Richard, and M. Vandevelde. Saponin treatment for in situ hybridization maintains good morphological preservation. *Journal of Histochemistry & Cytochemistry*, 41(1):105–109, 1993.

[225] Joseph Leighton, Larry W. Estes, Sunder Mansukhani, and Zbynek Brada. A cell line derived from normal dog kidney (MDCK) exhibiting qualities of papillary adenocarcinoma and of renal tubular epithelium. *Cancer*, 26(5):1022–1028, 1970.

[226] F. Lang and M. Paulmichl. Properties and regulation of ion channels in MDCK cells. *Kidney Int*, 48(4):1200–1205, 1995.

[227] A. Puliafito, L. Hufnagel, P. Neveu, S. Streichan, A. Sigal, D. K. Fygenson, and B. I. Shraiman. Collective and single cell behavior in epithelial contact inhibition. *Proceedings of the National Academy of Sciences*, 109(3):739–744, 2012.

[228] S. Erlinger and M. H. Saier Jr. Decrease in protein content and cell volume of cultured dog kidney epithelial cells during growth. *In vitro*, 18(3):196–202, 1982.

[229] Julia E. Lever. Regulation of dome formation in differentiated epithelial cell cultures. *Journal of Supramolecular Structure*, 12(2):259–272, 1979.

[230] R. Bacallao, C. Antony, C. Dotti, E. Karsenti, E. H. Stelzer, and K. Simons. The subcellular organization of Madin-Darby canine kidney cells during the formation of a polarized epithelium. *Journal of Cell Biology*, 109(6):2817–2832, December 1989.

[231] Julio L. Sampaio, Mathias J. Gerl, Christian Klose, Christer S. Ejsing, Hartmut Beug, Kai Simons, and Andrej Shevchenko. Membrane lipidome of an epithelial cell line. *Proceedings of the National Academy of Sciences of the United States of America*, 108(5):1903–1907, February 2011.

[232] J. H. Hoh and C.-A. Schoenenberger. Surface morphology and mechanical properties of MDCK monolayers by atomic force microscopy. *Journal of cell science*, 107(5):1105–1114, 1994.

[233] Sandra T. Cooper and Paul L. McNeil. Membrane Repair: Mechanisms and Pathophysiology. *Physiological Reviews*, 95(4):1205–1240, October 2015. WOS:000362670400004.

[234] K.-E. Peiponen, A. Zeitler, and M. Kuwata-Gonokami. *Terahertz spectroscopy and imaging*, volume 171. Springer, 2012.

[235] M.-A. Brun, F. Formanek, A. Yasuda, M. Sekine, N. Ando, and Y. Eishii. Terahertz imaging applied to cancer diagnosis. *Physics in Medicine and Biology*, 55(16):4615–4623, July 2010. Publisher: IOP Publishing.

[236] H. K. V. LOTSCH. Beam displacement at total reflection : The Goos-Hanchen effect I. *OPTIK*, 32(2):116–137, 1970.

[237] Olaf Stenzel. *The Physics of Thin Film Optical Spectra: An Introduction*. Springer Series in Surface Sciences. Springer International Publishing, 2 edition, 2016.

[238] C. Balut and others. Measurement of cytosolic and mitochondrial pH in living cells during reversible metabolic inhibition. *Kidney international*, 73(2):226–232, 2007.

[239] J. J. Gu, Y. F. Yu, E. P. Li, S. H. Ng, P. H. Yap, X. Q. Zhou, T. H. Cheng, and A. Q. Liu. Real-time measurement of cellular refractive index and thickness using cell culture chip. In *12 th International Conference on miniaturized systems for chemistry and life science, Oct 12–16, San Diego, USA*, 2008.

[240] G. Roy and R. Sauvé. Effect of anisotonic media on volume, ion and amino-acid content and membrane potential of kidney cells (MDCK) in culture. *The Journal of membrane biology*, 100(1):83–96, 1987.

[241] D. G. Spiller, R. V. Giles, J. Grzybowski, D. M. Tidd, and . E. Clark. Improving the intracellular delivery and molecular efficacy of antisense oligonucleotides in chronic myeloid leukemia cells: a comparison of streptolysin-O permeabilization, electroporation, and lipophilic conjugation. *Blood*, 91(12):4738–4746, 1998.

[242] Konstantinos Lymperopoulos, Alexander Kiel, Anne Seefeld, Katharina StÃ¶hr, and Dirk-Peter Herten. Fluorescent Probes and Delivery Methods for Single-Molecule Experiments. *ChemPhysChem*, 11(1):43–53, 2010.

[243] J. B. Delehanty, H. Mattoussi, and I. L. Medintz. Delivering quantum dots into cells: strategies, progress and remaining issues. *Analytical and Bioanalytical Chemistry*, 393(4):1091–1105, 2009.

[244] M. Grognot and G. Gallot. Probing living cells composition by THz attenuated total reflection #x2014; Application to quantitative permeabilization measurement. In *2016 41st International Conference on Infrared, Millimeter, and Terahertz waves (IRMMW-THz)*, pages 1–2, September 2016.

[245] K. Medepalli, B. W. Alphenaar, R. S. Keynton, and P. Sethu. A new technique for reversible permeabilization of live cells for intracellular delivery of quantum dots. *Nanotechnology*, 24(20), 2013.

[246] Juliane Deise Fleck, Andresa Heemann Betti, Francini Pereira Da Silva, Eduardo Artur Troian, Cristina Olivaro, Fernando Ferreira, and Simone Gasparin Verza. Saponins from Quillaja saponaria and Quillaja brasiliensis: Particular Chemical Characteristics and Biological Activities. *Molecules*, 24(1):171, January 2019. Number: 1 Publisher: Multidisciplinary Digital Publishing Institute.

[247] Max Mason and Warren Weaver. The Settling of Small Particles in a Fluid. *Physical Review*, 23(3):412–426, March 1924.

[248] Mark Ilton, Christian DiMaria, and Kari Dalnoki-Veress. Direct Measurement of the Critical Pore Size in a Model Membrane. *Physical Review Letters*, 117(25):257801, December 2016. Publisher: American Physical Society.

[249] F. Brochard-Wyart, P. G. de Gennes, and O. Sandre. Transient pores in stretched vesicles: role of leak-out. *Physica A: Statistical Mechanics and its Applications*, 278(1):32–51, April 2000.

[250] Rolf Ryham, Irina Berezovik, and Fredric S. Cohen. Aqueous Viscosity Is the Primary Source of Friction in Lipidic Pore Dynamics. *Biophysical Journal*, 101(12):2929–2938, December 2011.

[251] John Crank and Emeritus Professor John Crank. *The Mathematics of Diffusion*. Clarendon Press, 1979. Google-Books-ID: eHANhZwVouYC.

[252] Wilhelm Magnus, Fritz Oberhettinger, and Raj Pal Soni. *Formulas and Theorems for the Special Functions of Mathematical Physics*. Springer Science & Business Media, November 2013. Google-Books-ID: 2u3nCAAAQBAJ.

[253] John Crank. *The mathematics of diffusion*. Clarendon Press, Oxford, 2. ed., reprint edition, 1976. OCLC: 258428040.

[254] P. Seeman, D. Cheng, and G. H. Iles. Structure of membrane holes in osmotic and saponin hemolysis. *The Journal of Cell Biology*, 56(2):519–527, February 1973.

[255] Kakoli Mitra, Iban Ubarretxena-Belandia, Tomohiko Taguchi, Graham Warren, and Donald M. Engelman. Modulation of the bilayer thickness of exocytic pathway membranes by membrane proteins rather than cholesterol. *Proceedings of the National Academy of Sciences of the United States of America*, 101(12):4083–4088, March 2004.

[256] Mohit Kumar, Mario S. Mommer, and Victor Sourjik. Mobility of Cytoplasmic, Membrane, and DNA-Binding Proteins in Escherichia coli. *Biophysical Journal*, 98(4):552–559, February 2010.

[257] David R. Lide. *CRC Handbook of Chemistry and Physics, 84th Edition*. CRC Press, June 2003. Google-Books-ID: kTnxSi2B2FcC.

[258] H.-J. Hinz, editor. *Thermodynamic Data for Biochemistry and Biotechnology*. Springer-Verlag Berlin Heidelberg, 1986.

[259] I. Mehdi, G. Chattopadhyay, E. Schlecht, J. Ward, J. Gill, F. Maiwald, and A. Maestrini. Terahertz Multiplier Circuits. In *2006 IEEE MTT-S International Microwave Symposium Digest*, pages 341–344, June 2006.

[260] A. Maestrini, J. Ward, J. Gill, H. Javadi, E. Schlecht, G. Chattopadhyay, F. Maiwald, N.R. Erickson, and I. Mehdi. A 1.7-1.9 THz local oscillator source. *IEEE Microwave and Wireless Components Letters*, 14(6):253–255, June 2004.

[261] Benjamin S. Williams. Terahertz quantum-cascade lasers. *NATURE PHOTONICS*, 1(9):517–525, September 2007.

[262] B.S. Williams, S. Kumar, Q. Hu, and J.L. Reno. High-power terahertz quantum-cascade lasers. *Electronics Letters*, 42(2):89–91, January 2006. Conference Name: Electronics Letters.

[263] Erik Bründermann, Martina Havenith, Giacomo Scalari, Marcella Giovannini, Jérôme Faist, Johannes Kunsch, Lars Mechold, and Mario Abraham. Turn-key compact high temperature terahertz quantum cascade lasers: imaging and room temperature detection. *Optics Express*, 14(5):1829, 2006.

[264] Juraj Darmo, Vincas Tamosiunas, Gernot Fasching, Josef Kroll, Karl Unterrainer, Mattias Beck, Marcella Giovannini, Jerome Faist, Christian Kremser, and Paul Debbage. Imaging with a Terahertz quantum cascade laser. *Optics Express*, 12(9):1879, 2004.

[265] Masayoshi Tonouchi. Cutting-edge terahertz technology. *NATURE PHOTONICS*, 1(2):97–105, February 2007.

[266] A. Barkan, F. K. Tittel, D. M. Mittleman, R. Dengler, P. H. Siegel, G. Scalari, L. Ajili, J. Faist, H. E. Beere, E. H. Linfield, A. G. Davies, and D. A. Ritchie. Linewidth and tuning characteristics of terahertz quantum cascade lasers. *Optics Letters*, 29(6):575, March 2004.

[267] Benjamin S. Williams. Terahertz quantum-cascade lasers. *NATURE PHOTONICS*, 1(9):517–525, September 2007.

[268] Alan Wei Min Lee, Benjamin S. Williams, Sushil Kumar, Qing Hu, and John L. Reno. Tunable terahertz quantum cascade lasers with external gratings. *Optics Letters*, 35(7):910, April 2010.

[269] Orazio Svelto and David C. Hanna. *Principles of lasers*. Springer, New York, NY, 5. ed edition, 2010. OCLC: 699877195.

[270] K Wang and RR Reeber. The perfect crystal, thermal vacancies and the thermal expansion coefficient of aluminium. *PHILOSOPHICAL MAGAZINE A-PHYSICS OF CONDENSED MATTER STRUCTURE DEFECTS AND MECHANICAL PROPERTIES*, 80(7):1629–1643, July 2000.

[271] R. A. Cheville and D. Grischkowsky. Far-infrared foreign and self-broadened rotational linewidths of high-temperature water vapor. *Journal of the Optical Society of America B*, 16(2):317, February 1999.

[272] Robert Hull. *Properties of Crystalline Silicon*. IET, 1999. Google-Books-ID: C_TWB_0rRLgC.

[273] M. Balarin. Properties of Silicon. EMIS Datareviews Series No. 4. Einführung: C. Hilsum, Vorwort: T. H. Ning, INSPEC, The Institution of Electrical Engineering, London, New York 1988, 31 Kapitel, 1100 Seiten, 260 Datareviews, £ 195, ISBN 0-85296-4757. *Crystal Research and Technology*, 24(4):386–386, 1989. _eprint: https://onlinelibrary.wiley.com/doi/pdf/10.1002/crat.2170240410.

[274] Cecilie Ro/nne, Lars Thrane, Per-Olof Åstrand, Anders Wallqvist, Kurt V. Mikkelsen, and So/ren R. Keiding. Investigation of the temperature dependence of dielectric relaxation in liquid water by THz reflection spectroscopy and molecular dynamics simulation. *The Journal of Chemical Physics*, 107(14):5319–5331, October 1997.

[275] G. Cocorullo, F. G. Della Corte, and I. Rendina. Temperature dependence of the thermo-optic coefficient in crystalline silicon between room temperature and 550 K at the wavelength of 1523 nm. *Applied Physics Letters*, 74(22):3338–3340, May 1999.

[276] Atsushi Nakanishi, Takashi Yasuda, Kazuki Horita, and Hironori Takahashi. Tunable Terahertz Device Using Refractive Index Control. *Journal of Infrared, Millimeter, and Terahertz Waves*, 39(1):36–44, January 2018.

[277] Kareem Garriga Francis, Mervin Lim Pac Chong, Yiwen E, and Xi-Cheng Zhang. Terahertz Nonlinear Index Extraction via Full-Phase Analysis. *Optics Letters*, August 2020.

[278] Florin Garoi, Cristian Udrea, Cristian Damian, Petronela Prepelita, and Daniela Coltuc. THz Laser Beam Profiling by Homogeneous Photodoping of High Resistivity Silicon in a Compact Single-Pixel Detection Setup. *IEEE Transactions on Terahertz Science and Technology*, 9(2):200–208, March 2019.

[279] Simon M. Sze and Kwok K. Ng. *Physics of Semiconductor Devices*. John Wiley & Sons, November 2006. Google-Books-ID: o4unkmHBHb8C.

[280] T. F. Ciszek, Tihu Wang, T. Schuyler, and A. Rohatgi. Some Effects of Crystal Growth Parameters on Minority Carrier Lifetime in Float-Zoned Silicon. *Journal of The Electrochemical Society*, 136(1):230, January 1989. Publisher: IOP Publishing.

[281] N. E. Grant, F. E. Rougieux, D. Macdonald, J. Bullock, and Y. Wan. Grown-in defects limiting the bulk lifetime of p-type float-zone silicon wafers. *Journal of Applied Physics*, 117(5):055711, February 2015. Publisher: American Institute of Physics.

[282] Hiroto Kobayashi, Ryo Yokogawa, Kosuke Kinoshita, Yohichiroh Numasawa, Atsushi Ogura, Shin-ichi Nishizawa, Takuya Saraya, Kazuo Ito, Toshihiko Takakura, Shin-ichi Suzuki, Munetoshi Fukui, Kiyoshi Takeuchi, and Toshiro Hiramoto. Evaluations of minority carrier lifetime in floating zone Si affected by Si insulated gate bipolar transistor processes. *Japanese Journal of Applied Physics*, 58(SB):SBBD07, February 2019. Publisher: IOP Publishing.

[283] Y. Levy and J. N. Onuchic. Water mediation in protein folding and molecular recognition. *Annu. Rev. Biophys. Biomol. Struct.*, 35:389–415, 2006.

[284] J. Kitagawa, T. Ohkubo, M. Onuma, and Y. Kadoya. THz spectroscopic characterization of biomolecule/water systems by compact sensor chips. *Applied Physics Letters*, 89(4):041114, 2006.

[285] R. H. Henchman and J. A. McCammon. Structural and dynamic properties of water around acetylcholinesterase. *Protein Sci.*, 11:2080–2090, 2002.

[286] C. Mattea, J. Qvist, and B. Halle. Dynamics at the Protein-Water Interface from 17O Spin Relaxation in Deeply Supercooled Solutions. *Biophys. J.*, 95:2951–2963., 2008.

[287] R. G. Bryant. Dynamics of water in and around proteins characterized by 1H-spin-lattice relaxometry. *C. R. Phys.*, 11:128–135, 2010.

[288] P. Mukherjee, I. Kass, I. Arkin, and M. T. Zanni. Picosecond dynamics of a membrane protein revealed by 2D IR. *Proc Natl Acad Sci U S A*, 103(10):3528–3533, 2006.

[289] Nilashis Nandi and Biman Bagchi. Dielectric Relaxation of Biological Water †. *The Journal of Physical Chemistry B*, 101(50):10954–10961, December 1997.

[290] T. Arikawa, M. Nagai, and K. Tanaka. Characterizing hydration state in solution using terahertz time-domain attenuated total reflection spectroscopy. *Chemical Physics Letters*, 457(1-3):12–17, 2008.

[291] B. Born, S. J. Kim, S. Ebbinghaus, M. Gruebele, and M. Havenith. The terahertz dance of water with the proteins: the effect of protein flexibility on the dynamical hydration shell of ubiquitin. *Faraday Discuss.*, 141:161–173, 2009.

[292] B. Born and M. Havenith. Terahertz Dance of Proteins and Sugars with Water. *Journal of Infrared, Millimeter, and Terahertz Waves*, 2009.

[293] M. Heyden, E. Bründermann, U. Heugen, G. Niehues, D. M. Leitner, and M. Havenith. Long-Range Influence of Carbohydrates on the Solvation Dynamics of Water—Answers from Terahertz Absorption Measurements and Molecular Modeling Simulations. *Journal of the American Chemical Society*, 130(17):5773–5779, April 2008. Publisher: American Chemical Society.

[294] O. RAAB. Uber die wirkung Fluorescirender Stoffe auf Infusorien. *Z. Biol.*, 39:524–546, 1900.

[295] H. VON TAPPEINER. Therapeutische Versuche mit fluoreszierenden Stoffen. *Munch Med Wochenschr*, 1:2042–2044, 1903.

[296] Niels R. Finsen. The Red Light Treatment of Small-Pox. *British Medical Journal*, 2(1823):1412–1414, December 1895.

[297] H VON TAPPEINER. Ueber wirking der photodynamichen (fluorescierenden) Stoffe auf Protozoan und Enzyme. *Dtsch Arch Klin Med*, 80:427–487, 1904.

[298] J.V. Moore. Photodynamic Therapy: Basic Principles and Clinical Applications. *British Journal of Cancer*, 68(6):1257, December 1993.

[299] Peter Meisel and Thomas Kocher. Photodynamic therapy for periodontal diseases: State of the art. *Journal of Photochemistry and Photobiology B: Biology*, 79(2):159–170, May 2005.

[300] Laure Gibot, Arnaud Lemelle, Ugo Till, Béatrice Moukarzel, Anne-Françoise Mingotaud, Véronique Pimienta, Pascale Saint-Aguet, Marie-Pierre Rols, Mireille Gaucher, Frédéric Violleau, Christophe Chassenieux, and Patricia Vicendo. Polymeric Micelles Encapsulating Photosensitizer: Structure/Photodynamic Therapy Efficiency Relation. *Biomacromolecules*, 15(4):1443–1455, April 2014.

[301] Sulbha K. Sharma, Pawel Mroz, Tianhong Dai, Ying-Ying Huang, Tyler G. St. Denis, and Michael R. Hamblin. Photodynamic Therapy for Cancer and for Infections: What Is the Difference? *Israel journal of chemistry*, 52(8-9):691–705, September 2012.

[302] Annelies S. L. Derycke and Peter A. M. de Witte. Liposomes for photodynamic therapy. *Advanced Drug Delivery Reviews*, 56(1):17–30, January 2004.

[303] Pierre Couleaud, Vincent Morosini, Céline Frochot, Sébastien Richeter, Laurence Raehm, and Jean-Olivier Durand. Silica-based nanoparticles for photodynamic therapy applications. *Nanoscale*, 2(7):1083–1095, July 2010. Publisher: The Royal Society of Chemistry.

[304] D. Le Garrec, J. Taillefer, J.E. Van Lier, V. Lenaerts, and J.-C. Leroux. Optimizing pH-responsive Polymeric Micelles for Drug Delivery in a Cancer Photodynamic Therapy Model. *Journal of Drug Targeting*, 10(5):429–437, January 2002.

[305] J. Taillefer, N. Brasseur, J. E. van Lier, V. Lenaerts, D. Le Garrec, and J.-C. Leroux. In-vitro and in-vivo evaluation of pH-responsive polymeric micelles in a photodynamic cancer therapy model. *Journal of Pharmacy and Pharmacology*, 53(2):155–166, 2001. _eprint: https://onlinelibrary.wiley.com/doi/pdf/10.1211/0022357011775352.

[306] Woo-Dong Jang, Nobuhiro Nishiyama, Guo-Dong Zhang, Atsushi Harada, Dong-Lin Jiang, Satoko Kawauchi, Yuji Morimoto, Makoto Kikuchi, Hiroyuki Koyama, Takuzo Aida, and Kazunori Kataoka. Supramolecular Nanocarrier of Anionic Dendrimer Porphyrins with Cationic Block Copolymers Modified with Polyethylene Glycol to Enhance Intracellular Photodynamic Efficacy. *Angewandte Chemie International Edition*, 44(3):419–423, 2005. _eprint: https://onlinelibrary.wiley.com/doi/pdf/10.1002/anie.200461603.

[307] Nobuhiro Nishiyama, Yuji Morimoto, Woo-Dong Jang, and Kazunori Kataoka. Design and development of dendrimer photosensitizer-incorporated polymeric micelles for enhanced photodynamic therapy. *Advanced Drug Delivery Reviews*, 61(4):327–338, April 2009.

[308] L. Santamaria and G. Prino. List of the photodynamic substances. *Research Progress in Organic, Biological and Medicinal Chemistry*, 3 Pt 1:XI–XXXV, 1972.

[309] Tilahun Ayane Debele, Sydney Peng, and Hsieh-Chih Tsai. Drug Carrier for Photodynamic Cancer Therapy. *International Journal of Molecular Sciences*, 16(9):22094–22136, September 2015.

[310] J. Moan. Properties for optimal PDT sensitizers. *Journal of Photochemistry and Photobiology B: Biology*, 5(3):521–524, May 1990.

[311] Alexandra B. Ormond and Harold S. Freeman. Dye Sensitizers for Photodynamic Therapy. *Materials*, 6(3):817–840, March 2013.

[312] Clemens Fritsch, Günter Goerz, and Thomas Ruzicka. Photodynamic Therapy in Dermatology. *Archives of Dermatology*, 134(2):207–214, February 1998. Publisher: American Medical Association.

[313] Pablo Fonda-Pascual, Oscar M. Moreno-Arrones, Adrian Alegre-Sanchez, David Saceda-Corralo, Diego Buendia-Castaño, Cristina Pindado-Ortega, Pablo Fernandez-Gonzalez, Kyra Velazquez-Kennedy, María I. Calvo-Sánchez, Antonio Harto-Castaño, Bibiana Perez-Garcia, Lorea Bagazgoitia, Sergio Vaño-Galvan, Jesus Espada, and Pedro Jaen-Olasolo. In situ production of ROS in the skin by photodynamic therapy as a powerful tool in clinical dermatology. *Methods*, 109:190–202, October 2016.

[314] David Kessel and Christopher J. Dutton. Photodynamic Effects: Porphyrin Vs Chlorin. *Photochemistry and Photobiology*, 40(3):403–405, 1984. _eprint: https://onlinelibrary.wiley.com/doi/pdf/10.1111/j.1751-1097.1984.tb04607.x.

[315] B. Roeder, D. Naether, T. Lewald, M. Braune, C. Nowak, and W. Freyer. Photophysical properties and photodynamic activity in vivo of some tetrapyrroles. *Biophysical Chemistry*, 35(2):303–312, April 1990.

[316] John Trachtenberg, Robert A. Weersink, Sean R.H. Davidson, Masoom A. Haider, Arjen Bogaards, Mark R. Gertner, Andrew Evans, Avigdor Scherz, Joanne Savard, Joseph L. Chin, Brian C. Wilson, and Mostafa Elhilali. Vascular-targeted photodynamic therapy (padoporfin, WST09) for recurrent prostate cancer after failure of external beam radiotherapy: a study of escalating light doses. *BJU International*, 102(5):556–562, September 2008. Publisher: John Wiley & Sons, Ltd.

[317] Anna M. Wu, Wengang Chen, Andrew Raubitschek, Lawrence E. Williams, Michael Neumaier, Rainer Fischer, Shi-zhen Hu, Tamara Odom-Maryon, Jeffrey Y. C. Wong, and John E. Shively. Tumor localization of anti-CEA single-chain Fvs: improved targeting by non-covalent dimers. *Immunotechnology*, 2(1):21–36, February 1996.

[318] GP Adams, R Schier, AM McCall, RS Crawford, EJ Wolf', LM Weiner', and JD Marks. Prolonged in vivo tumour retention of a human diabody targeting the extracellular domain of human HER2Ineu. *British Journal of Cancer*, page 8, 1998.

[319] Kuan Chen, Annegret Preuß, Steffen Hackbarth, Matthias Wacker, Klaus Langer, and Beate Röder. Novel photosensitizer-protein nanoparticles for Photodynamic therapy: Photophysical characterization and in vitro investigations. *Journal of Photochemistry and Photobiology B: Biology*, 96(1):66–74, July 2009.

[320] H. MAEDA. Polymer conjugated macromolecular drugs for tumor-specific targeting. *Polymeric Site-specific Pharmacotherapy.*, pages 95–116, 1994. Publisher: John Wiley & Sons Ltd.

[321] Yasuhiro Matsumura and Hiroshi Maeda. A New Concept for Macromolecular Therapeutics in Cancer Chemotherapy: Mechanism of Tumoritropic Accumulation of Proteins and the Antitumor Agent Smancs. page 7.

[322] Patrick Ming-Kuen Tang, Xiao-Zhuo Liu, Dong-Mei Zhang, Wing-Ping Fong, and Kwok-Pui Fung. Pheophorbide a based photodynamic therapy induces apoptosis via mitochondrial-mediated pathway in human uterine carcinosarcoma. *Cancer Biology & Therapy*, 8(6):533–539, March 2009.

[323] Katrin Knop, Anne-Françoise Mingotaud, Naram El-Akra, Frédéric Violleau, and Jean-Pierre Souchard. Monomeric pheophorbide(a)-containing poly(ethyleneglycol-b-ε-caprolactone) micelles for photodynamic therapy. *Photochemical & Photobiological Sciences*, 8(3):396, 2009.

[324] Jérôme Ehrhart, Anne-Françoise Mingotaud, and Frédéric Violleau. Asymmetrical flow field-flow fractionation with multi-angle light scattering and quasi elastic light scattering for characterization of poly(ethyleneglycol-b-ε-caprolactone) block copolymer self-assemblies used as drug carriers for photodynamic therapy. *Journal of Chromatography A*, 1218(27):4249–4256, July 2011.

[325] Laure Gibot, Maxime Demazeau, Véronique Pimienta, Anne-Françoise Mingotaud, Patricia Vicendo, Fabrice Collin, Nathalie Martins-Froment, Stéphane Dejean, Benjamin Nottelet, Clément Roux, and Barbara Lonetti. Role of Polymer Micelles in the Delivery of Photodynamic Therapy Agent to Liposomes and Cells. *Cancers*, 12(2):384, February 2020. Number: 2 Publisher: Multidisciplinary Digital Publishing Institute.

[326] Ugo Till, Laure Gibot, Anne-Françoise Mingotaud, Jérôme Ehrhart, Luc Wasungu, Christophe Mingotaud, Jean-Pierre Souchard, Alix Poinso, Marie-Pierre Rols, Frédéric Violleau, and Patricia Vicendo. Drug Release by Direct Jump from Poly(ethylene-glycol-b-ε-caprolactone) Nano-Vector to Cell Membrane. *Molecules*, 21(12):1643, November 2016.

[327] Rachid Kerdous, Franck Sureau, Aurélien Bour, and Stéphanie Bonneau. Release kinetics of an amphiphilic photosensitizer by block-polymer nanoparticles. *International Journal of Pharmaceutics*, 495(2):750–760, November 2015.

[328] Pavel Kubát, Petr Henke, Rahul Kumar Raya, Miroslav Štěpánek, and Jiří Mosinger. Polystyrene and Poly(ethylene glycol)-b-Poly(ε-caprolactone) Nanoparticles with Porphyrins: Structure, Size, and Photooxidation Properties. *Langmuir*, December 2019. Publisher: American Chemical Society.

[329] Xiujun Zheng and Guilhem Gallot. High precision, high stability, dual modulation terahertz ATR sensor. (In preparation).

[330] Xiujun Zheng and Guilhem Gallot. PDT investigating on living cells using terahertz ATR sensing. (In preparation).

ECOLE DOCTORALE

Titre : Sonder des cellules vivantes par térahertz a atténué la réflexion totale : dynamique de perméabilisation de la membrane cellulaire.

Mots clés : térahertz, perméabilisation, detergent, réflexion totale atténuée, thérapie photodynamique

Résumé : Le rayonnement térahertz se situe dans la gamme électromagnétique entre l'infrarouge lointain et les micro-ondes, avec des fréquences entre 0.1 et 10 THz. Dans le domaine de la biologie, la gamme térahertz permet de quantifier et de discriminer des solutés d'intérêt biologique grâce à l'interaction avec les modes de vibration de l'eau liquide, et d'étudier les systèmes biologiques dans leur environnement physiologique. Nous avons dans un premier temps étudié la perméabilisation membranaire de cellules épithéliales soumis à un détergent, la saponine, qui crée des trous dans la membrane cellulaire. Les dynamiques obtenus ont ensuite été comparées à un modèle théorique décrivant le comportement physique de la couche cellulaire, et prenant en compte la diffusion des molécules de détergent ainsi que les caractéristiques physiques de la membrane. Dans un second temps, nous avons développé un système totalement nouveau, basé sur une source QCL continue térahertz à 2,5 THz. Ce nouvel instrument est avec un seul prisme ATR et un seul détecteur, et sur une double modulation du faisceau térahertz à l'aide d'un hacheur mécanique. La stabilité à long terme de cet appareil a été grandement améliorée grâce au contrôle précis de la température et de l'humidité à l'intérieur de l'appareil. Une sensibilité au moins 20 fois supérieure à celle de la littérature existante a ainsi été obtenue. Grâce à ce nouveau système très performant, nous avons étudié la dynamique de la perméabilisation des membranes suite à l'action de la thérapie photodynamique (PDT). Les premiers résultats ont montré que l'encapsulation des photosensibilisateurs par des vecteurs micellaires améliore significativement l'efficacité de la PDT.

Title : Probing living cells by terahertz attenuated total reflection: permeabilization dynamics of the cell membrane.

Keywords : terahertz, permeabilization, detergent, attenuated total reflection, photodynamic therapy

Abstract : Terahertz radiation is located in the electromagnetic range between far infrared and microwaves, corresponding to frequencies between 0.1 and 10 THz. This spectral range is currently largely underexploited, but its application to the study of biological objects has already shown a strong potential, in the detection of skin cancer, ion flow monitoring or biosensors. In the field of biology, which is of particular interest to us here, the terahertz range makes it possible to quantify and discriminate solutes of biological interest thanks to the interaction with low-frequency modes of liquid water, and thus to study biomolecules, microorganisms and cells in their physiological environment. The first part of this thesis work consisted in studying the dynamics of membrane permeabilization of living cells by attenuated total reflection (ATR) with our device based on a femtosecond laser and the generation of ultrashort terahertz pulses. Monolayers of MDCK epithelial cells were exposed to varying concentrations of saponin, a detergent that digs holes in the cell membrane. The dynamics obtained were then compared to a theoretical model describing the physical behavior of the cell layer, taking into account the diffusion of detergent molecules and the physical characteristics of the membrane. The good agreement between experiment and theory indicates that membrane permeabilization is limited mainly by the diffusion of detergent molecules and their binding to the membrane. In a second part, we developed a completely new system based on a continuous terahertz QCL source at 2.5 THz. This new instrument is based on a very simplified design, with a single ATR prism and a single detector, and on the dual modulation of the terahertz beam using a mechanical chopper. This chopper synchronizes the dual modulation and defines the measurement and reference zones. The long-term stability of this device has been greatly enhanced by the precise control of temperature and humidity inside the device. Performance is excellent in both the short and long term. A signal-to-noise ratio of 30 dB is achieved over 300ms, and remains above 30 dB for several hours. In addition, a theoretical and experimental study has been carried out to calibrate the instrument. Thus, the ATR reflection coefficients of several solutions of biological interest (ions, sugars and proteins) were obtained over a wide range of concentrations. A sensitivity at least 20 times higher than that of the existing literature was thus obtained. Thanks to this new high-performance system, we studied the dynamics of membrane permeabilization following the action of photodynamic therapy (PDT). The first results showed that the encapsulation of photosensitizers by micellar vectors significantly improves the efficiency of PDT.

Institut Polytechnique de Paris
91120 Palaiseau, France